

---

A study of  $^8\text{Be}$ ,  $^{12}\text{C}$  and  $^{27}\text{Al}$   
with state-of-the-art detector arrays

Michael Munch

---

---

PhD Dissertation

Department of Physics and Astronomy  
Aarhus University  
Denmark

Department of Physics  
University of York  
United Kingdom

Michael Munch  
Department of Physics and Astronomy  
Aarhus University  
Ny Munkegade 120, Building 1520  
8000 Aarhus C  
Denmark

© Michael Munch 2018  
Revision 9f574cf dated 2018-12-14.

A study of  $^8\text{Be}$ ,  $^{12}\text{C}$  and  $^{27}\text{Al}$   
with state-of-the-art detector arrays

A Dissertation Presented to the  
Faculty of Sciences of University of York and the  
Faculty of Science and Technology of Aarhus University  
in Partial Fulfillment of the Requirements  
for the PhD Degree

by  
Michael Munch  
October 2018



*We can hope to see the growth of nuclear physics through studies of a particular isotope or mass system. Given this point of view,  $^8\text{Be}$  is a worthy choice, very likely the best.*

*Louis Brown,  
“Beryllium-8 — A History of Nuclear Physics”, unpublished [1].*



# Contents

<b>Contents</b>	<b>i</b>
<b>Author's Declaration</b>	<b>v</b>
<b>Abstract</b>	<b>vii</b>
<b>Resumé</b>	<b>ix</b>
<b>Acknowledgments</b>	<b>xi</b>
<b>List of Publications</b>	<b>xiii</b>
<b>1 Preface</b>	<b>1</b>
<b>I Physics</b>	<b>3</b>
<b>2 <math>^{23}\text{Na}(\alpha, p)^{26}\text{Mg}</math> reaction rate at astrophysically relevant energies</b>	<b>5</b>
2.1 Motivation . . . . .	5
2.2 Method . . . . .	8
2.3 Results and discussion . . . . .	10
2.4 Astrophysical impact . . . . .	12

2.5	Contributions . . . . .	12
	Paper 1 . . . . .	13
<b>3</b>	<b>Independent measurement of the Hoyle state <math>\beta</math> feeding from <math>^{12}\text{B}</math> using Gammasphere</b>	<b>19</b>
3.1	Nuclear structure . . . . .	19
3.2	Second $2^+$ . . . . .	25
3.3	Hoyle state radiative decay . . . . .	28
3.4	Method . . . . .	30
3.5	Results and discussion . . . . .	32
3.6	Outlook . . . . .	32
3.7	Contribution . . . . .	33
	Paper 2 . . . . .	35
<b>4</b>	<b>Measurement of the full excitation spectrum of the <math>^7\text{Li}(p, \gamma)\alpha\alpha</math> reaction at 441keV</b>	<b>41</b>
4.1	Motivation . . . . .	41
4.2	Resonances and the continuum . . . . .	45
4.3	Prior work . . . . .	48
4.4	Indirect detection of $\gamma$ -rays . . . . .	53
4.5	Method . . . . .	54
4.6	Data reduction . . . . .	57
4.7	R-matrix . . . . .	57
4.8	Result and discussion . . . . .	59
4.9	Conclusion and outlook . . . . .	62
4.10	Contribution . . . . .	63
	Paper 3 . . . . .	65
	Appendix . . . . .	71
<b>5</b>	<b>The partial widths of the 16.1 MeV <math>2^+</math> state in <math>^{12}\text{C}</math></b>	<b>75</b>
5.1	Motivation . . . . .	75
5.2	The triple- $\alpha$ break-up . . . . .	78
5.3	The 16.1 MeV state . . . . .	83
5.4	Method . . . . .	84



5.5	Results and discussion . . . . .	87
5.6	Conclusion and outlook . . . . .	89
5.7	Contribution . . . . .	90
	Paper 4 . . . . .	91
<b>II Technique</b>		<b>99</b>
<b>6</b>	<b>AUSALib</b>	<b>101</b>
6.1	Detector abstraction . . . . .	102
6.2	Setup file . . . . .	104
6.3	Analysis pipeline . . . . .	105
6.4	Energy loss . . . . .	110
6.5	Calibration . . . . .	112
6.6	Conclusion and outlook . . . . .	117
6.7	Contribution . . . . .	117
<b>7</b>	<b>Data acquisition</b>	<b>119</b>
7.1	Front-end . . . . .	120
7.2	Acquisition control . . . . .	122
7.3	Readout . . . . .	125
7.4	Multiple crates . . . . .	126
7.5	Back-end . . . . .	127
7.6	DaqC . . . . .	129
7.7	Monitoring . . . . .	131
7.8	RunDB and RUP . . . . .	133
7.9	Alternatives . . . . .	134
7.10	Toggle mode . . . . .	135
7.11	Conclusion and outlook . . . . .	136
7.12	Contribution . . . . .	137
	Paper 5 . . . . .	139
<b>8</b>	<b>Summary and outlook</b>	<b>149</b>

<b>List of Figures</b>	<b>151</b>
<b>Abbreviations</b>	<b>159</b>
<b>Bibliography</b>	<b>161</b>

## Author's Declaration

I declare that this thesis is a presentation of original work and I am the sole author. This work has not previously been presented for an award at this, or any other, University. All sources are acknowledged as References.



# Abstract

This thesis reports on the results of four different experiments carried out at either Argonne National Laboratory or Aarhus University.

The first experiment was a cross section measurement of the  $^{23}\text{Na}(\alpha, p)$  reaction at astrophysical energies. This reaction acts as a proton source for the  $^{25}\text{Mg}(p, \gamma)^{26}\text{Al}$  reaction in asymptotic giant branch stars and  $^{26}\text{Al}$  is an direct observable of ongoing nucleosynthesis. Prior to this experiment a different group published the surprising result, that the cross section should be scaled up by a factor of 40. However, the present experiment was unable to reproduce this, and was instead a confirmation of the established statistical model.

The second experiment was a measurement of the  $\beta$  feeding of the Hoyle state from the  $^{12}\text{B}$  ground state. This experiment was carried out at Gammasphere in order to provide independent confirmation of a previous result obtained using charged particle spectroscopy, which disagreed from measurement performed in the seventies by roughly a factor of 2. The value of  $\beta$  feeding is an important constraint in the  $\beta$  decay studies of the  $2^+$  excitation of the Hoyle state. The result of the present experiment was a confirmation of the previous result.

In the third experiment the  $^8\text{Be}$  excitation spectrum, following the  $\gamma$  decay of the 17.6 MeV  $1^+$  state, was measured using charged particles. This technique yields unparalleled detection efficiency, resolution, and dynamic range allowing the resulting spectrum to be analyzed using R-matrix theory.

The results of this analysis were improved  $\gamma$  decay widths and a tentative broad  $0^+$  resonance at 12 MeV.

The last experiment was a measurement of the  $^{11}\text{B}(p, 3\alpha)$  cross section at an energy corresponding to the 16.1 MeV  $2^+$  state in  $^{12}\text{C}$ . For this state there exist multiple inconsistent measurements of its decay properties, and a majority of these inconsistencies can be traced to ambiguities in the normalization. With this experiment the normalization issue was circumvented by measuring the final state in full kinematics. The result was an improved cross section for this resonance and a suggestion to rescale the recommended cross section for  $^{11}\text{B}(p, 3\alpha)$  by a factor of 2/3 over the full energy range. This impacts the recommended reaction rate by NACRE and NACRE II, which should be scaled by roughly a factor of 2.

In addition to these experiments, this thesis reports on the technical development carried out at Aarhus University. Specifically, an analysis library for the analysis of nuclear physics experiment with silicon detectors was developed. This library is built on the concept of an analysis pipeline. Secondly, the Aarhus data acquisition has been rebuilt from the ground up. The different components and recent development allowing significantly higher rates will be presented.

# Resumé

Denne afhandling beskriver resultaterne opnået ved fire forskellige eksperimenter udført ved enten Aarhus Universitet eller Argonne National Laboratory.

Det første eksperiment var en måling af tværsnittet for  $^{23}\text{Na}(\alpha, p)$  ved energier relevant for astrofysik. Denne reaktion fungerer som en protonkilde for  $^{25}\text{Mg}(p, \gamma)^{26}\text{Al}$  reaktioner i asymptotiske kæmpestjerner. Produktionen af  $^{26}\text{Al}$  er interessant, da observationer af henfaldet af denne isotop beviser, at der stadig foregår kernesyntese i verdensrummet. Eksperimentet verificerede den hidtil brugte statistiske model.

Det andet eksperiment bestemte forgreningsforholdet for  $\beta$ -henfald af grundtilstanden af  $^{12}\text{B}$  til Hoyletilstanden. Dette forgreningsforhold var tidligere blevet målt med siliciumdetektorer. Med henblik på at opnå en uafhængig måling, blev dette eksperiment istedet udført med germaniumdetektorer; specifikt Gammasphere. Forgreningsforholdet for  $\beta$ -henfald til Hoyletilstanden er en vigtig restriktion i jagten på  $2^+$  excitationen af Hoyletilstanden. Resultatet bekræftede den tidligere måling.

I det tredje eksperiment blev excitationsspektret for  $^8\text{Be}$ , populæret ved  $\gamma$ -henfaldet af  $17.6\text{ MeV } 1^+$  tilstanden, bestemt ved måling af ladede partikler. Denne metode har en væsentlig forbedret detektionseffektivitet, opløsning og dynamisk rækkevidde ift. tidligere anvendte metoder. Dette tillod at det målte spektrum blev analyseret med R-matrix teori. Resultatet af eksperimentet var en forbedring af partielle  $\gamma$ -bredder og en mulig

observation af en  $0^+$  tilstand i  $^8\text{Be}$  ved 12 MeV.

Det sidste eksperiment var en måling af tværsnittet for  $^{11}\text{B}(p, 3\alpha)$  reaktionen for 16.1 MeV  $2^+$  tilstanden i  $^{12}\text{C}$ . Der har været adskillige tidligere målinger ved denne resonans, men de er alle inkonsistente. En kritisk gennemgang af disse viste, at inkonsistensen primært skyldtes forskellige valg af normalisering. I vores eksperiment blev dette problem omgået ved at måle alle partikler i sluttilstanden. Resultatet var en forbedret måling af tværsnittene for denne tilstand og en anbefaling om at reskalere NACRE-reaktionsraten med en faktor 2.

Ud over de fire eksperimenter beskriver afhandlingen også det tekniske udviklingsarbejde, som er blevet udført ved Aarhus Universitet. Det drejer sig om et analysebibliotek til eksperimenter indenfor kernefysik. Dette er baseret på konceptet om en analyse pipeline, som betydeligt letter analysearbejdet. Udover dette beskrives også de forskellige komponenter af datatagningssystemet, der bruges ved 5 MV acceleratoren ved Aarhus Universitet. Dette er blevet genopbygget fra bunden for at kunne håndtere væsentligt højere rater.



# Acknowledgments

Above all, I would like to thank my supervisor Hans Fynbo and supervisor in all but name Karsten Riisager. Your door is always open and this work is that much greater for it.

I am deeply indebted to Håkan Johansson, who took me under his wing and introduced me to the intricate world of data acquisition. By now you have probably answered a few thousand emails. I am also most thankful for your insightful comments on this manuscript. In this regard, I also owe thanks to Hans Törnqvist and Bastian Löher, who shared their little masterpiece, `nurdlib`, with me. This allowed me to hit the ground running when building my first `f_user`.

The results obtained in this thesis would not have been possible if not for a strong collaboration within the subatomic group. For this, I am grateful for many fruitful discussions with Jesper Halkjær, Oliver Kirsebom, Alan Howard, Jonas Refsgaard and Jacobus Swartz.

A big thanks to Erik Loft Larsen and Frank Daugaard is also in its place. The 5 MV accelerator is only still running due to their endless patience.

Last but not least, I am endlessly grateful for the love and support from my wife Anne-Sofie with a guy rambling about  $\alpha$  particles and pointers.

*Michael Munch,  
Aarhus, April 10, 2019.*



# List of Publications

The following manuscripts form part of this thesis

1. A. M. Howard, **M. Munch**, H. O. U. Fynbo, O. S. Kirsebom, K. L. Laursen, C. A. Diget, and N. J. Hubbard  *$^{23}\text{Na}(\alpha, p)^{26}\text{Mg}$  Reaction Rate at Astrophysically Relevant Energies*. *Physical Review Letters*, 115(5) (2015), p. 52701. DOI: 10.1103/PhysRevLett.115.052701 ARXIV: 1506.05983
2. **M. Munch**, M. Alcorta, H. O. U. Fynbo, M. Albers, S. Almaraz-Calderon, M. L. Avila, A. D. Ayangeakaa, B. B. Back, P. F. Bertone, P. F. F. Carnelli, M. P. Carpenter, C. J. Chiara, J. A. Clark, B. DiGiovine, J. P. Greene, J. L. Harker, C. R. Hoffman, N. J. Hubbard, C. L. Jiang, O. S. Kirsebom, T. Lauritsen, K. L. Laursen, S. T. Marley, C. Nair, O. Nusair, D. Santiago-Gonzalez, J. Sethi, D. Seweryniak, R. Talwar, C. Ugalde and S. Zhu *Independent measurement of the Hoyle state  $\beta$  feeding from  $^{12}\text{B}$  using Gammasphere*. *Physical Review C*, 93(6) (2016) p. 65803. DOI: 10.1103/PhysRevC.93.065803 ARXIV: 1601.02853
3. **M. Munch**, O. S. Kirsebom, J. A. Swartz, K. Riisager, and H. O. U. Fynbo *Measurement of the full excitation spectrum of the  $^7\text{Li}(p, \gamma)\alpha\alpha$  reaction at 441keV*. *Physics Letters B*, 782 (2018), p. 779–784. DOI: 10.1016/j.physletb.2018.06.013 ARXIV: 1802.10404

4. **M. Munch** *R-Matrix parametrization for  $\gamma$  decays to unbound states*. (2018). ARXIV: 1802.09297
5. **M. Munch** and H. O. U. Fynbo *The partial widths of the 16.1 MeV  $2^+$  resonance in  $^{12}\text{C}$* . The European Physical Journal A, 54 (2018), p. 138 DOI: 10.1140/epja/i2018-12577-3 ARXIV: 1805.10924
6. **M. Munch**, J. H. Halkjær, B. Löher, H. Törnqvist and H. T. Johansson *VME readout at and below the conversion time limit*. Submitted to IEEE Transactions on Nuclear Science. ARXIV: 1810.03574

Other papers not included in this thesis

1. J. J. W. H. Sørensen, M. K. Pedersen, **M. Munch**, P. Haikka, J. H. Jensen, T. Planke, M. G. Andreassen, M. Gajdacz, K. Mølmer, A. Lieberoth and J. F. Sherson *Exploring the quantum speed limit with computer games*. Nature, 532(7598) (2016), p. 210–213. DOI: 10.1038/nature17620 ARXIV: 1506.09091
2. M. Stachura, A. Gottberg, K. Johnston, M. L. Bissell, R. F. Garcia Ruiz, J. Martins Correia, A. R. Granadeiro Costa, M. Dehn, M. Deicher, A. Fenta, L. Hemmingsen, T. E. Mølholt, **M. Munch**, G. Neyens, S. Pallada, M. R. Silva, and D. Zakoucky *Versatile Ion-polarized Techniques On-line (VITO) experiment at ISOLDE-CERN*. Nuclear Instruments and Methods B 376, p. 369–373 (2016). DOI: 10.1016/j.nimb.2016.02.030
3. M. V. Lund, A. Andreyev, M. J. G. Borge, J. Cederkäll, H. De Witte, L. M. Fraile, H. O. U. Fynbo, P. T. Greenlees, L. J. Harkness-Brennan, A. M. Howard, M. Huyse, B. Jonson, D. S. Judson, O. S. Kirsebom, J. Konki, J. Kurcewicz, I. Lazarus, R. Lica, S. Lindberg, M. Madurga, N. Marginean, R. Marginean, I. Marroquin, C. Mihai, **M. Munch**, E. Nacher, A. Negret, T. Nilsson, R. D. Page, S. Pascu, A. Perea, V. Pucknell, P. Rahkila, E. Rapisarda, K. Riisager, F. Rotaru, C. Sotty, M. Stanoiu, O. Tengblad, A. Turturica, P. Van Duppen, V. Vedia, R.

- Wadsworth and N. Warr *Beta-delayed proton emission from  $^{20}\text{Mg}$* . The European Physical Journal A 52, 304 (2016). DOI: 10.1140/epja/i2016-16304-x
4. O. S. Kirsebom, O. Tengblad, R. Lica, **M. Munch**, K. Riisager, H. O. U. Fynbo, M. J. G. Borge, M. Madurga, I. Marroquin, A. N. Andreyev, T. A. Berry, E. R. Christensen, P. D. Fernández, D. T. Doherty, P. Van Duppen, L. M. Fraile, M. C. Gallardo, P. T. Greenlees, L. J. Harkness-Brennan, N. Hubbard, M. Huyse, J. H. Jensen, H. Johansson, B. Jonson, D. S. Judson, J. Konki, I. Lazarus, M. V. Lund, N. Marginean, R. Marginean, A. Perea, C. Mihai, A. Negret, R. D. Page, V. Pucknell, P. Rahkila, O. Sorlin, C. Sotty, J. A. Swartz, H. B. Sørensen, H. Törnqvist, V. Vedia, N. Warr and H. De Witte *First Accurate Normalization of the  $\beta$ -delayed  $\alpha$  Decay of  $^{16}\text{N}$  and Implications for the  $^{12}\text{C}(\alpha, \gamma)^{16}\text{O}$  Astrophysical Reaction Rate*. Physical Review Letters 121, 142701 (2018). DOI: 10.1103/PhysRevLett.121.142701
  5. O. S. Kirsebom, M. Hukkanen, A. Kankainen, W. H. Trzaska, K. Andersen, L. Canete, J. Cederkäll, T. Enqvist, T. Eronen, H. O. U. Fynbo, S. Geldhof, R. de Groote, D. G. Jenkins, A. Jokinen, P. Joshi, A. Khanam, J. Kostensalo, P. Kuusiniemi, I. Moore, **M. Munch**, D. A. Nesterenko, J. D. Ovejas, H. Penttilä, I. Pohjalainen, M. Reponen, S. Rinta-Antila, K. Riisager, A. de Roubin, P. C. Srivastava, J. Suhonen, J. A. Swartz, O. Tengblad, M. Vilen, S. Viñals and J. Äystö *First detection of the  $2^+ \rightarrow 0^+$  ground-state transition in the  $\beta$  decay of  $^{20}\text{F}$* . (2018). ARXIV: 1805.08149
  6. J. A. Swartz, H. O. U. Fynbo, K. L. Andersen, **M. Munch** and O. S. Kirsebom (2018). *Investigating  $^{16}\text{O}$  with the  $^{15}\text{N}(p, \alpha)^{12}\text{C}$  reaction*. Proceedings of the 4th International Conference on the State of the Art in Nuclear Cluster Physics (2018). ARXIV: 1810.07053



## Preface

This thesis summarizes the work I have carried out during my four years as a Ph.D student at the nuclear physics group at Aarhus University. The majority of the experiments presented in this work have been carried out at the 5 MV Van de Graff accelerator, which celebrated its 50 year anniversary in 2017. In addition, the isotopes studied were  $^8\text{Be}$  and  $^{12}\text{C}$ , both of which have been studied since the dawn of nuclear physics. This raises the question whether there is anything left to learn. Luckily, recent advances in detector technology facilitates measurements that were previously unfeasible.

This thesis is divided into two parts. The first part details four different experiments, three of which were conducted at the 5 MV accelerator at Aarhus University and the last at Gammasphere at Argonne National Laboratory. The first experiment was a study of the  $^{23}\text{Na}(\alpha, p)$  reaction with energies between 1.7 and 2.5 MeV in the center-of-mass system. This experiment was motivated by the impact of the cross section on the astrophysically relevant  $^{26}\text{Al}$  isotope. The second experiment was a measurement of the branching ratio for the  $\beta$  decay of the  $^{12}\text{B}$  ground state to the Hoyle state in  $^{12}\text{C}$ . The third experiment measured the full  $^8\text{Be}$  excitation spectrum populated in the  $\gamma$  decay of the 17.6 MeV  $1^+$  state. With this we sought to find possible  $^8\text{Be}$  intruder states and test state of the art *ab initio* calculations. In the last experiment the  $^{11}\text{B}(p, \alpha)$  cross section was measured for the 16.1 MeV  $^{12}\text{C}$  resonance. This was mainly motivated by substantial discrepancies in the existing literature. As each of these experiments have

their own motivation, they are written as self contained chapters. Each chapter is followed by the associated research paper.

The second part details the technical work I have performed during my thesis. This is structured as two chapters. The first describes a general purpose analysis framework built on top of CERN ROOT that substantially eases the analysis of data from silicon detectors. The second describes the substantially upgraded data acquisition system used at the Aarhus 5 MV setup and several ISOLDE experiments. This chapter is followed by a research paper on a newly proposed readout method.

It should be noted that in accordance with GSST rules, some illustrations of this thesis were also used in the progress report for the qualifying examination



**Part I**

**Physics**



## $^{23}\text{Na}(\alpha, p)^{26}\text{Mg}$ reaction rate at astrophysically relevant energies

This chapter discusses a measurement of the  $^{23}\text{Na}(\alpha, p)^{26}\text{Mg}$  cross section, which is important for the production of  $^{26}\text{Al}$  in hot stellar environments.

The chapter starts with a motivation that includes a review of prior experimental determinations of this cross section. This is followed by a section discussing our experiment and its strengths. The chapter concludes with a discussion of the results and its astrophysical impact. These results were published in ref. [2] and the paper can be found at page 13.

### 2.1 Motivation

The Big Bang model is the favored model for the cosmological evolution of our universe from very early times until today. Historically, it was supported by observational evidence of the cosmic microwave background, the cosmic expansion and primordial nucleosynthesis [3]. The latter is the fusion of protons and neutrons into primarily hydrogen and helium-4 in a 3:1 ratio. In addition, deuterium,  $^3\text{He}$ , lithium and heavier isotopes such as boron and carbon were also produced, but only at a ratio of  $< 10^{-5}$  compared to hydrogen.

This primordial collection of isotopes provided the seed for the first generation of stars consisting almost exclusively of hydrogen and helium. The present observations of heavier elements are then explained by the

occurrence of fusion in the hot stellar interior - primarily the core. These heavier elements are then reintroduced into the interstellar medium through various mechanisms. These mechanisms include thermal pulses in asymptotic giant branch (AGB) stars, supernovae explosions, and neutron star mergers [4, 5]. The latter two events are believed to be the primary source of r-process elements in which neutron-rich elements heavier than iron are created through rapid neutron capture. In both cases, significant mass loss occurs in the final stages of the event. As later generations of stars and planets are formed from the interstellar medium, they are “polluted” with heavier elements. This cycle is generally called nucleosynthesis. AGB stars also produce elements heavier than iron through the s-process in which a heavy element captures a neutron and subsequently  $\beta$  decays. The produced elements will thus occur predominantly along the line of  $\beta$  stability.

The first direct evidence for nucleosynthesis was the observation of spectral lines corresponding to entirely unstable element technetium in AGB stars [6]. The longest-lived isotope of this element is  $^{98}\text{Tc}$ , which has a half life of  $4.2 \times 10^6$  yr. As this is much shorter than the age of the universe,  $\sim 10^{10}$  yr, something must be producing this element. Additional evidence was provided in 1982 by the HEAO-3 satellite that observed the 1809 keV  $\gamma$ -line corresponding to a transition in  $^{26}\text{Mg}$  from the first excited state to the ground state [7]. The first excited state is populated by the  $\beta$  decay of  $^{26}\text{Al}$  with a half life of  $7.2 \times 10^5$  yr. Additional  $\gamma$  lines such as electron-positron annihilation,  $^{57}\text{Co}$ ,  $^{56}\text{Ni}$  and  $^{44}\text{Ti}$  have also been identified [8].

The initial satellite observation of  $^{26}\text{Al}$  was followed by two additional missions, COMPTEL [9] and INTEGRAL [10]. Over the years different sources for  $^{26}\text{Al}$  such as AGB stars, classical novae, Wolf-Rayet stars, and core-collapse supernovae have been suggested. Observational evidence has established that  $^{26}\text{Al}$  is primarily located in the Galactic plane and co-rotates with the Galaxy. Additionally, the  $^{26}\text{Al}$  distribution is significantly correlated with the population of massive stars. Thus, AGB stars are the currently favored source [10–13].

This prompted Iliadis *et al.* to perform a sensitivity study of reactions influencing the production of  $^{26}\text{Al}$  in massive stars [14]. In this reaction network,  $^{23}\text{Na}(\alpha, p)^{26}\text{Mg}$  acts as a proton source for the  $^{25}\text{Mg}(p, \gamma)^{26}\text{Al}$

reaction and it was found that increasing the  $^{23}\text{Na}(\alpha, p)$  reaction rate by a factor of 10 increased the  $^{26}\text{Al}$  production by a factor of 3. An illustration of the reaction is shown in fig. 2.1. In this context the proton decay to the ground state is denoted by  $p_0$ , decay to the first excited by  $p_1$ , etc. The available experimental data for this reaction was provided by two experiments performed in direct kinematics by Kuperus in 1964 and Whitmire *et al.* in 1974 [15, 16]. In both cases, the targets were backed by a significant amount of material essentially acting as a heat sink. This was necessary as NaCl evaporates at 801 °C and substantial beam currents were used. Thus, it seemed plausible that the cross section might be underestimated although Whitmire *et al.* claimed they periodically checked for target degradation. In both experiments the  $p_1$  transition was found to dominate the  $(\alpha, p)$  cross section.

Motivated by the work of Iliadis, Almaraz-Calderon *et al.* (AC) decided to remeasure the cross section using inverse kinematics, i.e. using a  $^{23}\text{Na}$

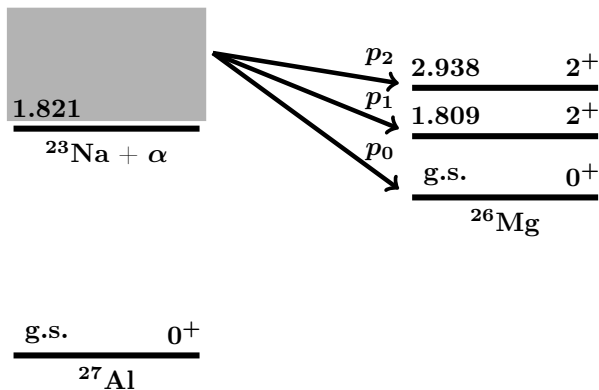


Figure 2.1: Illustration of the  $^{23}\text{Na}(\alpha, p)^{26}\text{Mg}$  reaction. A quasi-continuum of states in  $^{27}\text{Al}$  is populated using the  $^{23}\text{Na} + \alpha$  reaction. The excited state decays to  $^{26}\text{Mg}$  via proton emission.

beam impinging on a helium gas cell avoiding the evaporation issue [17]. Specifically, a  $2 \times 10^8$  pps  $^{23}\text{Na}$  beam with an energy of 23, 26, 28 or 30 MeV was produced by the Argonne ATLAS accelerator. The beam current was deduced from Rutherford scattering of a  $120 \mu\text{g cm}^{-2}$  gold foil placed before the gas cell. The gas cell was sealed with two  $1.40(5) \text{ mg cm}^{-2}$  Ti foils and filled with 550 Torr of  $^4\text{He}$  kept at liquid nitrogen temperature. The protons were detected with an annular silicon detector placed 20 cm downstream of the target with a  $70 \mu\text{m}$  aluminium foil placed in front of it in order to shield the detector from elastically scattered  $^{23}\text{Na}$  and  $^4\text{He}$  recoils. Surprisingly, their deduced cross section was larger by a factor of 40 compared to the previous measurements or statistical model calculations such as **NON-SMOKER** [18]. They attributed this to significant target evaporation in previous experiments. However, a subsequent review of  $\alpha$  particle induced reactions in the  $A = 20 - 50$  region showed that the newly obtained  $^{23}\text{Na}$  cross sections were an outlier when compared to the neighboring nuclei [19].

## 2.2 Method

Reviewing the experiment performed by AC the main weakness is the signal-to-noise ratio especially at low energy. This was caused by proton knock-out of hydrogen in the gas cell window, which becomes a problem since the sought cross section drops two orders of magnitude over the measured energy range. Their low energy cut-off was 3 MeV due to the Al foil in front of the detector, and the  $p_1$  cross section was only directly measured at the highest two energies. The limited angular information means the complete angular distribution cannot be determined. Instead, they chose to adopt the previously measured angular distribution for  $^{27}\text{Al}(\alpha, p)^{30}\text{Si}$  based on a shell model argument.

Our experiment sought to improve on shortcomings in all three prior experiments. The experiment was performed in direct kinematics with a solid NaCl target evaporated onto a thin carbon backing. This essentially eliminates the background problem. Charged particles were detected using modern large area double-sided silicon strip detectors (DSSD) with a

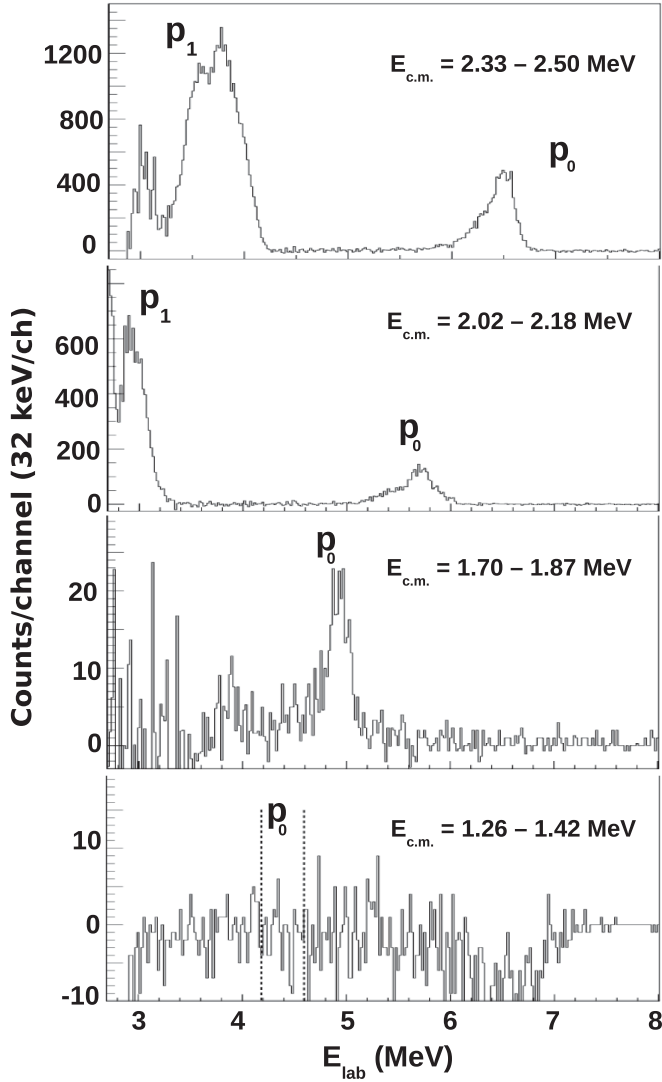


Figure 2.2: Proton spectra measured by Almaraz-Calderon *et al.* with the titanium background subtracted. Note that  $p_1$  can only be distinguished for the highest two energies. For the lowest energy only an upper bound for  $p_0$  was determined. Figure from ref. [17].

solid angle of  $\sim 20\%$  compared to  $\sim 0.03\%$  in the prior direct kinematics experiments. This made it feasible to reduce the beam current by roughly a factor of 1000. The detector setup is shown in figure 1 in the following paper and the angular coverage is improved significantly compared to the AC experiment. During the experiment, the absolute yield and ratio between Na and Cl was monitored in order to verify that no degradation was occurring. Additionally, the measured cross sections were normalized to the observed elastically scattered  $\alpha$  particles. This removed systematic uncertainties related to the target thickness, beam current integration and stoichiometry.

## 2.3 Results and discussion

Our experiment shows that the statistical model calculation generally reproduced the measured cross section within 30%, except at 2.16 MeV, where a strong resonance increases the discrepancy to 50%. This can be seen in figure 5 in the following paper. Assuming the energy dependence of **NON-SMOKER** to be correct the optimal scaling factor between our measurement and the model prediction was found to be 0.96(6). At the time of publication, we could not reproduce the results obtained by AC.

Our results were published simultaneously with the results from Tomlinson *et al.* that had repeated the experiment in inverse kinematics [21]. They were also unable to reproduce the work of AC. Shortly thereafter an erratum was published [20] in which AC acknowledged that they had not accounted for a factor of 100 downscaling thus artificially increasing their results by this factor. The inverse kinematic experiment was later repeated at Argonne National Laboratory using the MUSIC detector [22], which could also simultaneously measure the  $(\alpha, \alpha')$  and  $(\alpha, n)$  reaction. Figure 2.3 shows the results of all four experiments along with the statistical model of ref. [19]. Note that the result by AC have been rescaled. Generally, good agreement is observed between all datasets except around 2.75 MeV where the result from Tomlinson *et al.* deviates slightly.

Comparing the different experimental techniques, the method employed in the present experiment is more straightforward as it did not require



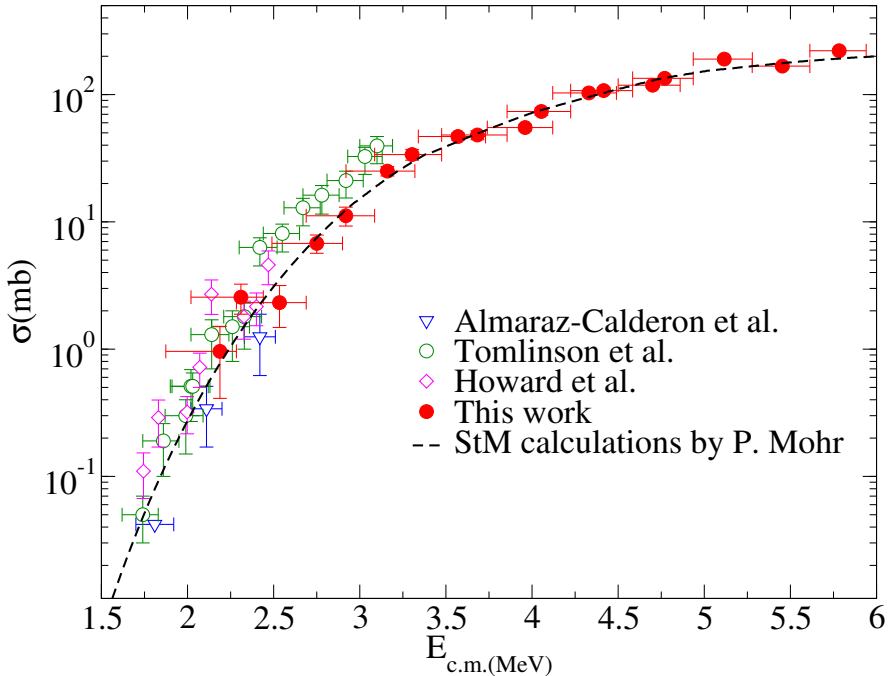


Figure 2.3: Comparison between all recent measurement of the  $^{23}\text{Na}(\alpha, p)$  cross section [2, 17, 20–22]. Note that the result by AC have been rescaled. The result from Tomlinson *et al.* deviates slightly around 2.75 MeV. Figure from ref. [22].

handling a cryogenic target or a radioactive beam (RIB) facility. The lack of a cryogenic target and the associated cooling systems also meant that a significantly larger angular range could be covered, which made it possible to determine angular distributions. On the other hand, the location at a RIB facility means the work could be extended to more exotic nuclei. The experimental technique used with the MUSIC detector is quite elegant as it is possible to measure the cross section for several reaction channels at multiple energies using a single beam energy. Considering beam time is a scarce commodity; this is very powerful.

## **2.4 Astrophysical impact**

Prior to these recent experimental investigations, it was expected that prior measurements suffered from target issues at an unknown level and thus a statistical model was used in stellar calculations. Based on the performance of the statistical model for other reactions, it was expected to be accurate within a factor of 2 to 10 [19].

The results obtained in this work show that for this particular reaction the statistical model is accurate within 30 % and 50 % at strong resonances. N. Hubbard, one of the co-authors of the paper, explored the astrophysical consequences of this result [23]. The main conclusion was in agreement with prior investigations, but the new experimental measurements significantly reduce the uncertainties on the reaction rate.

## **2.5 Contributions**

The work presented in the following paper was performed by a collaboration. A. Howard was the principal investigator and as such was responsible for the majority of the experimental work. Additionally, he wrote the majority of the paper. I was responsible for the entire analysis of the experimental data, i.e. the extraction of angular distributions, determination of target stoichiometry, Rutherford yield, etc. N. Hubbard explored the astrophysical consequences.

**$^{23}\text{Na}(\alpha, p)^{26}\text{Mg}$  Reaction Rate at Astrophysically Relevant Energies**A. M. Howard,<sup>\*</sup> M. Munch, H. O. U. Fynbo, O. S. Kirsebom, and K. L. Laursen  
*Department of Physics and Astronomy, Aarhus University, 8000 Aarhus C, Denmark*C. Aa. Diget and N. J. Hubbard  
*Department of Physics, University of York, York YO10 5DD, United Kingdom*  
(Received 18 March 2015; published 29 July 2015)

The production of  $^{26}\text{Al}$  in massive stars is sensitive to the  $^{23}\text{Na}(\alpha, p)^{26}\text{Mg}$  cross section. Recent experimental data suggest the currently recommended cross sections are underestimated by a factor of  $\sim 40$ . We present here differential cross sections for the  $^{23}\text{Na}(\alpha, p)^{26}\text{Mg}$  reaction measured in the energy range  $E_{\text{c.m.}} = 1.7\text{--}2.5$  MeV. Concurrent measurements of Rutherford scattering provide absolute normalizations that are independent of variations in target properties. Angular distributions are measured for both  $p_0$  and  $p_1$  permitting the determination of total cross sections. The results show no significant deviation from the statistical model calculations upon which the recommended rates are based. We therefore retain the previous recommendation without the increase in cross section and resulting stellar reaction rates by a factor of 40, impacting the  $^{26}\text{Al}$  yield from massive stars by more than a factor of 3.

DOI: 10.1103/PhysRevLett.115.052701

PACS numbers: 25.60.Dz, 26.30.-k, 26.50.+x, 27.30.+t

The observation of  $^{26}\text{Al}$  in the Galactic medium, through  $\gamma$ -ray emission from its daughter nucleus  $^{26}\text{Mg}$ , provided direct evidence for ongoing nucleosynthesis in the Galaxy [1]. While the origins of  $^{26}\text{Al}$  remain the subject of discussion, the C/Ne convective shell within massive stars is a candidate site [2]. A sensitivity study of the reactions influencing  $^{26}\text{Al}$  production in massive stars has indicated a significant dependence on the  $^{23}\text{Na}(\alpha, p)^{26}\text{Mg}$  reaction rate, which acts as a proton source for the  $^{25}\text{Mg}(p, \gamma)^{26}\text{Al}$  reaction [3]. Specifically, it was found that an increase in the  $^{23}\text{Na}(\alpha, p)^{26}\text{Mg}$  rate by a factor of 10 would lead to an increase in  $^{26}\text{Al}$  production by a factor of 3.

The  $^{23}\text{Na}(\alpha, p)^{26}\text{Mg}$  rate adopted in Ref. [3] is obtained from statistical model calculations. While earlier experimental data do exist [4,5], these were excluded due to a lack of understanding of the target properties during the intense beam bombardment. As a consequence there are significant uncertainties in the experimentally determined resonance strengths.

A recent direct measurement of the reaction cross section in inverse kinematics was made to resolve these experimental uncertainties [6]. A  $^{23}\text{Na}$  beam was incident on a gas cell containing  $^4\text{He}$  and outgoing protons corresponding to the ground and first-excited states in  $^{26}\text{Mg}$  were detected. The cross sections measured in the region  $E_{\text{c.m.}} = 1.7\text{--}2.5$  MeV were  $\sim 40$  times greater than statistical model calculations. Such an increase is significantly larger than that required to alter the production of  $^{26}\text{Al}$  by a factor of 3.

A similar, although less dramatic, disagreement with statistical model calculations has been reported for the  $^{33}\text{S}(\alpha, p)^{36}\text{Cl}$  reaction [7]. It is noted in Ref. [8] that the measured cross sections significantly exceed the expected

single particle strength and that, in light of the  $^{23}\text{Na}(\alpha, p)^{26}\text{Mg}$  results also, there is an urgent need for additional  $(\alpha, p)$  data in the  $20 \leq A \leq 50$  region.

In this Letter we report on a new measurement of the  $^{23}\text{Na}(\alpha, p)$  cross section in forward kinematics covering the energy range  $E_{\text{c.m.}} = 1.7\text{--}2.5$  MeV. Our methodology exploits the simultaneous detection of Rutherford scattered  $\alpha$  particles to remove dependencies on properties of the target, such as thickness and stoichiometry, that have impacted previous measurements. Discussions of this methodology may be found in, for example, Refs. [9,10].

Measurements were made at the Aarhus University 5-MV Van de Graaff accelerator. A schematic of the

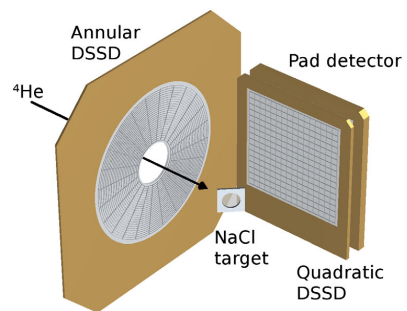


FIG. 1 (color online). A schematic of the experimental setup within the scattering chamber. The incoming  $^4\text{He}$  beam is indicated by the arrow. The NaCl target was orientated at  $45^\circ$  relative to the beam axis. Two double-sided silicon strip detectors were used to detect outgoing protons and  $\alpha$  particles, see the text for details. For clarity both front- and back-side segmentation of the detectors are shown.

experimental setup is shown in Fig. 1. A  $^4\text{He}$  beam with laboratory energy between 1.99 and 2.94 MeV was used to bombard a carbon-backed NaCl target. The beam was stopped 70 cm downstream of the target position in a suppressed Faraday cup connected to a current integrator. Typical beam currents were in the range 200–500 ppA.

Two double-sided silicon strip detectors (DSSDs) were mounted in the scattering chamber to provide energy and angle information for outgoing charged particles. A 322- $\mu\text{m}$  annular DSSD was mounted upstream of the target, covering laboratory angles between  $140^\circ$  and  $163^\circ$  and a 40- $\mu\text{m}$ -thick, quadratic DSSD provided coverage at laboratory angles between  $60^\circ$  and  $120^\circ$ . The annular detector was mounted with the junction side, which has a 4- $\mu\text{m}$  dead layer, facing the target. In this orientation the dead layer acts as a degrader foil, increasing the energy separation between backscattered  $\alpha$  particles and protons populating  $^{26}\text{Mg}$ . Protons populating the ground and first excited states in  $^{26}\text{Mg}$  were sufficiently energetic to punch through the quadratic DSSD and were stopped, and unambiguously identified, in a 1500- $\mu\text{m}$  silicon pad detector.

The target was prepared at Aarhus University by evaporating NaCl onto a 10  $\mu\text{g}/\text{cm}^2$  carbon foil. The beam energy loss in the target was calibrated using alpha particles backscattered from the carbon backing into the annular DSSD. As the target is rotated through  $180^\circ$  the energies are shifted due to losses within the NaCl layer (see, for example, Ref. [11] for details of this technique). A thickness of 65 keV at a beam energy of 3 MeV was determined. It should be noted that the target was tilted  $45^\circ$  to the beam axis during all other measurements giving an effective

thickness of between 92 and 115 keV for the range of beam energies used.

During the experiment elastically scattered alpha particles were continuously measured in the quadratic DSSD. For pure Rutherford scattering the elastic yield is a product of the target thickness and incident beam current. This removes any uncertainties due to changes in the target thickness or stoichiometry, in addition to uncertainties in the integration of beam charge. The  $\alpha$  scattering data presented in Ref. [12] demonstrate that elastic scattering from Na is well described by the Rutherford formula for beam energies up to 3 MeV, which covers the entire range of measurements here. This is supported by a measurement of the angular distribution for elastically scattered  $\alpha$  particles from Na measured with our setup, shown in Fig. 2, which shows excellent agreement with Rutherford scattering.

Rutherford scattering data were also collected for Cl throughout the experiment. A comparison between the relative amounts of Na and Cl in the target shows no deviation from a ratio of 1:1 to within 10% for the duration of the experiment, see Fig. 2. Repeat measurements of the target thickness were also consistent, indicating no significant changes in the target properties during the experiment. This is not surprising given the relatively low beam currents employed, 3 orders of magnitude lower than those used in Ref. [5] where significant target degradation was observed.

Energy spectra for the annular DSSD and quadratic DSSD plus the pad detector telescope are shown in Fig. 3. Proton yields were extracted for both  $p_0$  and  $p_1$  transitions across the full energy range covered. Differential cross sections were obtained using the normalization provided by Rutherford scattering of  $\alpha$  particles into the quadratic DSSD.

Examples of measured angular distributions are shown in Fig. 4. To permit total cross sections to be determined measured differential cross sections were fitted using a sum of even-termed Legendre polynomials. This assumes a distribution symmetric around  $\theta_{\text{c.m.}} = 90^\circ$ , which is expected when the cross section is dominated by compound nucleus formation. In the measurements reported in Ref. [4] only a single, relatively minor resonance was found to exhibit forward-backward asymmetry in the energy region covered here. Nonetheless, a conservative 20% uncertainty on the total cross section is assumed.

At beam energies below  $\sim 2.2$  MeV, some fraction of  $p_1$  protons reaches the pad detector with insufficient energy to be registered. The result is a decrease in the detection efficiency that is not easily quantified. For the two data sets collected below this energy the  $p_1$  data collected using the pad detector are therefore not used for the fitting of angular distributions. Instead, only data from the annular DSSD, which suffers no decrease in detection efficiency, are used and an isotropic angular distribution is assumed. Applying the same procedure to the  $p_1$  data sets at higher energy

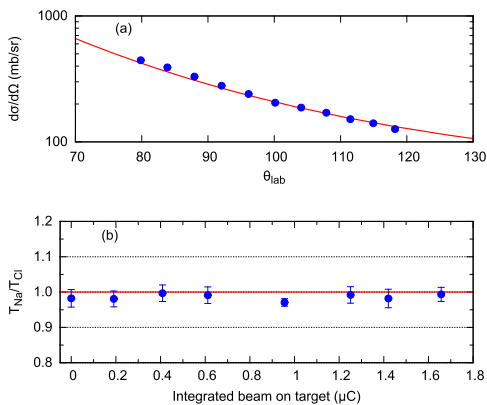


FIG. 2 (color online). (a) The measured angular distribution of elastically scattered alpha particles from  $^{23}\text{Na}$  at a beam energy of 2.94 MeV. The solid line is the distribution expected for pure Rutherford scattering. (b) The stoichiometric ratio of Na and Cl in the target foil, as determined by Rutherford scattering, as a function of the integrated beam impinging on the foil.

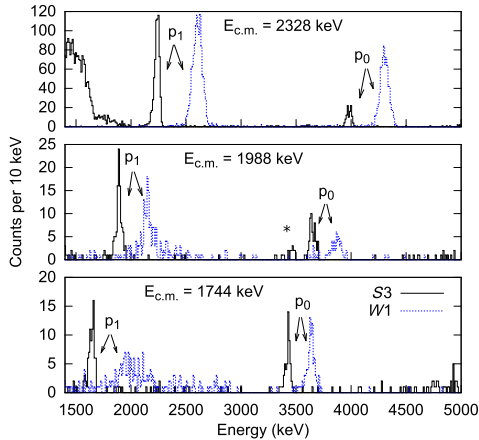


FIG. 3 (color online). Representative energy spectra from the annular DSSD (S3) and the quadratic DSSD plus the pad detector telescope (W1). In the latter case a coincidence between the two detectors is required to remove the background due to  $\alpha$  particles stopping in the quadratic DSSD. The effective center of mass energy in each case is given in the plot, see the text for details. The small peak at \* has an energy consistent with the  $p_0$  transition in  $^{19}\text{F}(\alpha, p)^{22}\text{Ne}$ , and may therefore be indicative of a thin layer of  $^{19}\text{F}$  on the target surface, see the text for further discussion.

results in a decrease in total cross section of between 10% and 30%. A 30% uncertainty is assumed for the two lowest  $p_1$  data points to reflect this.

In two of the eight measurements a weak peak was observed  $\sim 200$  keV in energy below  $p_0$  (see the middle panel of Fig. 3). This peak may be indicative of a thin layer of fluorine on the target surface since it lies at the

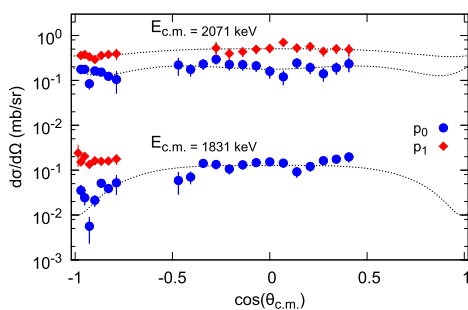


FIG. 4 (color online). Proton angular distributions from the  $^{23}\text{Na}(\alpha, p)^{26}\text{Mg}$  reaction. The energies given are the effective center of mass energies, corrected for the target thickness. For the lowest energy  $p_1$  data shown reliable differential cross sections could only be obtained in the annular DSSD detector, located at backward angles in the laboratory frame. The dotted lines show fits of Legendre polynomials to the data.

approximate energy expected for  $^{19}\text{F}(\alpha, p_0)^{22}\text{Ne}$ . Under these circumstances there may be a contribution from  $^{19}\text{F}(\alpha, p_1)^{22}\text{Ne}$  also, which would not be resolved from  $^{23}\text{Na}(\alpha, p_1)^{26}\text{Mg}$ . The only possible effect of this could be to increase the observed cross section. Based upon the data presented in Ref. [13] it is estimated that this contribution should always be below 10% of the total peak yield. Out of caution an additional 10% uncertainty is therefore assumed on the lower bound of all  $p_1$  cross sections.

Protons populating higher lying states in  $^{26}\text{Mg}$  were not observed in this work due to the background from the scattered beam. The contribution from these states to the total reaction cross section at the energies measured in this work is expected to be minor due to the reduced penetrabilities. In Ref. [6] a Hauser-Feshbach calculation is reported that indicates negligible contribution from  $p_2$  within the Gamow window ( $E_{c.m.} \approx 1.2$ – $2.2$  MeV).

To account for energy losses within the NaCl layer of the target, the measured cross sections are associated with an effective beam energy. This is calculated using an energy dependence for the cross section as given by the statistical model code NON-SMOKER [14]. The resulting effective energies are within 15 keV of the beam energy at the target midpoint for all measurements. It should be noted that for Rutherford scattering the effective energies are slightly lower, and are within 1 keV of the midpoint energy for all measurements.

Total cross sections for  $p_0$  and  $p_1$  are presented in Table I. These values are plotted in Fig. 5 together with results from Ref. [6] and the statistical model code NON-SMOKER [14]. We find a significant discrepancy with the results reported in Ref. [6], these values being consistently an order of magnitude higher than measured here. We can offer no explanation for this discrepancy; however, it cannot be accounted for by the form of the angular distributions assumed in Ref. [6], where data were only

TABLE I. Angle-integrated cross sections for the  $p_0$  and  $p_1$  branches of the  $^{23}\text{Na}(\alpha, p)^{26}\text{Mg}$  reaction. The final column gives the ratio of the measured cross section to that calculated using the statistical model code NON-SMOKER.

$E_{c.m.}$ (keV) <sup>a</sup>	$\sigma_{p_0}$ (mb)	$\sigma_{p_1}$ (mb)	$\sigma_{(p_0 + p_1)}/\sigma_{N.S.}$
1744	0.05 (1)	0.06 <sup>(+2)</sup> <sub>(-2)</sub>	1.50 (29)
1831	0.09 (2)	0.20 <sup>(+6)</sup> <sub>(-7)</sub>	2.09 (46)
1998	0.08 (2)	0.24 <sup>(+5)</sup> <sub>(-5)</sub>	0.81 (13)
2071	0.20 (4)	0.52 <sup>(+11)</sup> <sub>(-12)</sub>	1.19 (19)
2139	0.28 (6)	2.42 <sup>(+49)</sup> <sub>(-53)</sub>	3.20 (58)
2328	0.28 (6)	1.52 <sup>(+31)</sup> <sub>(-34)</sub>	0.84 (14)
2400	0.57 (11)	1.59 <sup>(+32)</sup> <sub>(-35)</sub>	0.73 (11)
2469	1.62 (33)	2.97 <sup>(+60)</sup> <sub>(-66)</sub>	1.18 (17)

<sup>a</sup>Effective energy corrected for energy loss within the target. See the text for details.

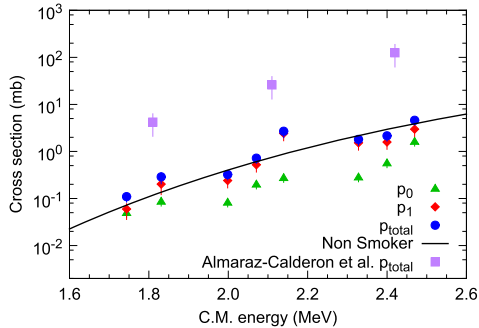


FIG. 5 (color online). Cross sections for the  $^{23}\text{Na}(\alpha, p)^{26}\text{Mg}$  reaction. The energies given are effective energies, corrected for energy losses within the target. See the text for details. For comparison cross sections from the statistical model code NON-SMOKER [14] and the measurement reported in Ref. [6] are also shown.

obtained backwards of  $\theta_{\text{c.m.}} = 160^\circ$ . In the narrow angular range between  $\theta_{\text{c.m.}} = 165^\circ$  and  $170^\circ$  where overlapping differential cross section measurements exist, the absolute values again differ by at least an order of magnitude. It is again worth noting that the absolute normalization in the present work is provided by the Rutherford scattered beam from the  $^{23}\text{Na}$  component of the target itself. Combined with the relative simplicity of the experimental setup, this provides an extremely robust method for the determination of absolute cross sections.

The NON-SMOKER results reproduce the measured cross sections extremely well in terms of both trend and magnitude. The only significant deviation is found at  $E_{\text{c.m.}} = 2.16$  MeV and can be understood in terms of the strong individual resonance reported in Ref. [5] at  $E_{\text{c.m.}} = 2.14$  MeV. If the energy dependence of the NON-SMOKER results is fixed and only the absolute magnitude is allowed to vary we find that a scaling factor of  $0.96 \pm 0.06$  is required to best fit our data.

In conclusion, we have presented cross sections for the  $^{23}\text{Na}(\alpha, p)^{26}\text{Mg}$  reaction in the region  $E_{\text{c.m.}} = 1.74$  to 2.47 MeV. The overall trend and magnitude of the cross section are in general found to be very well reproduced by the statistical model code NON-SMOKER. The results are also largely consistent with the previous measurements of Whitmire *et al.* [5] and Kuperus *et al.* [4], though in general slightly higher than their results, whereas our measurement is inconsistent with the recent measurement by Almaraz-Calderon *et al.* [6].

As mentioned, the only significant discrepancy between the NON-SMOKER statistical model and our measurement is at the energy of the strongest  $(\alpha, p)$  resonance at  $E_{\text{c.m.}} = 2.14$  MeV, a resonance that is particularly strong in the  $p_1$  channel. From the difference between the observed cross sections around the 2.07 and 2.14 MeV

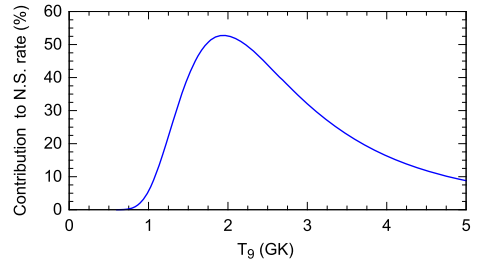


FIG. 6 (color online). The single-resonance contribution to the total rate obtained from NON-SMOKER calculations based upon the measured strength of the resonance at  $E_{\text{c.m.}} = 2.14$  MeV (see text for details).

center of mass energy, we estimate the  $p_1$  and  $p_0$  resonance strengths for this resonance to be  $\omega\gamma_1 = 1000(300)$  eV and  $\omega\gamma_0 = 42(13)$  eV, respectively. Based on these resonance strengths, the corresponding single-resonance contribution to the reaction rate is shown in Fig. 6 compared to the NON-SMOKER reaction rate. The contribution from this resonance in itself exhausts up to 50% of the NON-SMOKER reaction rate (at 2 GK), and could therefore potentially increase the total reaction rate beyond that of the NON-SMOKER rate. At the most important temperature 1.4 GK, the temperature at termination of convective shell C/Ne burning [3], the single-resonance contribution to the reaction rate is 35% of the NON-SMOKER reaction rate, with a reduced contribution below that temperature. Based on this, we would still recommend usage of the NON-SMOKER reaction rate for the  $^{23}\text{Na}(\alpha, p)^{26}\text{Mg}$  reaction in astrophysical scenarios, rather than the reaction rate indicated in Ref. [6]. The error on the reaction rate as evaluated from our experimental data is significantly reduced to the level of 30% relative error on the reaction rate, except in the temperature region around 2 GK where the contribution from the resonance could increase the reaction rate by up to 50% as shown in Fig. 6, with a corresponding increase in the upper limit on the reaction rate.

In summary, we therefore conclude that the reaction rate in the key temperature region, around 1.4 GK, is consistent with that of the statistical model (NON-SMOKER), to within approximately 30%. Based on this, the resulting  $^{26}\text{Al}$  production in massive stars as presented in Ref. [3] still stands. From the results of this sensitivity study, in which a 30%  $^{26}\text{Al}$  production increase is found for a rate increase of a factor of 2, the uncertainty in the  $^{26}\text{Al}$  production corresponding to our reaction-rate uncertainty of 30% is expected to be at most 10%–20%. This level of precision in the  $^{23}\text{Na}(\alpha, p)^{26}\text{Mg}$  reaction rate should therefore be sufficient for detailed comparisons of observed and simulated astrophysical  $^{26}\text{Al}$  production.

The authors would like to thank Folmer Lyckegaard for preparation of the NaCl targets used in this work. We also

acknowledge financial support from the European Research Council under ERC Starting Grant LOBENA, No. 307447 and from the UK Science & Technology Facilities Council under Grant No. ST/J000124/1.

*Note added.*—We have been made aware of very recent, complementary results from an independent remeasurement of the  $^{23}\text{Na}(\alpha, p)^{26}\text{Mg}$  cross section performed in inverse kinematics [15]. The obtained cross sections are in good agreement with those presented here. There is a discrepancy at the lowest energy point, which may be accounted for by the assumption of an isotropic angular distribution in Ref. [15].

---

\*alan.howard@phys.au.dk

- [1] W. A. Mahoney, J. C. Ling, A. S. Jacobson, and R. E. Lingenfelter, *Astrophys. J.* **262**, 742 (1982).
- [2] W. D. Arnett and J. P. Wefel, *Astrophys. J.* **224**, L139 (1978).
- [3] C. Iliadis, A. Champagne, A. Chieffi, and M. Limongi, *Astrophys. J., Suppl. Ser.* **193**, 16 (2011).
- [4] J. Kuperus, *Physica (Utrecht)* **30**, 2253 (1964).
- [5] D. P. Whitmire and C. N. Davids, *Phys. Rev. C* **9**, 996 (1974).
- [6] S. Almaraz-Calderon, P. F. Bertone, M. Alcorta, M. Albers, C. M. Deibel, C. R. Hoffman, C. L. Jiang, S. T. Marley, K. E. Rehm, and C. Ugalde, *Phys. Rev. Lett.* **112**, 152701 (2014).
- [7] M. Bowers, Y. Kashiv, W. Bauder, M. Beard, P. Collon, W. Lu, K. Ostdiek, and D. Robertson, *Phys. Rev. C* **88**, 065802 (2013).
- [8] P. Mohr, *Phys. Rev. C* **89**, 058801 (2014).
- [9] C. Rowland, C. Iliadis, A. E. Champagne, and J. Mosher, *Phys. Rev. C* **65**, 064609 (2002).
- [10] C. Ugalde, R. E. Azuma, A. Couture, J. Görres, H. Y. Lee, E. Stech, E. Strandberg, W. Tan, and M. Wiescher, *Phys. Rev. C* **77**, 035801 (2008).
- [11] M. Chiari, L. Giuntini, P. Mand, and N. Taccetti, *Nucl. Instrum. Methods Phys. Res., Sect. B* **184**, 309 (2001).
- [12] H. Sheng Cheng, X. Yang Lee, and F. Yang, *Nucl. Instrum. Methods Phys. Res., Sect. B* **56–57**, 749 (1991).
- [13] J. Kuperus, *Physica (Utrecht)* **31**, 1603 (1965).
- [14] T. Rauscher and F.-K. Thielemann, *At. Data Nucl. Data Tables* **79**, 47 (2001).
- [15] J. R. Tomlinson *et al.*, *Phys. Rev. Lett.* **115**, 052702 (2015).





## Independent measurement of the Hoyle state $\beta$ feeding from $^{12}\text{B}$ using Gammasphere

In this chapter, I will summarize and elaborate on a measurement of the  $\beta$  decay branching ratio from the ground state (GS) of  $^{12}\text{B}$  to the 7.65 MeV  $0^+$  state in  $^{12}\text{C}$ , known as the Hoyle state. The Hoyle state has been the subject of intense research since the late Sir Fred Hoyle postulated its existence in 1954 [24]. I will start by reviewing some models describing the structure of the state and some recent experimental results seeking to constrain these models. The current state of the art for the  $2^+$  excitation of the Hoyle state will be described. The work presented here is mainly motivated by  $\beta$  decay searches for the  $2^+$  excitation for which the branching ratio serves as a crucial constraint. The astrophysical impact of the Hoyle state and its excitation will be summarized. In the end, the results of the paper will be summarized along with its consequences and an outlook. The results were published in ref. [25] and the paper can be found at page 35.

### 3.1 Nuclear structure

#### $\alpha$ Clustering

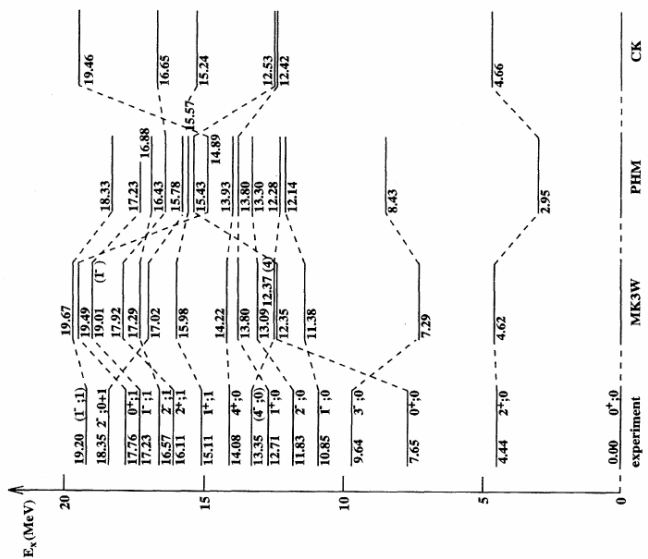
Nuclei composed of multiple  $\alpha$  particles also known as  $4n$  nuclei or  $\alpha$ -conjugate nuclei highlight the complexity associated with understanding the nuclear structure even in light nuclei. In the single-particle picture,

$^{12}\text{C}$  consists of six protons and six neutrons, which must obey the Pauli Exclusion Principle (PEP). This naturally leads to a shell model picture, where nucleons are placed in different orbitals analogous to the description of electronic orbitals in atoms. Figure 3.1(b) shows the resulting level scheme from three different shell model calculations for  $^{12}\text{C}$  compared to the experimental spectrum [26]. Focusing on the MK3W calculation, it reproduces the majority of the observed spectrum, except for the Hoyle state. A similar picture as seen in  $^8\text{Be}$ , where the GS and two first excited states are poorly described by the shell model, while higher lying states are well described. It seems that nuclei have some degrees of freedom not captured in the single particle picture.

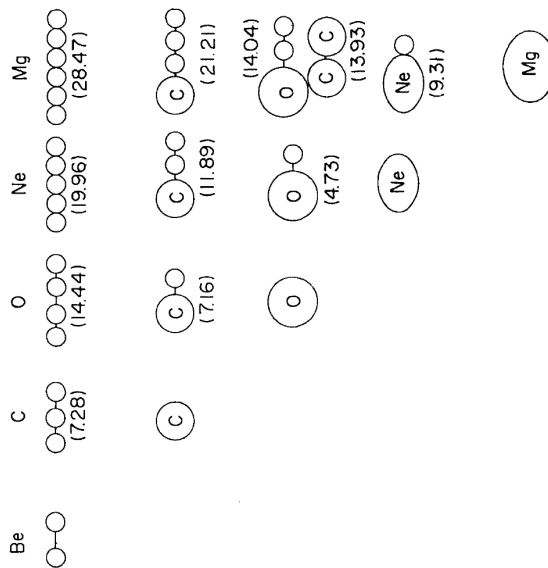
Key insight into this issue was provided by Ikeda *et al.*, who recognized that the PEP would prohibit  $\alpha$  cluster formation within a compact nucleus, but  $\alpha$  cluster formation would be possible in spatially large nuclei, where the PEP inhibits the dissolution into constituents [27]. Furthermore, they postulated that the band head for rotational states that is built upon the cluster configuration would appear at the threshold. Based on this hypothesis, they constructed the diagram seen in fig. 3.1(a), which shows the various  $4n$  nuclei and the respective thresholds. Note that in this context it is also possible for  $^{12}\text{C}$  and  $^{16}\text{O}$  clusters to form. In  $^{12}\text{C}$ , the Hoyle state is the only state situated just above the  $3\alpha$  threshold and it is expected to have a dominant  $\alpha$ -cluster configuration. This hypothesis has been corroborated by experimental evidence from inelastic electron scattering, which finds that the radius of the Hoyle state is 1.30 – 1.60 larger than the GS [28–31]. In a recent paper by Okołowicz *et al.*, the near-threshold phenomenon was ascribed to the strong coupling to the continuum [32].

## Models

Unfortunately, it is not possible to directly image the interior configuration of nuclei, and instead observable properties of the wave function must be measured and connected to theoretical models of the nuclear structure. For a model to completely describe this system, it should incorporate both single particle and cluster degrees of freedom in order to reproduce the spectrum



(b) Comparison between theoretical and experimental level schemes. Note that the Hoyle state (7.65 MeV,  $0^+$ ) is not reproduced. Figure from ref. [26].



(a) “Ikeda diagram” illustrating the different cluster configurations in four nucleon nuclei and their proposed energy. Figure from ref. [27].

Figure 3.1

seen in fig. 3.1(b). The relevant models can roughly be categorized as either explicit cluster models, molecular dynamics models or *ab initio* models. I will focus on the former two.

**Explicit cluster models** include both micro- and macroscopic models, i.e. models with and without nucleonic degrees of freedom. I will focus on two typical microscopic Alpha Cluster Models, namely the Brink [33] and THSR [34] wave functions. In both models, the full wave function is assumed to factorize into the center-of-mass (CM) wave function,  $\chi$ , and  $n$ -particle quartets ( $\alpha$  particles),

$$\Phi_{n\alpha}(r_{1,1}, \dots, r_{n,4}) = \mathcal{A} \left[ \phi_{\alpha_1}(r_{1,1}, \dots, r_{1,4}) \cdots \phi_{\alpha_n}(r_{n,1}, \dots, r_{n,4}) \right. \\ \left. \times \chi(R_1, \dots, R_n) \right], \quad (3.1)$$

where  $\mathcal{A}$  is the antisymmetrization operator, which ensures an overall fermionic wave function and  $R_i$  is the CM coordinate of the  $i$ 'th  $\alpha$  particle. The antisymmetrization enforces the PEP at small distances and destroys the clusterization for compact states such as the GS. In both models the intrinsic quartet wave function is described as a normalized Gaussian wavepacket of size  $b$

$$\phi_{\alpha_k}(r_{k,1}, \dots, r_{k,4}) \propto \exp \left[ - \sum_{i \neq j} (r_{k,i} - r_{k,j})^2 / (4b)^2 \right], \quad (3.2)$$

which provides a good description for a free  $\alpha$  particle [35].

The difference between the models is in their description of the CM motion, where the Brink wave function gives a crystal-like structure. For  $^8\text{Be}$ , the CM wave function is particularly simple and reads

$$\chi_R^{\text{Brink}}(R_1, R_2) \propto \exp \left[ - \left( R_1 - R/2 - (R_2 + R/2) \right)^2 / \tilde{b}^2 \right]. \quad (3.3)$$

Often  $\tilde{b}$  is chosen equal to the size of a free  $\alpha$  particle,  $b$ . In this case eq. (3.3) corresponds to two  $\alpha$  particles at a distance  $R$ , i.e. a crystal lattice.

The THSR wave function takes a quite different form in which the CM wave function is assumed to factorize into a product of  $0S$  wave functions [34]

$$\chi_{n\alpha}^{\text{THSR}}(R_1, \dots, R_n) = \prod_n \chi_0(\mathcal{R}_i), \quad (3.4)$$

with  $\mathcal{R}_I = R_I - X_G$  being the cluster coordinate relative to the CM,  $X_G = \sum_i R_i/n$ , and

$$\chi_0(\mathcal{R}) = \exp[-2(\mathcal{R}^2/B^2)]. \quad (3.5)$$

The size of the nucleus is determined by  $B$ , which is generally chosen significantly larger than the size of the quartets,  $b$ . Thus, this wave function represents  $n$  loosely bound  $0S$  bosons constrained to a region of size  $B$ . This is interpreted as a boson condensate by the authors [34] but this view has been challenged by others [36].

The most significant result from the THSR is its reproduction of the inelastic form factor from inelastic electron scattering without an arbitrary normalization [37].

**Molecular dynamics** include Antisymmetrized Molecular Dynamics (AMD) [38] and Fermionic Molecular Dynamics (FMD) [39]. The strength of these models compared to the explicit cluster models are that they do not assume a specific type of clustering. Instead, the internal degrees of freedom are the nucleons with a Slater determinant wave function

$$\Phi = \frac{1}{\sqrt{A!}} \mathcal{A}\{\phi_1, \phi_2, \dots, \phi_n\}. \quad (3.6)$$

This class of models can describe other nuclei than  $4n$  nuclei. The spatial single nucleon wave function,  $\phi_i$ , is described by a Gaussian wavepacket. In FMD it is possible for the individual nucleon wavepackets to have different widths. In addition, the molecular dynamic frameworks also include spin and isospin degrees of freedom. The models use effective nucleon-nucleon interactions.

Cluster formation is not assumed. Instead, it emerges as the minimal energy solution, which is found with a variational approach. An example of

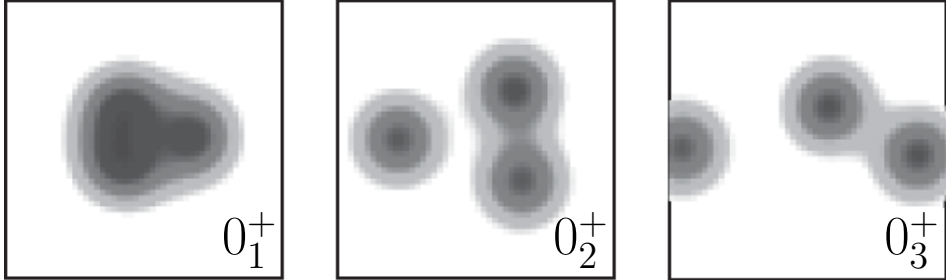


Figure 3.2: Observed cluster structures in AMD calculations of  $^{12}\text{C}$ . The figures shows the density in a plane for the lowest three  $0^+$  states. Note the  $\alpha + {}^8\text{Be}$  structure of the Hoyle state while the GS looks like a compressed triangle. Figure from ref. [40].

the emerging structures for the three lowest-lying  $0^+$  AMD states in  $^{12}\text{C}$  are shown in fig. 3.2 from ref. [40]. The second frame is interpreted as the Hoyle state, which shows a structure similar to  ${}^8\text{Be} + \alpha$  having two overlapping clusters orbited by a third cluster. Compared to the Hoyle state the GS is more compact, and the cluster structure is less developed, although still visible.

### Experimental evidence

There exist an even greater variety of models than those described in the previous section, and there is currently no consensus on the internal structure of the Hoyle state. The predicted shapes include equilateral triangle, Bose-Einstein Condensate, “bent arm”,  ${}^8\text{Be} + \alpha$ , linear chain, etc. Clearly, experimental evidence is needed in order to constrain the models.

In the last few years, a significant experimental effort has been devoted to measure the energy distribution of all three final-state  $\alpha$ . The aim is to discriminate between the following scenarios: sequential decay via the  ${}^8\text{Be}$  GS, equal energy sharing, collinear decay, and phase-space decay. The hypothesis is that different internal structures would populate the various channels differently, e.g. the  ${}^8\text{Be} + \alpha$  structure observed in AMD seen in

fig. 3.2 would predominantly decay sequentially. In the experiments, the sequential decay was distinguished by an  $\alpha$  particle with well-defined energy. This is due to the narrow width of the  $^8\text{Be}$  GS and the Hoyle state. In practice, the majority of observed events correspond to sequential decays, and the experiments constrain the contributions from the non-sequential channels. The current state of the art is two independent 95% confidence levels on the upper limits of 0.043 and 0.047% on the non-sequential branches [41, 42].

However, in a comment to the recent experimental results Refsgaard *et al.* used a simple toy-model to analyze the effect of Coulomb interactions between the three  $\alpha$  particles in the final state [43]. They found that the separation of the primary  $\alpha$  particle and  $^8\text{Be}$  at the time of the secondary break-up is  $\sim 15$  fm and the observed energy is modified by the mutual Coulomb repulsion. The consequence of this is an altered signature both for the sequential and direct decay at the  $10^{-5}$  level, essentially limiting the information that can be extracted from the energy distribution. The current upper limit is  $\sim 4 \times 10^{-4}$  non-sequential, so this will be crucial for the next generation of experiments.

### 3.2 Second $2^+$

A result that emerges both in molecular dynamics and explicit cluster models is the existence of a  $2^+$  excitation of the Hoyle state. THSR predicts the excitation to be at 9.4 MeV with a width of 0.6 MeV [44, 45]. Both FMD and AMD overestimate the excitation energy of the Hoyle state itself by 1.9 and 0.5 MeV respectively, but predict a second  $2^+$  state at either 2.3 or 2.6 MeV above it.

From an experimental point of view, this region is difficult to investigate since there are contributions from several broad states in addition to the high energy tail of the Hoyle state (also called the “ghost anomaly”) [46]. However, experimental evidence has recently been provided by inelastic proton- and  $\alpha$  scattering [47–49] and from  $^{12}\text{C}(\gamma, \alpha)$  [50, 51]. The observed energy and width was 9.6(1) MeV and 0.6(1) MeV for the scattering experiment

and  $10.13^{+0.06}_{-0.05}$  MeV and  $2080^{+330}_{-260}$  keV for the capture experiment. Both observations are compatible with the theoretical predictions, but interestingly incompatible with each other.

An alternative technique is to study the  $\beta$  decay of  $^{12}\text{B}$  and  $^{12}\text{N}$ . Due to the  $\beta$  decay selection rules, the  $3^-$  state at 9.6 MeV is not fed. As this state was the dominant signal in the inelastic scattering experiments,  $\beta$  decay experiment should provide a much cleaner probe. This technique has been used in several studies, but none of these observed a  $2^+$  level at 10 MeV [52–57]. The observed spectrum from the latest experiment can be seen in fig. 3.3 [52]. The region between an excitation energy of 8 and 11 MeV is a broad featureless distribution, which was analyzed using R-matrix theory. A significant contribution in this region is the high energy tail of the Hoyle state. The level profile of this is shown in fig. 3.4 and clearly shows that the “sharpness” of the peak is deceptive.

When decomposing this region into its various constituents, the contribution from the Hoyle state ghost can be constrained through its relation to the peak. Thus a well-determined  $\beta$  decay branching ratio to the Hoyle state peak is a prerequisite. The branching ratios for the ground state of  $^{12}\text{B}$  and  $^{12}\text{N}$  to various states in  $^{12}\text{C}$  was remeasured in 2009 [57]. The result was a revision of several branching ratios by roughly a factor of 2. This measurement should be very robust since the radioisotope was directly implanted into a silicon detector resulting in very low thresholds and trivial absolute normalization. Specifically, the branching ratio from the  $^{12}\text{B}$  GS to the Hoyle state was determined to be 0.58(2) %, compared to the previous result 1.2(3) % [58] (originally reported as 1.5(3) %, but should be revised [57]). As the branching ratio to the Hoyle state has a crucial role in the search for the second  $2^+$ , the experiment reported on in the following paper was carried out to provide an independent determination of this value.



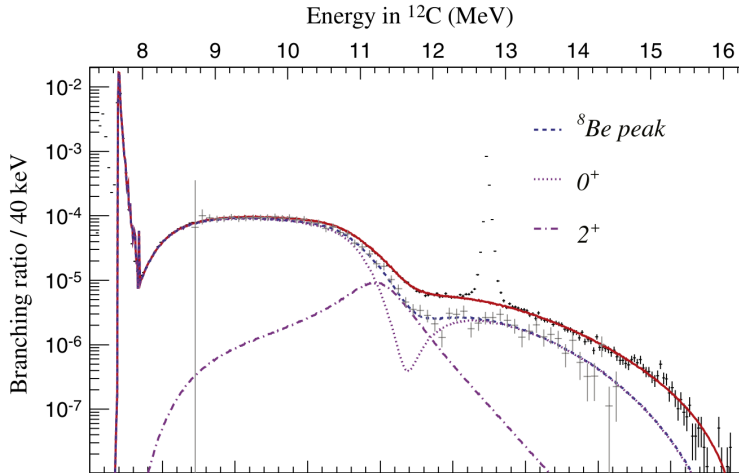


Figure 3.3: Observed  $^{12}\text{C}$  excitation spectrum in the  $\beta$  decay of  $^{12}\text{N}$ . This spectrum is for  $^{12}\text{C}$  break-up through the  $^8\text{Be}$  GS. Note the broad featureless nature of most of the spectrum. Figure from ref. [52].

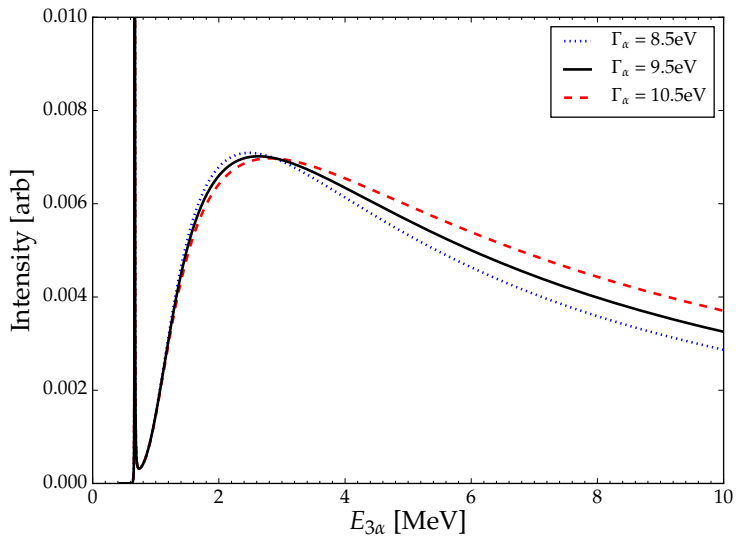


Figure 3.4: The level profile of the Hoyle state for decays via  $\alpha + ^8\text{Be}(\text{GS})$ . The peak height is normalized to 1 and the axis truncated. The high energy tail is called the “ghost anomaly” and the peak to tail ratio is roughly 10:1. The different curves correspond to different widths of the Hoyle state.

### 3.3 Hoyle state radiative decay

The Hoyle state is likely the most important resonance in nucleosynthesis. It plays a crucial role in the triple- $\alpha$  process in which three  $\alpha$  particles fuse into stable  $^{12}\text{C}$ , circumventing the unbound  $^8\text{Be}$  nuclei. The current understanding is that this predominantly occurs in red giant stars at a temperature of roughly  $10^8$  K, corresponding to a Gamow peak of approximately 80 keV, in a two-step reaction [59, 60]:



Due to  $^8\text{Be}$  being unbound, an equilibrium concentration of  $^8\text{Be}/^4\text{He}$  of roughly  $10^{-10}$  is established. For  $^{12}\text{C}$ , the equilibrium is broken by the radiative decay of the Hoyle state to the bound ground state. The effect of the Hoyle state is to increase the  $^{12}\text{C}$  build-up by roughly 7-8 orders of magnitude compared to the non-resonant capture [24].

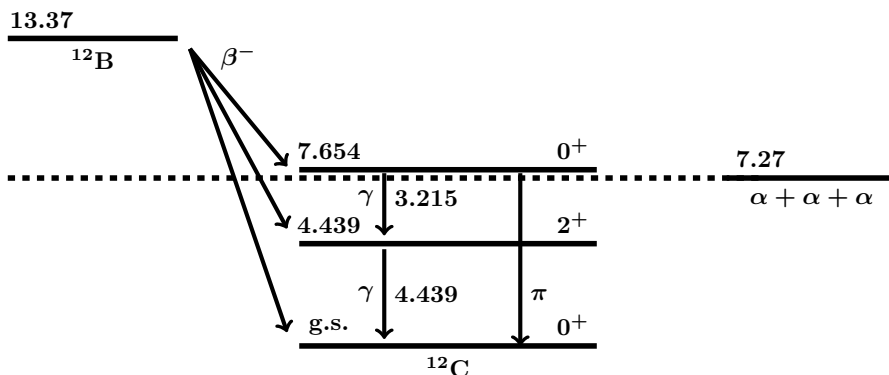


Figure 3.5: Illustration of the radiative decay of the Hoyle state. It can either  $\gamma$  decay via the FES, which subsequently decays to the GS. Alternatively, it may decay directly to the GS by emitting an  $e^-e^+$  pair or a conversion electron. Both the GS and FES are fed in the  $\beta$  decay of the  $^{12}\text{B}$  GS.

The radiative decay of the Hoyle state is illustrated in fig. 3.5. As both the Hoyle state and the GS is  $0^+$ , the direct  $\gamma$  decay is forbidden. Instead, the decay might either proceed through an E2 cascade decay via the FES, or it might decay directly to the GS by emission of a  $e^+e^-$  pair ( $\pi$ ), or emit a conversion electron (CE). Note that the first excited state is below all particle emission thresholds, so it must  $\gamma$  decay. From its resonance width, the lifetime is approximately 60 fs. The full radiative width can be written as

$$\Gamma_{\text{rad}} = \Gamma_{\gamma}^{\text{E2}} + \Gamma_{\pi}^{\text{E0}} + \Gamma_{\pi}^{\text{E2}} + \Gamma_{\text{CE}}^{\text{E0}} + \Gamma_{\text{CE}}^{\text{E2}}, \quad (3.8)$$

where the terms are ordered by their magnitude, which is 98.5%, 1.5%, 0.09% respectively for the first three terms and  $< 0.01\%$  for the last two [61]. If  $\Gamma_{\text{rad}}$  is approximated by the first two terms, it can be rewritten in the following form

$$\Gamma_{\text{rad}} \approx \Gamma_{\gamma}^{\text{E2}} + \Gamma_{\pi}^{\text{E0}} = \frac{\Gamma_{\gamma}^{\text{E2}} + \Gamma_{\pi}^{\text{E0}}}{\Gamma} \cdot \frac{\Gamma}{\Gamma_{\pi}^{\text{E0}}} \cdot \Gamma_{\pi}^{\text{E0}}, \quad (3.9)$$

where  $\Gamma$  is the full width of the resonance. This rewrite is performed since  $\Gamma_{\pi}^{\text{E0}}$  is the only part which has been measured directly [62]. The errors on the three terms amounts to 2.7%, 9.2% and 2.7% which leads to an overall error of 13%. It should be noted that the adopted value for the first term is a combination of eight different measurements, each with roughly 5 to 10% precision.

While the triple- $\alpha$  process is relatively well constrained when it predominantly proceeds via the Hoyle state, the situation is more unclear at higher energies relevant for explosive burning. Figure 3.6 shows the reaction rate dependence on the  $^{12}\text{C}$  resonances. The first resonance above the Hoyle state is a  $3^-$  state at 9.6 MeV, but as can be seen from the figure the  $3^-$  only contributes a factor of 2 at very high energies. This is due to a significant centrifugal barrier. However, a  $2^+$  state in the same region changes the reaction rate by as much as a factor of 10.

### 3.4 Method

This experiment aimed at providing an independent determination of the  $\beta$  decay branching of the  $^{12}\text{B}$  GS to the Hoyle state. The branching ratio was determined from a measurement of  $\gamma$  rays instead of charged particles.

Specifically, we sought to measure the cascade decay of the Hoyle state via the first excited state by simultaneously detecting the two  $\gamma$  rays. In order to normalize this measurement, the singles spectrum was also recorded. From the singles spectrum, it is possible to determine how much the FES was

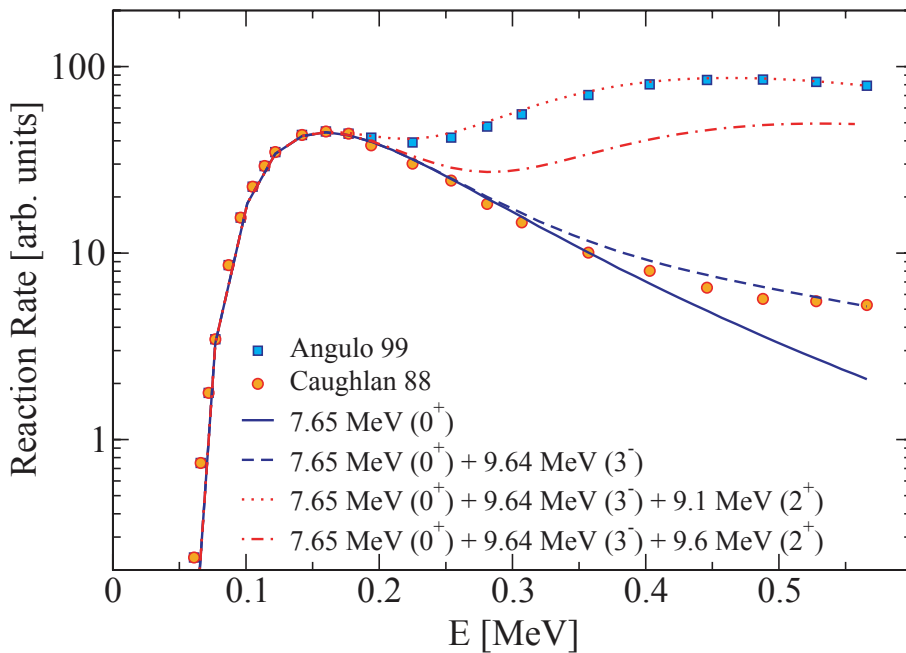


Figure 3.6: Calculated reaction rate with the Hoyle state,  $3^-$  and  $2^+$ . The  $3^-$  state has a small impact for energies above 0.25 MeV, while the  $2^+$  has a significant impact irrespective of its location. Figure from ref. [48].

populated based on the number of  $\gamma$  rays with an energy of 4.44 MeV. As the  $\beta$  decay branching ratio to the FES is known, the Hoyle state  $\beta$  feeding can be determined from the ratio of coincidences and singles, provided corrections for angular correlations and efficiencies are applied

$$B(7.65) \frac{\Gamma_{\gamma}^{\text{E2}}}{\Gamma} = B(4.44) \frac{N_{\gamma\gamma}}{N_{4.44} \epsilon_{3.21} C_{\theta}}, \quad (3.10)$$

where  $\Gamma$  is the total resonance width of the Hoyle state,  $\Gamma_{\gamma}^{\text{E2}}$  its  $\gamma$  decay width,  $N_{\gamma\gamma}$  the number of coincidences,  $N_{4.44}$  the number of counts in the 4.44 MeV peak,  $\epsilon_{3.21}$  the efficiency for detecting a 3.21 MeV  $\gamma$  ray,  $C_{\theta}$  corrects for angular correlations and  $B(4.44)$  and  $B(7.65)$  is the  $\beta$  decay branching ratio to the FES and Hoyle state respectively.  $C_{\theta}$  was expected to be small due to the large angular coverage of Gammasphere. This was confirmed with simulations. See paper for more details.

In addition, we also sought to measure the angular distribution between the two  $\gamma$  rays as this had not been done before. From the angular distribution, it is possible to determine the spin of the individual levels [63].

The success of the experiment hinged on detecting a sufficient number of cascade decays of the Hoyle state to allow discrimination between the two candidates. The branching ratio for a cascade decay can be estimated from the product of the Hoyle  $\beta$  feeding,  $B(7.65) \sim 1\%$ , and the relative  $\gamma$  width of the Hoyle state  $\frac{\Gamma_{\gamma}}{\Gamma} \sim 4 \times 10^{-4}$  and is thus  $\sim 4 \times 10^{-6}$ . In addition, the experimental equipment must have a good angular coverage in order to provide a high coincidence detection efficiency. Good resolution is also a requirement in order to avoid background contamination. There exist very few devices in the world, which fulfill these requirements, but Gammasphere at Argonne National Laboratory is one of them. It is an array of 110 high-purity Compton suppressed Germanium detectors (HPGe). During the experiment 98 of the detectors were operational, which gave a  $\sim 3\%$  detection efficiency at 3 MeV for the array.

### 3.5 Results and discussion

During the 67-hour experiment 58(9) cascade decays and  $9.20(2) \times 10^6$  decays of the FES were observed. Correcting for angular correlations and detection efficiency this yielded a Hoyle state  $\beta$  feeding of 0.64(11) %. From this a  $\log ft = 4.50(7)$  can be determined using the lifetime from the latest evaluation [61]. The angular distribution was also extracted and found to be consistent with a  $0 \rightarrow 2 \rightarrow 0$  cascade.

This experiment confirmed the branching ratio of ref. [57]. As such, the results of the R-matrix analysis of the  $^{12}\text{B}$  and  $^{12}\text{N}$   $\beta$  decays in ref. [52] stand. The null result of the R-matrix analysis could be explained with the  $2^+$  excitation being more clustered than the Hoyle state. An improved  $\beta$  decay experiment was performed in 2014, but again the analysis showed a dominant  $0^+$  contribution [64]. However, with the limited statistics available, a  $2^+$  contribution could not be excluded.

The  $\beta$  decay matrix element between a pure  $3\alpha$  wave function and  $^{12}\text{B}$  or  $^{12}\text{N}$  is 0 due to the PEP [40]. Thus the  $\beta$  decay probes the non-cluster properties of the Hoyle state. This observable is not affected by final state corrections, discussed in section 3.1, and could serve as a sensitive probe of the Hoyle state structure. The matrix element is proportional to  $\log ft$  which can be compared to theoretical calculations. The result using the AMD approach is not consistent with the updated branching ratio and unfortunately this value has not been computed using different frameworks.

### 3.6 Outlook

The property directly measured in this experiment is  $B(7.65) \frac{\Gamma_\gamma}{\Gamma}$ . Thus, with the branching ratio well established a precise determination of the relative  $\gamma$  width of the Hoyle state could be made. Since this experiment was conducted, the Gammasphere data acquisition system has been upgraded. We have also initiated a collaboration in order to make deuterated hafnium targets, which have a higher Coloumb barrier than titanium. Both of these improvements would facilitate more intense beams. In the conclusion of

the article, an error analysis is performed. The limiting factor for such an experiment is the precision of the  $\beta$  feeding of the FES. However, it would be possible to provide an independent measurement the relative  $\gamma$  width with a precision of 6 %, which would put it on par with the previous measurement. This determination was also the subject of the recently defended thesis of Alshahrani, who measured  $4.07(22) \times 10^{-4}$  using the alternative  $p\gamma\gamma$  method [65]. The same experimental group have also built a new pair spectrometer with the aim of improving upon the uncertain  $\frac{\Gamma_\pi}{\Gamma}$  value [66]. However, the work does not seem to have progressed since 2013.

Another interesting aspect related to this work is the  $4\alpha$  Hoyle state equivalent in  $^{16}\text{O}$ . In a series of theoretical investigations Funaki *et al.* found the sixth  $0^+$  at 15.1 MeV to have a large spatial structure similar to the Hoyle state [67, 68]. However, later investigations at iThemba labs identified a previously unresolved non  $0^+$  resonance in the same region [69]. In order to investigate this, the Aarhus group have had a solid  $^{15}\text{N}$  target manufactured. Preliminary results on the yield of the  $(p, \alpha_0)$  and  $(p, \alpha_1)$  channels have been published, but so far the signature of a  $4\alpha$  state has not been identified [70].

### 3.7 Contribution

The results reported in the following paper are the outcome of a three-part experimental campaign. A feasibility study was conducted in 2010. This was followed by an experiment in 2012 and another in 2015. I participated in the third part. However, that experiment eventually failed due to target problems, so the data in the following paper is from the 2012 experiment. A preliminary analysis of the data was performed by Martin Alcorta and the results published in a conference proceeding [71]. However, the results reported in the following paper are based on an entirely independent data analysis performed by me. I wrote most of the paper with inputs from co-authors.





## Independent measurement of the Hoyle state $\beta$ feeding from $^{12}\text{B}$ using Gammasphere

M. Munch,<sup>1</sup> M. Alcorta,<sup>2,3</sup> H. O. U. Fynbo,<sup>1,\*</sup> M. Albers,<sup>3</sup> S. Almaraz-Calderon,<sup>3,†</sup> M. L. Avila,<sup>3</sup> A. D. Ayangeakaa,<sup>3</sup> B. B. Back,<sup>3</sup> P. F. Bertone,<sup>3,‡</sup> P. F. F. Carnelli,<sup>4</sup> M. P. Carpenter,<sup>3</sup> C. J. Chiara,<sup>3,5</sup> J. A. Clark,<sup>3</sup> B. DiGiovine,<sup>3</sup> J. P. Greene,<sup>3</sup> J. L. Harker,<sup>3,5</sup> C. R. Hoffman,<sup>3</sup> N. J. Hubbard,<sup>6</sup> C. L. Jiang,<sup>3</sup> O. S. Kirsebom,<sup>1</sup> T. Lauritsen,<sup>3</sup> K. L. Laursen,<sup>1</sup> S. T. Marley,<sup>3,7,8</sup> C. Nair,<sup>3</sup> O. Nusair,<sup>3</sup> D. Santiago-Gonzalez,<sup>3,8</sup> J. Sethi,<sup>3,5</sup> D. Seweryniak,<sup>3</sup> R. Talwar,<sup>3</sup> C. Ugalde,<sup>3,9,10</sup> and S. Zhu<sup>3</sup>

<sup>1</sup>Department of Physics and Astronomy, Aarhus University, 8000 Aarhus C, Denmark

<sup>2</sup>TRIUMF, 4004 Westbrook Mall, Vancouver, British Columbia V6T 2A3, Canada

<sup>3</sup>Physics Division, Argonne National Laboratory, Argonne, Illinois 60439, USA

<sup>4</sup>Laboratorio Tandar, Comisin Nacional de Energia Atmica, B1650KNA Buenos Aires, Argentina

<sup>5</sup>Department of Chemistry and Biochemistry, University of Maryland, College Park, Maryland 20742, USA

<sup>6</sup>Department of Physics, University of York, York YO10 5DD, United Kingdom

<sup>7</sup>Physics Department, Western Michigan University, Kalamazoo, Michigan 49008, USA

<sup>8</sup>Louisiana State University, Department of Physics and Astronomy, 224 Nicholson Hall, Tower Drive, Baton Rouge, Louisiana 70803-4001, USA

<sup>9</sup>Department of Astronomy and Astrophysics, University of Chicago, Chicago, Illinois 60637, USA

<sup>10</sup>Joint Institute for Nuclear Astrophysics, Chicago, Illinois 60637, USA

(Received 12 January 2016; published 7 June 2016)

Using an array of high-purity Compton-suppressed germanium detectors, we performed an independent measurement of the  $\beta$ -decay branching ratio from  $^{12}\text{B}$  to the second-excited state, also known as the Hoyle state, in  $^{12}\text{C}$ . Our result is 0.64(11)%, which is a factor  $\sim 2$  smaller than the previously established literature value, but is in agreement with another recent measurement. This could indicate that the Hoyle state is more clustered than previously believed. The angular correlation of the Hoyle state  $\gamma$  cascade has also been measured for the first time. It is consistent with theoretical predictions.

DOI: [10.1103/PhysRevC.93.065803](https://doi.org/10.1103/PhysRevC.93.065803)

### I. INTRODUCTION

Carbon is the fourth most abundant element in the universe and it plays a key role in stellar nucleosynthesis. It is mainly formed in stars at temperatures of  $10^8$  to  $10^9$  K in the triple- $\alpha$  fusion reaction, which proceeds via the second excited state, also known as the Hoyle state, at 7.65 MeV in  $^{12}\text{C}$ , famously proposed by Hoyle in 1953 [1].

The first attempt to theoretically explain the structure of the state was the linear  $\alpha$  chain model by Morinaga in 1956 [2], where he conjectured a  $2^+$  state in the 9- to 10-MeV region. Several more sophisticated models have been developed since, as summarized in Ref. [3]. Most of these models predict a collective  $2^+$  excitation of the Hoyle state in the region of 0.8–2.3 MeV above it. Interestingly, the collective state increases the triple- $\alpha$  reaction rate at  $T > 10^9$  K by a factor of 5–10 compared to the results of Caughlan *et al.* [4,5]. This makes it highly relevant for core-collapse supernovae [6–9].

Experimentally, it is challenging to investigate this energy region, since there are contributions from several broad states and from the so-called Hoyle state *ghost anomaly* [10–12].

Using inelastic proton scattering, Freer *et al.* provided the first evidence for a broad  $2^+$  contribution at 9.6(1) MeV with a width of 600(100) keV [5]. Itoh *et al.* corroborated these results using inelastic  $\alpha$  scattering [13] and a simultaneous analysis was published as well [14]. Results from an experiment using the alternative  $^{12}\text{C}(\gamma, \alpha)^8\text{Be}$  reaction also identified a  $2^+$  state in this region, but at  $10.13_{-0.05}^{+0.06}$  MeV and with a much larger width of  $2080_{-260}^{+330}$  keV [15,16]. The reason for this discrepancy is presently not understood. A natural explanation would be that several  $2^+$  resonances are present in the region and that the different reaction mechanisms populate these with different strengths.

An alternative experimental probe is the  $\beta$  decay of  $^{12}\text{B}$  and  $^{12}\text{N}$ . Due to the selection rules, decay of these  $1^+$  systems will predominantly populate states with spin and parity  $0^+$ ,  $1^+$ , or  $2^+$  and not the  $3^-$  state at 9.64 MeV, which is the dominant channel in inelastic scattering experiments. This technique has been used in several studies of  $^{12}\text{C}$  [17–22], but none of these has identified a  $2^+$  state at 10 MeV. The  $\beta$  decay populates a somewhat featureless excitation spectrum in  $^{12}\text{C}$ , which is analyzed with the  $R$ -matrix formalism in Ref. [22]. This analysis identified both  $0^+$  and  $2^+$  resonances in the 10.5- to 12-MeV region with recommended energies for both resonances at 11 MeV. The  $R$ -matrix analysis includes a large contribution from the high-energy tail of the Hoyle state, which is sometimes referred to as the *ghost anomaly* [10,11]. This contribution is strongly dependent on the branching ratio with which the Hoyle state is populated in the  $\beta$  decay.

In the most recent experimental study of the  $\beta$  decay, the beam was implanted in a silicon detector, which provided

\*Corresponding author: [fynbo@phys.au.dk](mailto:fynbo@phys.au.dk)

<sup>†</sup>Present address: Department of Physics, Florida State University, Tallahassee, Florida 32306, USA.

<sup>‡</sup>Present address: Marshall Space Flight Center, Huntsville, Alabama 35811, USA.

<sup>§</sup>Present address: Louisiana State University, Department of Physics and Astronomy, 224 Nicholson Hall, Tower Drive, Baton Rouge, Louisiana 70803-4001, USA.

accurate normalization of the branching ratios, resulting in a revision of several of these [21]. More specifically, the branching ratio to the Hoyle state from the decay of  $^{12}\text{B}$  was determined to be 0.58(2)%, which is inconsistent with the previously established value of 1.2(3)% [12,23] (1.5(3)% is listed in Ref. [12], but this should be revised [23]). The reduced branching ratio for the population of the Hoyle state was used in the  $R$ -matrix analysis [22]. Furthermore, as the  $\beta$  decay to a pure  $3\alpha$ -cluster system is forbidden, a precise measurement of the branching ratio will provide insight into the strength of the cluster-breaking component of the Hoyle state [24]. It is therefore important to provide experimental confirmation of the reduced branching ratio measured in Ref. [21].

Here, we report on an independent measurement of this branching ratio through a measurement of the  $\gamma$  decay of the Hoyle state with an array of high-purity germanium detectors. The results of a preliminary analysis have been reported in Ref. [25].

## II. METHOD

Figure 1 shows the lowest states in  $^{12}\text{C}$ , the triple- $\alpha$  threshold, and the ground state of  $^{12}\text{B}$ . The first excited state is below the  $\alpha$  threshold and will only  $\gamma$  decay, whereas the Hoyle state cannot  $\gamma$  decay directly to the ground state as it is a  $0^+$  level. It can, however, decay via the first excited state by emission of a 3215-keV photon.

The number of  $\gamma$  decays from the Hoyle state can be determined by counting the number of 3215-keV photons, and by furthermore requiring a simultaneous detection of a 4439-keV  $\gamma$  ray, the background is vastly reduced. The product of the branching ratio to the Hoyle state and its relative  $\gamma$  width can then be determined by normalizing to the decay of the first excited state

$$B(7.65) \frac{\Gamma_\gamma}{\Gamma} = B(4.44) \frac{N_{\gamma\gamma}}{N_{4.44} \epsilon_{3.21} C_\theta}, \quad (1)$$

where  $N_{\gamma\gamma}$  is the number of coincidence events,  $\epsilon_{3.21}$  is the efficiency for detecting a 3215-keV photon, and  $C_\theta$  corrects for the angular correlation between the two photons.

The relative  $\gamma$  width can be determined from all available data for the relative radiative width [26], excluding the work of Seeger *et al.* [27], by subtracting the recommended relative pair width from [3], which yields  $\frac{\Gamma_\gamma}{\Gamma} = 4.07(11) \times 10^{-4}$ . A

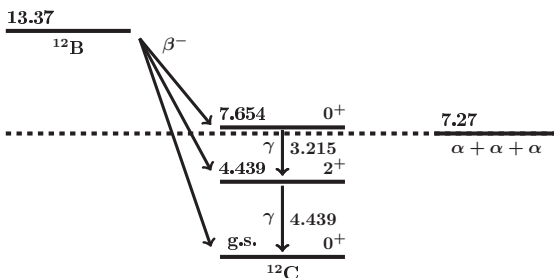


FIG. 1. Level scheme of  $^{12}\text{C}$  also showing the  $\alpha$  threshold and the  $^{12}\text{B}$  ground state. Energies are given in MeV relative to the ground state of  $^{12}\text{C}$  [12].

conservative estimate of the branching ratio to the first excited state,  $B(4.44) = 1.23(5)\%$ , has been published [12].

Using this method, the branching ratio can be determined solely with  $\gamma$ -ray detectors, providing an experiment with entirely different systematic uncertainties than previous measurements based on detection of  $\alpha$  or  $\beta$  particles.

## III. EXPERIMENT

$^{12}\text{B}$  was produced via the  $^{11}\text{B}(d,p)^{12}\text{B}$  reaction in inverse kinematics, using a pulsed (40 ms on, 40 ms off) 40-MeV  $^{11}\text{B}$  beam delivered by the Argonne Tandem-Linac Accelerator System (ATLAS) located at Argonne National Laboratory. A deuterated titanium foil ( $\text{TiD}_2$ ), sufficiently thick to stop the beam, was used as target. The target was manufactured according to the method discussed in Ref. [28] and it contained approximately 1.5 mg/cm<sup>2</sup> deuterium (estimated by weight).

Photons were detected using Gammasphere [29], which is an array of 110 high-purity Compton-suppressed germanium detectors, of which 98 were operational during the experiment. The array was operated in singles mode, where any of the detectors could trigger the data acquisition (DAQ). Data were only acquired during the beam-off period. Therefore, only delayed activity was measured (the half-life of  $^{12}\text{B}$  is 20.20(2) ms [12]). For each event, the time relative to beam off as well as the energy and time for each  $\gamma$  ray in the detectors were recorded.

In order to minimize bremsstrahlung caused by high-energy  $\beta$  particles, a low- $Z$  chamber was designed; see Fig. 2. The chamber was manufactured from a Bonner sphere and was designed to minimize contribution from bremsstrahlung while maintaining high  $\gamma$ -ray efficiency.

## IV. ANALYSIS

### A. Yield

During the experiment  $\sim 10^9$   $\gamma$  rays were collected in 67 h. The singles spectrum is displayed in Fig. 3, where the transition from the first excited state in  $^{12}\text{C}$  at  $4439.5 \pm 0.7(\text{sys})$  keV

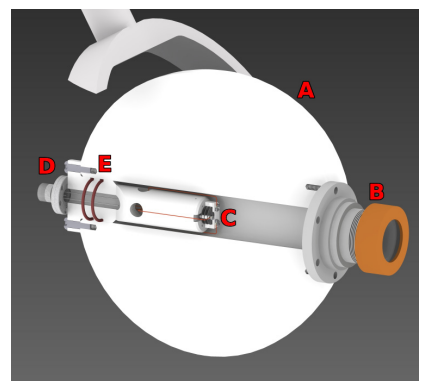


FIG. 2. CAD drawing of the chamber manufactured from a Bonner sphere. (A) Bonner sphere, (B) vacuum flange, (C) target holder/Faraday cup, (D) electrical feed through, (E) O-rings

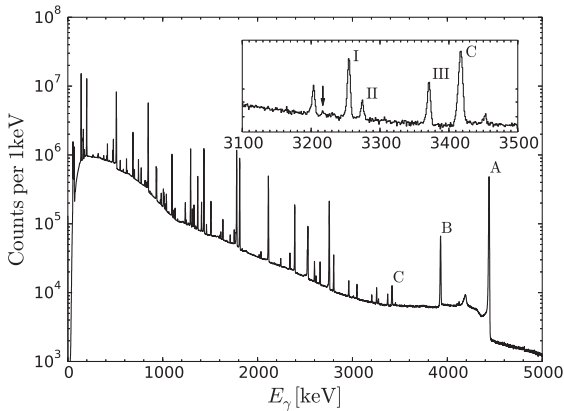


FIG. 3. The entire singles spectrum acquired during the beam-off period. The 4439-keV peak (A) and its escape peaks (B,C) are clearly visible. The insert shows the 3.1- to 3.5-MeV region. A small structure is visible around 3215 keV, indicated by an arrow.

(A) together with the first (B) and second escape (C) peaks at lower energy are clearly seen. The insert shows the region from 3.1 to 3.5 MeV in which a structure around 3215 keV is visible, as indicated by an arrow. However, the region is dominated by a peak at 3200 keV.

The 4439-keV peak was fitted with a sum of a Gaussian distribution, a skewed Gaussian distribution, a linear background, and a smoothed step function [30]. In order to minimize systematic effects, the fit was performed with the Poisson log likelihood ratio [31] using the MINUIT minimizer [32]. From this procedure, the area of the peak was determined to be  $N_{4,44} = 9.20(2) \times 10^6$ , where the error was dominated by uncertainties in the functional form of the peak.

### B. Coincidence spectrum

To obtain a coincidence spectrum, a gate was placed on the relative time between the two  $\gamma$  rays and on the energy of the 4439-keV transition. The widths of these gates were chosen to minimize any systematic effects.

The coincidence spectrum is given in Fig. 4, where a clear peak centered at  $3216.9^{+0.7(\text{sys})}_{\pm 0.4(\text{stat})}$  keV is visible. This is consistent with a cascade decay of the Hoyle state via the first excited level. The peak was fitted with the same functional form as in the previous section, but the parameters for the skewed Gaussian are determined from peaks I–III in Fig. 3. Peaks I–III originate from  $^{56}\text{Mn}$  and  $^{56}\text{Co}$  produced in beam by reactions with Ti. The area of the peak, determined from the fit, is  $N_{\gamma\gamma} = 58(9)$ .

### C. Efficiency

The relative efficiency was determined using the standard calibration sources  $^{152}\text{Eu}$  and  $^{56}\text{Co}$  mounted at the target position. This provides calibration points, both at low energy and in the important 3-MeV region. The absolute efficiency was calculated using the coincidence method, including a correction for random coincidence events, for both a  $^{60}\text{Co}$

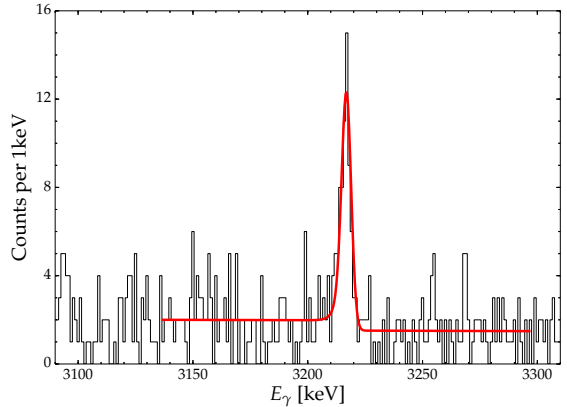


FIG. 4. Coincidence spectrum, acquired by gating on the 4439-keV peak and the time difference. A clear peak centered at 3217 keV is consistent with the Hoyle state decaying via the first excited state.

source and  $^{24}\text{Mg}$ , which was produced by in-beam reactions [33]. From this procedure, the absolute efficiency at 3217 keV was determined to be  $\epsilon_{3,21} = 2.94(2)\%$ .

### D. Angular correlation

Due to the excellent angular coverage of Gammasphere, it is possible to measure the angular correlation of the two  $\gamma$  rays, which had not been measured previously. Using the gates described above and in addition requiring the energy of the second  $\gamma$  ray to be within 10 keV of 3217 keV, it is possible to extract the true coincidence events plus some background. The shape of the background was determined by gating outside the peak, and was found to be flat.

The angular correlation, corrected for the geometric efficiency (number of detector pairs with a given angle between them), is shown in Fig. 5, together with the best fit to the equation

$$W(\theta) = k[1 + a_2 \cos^2(\theta) + a_4 \cos^4(\theta)], \quad (2)$$

where  $\theta$  is the angle between the two  $\gamma$  rays. The result of the fit is  $a_2 = -3.3(7)$  and  $a_4 = 4.2(9)$ , which is consistent with the theoretical expectations  $a_2 = -3$  and  $a_4 = 4$  for a  $0 \rightarrow 2 \rightarrow 0$  cascade [34].

With the theoretical angular correlation confirmed, it can be used to estimate the correction factor  $C_\theta$  from Eq. (1). This is done with a simple Monte Carlo simulation of the detector setup, which gives  $C_\theta = 1.00(1)$ , as was expected from the large angular coverage by Gammasphere.

### E. Extraction of branching ratio

The property directly measured in this experiment is the product of the relative  $\gamma$  width and the  $\beta$  feeding of the Hoyle state

$$B(7.65) \frac{\Gamma_\gamma}{\Gamma} = 2.6(4) \times 10^{-4}. \quad (3)$$

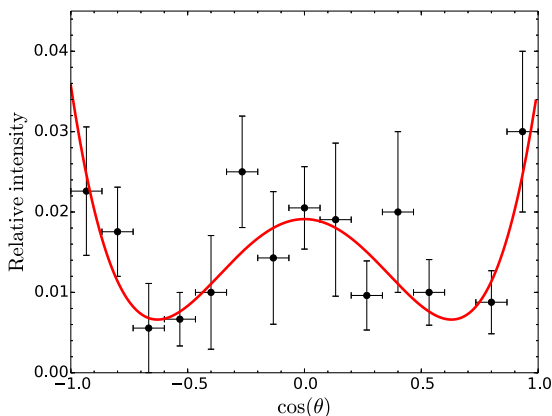


FIG. 5. Angular correlation of the Hoyle state  $\gamma$  cascade corrected for the geometric efficiency (number of detector pairs with a given angle between them). The solid line shown is the best fit to Eq. (2).

Inserting the calculated value for the relative  $\gamma$  width into Eq. (3) gives

$$B(7.65) = 0.64(11)\%, \quad (4)$$

which is clearly inconsistent with the previous literature value of 1.2(3)% [12,23], but agrees with that of 0.58(2)% found in Ref. [21]. Therefore, the feeding of the Hoyle state from  $^{12}\text{B}$  is roughly a factor of 2 smaller than indicated by Refs. [12,23].

## V. DISCUSSION

The branching ratio from  $^{12}\text{B}$  and  $^{12}\text{N}$  to the Hoyle state is a sensitive way to probe the clustering of this state, as the  $\beta$ -decay matrix element to the pure  $3\alpha$  system is exactly zero due to the Pauli principle [24]. The fact that  $\beta$  decay is possible means that the Hoyle state must contain some  $\alpha$ -cluster breaking component. Theoretically, this is obtained by mixing shell-model-like states with cluster states as it is done, e.g., in fermionic molecular dynamics (FMD) [35,36] and antisymmetrized molecular dynamics (AMD) approaches [24].  $\alpha$ -cluster breaking was explicitly investigated in Ref. [37] using a hybrid shell-cluster model, where it was found that the spin-orbit force significantly changes the excited  $0^+$  states.

Here, we compute the  $\log ft$  value, which can be directly compared with these models. The available phase space ( $f$  factor) for  $\beta$  decay from the ground state of  $^{12}\text{B}$  to the Hoyle state was computed using the method in Ref. [38], with the excitation energy and half-life from Ref. [12]. With this input our result is

$$\log ft = 4.50(7). \quad (5)$$

Due to the large change of the measured branching ratio compared to previous results [12], the theoretical prediction of the AMD model,  $\log ft = 4.3$  [24], is no longer compatible with the experiment.

Hence, our branching ratio, together with the branching ratio for both  $^{12}\text{B}$  and  $^{12}\text{N}$  from Hyldegaard *et al.* [21], indicate that the  $\alpha$  clustering of the Hoyle state is more pronounced than previously believed.

## VI. CONCLUSION AND OUTLOOK

The  $\beta$ -decay branching ratio from  $^{12}\text{B}$  to the second-excited state of  $^{12}\text{C}$  has been measured using an array of high-purity Compton-suppressed germanium detectors. The branching ratio was determined by counting the Hoyle state  $\gamma$  decay, and normalizing to the decay of the first excited state. The result is 0.64(11)%, consistent with the value found in Ref. [21], but is a factor  $\sim 2$  smaller than the previously established value from Ref. [12]. The updated branching was used to compute  $\log ft = 4.50(7)$ , which is not consistent with latest results from AMD calculations [24]. Our results indicate that the clustering of the Hoyle state is more pronounced than previously thought.

The angular correlation between the two photons emitted in the decay of the Hoyle state has also been measured. The distribution was consistent with theoretical expectations [34].

The errors on the present measurement are dominated by the uncertainty on the number of coincidence events, which contributes 91% of the total error, while 6% and 2% come from the branching ratio to the first excited state and the relative  $\gamma$  width of the Hoyle state, respectively. Therefore, it is possible to make a  $\sim 6\%$  measurement of either the  $\gamma$  width or the  $\beta$ -branching ratio by increasing statistics.

During the experiment, the beam current was limited to 2 pA in order to minimize neutron damage to Gammasphere. The main source for these neutrons was reactions with titanium since the beam energy is above the Coulomb barrier. Exchanging titanium with hafnium permits running with higher beam currents which, when combined with digital Gammasphere [39], would make it possible to accumulate sufficient statistics. Research into production of such a target is ongoing.

## ACKNOWLEDGMENTS

This work is supported by the U.S. Department of Energy, Office of Science, Office of Nuclear Physics, under Contracts No. DE-AC02-06CH11357 and No. DE-FG02-04ER41320 and Grant No. DE-FG02-94ER40834. This research used resources of ANL's ATLAS facility, which is a DOE Office of Science User facility. O.S.K. acknowledges support from the Villum Foundation. We also acknowledge financial support from the European Research Council under ERC starting grant LOBENA, No. 307447

- [1] F. Hoyle, *Astrophys. J. Suppl. Ser.* **1**, 121 (1954).
- [2] H. Morinaga, *Phys. Rev.* **101**, 254 (1956).
- [3] M. Freer and H. Fynbo, *Prog. Part. Nucl. Phys.* **78**, 1 (2014).
- [4] G. R. Caughlan and W. A. Fowler, *At. Data Nucl. Data Tables* **40**, 283 (1988).

- [5] M. Freer, H. Fujita, Z. Buthelezi, J. Carter, R. W. Fearick, S. V. Förtisch, R. Neveling, S. M. Perez, P. Papka, F. D. Smit, J. A. Swartz, and I. Usman, *Phys. Rev. C* **80**, 041303 (2009).
- [6] C. Tur, A. Heger, and S. M. Austin, *Astrophys. J.* **671**, 821 (2007).

- [7] C. Tur, A. Heger, and S. M. Austin, *Astrophys. J.* **718**, 357 (2010).
- [8] G. Magkotsios, F. X. Timmes, and M. Wiescher, *Astrophys. J.* **741**, 78 (2011).
- [9] L. The, D. D. Clayton, L. Jin, and B. S. Meyer, *Astrophys. J.* **504**, 500 (1998).
- [10] F. C. Barker and P. B. Treacy, *Nucl. Phys.* **38**, 33 (1962).
- [11] D. H. Wilkinson, D. E. Alburger, A. Gallmann, and P. F. Donovan, *Phys. Rev.* **130**, 1953 (1963).
- [12] F. Ajzenberg-Selove, *Nucl. Phys. A* **506**, 1 (1990).
- [13] M. Itoh, H. Akimune, M. Fujiwara, U. Garg, N. Hashimoto, T. Kawabata, K. Kawase, S. Kishi, T. Murakami, K. Nakanishi, Y. Nakatsugawa, B. K. Nayak, S. Okumura, H. Sakaguchi, H. Takeda, S. Terashima, M. Uchida, Y. Yasuda, M. Yosoi, and J. Zenihiro, *Phys. Rev. C* **84**, 054308 (2011).
- [14] M. Freer, M. Itoh, T. Kawabata, H. Fujita, H. Akimune, Z. Buthelezi, J. Carter, R. W. Fearick, S. V. Förtsch, M. Fujiwara, U. Garg, N. Hashimoto, K. Kawase, S. Kishi, T. Murakami, K. Nakanishi, Y. Nakatsugawa, B. K. Nayak, R. Neveling, S. Okumura, S. M. Perez, P. Papka, H. Sakaguchi, Y. Sasamoto, F. D. Smit, J. A. Swartz, H. Takeda, S. Terashima, M. Uchida, I. Usman, Y. Yasuda, M. Yosoi, and J. Zenihiro, *Phys. Rev. C* **86**, 034320 (2012).
- [15] W. R. Zimmerman, M. W. Ahmed, B. Bromberger, S. C. Stave, A. Breskin, V. Dangendorf, T. Delbar, M. Gai, S. S. Henshaw, J. M. Mueller, C. Sun, K. Tittelmeier, H. R. Weller, and Y. K. Wu, *Phys. Rev. Lett.* **110**, 152502 (2013).
- [16] W. R. Zimmerman, Ph.D. thesis, University of Connecticut, 2013 (unpublished).
- [17] C. W. Cook, W. A. Fowler, C. C. Lauritsen, and T. Lauritsen, *Phys. Rev.* **107**, 508 (1957).
- [18] D. E. Alburger, *Phys. Rev. C* **16**, 2394 (1977).
- [19] H. O. U. Fynbo, C. A. A. Diget, U. C. Bergmann, M. J. G. Borge, J. Cederkäll, P. Dendooven, L. M. Fraile, S. Franchoo, V. N. Fedosseev, B. R. Fulton, W. Huang, J. Huikari, H. B. Jeppesen, A. S. Jokinen, P. Jones, B. Jonson, U. Köster, K. Langanke, M. Meister, T. Nilsson, G. Nyman, Y. Prezado, K. Riisager, S. Rinta-Antila, O. Tengblad, M. Turrion, Y. Wang, L. Weissman, K. Wilhelmsen, and J. Äystö, *Nature (London)* **433**, 136 (2005).
- [20] C. Diget, F. Barker, M. Borge, J. Cederkäll, V. Fedosseev, L. Fraile, B. Fulton, H. Fynbo, H. Jeppesen, B. Jonson, U. Köster, M. Meister, T. Nilsson, G. Nyman, Y. Prezado, K. Riisager, S. Rinta-Antila, O. Tengblad, M. Turrion, K. Wilhelmsen, and J. Äystö, *Nucl. Phys. A* **760**, 3 (2005).
- [21] S. Hyldegaard, C. Forssén, C. Diget, M. Alcorta, F. Barker, B. Bastin, M. Borge, R. Boutami, S. Brandenburg, J. Büscher, P. Dendooven, P. Van Duppen, T. Eronen, S. Fox, B. Fulton, H. Fynbo, J. Huikari, M. Huyse, H. Jeppesen, A. Jokinen, B. Jonson, K. Jungmann, A. Kankainen, O. Kirsebom, M. Madurga, I. Moore, P. Navrátil, T. Nilsson, G. Nyman, G. Onderwater, H. Penttilä, K. Peräjärvi, R. Raabe, K. Riisager, S. Rinta-Antila, A. Rogachevskiy, A. Saastamoinen, M. Sohani, O. Tengblad, E. Traykov, J. Vary, Y. Wang, K. Wilhelmsen, H. Wilschut, and J. Äystö, *Phys. Lett. B* **678**, 459 (2009).
- [22] S. Hyldegaard, M. Alcorta, B. Bastin, M. J. G. Borge, R. Boutami, S. Brandenburg, J. Büscher, P. Dendooven, C. A. Diget, P. Van Duppen, T. Eronen, S. P. Fox, L. M. Fraile, B. R. Fulton, H. O. U. Fynbo, J. Huikari, M. Huyse, H. B. Jeppesen, A. S. Jokinen, B. Jonson, K. Jungmann, A. Kankainen, O. S. Kirsebom, M. Madurga, I. Moore, A. Nieminen, T. Nilsson, G. Nyman, G. J. G. Onderwater, H. Penttilä, K. Peräjärvi, R. Raabe, K. Riisager, S. Rinta-Antila, A. Rogachevskiy, A. Saastamoinen, M. Sohani, O. Tengblad, E. Traykov, Y. Wang, K. Wilhelmsen, H. W. Wilschut, and J. Äystö, *Phys. Rev. C* **81**, 024303 (2010).
- [23] S. Hyldegaard, C. A. Diget, M. J. G. Borge, R. Boutami, P. Dendooven, T. Eronen, S. P. Fox, L. M. Fraile, B. R. Fulton, H. O. U. Fynbo, J. Huikari, H. B. Jeppesen, A. S. Jokinen, B. Jonson, A. Kankainen, I. Moore, G. Nyman, H. Penttilä, K. Peräjärvi, K. Riisager, S. Rinta-Antila, O. Tengblad, Y. Wang, K. Wilhelmsen, and J. Äystö, *Phys. Rev. C* **80**, 044304 (2009).
- [24] Y. Kanada-En'yo, *Prog. Theor. Phys.* **117**, 655 (2007).
- [25] M. Alcorta, H. O. U. Fynbo, M. Albers, S. Almaraz-Calderon, P. F. Bertone, P. F. F. Carnelli, M. Carpenter, C. J. Chiara, B. DiGiovine, C. J. P. Greene, R. Hoffman, R. V. F. Janssens, T. Lauritsen, K. L. Laursen, S. T. Marley, C. Nair, K. O. Nusair, E. Rehm, D. Seweryniak, C. Ugalde, and S. Zhu, in *EPJ Web of Conferences*, Vol. **66**, edited by S. Lunardi, P. Bizzeti, C. Bucci, M. Chiari, A. Dainese, P. Di Nezza, R. Menegazzo, A. Nannini, C. Signorini, and J. Valiente-Dobon (EDP Sciences, London, 2014), p. 07001.
- [26] A. W. Obst and W. J. Braithwaite, *Phys. Rev. C* **13**, 2033 (1976).
- [27] P. Seeger and R. Kavanagh, *Nucl. Phys.* **46**, 577 (1963).
- [28] J. P. Greene, H. Young Lee, and H.-W. Becker, *Nucl. Instrum. Methods Phys. Res., Sect. A* **613**, 462 (2010).
- [29] I.-Y. Lee, *Nucl. Phys. A* **520**, c641 (1990).
- [30] K. Debertin and R. Helmer, *Gamma- and X-ray Spectrometry with Semiconductor Detectors* (North Holland, Amsterdam, 1988).
- [31] U. Bergmann and K. Riisager, *Nucl. Instrum. Methods Phys. Res., Sect. A* **489**, 444 (2002).
- [32] F. James and M. Roos, *Comput. Phys. Commun.* **10**, 343 (1975).
- [33] K. Siegbahn, *Alpha, Beta, and Gamma Ray Spectroscopy* (Elsevier Science, Amsterdam, 1965).
- [34] E. L. Brady and M. Deutsch, *Phys. Rev.* **72**, 870 (1947).
- [35] R. Roth, T. Neff, H. Hergert, and H. Feldmeier, *Nucl. Phys. A* **745**, 3 (2004).
- [36] M. Chernykh, H. Feldmeier, T. Neff, P. von Neumann-Cosel, and A. Richter, *Phys. Rev. Lett.* **98**, 032501 (2007).
- [37] T. Suhara and Y. Kanada-En'yo, *Phys. Rev. C* **91**, 024315 (2015).
- [38] D. Wilkinson and B. Macefield, *Nucl. Phys. A* **232**, 58 (1974).
- [39] J. T. Anderson, M. Albers, M. Alcorta, C. Campbell, M. P. Carpenter, C. J. Chiara, M. Cromaz, H. M. David, D. Doering, D. T. Doherty, C. R. Hoffman, R. V. F. Janssens, J. Joseph, T. L. Khoo, A. Kreps, T. Lauritsen, I. Y. Lee, C. Lionberger, C. J. Lister, T. Madden, M. B. Oberling, A. M. Rogers, D. Seweryniak, P. Wilt, S. Zhu, and S. Zimmermann, in *2012 IEEE Nuclear Science Symposium and Medical Imaging Conference Record (NSS/MIC)* (IEEE, Anaheim, 2012), p. 1536.



## Measurement of the full excitation spectrum of the ${}^7\text{Li}(p, \gamma)\alpha\alpha$ reaction at 441keV

This chapter reports on a measurement of the  ${}^8\text{Be}$  excitation spectrum populated in the  $\gamma$  decay of the 17.6 MeV resonance. Measurements of  ${}^8\text{Be}$  have a long history that is deeply intertwined with the development of nuclear physics as a whole. As such this chapter will touch upon quite a few subjects.

The chapter starts with a motivation, which will summarize the various measurements and theoretical works relevant for the low energy part of the  ${}^8\text{Be}$  excitation spectrum. As some of the tentative resonances are extremely broad, the following section will investigate the concepts of continuum and resonances in a toy model. An in-depth review of the existing  $\gamma$ -ray spectra obtained for the 17.6 MeV resonance is then presented in order to motivate the need for an alternative method. The last few sections then describe the method used in the present experiment and summarize and discusses the results. These results were published in ref. [72] and the paper can be found at page 65.

### 4.1 Motivation

#### **Intruders in ${}^8\text{Be}$**

${}^8\text{Be}$  has been studied since the dawn of nuclear physics, starting with the

first accelerated beam by Cockcroft and Walton in 1932 [73] and is perhaps one of the most well-studied nuclei. This is partly motivated by its rather peculiar structure. The level scheme, according to the latest evaluation, can be seen in fig. 4.1 [74]. The three lowest states are well described using an  $\alpha\alpha$  cluster picture, while the higher-lying states show a shell-model-like structure. Consistently describing these different degrees of freedom within a single model is a challenge – even for modern *ab initio* theory [75].

The high degree of  $\alpha$ -clusterization causes the low lying states to have a very short lifetime, leading to very broad resonances. The observed width is

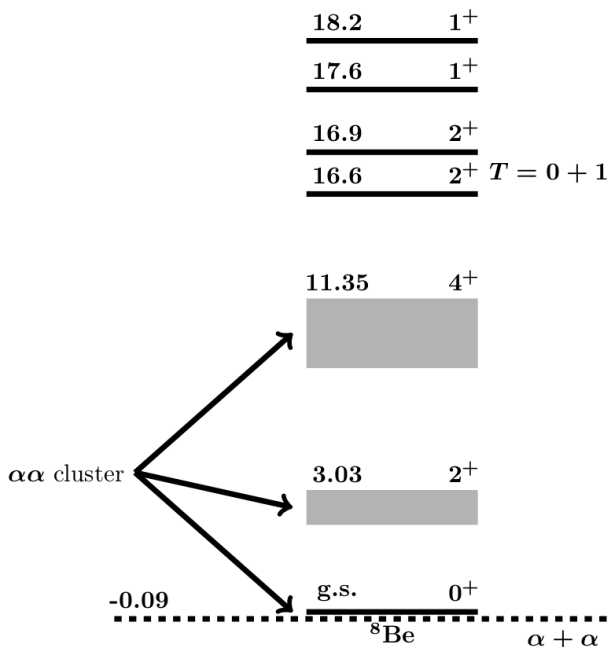


Figure 4.1: The lower part of the  ${}^8\text{Be}$  level scheme. All levels are unbound. The three lowest resonances are highly clustered. The  $2^+$  doublet at 16.6 and 16.9 MeV is isospin mixed.



roughly 1.5, and 3.5 MeV for the lowest  $2^+$  and  $4^+$  states, respectively [74]. Remembering that  $\Gamma$  roughly<sup>1</sup> corresponds to the full width at half max (FWHM), the region below 17 MeV is characterized by broad overlapping levels. In addition, the first excited state (FES) can and will interfere with the higher-lying  $2^+$  doublet.

Quantum mechanically it is impossible to disentangle the individual interfering contributions to an observed spectrum, i.e. the interference cannot be deconvoluted. The experimentalist is left with two choices: ignore the interference or construct a model, which reproduces the observed spectrum.

An often used model is the phenomenological R-matrix, in which the configuration space is divided into an internal and external region at some channel radius,  $a_c$ . In the external region, the interaction is assumed to be purely Coulomb, and anti-symmetrization is neglected [76]. This model will be described in more detail in section 4.7. At present, it is important to note that the model includes resonances and a description of the continuum of scattering states via background poles.

In a series of articles, Barker *et al.* (BA) sought to investigate  $0^+$  and  $2^+$  resonances in  $^8\text{Be}$  by performing an R-matrix analysis of s- and d-wave phase shift from  $\alpha\alpha$  scattering combined with data from  $^9\text{Be}(p, d)^8\text{Be}$  and  $\beta$  decay data. According to their analysis, there is an additional  $0^+$  resonance at 6(3) MeV with a width of 9(4) MeV and a  $2^+$  resonance at 9 MeV with a width of roughly 10 MeV [77, 78]. BA argued that  $0^+$  states of similar energies and widths had been seen in neighboring nuclei and thus found it plausible that  $^8\text{Be}$  could also have such a level. Such a state would correspond to a level from a higher lying shell intruding, i.e. having lower energy, into a lower lying shell.

Here it should be noted that while the lowest  $2^+$  and  $4^+$  states are very broad, they do give rise to observable peaks in the spectrum [79, 80]. The resonances proposed by BA do not. In fact, the claim by BA has been challenged by quite a few people [81–85]. Historically, Warburton was the first to challenge BA. He did so on the basis of an R-matrix analysis of an

---

<sup>1</sup>This is true for at Breit-Wigner shaped resonance. The observed peaks are asymmetric due to the  $\alpha$  penetrability increasing with energy.

improved  $\beta^\pm$  decay dataset and achieved a good fit to their data without a  $2^+$  intruder state, but with a broad background pole at 37 MeV [81]. This may be interpreted as an effective parametrization of contributions from the continuum. Thus it would seem that the conclusion is model dependent. This was confirmed in the thesis work of Hyldegaard, where she showed that the obtained  $\beta$ -delayed  $\alpha$  spectrum could be described equally well using either model [86].

Theoretically, this region was investigated in several papers within the shell-model framework, which spurred a discussion regarding its validity [82, 87, 88]. The authors concluded that their model did not support  $0^+$  or  $2^+$  intruder states in the proposed region, e.g. the lowest observed  $0^+$  intruder state was located above 17 MeV. These calculations were performed by expanding the wave function in the harmonic oscillator basis; allowing for excitations up to  $4\hbar\omega$ , where  $\omega$  is the frequency of the harmonic oscillator. A contemporary No Core Shell Model (NCSM) calculation, allowing for excitations up to  $10\hbar\omega$ , found a  $0^+$  state at  $\sim 18$  MeV with the energy decreasing to  $\sim 12$  MeV when extrapolated [89]. Recent NCSM calculations that also included three-nucleon interactions found a  $0^+$  state in the same region showing a large decrease in energy with  $\hbar\omega$  [90]. However, calculations using the Green's function Monte Carlo (GFMC) method did not find evidence for an intruder state [91].

### $\gamma$ transitions in ${}^8\text{Be}$

Another motivation for this experiment was the recent publication of  $\gamma$  decay widths in  ${}^8\text{Be}$  calculated using the GFMC method [75]. The calculation included M1 and E2 transitions between the ground state (GS) and nine excited states. These transitions have previously been measured experimentally, but the interference effects between different final states were not included in the analysis.

With this work, we seek to measure the full  ${}^8\text{Be}$  excitation spectrum populated in the  $\gamma$  decay of the 17.6 MeV state. The 17.6 MeV was chosen as it is relatively narrow and has  $1^+$  spin-parity. This substantially increases the  $\gamma$

ray branching ratio as  $\alpha$  decay is forbidden. In addition, the  $1^+$  spin-parity nature of the resonance allows it to populate both  $0^+$  and  $2^+$  resonances via M1 transitions.

## 4.2 Resonances and the continuum

The proposed resonances from section 4.1 are all several MeV wide, and one can question whether it is still meaningful to describe this as a resonance. The question is, however: what else can it be? In order to explore this, it is instructive to study the concept of resonances and continuum states in a simple toy model. The model consists of a finite square well as shown in fig. 4.2. States with  $E > 0$  are unbound. As the physics is sufficiently illustrated with S-wave neutrons, the discussion will be restricted to this case. This section is based on ref. [92].

Assuming a central potential,  $V(\vec{r}) = V(r)$ , the Schrödinger equation is separable into radial and angular parts,  $\psi(r, \theta, \phi) = R(r)Y(\theta, \phi)$ . The

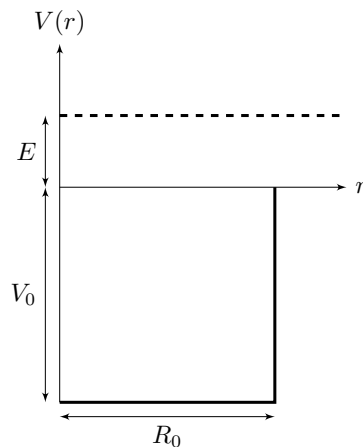


Figure 4.2: A radial square well potential of depth  $V_0$  and width  $R_0$ . The particle has a positive energy  $E$  and is unbound.

angular part can be solved generally, and the solution is the spherical harmonics. Introducing  $u(r) = rR(r)$ , the radial wave equation for  $\ell = 0$  can be written as

$$\frac{d^2u}{dr^2} + \frac{2m}{\hbar^2}[E - V(r)]u = \frac{d^2u}{dr^2} + \hat{k}^2u = 0, \quad (4.1)$$

where  $\hat{k}^2 = \frac{2m}{\hbar^2}[E - V(r)]$ . When  $E - V > 0$ , corresponding to an unbound particle, the solution to the radial equation is given by

$$u = \alpha e^{i\hat{k}r} + \alpha e^{-i\hat{k}r}. \quad (4.2)$$

Requiring  $R$  to be finite at the origin leads to  $u(0) = 0$ . The general solutions in the two regions can then be determined with a bit of algebra

$$u_{\text{in}} = A \sin(Kr) \quad (4.3)$$

$$u_{\text{out}} = C \sin(kr + \delta_0), \quad (4.4)$$

where  $K^2 = \frac{2m}{\hbar^2}(E + V_0)$ ,  $k^2 = \frac{2m}{\hbar^2}E$  and  $\delta_0$  is the  $\ell = 0$  phase shift. The effect of the potential is an increase of the frequency for the wave function in the interior region.

For a given energy, the solution for the entire region can be found by requiring the value and first derivative to match at the boundary  $R_0$ ,

$$A \sin(KR_0) = C \sin(kR_0 + \delta_0), \quad (4.5)$$

$$AK \sin(KR_0) = Ck \sin(kR_0 + \delta_0). \quad (4.6)$$

From these equations, one can determine the ratio between the wave function in the exterior and interior region

$$\frac{|A|^2}{|C|^2} = \frac{k^2}{k^2 + [K^2 - k^2] \cos^2(KR_0)}. \quad (4.7)$$

A plot of this expression as a function of energy is shown in fig. 4.3. It shows a clear resonance structure with peaks at the discrete energies,  $E_i$ , corresponding to  $\cos^2 KR_0 = 0$ . This corresponds to the wavelength of

$\lambda = R/(\frac{n}{2} + \frac{1}{4})$  or alternatively  $\frac{n}{2} + \frac{1}{4}$  wavelengths within the interior region. However, here it should be stressed that solutions for the energies  $E \neq E_i$  are not forbidden merely suppressed. From this, we can conclude that the complete spectrum consists of both continuum and resonance states.

While the above toy model serves to illustrate the point that resonances and continuum state coexist, reality is a bit more complex. One of the first break-throughs on this subject came from Berggren in 1968, who showed the following completeness relation [93]

$$\sum_{n \in (b,d)} |u_n\rangle \langle u_n| + \int_{L^+} |u(k)\rangle \langle u(k)| dk = 1. \quad (4.8)$$

The sum is over all bound and decaying states, as expected. However, in order to have a complete set, the entire continuum of scattering states must

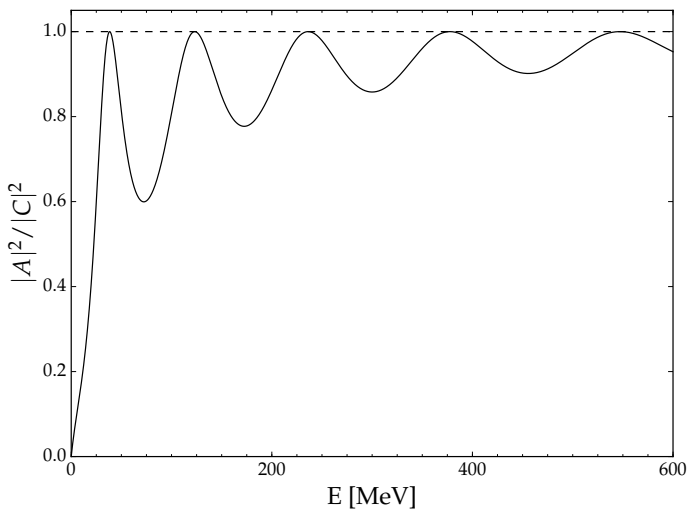


Figure 4.3: Single particle resonances in  $n + {}^7\text{Be}$  with  $R_0 = 1.4 \text{ fm} \cdot (1^{1/3} + 7^{1/3}) \approx 4 \text{ fm}$  and  $V_0 = 50 \text{ MeV}$  evaluated with eq. (4.7). Note in this simple picture the amplitude of the interior wave function can only be equal to the exterior amplitude.

also be included. Thus it is expected that a resonance can couple to a continuum state in a  $\gamma$  decay. This is the key point here. A full review of how to treat continuum states in theoretical models is outside the scope of this work and the reader is directed to the recent review in ref. [94].

### 4.3 Prior work

Before describing the present experiment let us for a moment study the prior work on this system. In the first section below I will describe the current state of the art  $\beta$  decay experiments, as these are the closest “relative” to the  $\gamma$  decay experiments and set the bar for what must be achieved in terms of both energy and signal to background resolution. The second section reviews the prior  $\gamma$ -decay studies.

#### $\beta$ decay experiments

$\beta$  decay is a versatile instrument in nuclear experiments, serving as a well-defined probe of the nuclear structure due to the associated selection rules. Much of the discussion regarding intruder states have surrounded increasingly sophisticated measurements of the  $\beta$  delayed  $\alpha$  spectrum. The current state of the art analysis of this spectrum can be found in ref. [86] and the  $2\alpha$  coincidence spectrum can be seen in fig. 4.4. The spectrum has been obtained using double-sided silicon strip detector (DSSD) detectors, which essentially removes background contributions such as  $\beta\alpha$  summing. The red dashed line shows the best fit to three  $2^+$  levels and a  $2^+$  background pole at  $\sim 37$  MeV (Warburtons model) while the dashed lines show the contribution from the individual levels. As can be seen from the figure, this model provides a good description of the data. From the figure, the intensity in the 6 to 14 MeV region can be estimated to be approximately 2 to 3 orders of magnitude less than the FES peak.

A challenge for the analysis of this spectrum is that only five counts were observed in the 16.9 MeV peak. This was partly overcome by treating the doublet as a splitting of two isospin mixed states — see ref. [88] for details. However, in 2017 the decay experiment was repeated at the ISOLDE

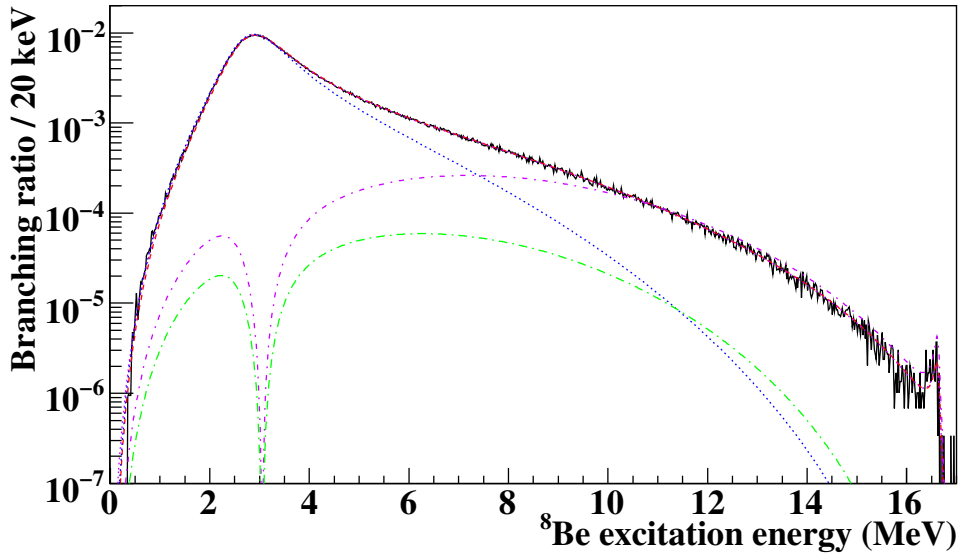


Figure 4.4: The observed branching ratio for the  $\beta$  decay of  ${}^8\text{B}$  along with best fit to an R-matrix model (dashed red) with  $2^+$  3 MeV state (dotted blue),  $2^+$  doublet (dot dashed purple) and a  $2^+$  37 MeV background pole (dot dashed green). Figure from ref. [86].

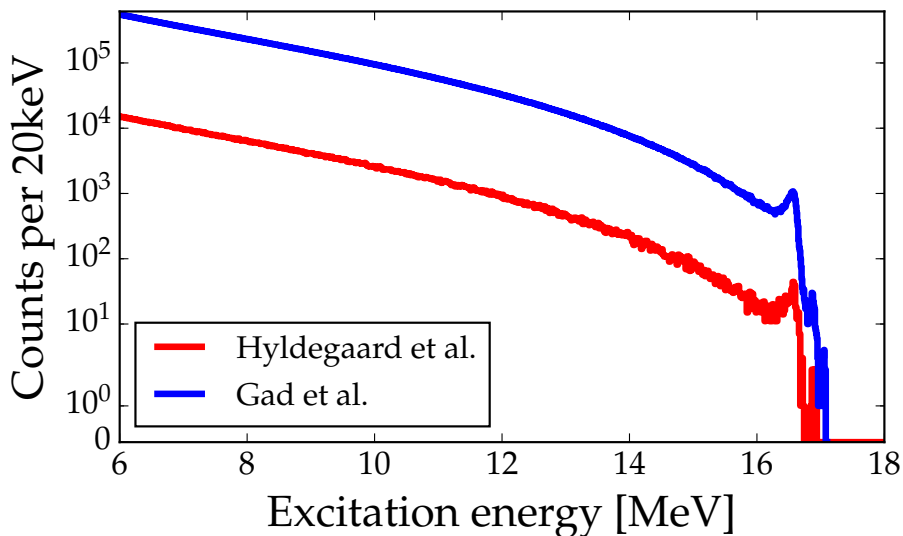


Figure 4.5: The observed number of  $2\alpha$  coincidences from the  $\beta$  decay of  ${}^8\text{B}$  by refs. [86, 95]. The most recent experiment improved the counting statistics by approximately a factor of 100. Figure courtesy of Andreas Gad [95].

facility at CERN. The result of the experiment was a measurement of the  $2\alpha$  coincidence spectrum above 6 MeV with a factor  $\sim 100$  improvement in counting statistics. A comparison between the two spectra can be seen in fig. 4.5. Notice the significant improvement at the doublet. A preliminary analysis of the improved spectrum can be found in ref. [95].

### $\gamma$ decay experiments

The 17.6 MeV state is known to be a  $1^+$  resonance and can thus M1 or E2 decay to either  $0^+$  or  $2^+$  levels. Thus, the relevant levels in  ${}^8\text{Be}$  are the ground state and the lowest three  $2^+$  levels. Prior investigations have focused on either the transitions to the GS and FES or the  $2^+$  doublet as the latter present quite different challenges.

**Ground- and first excited state** transitions have been the subject of many investigations [79, 98–104] using a variety of experimental techniques. The first experiments focused on the yield curve as a function of beam energy since they only had electroscopes and Geiger-Müller counters at their disposal [98–100]. Later experiments had multi-channel analyzers and modern detectors such as NaI or Ge(Li). Figure 4.6 shows what can be achieved with a Ge(Li) detector. Note that the spectrum is the result of irradiating the target with 8.7 mC of beam. The ground state transition is visible at high energy as a small sharp peak. However, the magnitude of the escape peaks is roughly one order of magnitude larger than the photopeak. This, together with the Compton-edge, dominates the 15 to 17 MeV region. For comparison, fig. 4.7 shows the resulting spectrum from a  $4\pi$  NaI crystal with three orders of magnitude less beam. While the efficiency is clearly better, the resolution is significantly worse, e.g.  $\sim 1$  MeV FWHM for the GS transition. With both choices of detectors, the low energy region is dominated by room background and response tails, and they are therefore unsuitable for the proposed experiment.

The decay widths to the GS and FES in the latest evaluation is based on the cross sections measured by ref. [79]. These were determined by



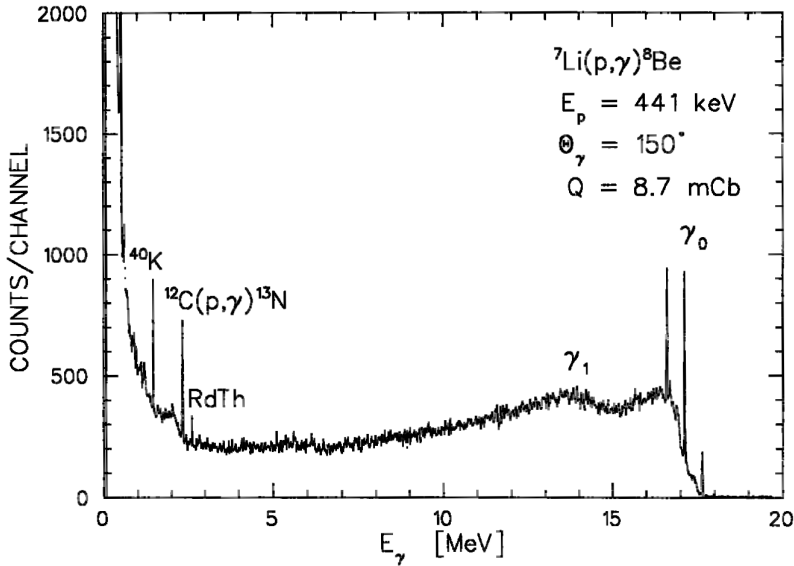


Figure 4.6: Recorded  $\gamma$  spectrum using a Ge(Li) detector. The photopeak at 17.6 MeV from the GS transition is visible, but the region below is dominated by escape peaks and Compton edges. The room background dominates the low energy region. Figure from ref. [79].

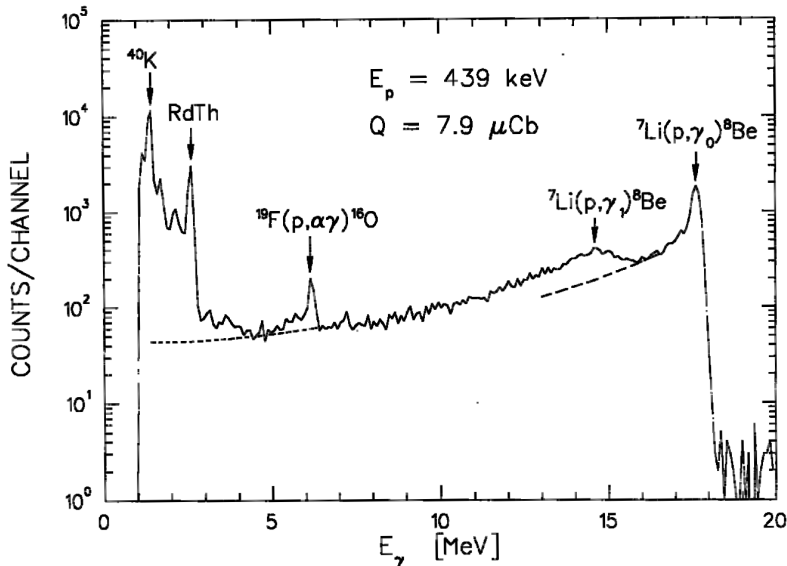


Figure 4.7: Recorded  $\gamma$  ray spectrum using the  $12 \times 12$ -in NaI crystal BICRON. The transitions to the GS and FES are visible, but room background and response tails dominate the low energy spectrum. Figure from ref. [79].

CHAPTER 4. MEASUREMENT OF THE FULL EXCITATION SPECTRUM OF THE  ${}^7\text{Li}(p, \gamma)\alpha$  REACTION AT 441KEV

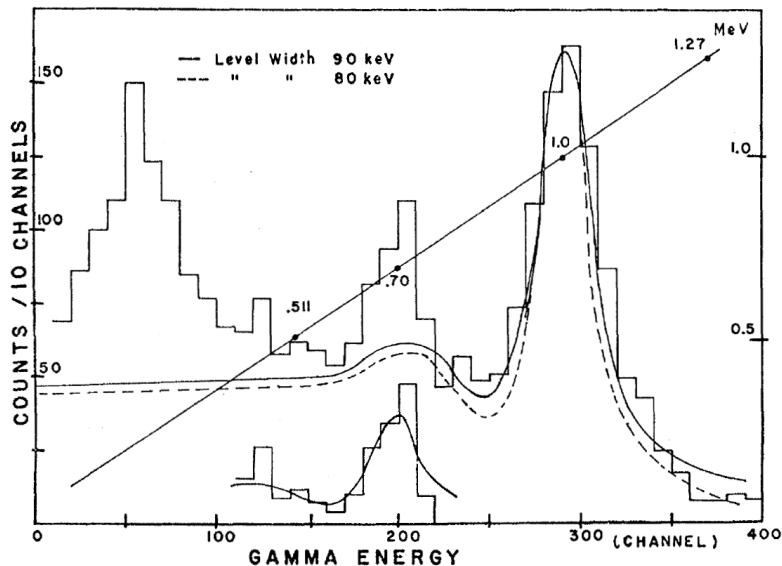


Figure 4.8:  $\alpha$ -gated  $\gamma$  ray spectrum observed in a  $3 \times 3$ -in NaI crystal. The solid line gives the energy calibration. Figure from ref. [96].

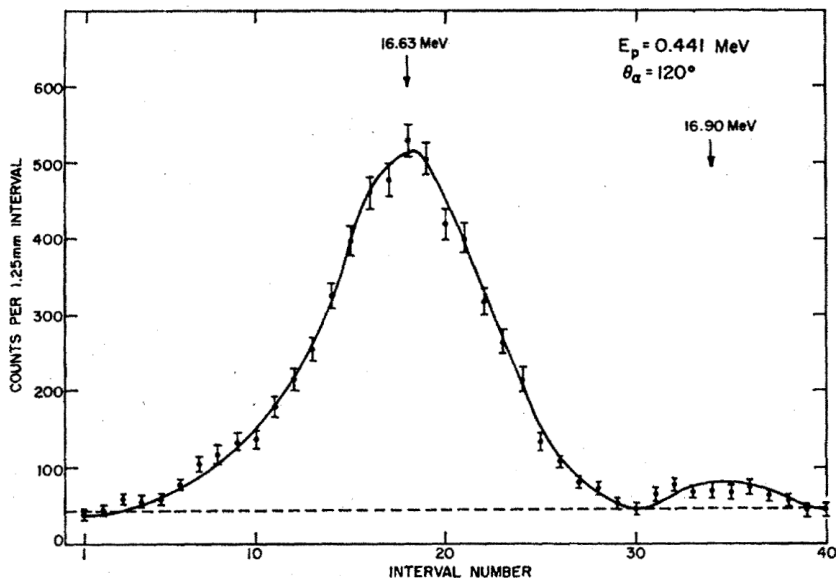


Figure 4.9: Position spectrum measured with a magnetic spectrometer and a position sensitive detector. The solid line is "approximate line shapes". Figure from ref. [97].

extrapolating the dashed lines in fig. 4.7 to zero energy and integrating. Interference is not taken into account.

**The  $2^+$  doublet** transitions were measured in the 1960s using two different techniques.

The  $\gamma$  ray spectrum measured in the first experiment can be seen in fig. 4.8. It was recorded by a  $3 \times 3$ -in NaI crystal in coincidence with a silicon detector for  $\alpha$  particles [96]. The coincidence requirement provided sufficient suppression of the room background, allowing the doublet to be distinguished. However, the resolution is somewhat limited.

The latter experiment used a magnetic spectrometer to implant the  $\alpha$  particles from the  $^8\text{Be}$  break-up into a position sensitive detector [97]. The magnetic spectrometer served to remove the proton beam. The resulting position spectrum, when initially populating the 17.64 MeV state, can be seen in fig. 4.9. The two doublet components are clearly visible with an excellent signal to noise ratio. However, the full lines are hand drawn “approximate line shapes”. The authors acknowledge that interference should be included, but neglect it due to “Lacking the detailed knowledge necessary to calculate the interference correctly” [97]. While the experiment produced excellent spectra, the dynamic energy range is simply too limited.

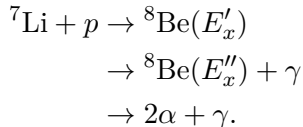
The widths listed in the latest evaluation is based on the results of ref. [97].

## 4.4 Indirect detection of $\gamma$ -rays

From the previous section, it is quite clear that the conventional techniques for  $\gamma$  detection cannot produce an excitation spectrum of comparable quality to the  $\beta$  decay experiments in terms of signal to background ratio and dynamic range. A different method must be used.

Indirect detection of  $\gamma$  rays is an experimental technique to infer the  $\gamma$  ray energy by means of missing energy. Using the present case as an

example the reaction proceeds as follows:



The initial excitation energy,  $E'_x$ , is determined by the beam energy, while  $E''_x$  is determined by a measurement of the energies of the  $\alpha$  particles. If  $E''_x < E'_x$  then a  $\gamma$  decay must have taken place. The  ${}^8\text{Be}$  recoil energy is approximately  $E_r = \frac{E_\gamma^2}{2m_{\text{Be}}}$  and amounts to only 20 keV for a ground state decay. If this is neglected, the  $\gamma$  ray energy can easily be determined  $E_\gamma = E'_x - E''_x$ .

This technique has been used successfully in studies of  $\gamma$  decays to broad unbound levels in  ${}^{12}\text{C}$ . It has been demonstrated to reliably measure branching ratios as small as  $\sim 10^{-6}$  with little to no background and a simple detector response function [105, 106].

## 4.5 Method

The experiment was carried out with a proton beam provided by the Aarhus University 5 MV Van de Graaff (VdG) accelerator. The beam impinged a natural LiF target on a thin carbon backing, which was oriented  $45^\circ$  with respect to the beam axis. This allows us to populate the known  ${}^8\text{Be}$  resonances above 17.25 MeV and in this experiment, the 17.6 MeV state was addressed. An illustration of the reaction is seen in fig. 4.10 with the 17.6 MeV state populated. It will subsequently  $\gamma$  decay with a branching of  $\sim 1\%$  followed by an  $\alpha$  decay. In addition, the  ${}^7\text{Li} + p$  channel may couple directly to the  $2\alpha$  channel.

Charged particles were detected with two large area DSSDs in close geometry. Figure 4.11(a) shows the detection efficiency for the two  $\alpha$  particles as a function of  ${}^8\text{Be}$  excitation energy. In comparison the 98 Germanium detectors, discussed in chapter 3, achieved a detection efficiency of  $\sim 3\%$  at 3 MeV. With this small setup  $\sim 6\%$  is achieved for energies up to  $\sim 16$  MeV.

The  $2\alpha$  response function can be determined from the direct  $\alpha$  particles. This is shown in fig. 4.11(b). These give rise to a peak at 17.6 MeV with an intrinsic width corresponding to the target thickness of 18.1(16) keV (see article at the end of the chapter). Additional energy losses in the target foil and detector dead layer give rise to the asymmetric shape. The shape of the peak is well described using the one-tail variant of the analytical expression given in [107]

$$f(E) = \frac{A}{2\tau} \exp \left\{ \frac{E - \mu}{\tau} + \frac{\sigma^2}{2\tau} \right\} \operatorname{erfc} \left[ \frac{1}{\sqrt{2}} \left( \frac{E - \mu}{\sigma} + \frac{\sigma}{\tau} \right) \right]. \quad (4.9)$$

The best fit was achieved with  $\sigma = 27.07(15)$  keV and  $\tau = 39.6(2)$  keV. Compared to the resolution achievable with state of the art germanium detectors this is quite poor. However, considering the  $\sim 1$  MeV FWHM with a NaI detector, it is a vast improvement. The tails are also considerably smaller.

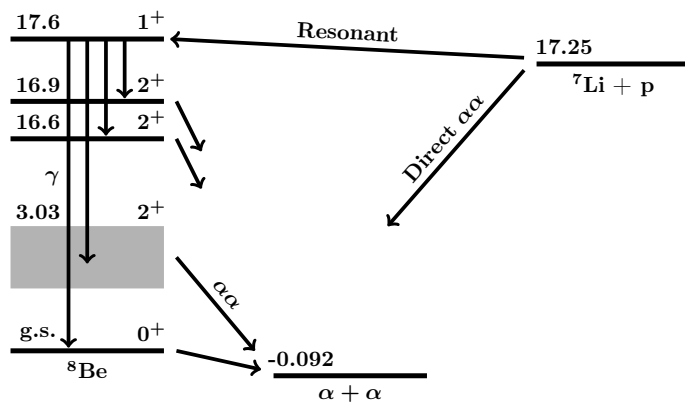
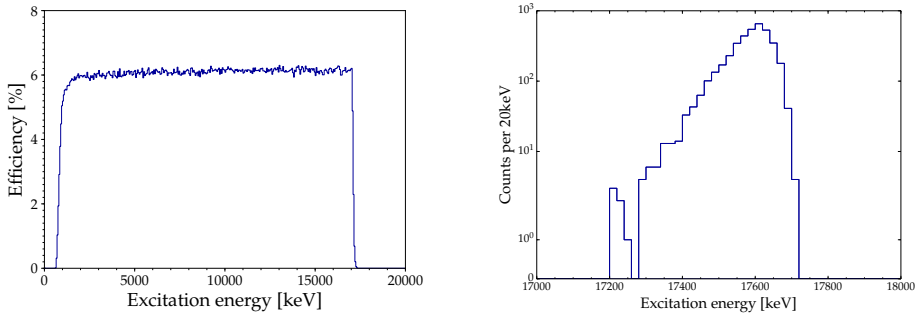


Figure 4.10: Illustration of the reaction. The 17.6 MeV resonance is populated using the  $p + {}^7\text{Li}$  reaction. The resonance might subsequently  $\gamma$  decay to lower lying resonances or the continuum, which then  $\alpha$  decays.  $p + {}^7\text{Li}$  may also couple directly to the  $2\alpha$  channel. Figure from ref. [72]



(a) Detection efficiency as a function of  ${}^8\text{Be}$  excitation energy. The efficiency is essentially flat and  $\sim 6\%$ .

(b) Observed peak from the direct  $\alpha$  particles. With no response effects, a sharp 10 keV wide peak at 17.64 keV would be observed.

Figure 4.11

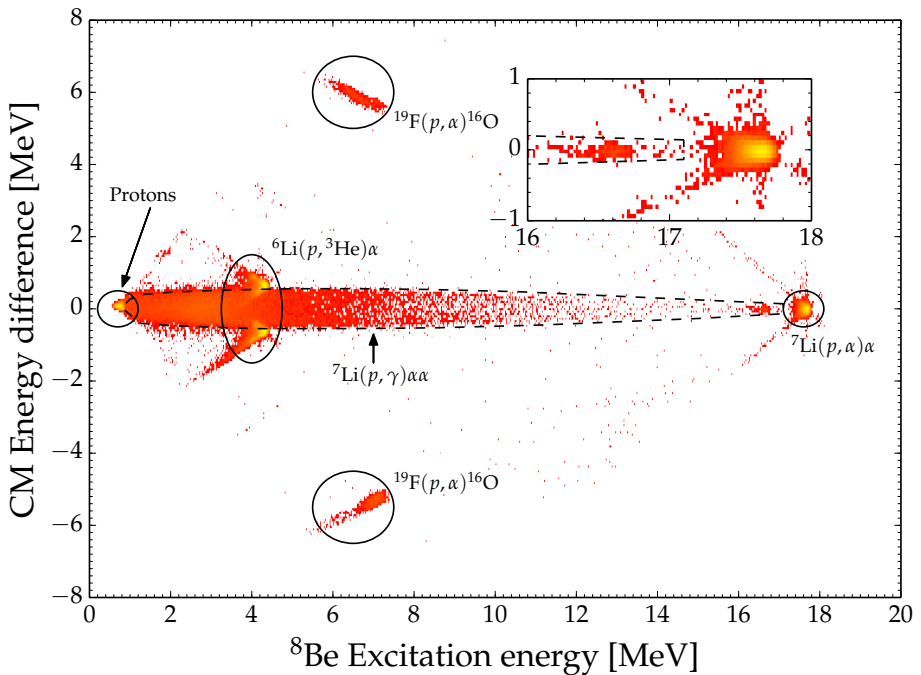


Figure 4.12: Difference in CM energy for all possible  $\alpha\alpha$  pairs. The various circles shows different background reactions, while the dashed contour highlight the events corresponding to  $\gamma$ -delayed  $\alpha$  break-up. Figure from ref. [72].

## 4.6 Data reduction

Each detector was approximately  $70\ \mu\text{m}$  thick and provided a simultaneous detection of position and energy each time a particle struck them. As the penetration energy for  $\alpha$  particles through  $70\ \mu\text{m}$  silicon is  $\sim 10\ \text{MeV}$ , the particles stop in the DSSDs, and this experiment had no means to perform particle identification for each hit. Instead, the analysis relies on full kinematic reconstruction in order to perform the identification. To this end, it was assumed that all hits were  $\alpha$  particles originating from a  $p + {}^7\text{Li}$  reaction and energy loss corrections in the detector dead layer and target foil were carried out under this assumption. Rough selection of  $\alpha\alpha$  coincidence identification was performed for each pair by requiring their detection to occur within  $13\ \text{ns}$  of each other and deviate less than  $10^\circ$  from back-to-back. For the events surviving these cuts, the CM energy difference and  ${}^8\text{Be}$  excitation energy were computed. These parameters are plotted against each other and are shown in fig. 4.12. The figure shows a band along zero energy difference corresponding to  $\gamma$  delayed  ${}^8\text{Be}$  decay marked with a dashed contour and several peaks outside this band corresponding to background reactions. This plot highlights the strength of the method as it allows clear separation of the background. The only exception is the  ${}^6\text{Li}(p, \alpha)$  reaction, which is too similar to the reaction of interest. The excitation spectrum shown is extracted by projecting the events within the dashed contour.

## 4.7 R-matrix

In order to include interference in the analysis of the excitation spectrum, an R-matrix model of  ${}^8\text{Be}$  is constructed. R-matrix theory has been thoroughly reviewed in refs. [76, 108] and a detailed derivation can be found in [86]. I will only sketch the basics of the theory.

R-matrix theory considers a compound nucleus, which can be formed via multiple two-body channels,  $c$ , defined by the two nuclei and their relative and internal quantum numbers. For this compound nucleus, it is

assumed that the configuration space can be divided into an internal and external region, with a boundary at the channel radius,  $a_c$ . The external region is characterized by only having long-range interactions, i.e. Coulomb interaction for charged particles and possibly an angular momentum barrier. The wave function in the interior is treated as confined and is expanded in terms of square-integrable eigenstates called levels. The levels are labeled with  $\lambda$  and are associated with specific energies  $E_\lambda$ . As the nuclear potential is finite, the logarithmic derivative of the internal and external wave functions must match at the boundary. From the matching criterion follows the definition of the reduced widths,

$$\gamma_{\lambda c} \propto \int_S X_\lambda^* \phi_c dS, \quad (4.10)$$

where  $X_\lambda$  is an internal eigenstate,  $\phi_c$  the channel wave function and  $S$  the spherical surface at the channel radius. The square of the reduced width is thus a measure for the probability of performing the channel nuclei separated by the channel radius. However, in order to be observed, the Coulomb and centrifugal barrier must be tunneled, and hence the partial width is expressed as

$$\Gamma_{\lambda c} = 2P_c(E)\gamma_{\lambda c}^2, \quad (4.11)$$

where  $P_c(E)$  is proportional to the probability of transmission through the barriers for a specific energy.

Using the R-matrix framework, it is possible to calculate the cross section for one or more channels. The requirement is a set of levels,  $\lambda$ , with energies,  $E_\lambda$ , that couple to a set of channels,  $c$ . The coupling strength is given by a set of reduced-width parameters  $\gamma_{\lambda c}$ . These three sets of parameters are then adjusted until the observed spectrum is reproduced.

Ordinarily, one would find the correct cross section expression in ref. [108] or more recently use AZURE2 to perform the calculations [109]. However, ref. [108] does not consider the case of  $\gamma$ -delayed  $\alpha$  emission. I have therefore derived an expression for this based on an R-matrix expression for a sequential process. The resulting note was uploaded to arXiv and is placed as an appendix after the paper [110]. To perform the R-matrix calculations,



I wrote the Open R-matrix (ORM) program together with Oliver Kirsebom and Jonas Refsgaard [111].

## 4.8 Result and discussion

A secondary objective of this experiment was to extract  $\gamma$  decay widths. This allows us to perform a direct comparison of the present work with the experiments summarized in section 4.3 and the recent GFMC calculation of decay widths in ref. [75]. Decay widths were extracted both using simple bin integration and R-matrix analysis. This serves to illustrate the impact of interference. The normalization of these decay widths was extracted from a resonance scan.

Bin integration  $\gamma$  decay widths were determined by integration of the shaded area in figure 3 in the article. The resulting widths are listed in table 1 as “Present”.

In addition, an R-matrix analysis was performed of the extracted spectrum. The discussion of this analysis from the article will now be summarized and expanded upon. Figure 4.13 shows the spectrum fitted with three different models. Model 1 consists of a  $0^+$  GS and three  $2^+$  levels. The model included M1 transitions to all levels and an E2 transition to the FES. The initial parameter guesses for the model optimization was taken from the latest evaluation [74]. All three models reproduce the majority of the observed spectrum and the parameters corresponding to the best fit are listed in table 2 in the article.

However, with a closer inspection, it is clear that model 1 has systematic problems with the 16.9 MeV peak, which has been underestimated. Thus an R-matrix model with only the lowest four  $^8\text{Be}$  levels cannot reproduce the observed spectrum. This is the same conclusion reached when analyzing  $\alpha\alpha$  scattering data or  $\beta$  decay data [78, 81]. Model 2 remedies this situation by adding an additional  $2^+$  level. The energy, width and  $\gamma$  feeding were allowed to vary freely, and multiple initial conditions for the energy were tried. In all cases, the fit converged to a solution with a broad  $2^+$  level above the doublet. The issue is how to interpret this. Naively there exists a  $2^+$  at

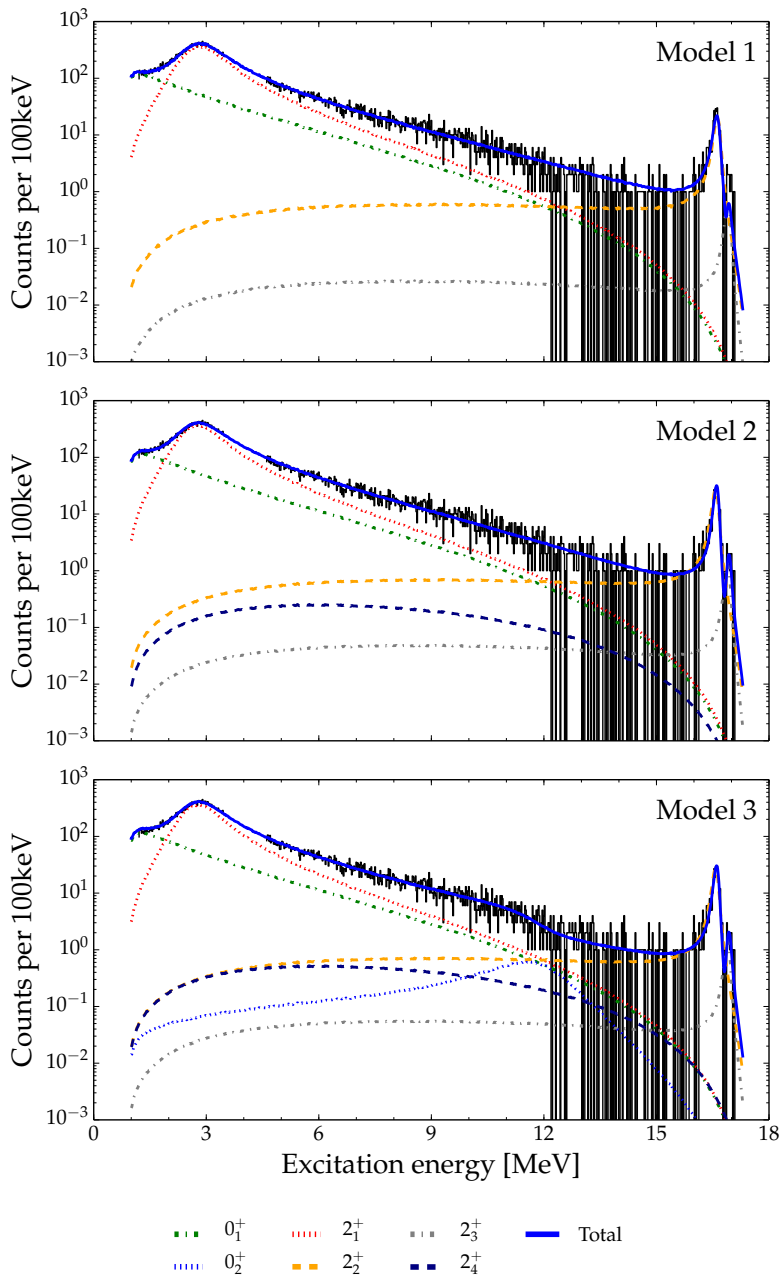


Figure 4.13: Observed excitation spectrum and best fit to the three different R-matrix models. Figure from ref. [72].

25.2 MeV [74]. However, the fitted  $2^+$  has a width of 20(8) MeV, while the 25.2 MeV state is much narrower. These are not equivalent. Figure 5 of paper 4 shows the single level profile of the additional  $2^+$  level, and it has a broad featureless distribution. This is interpreted as an effective parametrization of a significant non-resonant contribution from the continuum. Comparing the obtained fit for the 16.9 MeV resonance between the two models it is clear that the systematic problems have been alleviated. This improvement is achieved through interference with the continuum. Hence, it would seem that contributions from the continuum are essential to describe the observed spectrum. Model 3 introduces an additional  $0^+$  level with completely free parameters. The optimal solution is a  $0^+$  component at 12.0(3) MeV with a width of 2.4(5) MeV. The improvement in fit quality is achieved via interference with the GS, causing a decrease of the amplitude in the 12 to 16 MeV region. Unlike the  $2^+$  component, the single-level profile for the  $0^+$  shows resonance characteristics. Interestingly, it coincides with the position obtained in NCSM calculations [89, 90].

When discussing these different models, a question arises: is the improvement in fit quality significant or merely an effect of additional fit parameters? The improvement observed in model 2 was a decrease of  $\chi^2/\text{ndf}$  by 30 for three extra parameters or put differently; an order of magnitude improvement of the P-value. Considering that only 18 counts have been observed in the 16.9 MeV peak, this improvement cannot be ascribed to a local improvement of this region, but rather a global improvement, most likely a better description of the intermediary region. A similar behavior has been observed in  $\beta$  decay studies, where substantial improvements were observed with the addition of background poles.

A comparison of the  $\gamma$  decay widths determined using bin integration or R-matrix analysis is shown in table 1 in the article. The values from the latest evaluation and GFMC calculation are also shown. From this, it is quite clear that the GFMC struggles with the GS and FES, which has a large reduced  $\alpha$  width. The results from the two different methods differ systematically, and this underlines that it is important to properly treat interference when dealing with systems with broad overlapping resonances.

## 4.9 Conclusion and outlook

With this experiment, the  ${}^8\text{Be}$  excitation spectrum has been measured for the 1 to 17 MeV region. This excitation spectrum is on par with the  $\beta$  decay data and is of sufficient quality to allow an R-matrix analysis to be performed. Decay widths were extracted using both simple bin integration and R-matrix analysis, and it was found that the inclusion of interference has a significant impact, especially for the FES.

The R-matrix analysis was performed using three different models. It was found that a simple model including only the levels below 17 MeV could not adequately describe the observed spectrum. However, with the inclusion of a  $2^+$  background pole and a  $0^+$  resonance at 12 MeV a good fit could be achieved.

In the article, we have stated that this experiment and the analysis is tentative proof for a 12 MeV  $0^+$  resonance. However, considering the many previous claims in this region, more experimental work is needed. The plan is to repeat this experiment for higher-lying resonances in  ${}^8\text{Be}$  with a specific focus on the 18.1 MeV  $1^+$  level, which should also be able to M1 decay to this tentative state. Decays of higher-lying  $2^-$  and  $3^+$  should be able to address the universality of the observed  $2^+$  background pole. Preliminary data have been collected. However, punch-through of the direct  $\alpha$  particles was an issue. To this end, the setup has been upgraded with  $\sim 1.5$  mm silicon pad detectors behind both DSSDs. These additional data sets should be fitted both individually and together. A combined fit with the improved  $\beta$  decay dataset would also be highly interesting.

In addition, a 99.99% enriched  ${}^7\text{Li}$  compound has been ordered and is expected to be delivered in July 2018. As natural lithium contains roughly 7.7% of  ${}^6\text{Li}$  this should provide a factor  $\sim 750$  suppression of the primary background component. Most likely, it would not be necessary to exclude the 4 MeV region. This should allow a better characterization of the high-energy flank of the FES peak.

## 4.10 Contribution

I have been the principal investigator in all aspects of this work. Open R-matrix (ORM) was built upon a set of R-matrix functions developed by Jonas Refsgaard. Oliver Kirsebom contributed code handling  $\beta$ -delayed  $\alpha$  decay.





# Measurement of the full excitation spectrum of the ${}^7\text{Li}(p, \gamma)\alpha\alpha$ reaction at 441 keV

Michael Munch\*, Oliver Sølund Kirsebom, Jacobus Andreas Swartz, Karsten Riisager, Hans Otto Uldall Fynbo

Department of Physics and Astronomy, Aarhus University, Denmark



## ARTICLE INFO

### Article history:

Received 28 February 2018  
Received in revised form 1 May 2018  
Accepted 5 June 2018  
Available online 14 June 2018  
Editor: D.F. Geesaman

### Keywords:

*Ab initio*  
R-matrix  
 ${}^8\text{Be}$   
Radiative decay width  
Light nuclei

## ABSTRACT

A current challenge for *ab initio* calculations is systems that contain large continuum contributions such as  ${}^8\text{Be}$ . We report on new measurements of radiative decay widths in this nucleus that test recent Green's function Monte Carlo calculations.

Traditionally,  $\gamma$  ray detectors have been utilized to measure the high energy photons from the  ${}^7\text{Li}(p, \gamma)\alpha\alpha$  reaction. However, due to the complicated response function of these detectors it has not yet been possible to extract the full  $\gamma$  ray spectrum from this reaction. Here we present an alternative measurement using large area Silicon detectors to detect the two  $\alpha$  particles, which provides a practically background free spectrum and retains good energy resolution.

The resulting spectrum is analyzed using a many-level multi channel R-matrix parametrization. Improved values for the radiative widths are extracted from the R-matrix fit. We find evidence for significant non-resonant continuum contributions and tentative evidence for a broad  $0^+$  resonance at 12 MeV.

© 2018 The Authors. Published by Elsevier B.V. This is an open access article under the CC BY license (<http://creativecommons.org/licenses/by/4.0/>). Funded by SCOAP<sup>3</sup>.

## 1. Introduction

In recent years *ab initio* calculations of atomic nuclei, such as Green's function Monte Carlo (GFMC) [1] and No Core Shell Model (NCSM) [2], have advanced tremendously and now provide quite accurate predictions for light nuclei. Historically, NCSM has struggled with highly clustered states. However, the method has recently been combined with the resonating group method (RGM) to better describe clustered nuclei including continuum properties [2].

In this context  ${}^8\text{Be}$  provides an interesting benchmark. All states in this isotope are unbound with its ground state located just 92 keV above the  $2\alpha$  threshold. The lowest two states are highly clustered while some of the resonances at higher energy couple relatively weakly to the  $2\alpha$  final state.

GFMC calculations of electromagnetic transitions in  ${}^8\text{Be}$  have been performed by Pastore et al. [1], and experimentally  $\gamma$  decays of several states in  ${}^8\text{Be}$  have been measured. The focus of the present letter is the  $\gamma$  decay of the 17.64 MeV  $1^+$  state. M1 decays of this state could populate both  $0^+$  and  $2^+$  states. There are two measurements of the transition strength to the ground- and first

excited states in  ${}^8\text{Be}$  [3,4], and two measurements of transitions to the  $2^+$  doublet at 16.6–16.9 MeV [5,6]. However, due to the complicated response function of previous measurements it has not been possible to extract the full  $\gamma$  ray spectrum – specifically none of the previous measurements were sensitive to  $\gamma$  decays into the unresolved energy region below the  $2^+$  doublet.

This region was resolved experimentally using e.g.  $\alpha$ - $\alpha$  scattering and the  $\beta$ -decay of  ${}^8\text{B}$  and  ${}^8\text{Li}$  [7]. To understand these different ways of populating  ${}^8\text{Be}$ , it is necessary to have contributions not only from the known resonances, but also a broad contribution [7] between the first excited state at 3 MeV and the isospin mixed  $2^+$  doublet at 16.6–16.9 MeV. It is unclear if this contribution represents a  $2^+$  intruder state, a non-resonant continuum contribution, or the low energy tails of high energy resonances [7,8]. From theory there is also a prediction of a  $0^+$   $T = 0$  intruder state at around 12 MeV [9].

In this letter we will present a measurement of the  $\gamma$  decay of the 17.64 MeV  $1^+$  state using a method which is sensitive to this region of interest and essentially background free. By this method we will not only address the question of intruder states, but also derive new more reliable values for the partial decay widths of the already measured transitions.

It should be noted that electromagnetic transitions from the  $1^+$  states of  ${}^8\text{Be}$  are also of high current interest due to the obser-

\* Corresponding author.

E-mail address: [munch@phys.au.dk](mailto:munch@phys.au.dk) (M. Munch).

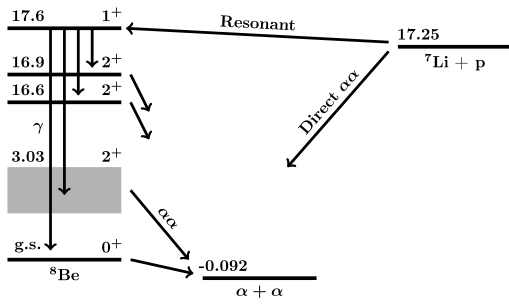


Fig. 1. Decay scheme. Only levels populated in the  $p + {}^7\text{Li}$  reaction or the  $\gamma$  subsequent decay is shown. Energies are in MeV relative to the  ${}^8\text{Be}$  ground state.

vation of anomalous internal pair creation in  ${}^8\text{Be}$  and the interpretation of that as a possible indication of a new light, neutral boson [10,11].

## 2. Experiment

The experiment was conducted at the 5 MV Van de Graaff accelerator at Aarhus University that provided a beam of  $\text{H}_3^+$  with energies between 1305 keV and 1410 keV. The 17.64 MeV state was populated using the  ${}^7\text{Li}(p, \gamma)$  reaction as illustrated in Fig. 1. The beam current was measured using a suppressed Faraday cup 1 m downstream of the target. Typical beam currents were between 200 pA and 1 nA and the beam spot was defined by a pair of  $1 \times 1$  mm vertical and horizontal slits. The beam impinged on a natural LiF target manufactured in house by evaporation of a 160 nm ( $\pm 10\%$ ) layer of natural lithium fluoride onto a thin  $\sim 4 \mu\text{g cm}^{-2}$  carbon backing.

The 17.64 MeV state was populated resonantly via  ${}^7\text{Li}(p, \gamma)$ , as depicted in Fig. 1. While gamma rays were not directly observed, the occurrence of electromagnetic de-excitation was inferred indirectly from the energies of the two  $\alpha$  particles emitted in the subsequent breakup. Charged particles were detected with two double-sided silicon strip detectors (DSSD) of the W1 type from Micron Semiconductors [12] giving a simultaneous measurement of position and energy. Each detector had an active area of  $5 \times 5$  cm divided into  $16 \times 16$  orthogonal strips and was positioned 4 cm from the target at 90 deg with respect to the beam axis.

A resonance scan was performed with proton energies from 435 to 470 keV and afterwards data was acquired at 446 keV for 52 hours and at 455 keV for 63 hours.

## 3. Data reduction

The data was analyzed using the full kinematic approach as described in Ref. [13]. The signal of interest is two coincident  $\alpha$  particles with missing energy corresponding to the reaction  $p + {}^7\text{Li} \rightarrow {}^8\text{Be}^* \rightarrow \gamma + \alpha + \alpha$  as illustrated in Fig. 1.

Our coincidence requirement is a time difference of less than 13 ns. As our coincidence timing resolution is 9.3 ns FWHM this includes  $> 99\%$  of all true coincidences. All coincidences surviving this cut are then corrected for energy loss in the detector dead-layer and target foil assuming they were  $\alpha$  particles. The energy of each particle in the center of mass (CM) of  $p + {}^7\text{Li}$  reaction was determined from its direction and energy. With a simultaneous detection of two  $\alpha$  particles one can infer the corresponding  ${}^8\text{Be}$  excitation energy from their summed 4-momentum. Fig. 2 shows the difference in CM energy versus the  ${}^8\text{Be}$  excitation energy. In the limit of zero recoil, conservation of energy and momentum

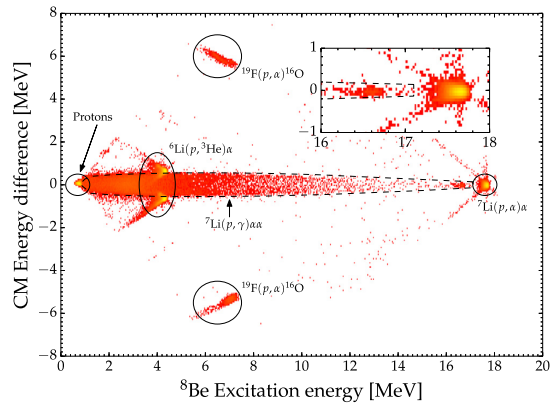


Fig. 2. Difference in CM energy vs  ${}^8\text{Be}$  excitation energy. The circles mark various background reactions while the band within the dashed contour stretching from 1 to 17 MeV corresponds to  $\gamma$  delayed  $\alpha$  particles. The color scale is logarithmic. The insert shows the high excitation energy region.

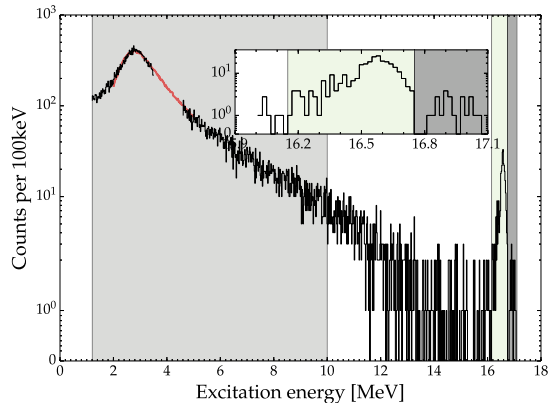
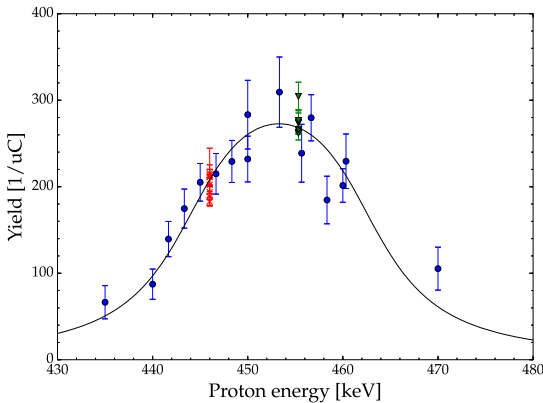


Fig. 3. Projected excitation spectrum. The superimposed curve is the best fit to the peak of first excited state with a single level R-matrix formula. See Section 4.1 for details.

dictates that the two alpha particles should have equal CM energies. When the small, but finite, recoil is taken into account, the CM energy-difference distribution remains centered very close to zero, but acquires a sizable spread. Hence the horizontal band in the figure corresponds to the  ${}^7\text{Li}(p, \gamma)\alpha\alpha$  reaction. At high excitation energy there is a distinct peak corresponding to the direct reaction  ${}^7\text{Li}(p, \alpha)\alpha$ . The two weak diagonal bands extending from the peak correspond to events with insufficient energy loss correction. These do not interfere with the region of interest and their strength is negligible compared to the peak. There are two similar peaks at roughly 4 MeV, which both correspond to  ${}^6\text{Li}(p, \alpha){}^3\text{He}$ . At 7 MeV there are two bands with large deviations from equal energy. This is a background reaction on fluorine  ${}^{19}\text{F}(p, \alpha){}^{16}\text{O}$ . At low energy we see random coincidences with the beam. The identity of the various components was verified with a Monte Carlo simulation. The  $\alpha$ -source energy calibration of the excitation spectrum was cross checked against the  ${}^6\text{Li}(p, \alpha){}^3\text{He}$  and  ${}^7\text{Li}(p, \alpha)\alpha$  peaks and was found to agree within 4 keV with the tabulated values [8]. It should be stressed that this spectrum is essentially background free in the region of interest, except for the small re-





**Fig. 4.** Resonance scan showing the yield of events with an excitation energy between 2 and 3 MeV as a function of beam energy. The red crosses and green triangles correspond to the long measurements. Each datapoint corresponds to a run and thus slightly different accelerator settings. The curve is the best fit to Eq. (1) – see text for details.

gion around the  ${}^6\text{Li}(p, \alpha){}^3\text{He}$  peaks, which will be excluded from the further analysis.

In order to completely remove random coincidences with the beam we require the angle between a pair to be  $> 170^\circ$  and place a low energy cut at 1 MeV. These cuts preserve 99% of the good events. The events corresponding to  $\gamma$  delayed  $\alpha$  emission are selected as those within the dashed contour seen on Fig. 2.

Fig. 3 shows the projected excitation spectrum with the first excited state visible at 3 MeV and the two contributions from the doublet at high energy in the insert. The superimposed curve will be discussed in Section 4.1. The extracted excitation spectrum can be found in [14].

### 3.1. Normalization

Fig. 4 shows the yield of events with an excitation energy between 2 and 3 MeV. The red crosses and green triangles correspond to the two long measurements. The solid line shows the best fit to equation 14 from Ref. [15].

$$Y = \left[ \tan^{-1} \frac{E_p - E_r}{\Gamma_{\text{lab}}/2} - \tan^{-1} \frac{E_p - E_r - \Delta E}{\Gamma_{\text{lab}}/2} \right] \frac{2\pi}{k_r^2} \frac{g_J}{\epsilon} \Gamma_\gamma, \quad (1)$$

where  $\Gamma_{\text{lab}}$  is the resonance width in the lab system,  $E_p$  is the beam energy,  $E_r$  the resonance energy,  $\Delta E$  the energy loss through the target,  $g_J$  the statistical factor from spin coupling,  $k_r$  the  ${}^7\text{Li}$ - $p$  wave number at the resonance energy, and  $\epsilon = \frac{1}{N} \frac{dE}{dx}$ , where  $N$  is the number density of target nuclei and  $\frac{dE}{dx}$  the stopping power.

$\Gamma_{\text{lab}}$  was fixed to 8/7 of the literature value of 10.7(5) keV [8]. The last part of the equation was treated as a scaling constant and fitted. The best fit was achieved with  $\Delta E = 18.1(16)$  keV and  $E_r = 444.3(6)$  keV. The resonance energy is slightly higher than the latest literature value of 441.4(5) keV [8].

Upon impinging on the target foil the  $\text{H}_3^+$  molecule will break up. In this process additional electron stripping, neutralization and scattering outside the Faraday cup might occur. The effect of these processes can be determined by measuring the integrated current with and without target foil placed in the beam. The ratio of these two measurements gives the effective charge state of the  $\text{H}_3^+$  molecule as observed at the Faraday cup, when the beam passes through the foil. The result was 2.50(7) $e$  over the measured energy range.

**Table 1**

Widths extracted from bin integration of the excitation spectra. Literature values are from Ref. [8]. The GFMC results are from Ref. [1]. The R-matrix results are from Section 4.2.  $\Gamma_{0_1}$  of the R-matrix results is from model 2, while the rest is from model 3.

Parameter	Present	Lit.	GFMC	R-Mat.
$\Gamma_{0_1}$ (eV)	–	15.0(18)	12.0(3)	13.8(4)
$\Gamma_{2_1}$ (eV)	6.0(3)	6.7(13)	3.8(2)	5.01(11)
$\Gamma_{2_2}$ (meV)	35(3)	32(3)	29.7(3)	38(2)
$\Gamma_{2_3}$ (meV)	2.1(6)	1.3(3)	2.20(5)	1.6(5)

## 4. Extraction of radiative widths

As previous experiments have determined the widths using simple integration of the excitation spectrum, we will first determine the widths using this method. In addition, we will perform an R-matrix analysis of the measured spectrum in order to take interference into account. The R-matrix parametrization is described elsewhere [16]. The R-matrix implementation can be found in Ref. [17].

### 4.1. Bin integration

The excitation spectrum, shown in Fig. 3, has been subdivided into four regions covering the first excited state from 1 to 10 MeV, the continuum from 10 to 16.1 MeV and the two doublet states from 16.1 to 16.75 MeV and 16.75 to 17.1 MeV respectively. The choice of 10 MeV is somewhat arbitrary. It is placed sufficiently high to include the majority of the peak. Superimposed on the data is the best fit between 2 and 6 MeV to a single level R-matrix expression fed by an M1 decay.

The widths were determined by integration of the three regions with solid shading. The contribution from the excluded region was determined from the superimposed R-matrix curve. The integrals were converted into absolute decay widths using Eq. (1) and the parameters determined in Section 3.1.

The results and statistical errors are listed in Table 1 along with the current literature values from Ref. [8] and the results of GFMC calculations [1].

### 4.2. R-matrix analysis

We will analyze the excitation spectrum using three different models. Model 1 is a model with one  $0^+$  ground state and three  $2^+$  resonances. All states are fed by M1  $\gamma$  decays while the  $2_1^+$  resonance is also fed by E2 decays. All initial values were taken from Ref. [8]. To ensure convergence the energy of the  $2_3^+$ , as well as the  $\alpha$  widths of the two highest  $2^+$  resonances and the ground state, were fixed. Model 2 adds an additional  $2^+$  level at high energy fed by an M1 transition. All parameters for this additional level were allowed to vary freely. Furthermore, it was no longer necessary to fix  $E_{2_3}$ . Model 3 adds another  $0^+$  state. However, in order to achieve convergence it was necessary to fix the ground state feeding and the position of the  $2^+$  background pole to the values from model 2. The M1 feeding of all  $2^+$  levels were summed coherently while the M1 contribution to the  $0^+$  and the E2 feeding were added incoherently. Model 1 has 8 free parameters, model 2 has 12 and model 3 has 13.

In order to directly compare the experimental spectrum with the spectrum obtained from R-matrix theory, it is necessary to fold the theoretical spectrum with the experimental response function. For this experimental setup the response function is well described as a Gaussian function with an exponential tail – the one tail variant of Ref. [18]. The parameters were determined with a fit to the  ${}^7\text{Li}(p, \alpha)$  peak as the effect of the response function is

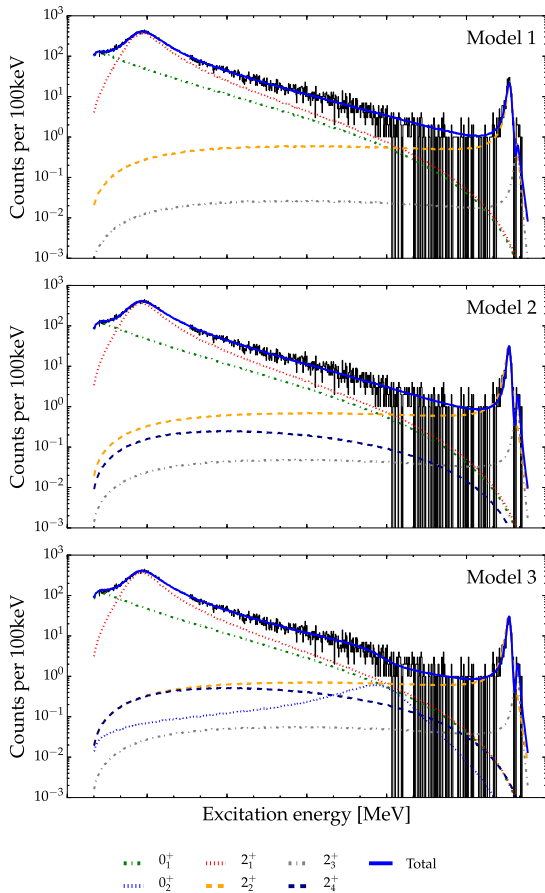


**Fig. 5.** Best fit for a channel radius of 5 fm. The solid blue line shows the sum of all contributions, while the dotted shows the single level profile of the individuals levels.

most important for the narrow  $2^+$  levels above 16 MeV. The best fit was achieved with  $\mu = 23.5(5)$  keV,  $\sigma = 27.07(15)$  keV and  $\tau = 39.6(2)$  keV.

Fig. 5 shows the best fit for all models with a channel radius of 5 fm. The dashed curves show the single level contributions. It should be noted that all models have a weak dependence on the chosen channel radius, as this influences the shape and peak to tail ratio for the  $0^+$  ground state. A channel radius of 5 fm was chosen, as it minimized  $\chi^2$ .

The parameters corresponding to the best fit are listed in Table 2 along with their errors. In order to minimize bias a Poisson likelihood estimator has been used [19]. Errors have been estimated using the MINOS routine and are symmetric unless noted otherwise. Propagated errors have been calculated using the Hessian approximation.

## 5. Discussion

Comparing the radiative widths determined using integration with those from the literature, we find agreement for the doublet. Previous measurements assigned everything below the ground state peak in the  $\gamma$  spectrum to the  $2_1$  distribution. In light of

this and considering that our measurement of the  $2_1$  distribution has not been extrapolated to zero energy, the agreement with literature is reasonable.

The excitation spectrum produced by the three R-matrix models can be seen in Fig. 5 and in all cases the majority of the experimental spectrum has been reproduced. The main qualitative improvement between model 1 and 2 is observed around the 16.9 MeV peak, which model 1 systematically undershoots. In addition, an order of magnitude improvement of the P-value is observed for each subsequent model. The single level shape of the model 2 background pole is a broad featureless distribution. We interpret this as non-resonant continuum contributions. An interesting aspect of all models is the significant contribution of the ground state in all energy regions and its dominance below 2 MeV. From this rather remarkable feature it is possible to determine the ground state strength from a measurement well above the peak. This behavior is the well known “ghost anomaly” expected both from theory [20] and observed in previous experiments on the  $^8\text{Be}$  system [21]. This implies that previous measurements, which have ignored the anomaly, have overestimated the  $2_1$  strength by at least 20%. This estimate is based on the difference between our two different methods.

Additionally, it should be noted that the observed strength in the intermediate region between 6 and 16 MeV cannot be attributed to a single resonance but rather a result of several interfering levels and non-resonant continuum contributions. The extracted  $\gamma$  widths for the three models agree within the statistical errors except for the  $2_2$  width. However, as model 1 systematically deviates in that region we recommend that the model 3 parameters are used. The change in resonance energy is expected from interference and similar effects were observed in  $\beta$  decay experiments [22].

The second  $0^+$  level, introduced in model 3, interferes destructively with the ground state, as can be observed in the 12 to 16 MeV region where it improves the agreement substantially. Its location is interesting as it coincides precisely with the energy predicted by [9].

The current literature value of 0.12(5) eV in Ref. [8] for the E2 strength is based on the width listed in Table 1 and a measurement of the E2/M1 mixing ratio 0.018(7) [23]. However, all our models yield a significantly smaller ratio  $< 0.002$ . While the errors involved are too large to draw a conclusion, it is important to note that there is significant spread in the reported mixing values [24–26]. A more detailed measurement of the  $\alpha - \gamma$  correlation function could resolve this issue.

Compared with the GFMC calculation in Ref. [1] we find poor agreement for the transitions to the  $0^+$  and  $2_1^+$  states. For the  $2_1^+$  discrepancy, Ref. [1] suggests that a lack of continuum contributions could explain this. No explanation is given for the  $0^+$  discrepancy. It is interesting to note that a value of  $\Gamma_{2_1, E2} = 0.63(5)$  eV, as suggested by GFMC, can only be accommodated if the first excited state is made extremely wide  $\sim 1.8$  MeV. A similar disagreement is observed for the transitions to the doublet. However, the strength of these transitions depend on isospin mixing of the  $1^+$  doublet states which was first determined by Barker [27]. Using slightly different mixing coefficients resolves some of the issues but create others – see Ref. [1] for details. As these states should be well described in the shell-model, it would be interesting to compare with NCSM calculations of the transition rates.

## 6. Conclusion

Coincident  $\alpha$  particles from the  $^7\text{Li}(p, \gamma)\alpha\alpha$  reaction at a proton energy of roughly  $E_p = 441$  keV have been measured using close geometry silicon strip detectors. This yields a background

**Table 2**

Parameters for the best fit for both models with a channel radius of 5 fm. Parameters in square brackets were fixed. Decay widths were calculated with eq. (6) from the supplementary information. All errors are statistical. Propagated errors are calculated using the Hessian approximation.

Parameter	Model 1	Model 2	Model 3
$E_{01}$ (keV)	[0]	[0]	[0]
$\gamma_{01,M1}$ ( $10^{-11} \times \text{eV}^{-1}$ )	$4.35 \pm 0.05$	$4.36 \pm 0.06$	[4.36]
$\Gamma_{01,M1}^0$ (eV)	$13.7 \pm 0.3$	$13.8 \pm 0.4$	[13.8]
$\gamma_{01,\alpha_0}$ ( $\sqrt{\text{keV}}$ )	[22.1]	[22.1]	[22.1]
$\Gamma_{01,\alpha_0}^0$ (eV)	[5.57]	[5.57]	[5.57]
$E_{02}$ (MeV)	–	–	$12.0 \pm 0.3$
$\gamma_{02,M1}$ ( $10^{-11} \times \text{eV}^{-1}$ )	–	–	$0.58 \pm 0.08$
$\Gamma_{02,M1}^0$ (eV)	–	–	$12 \pm 3$
$\gamma_{02,\alpha_0}$ ( $\sqrt{\text{keV}}$ )	–	–	$-15.2 \pm 1.5$
$\Gamma_{02,\alpha_0}^0$ (MeV)	–	–	$2.4 \pm 0.5$
$E_{21}$ (keV)	$3008^{+55}_{-9}$	$2960 \pm 22$	$2969 \pm 11$
$\gamma_{21,M1}$ ( $10^{-11} \times \text{eV}^{-1}$ )	$3.31 \pm 0.03$	$3.22 \pm 0.06$	$3.13 \pm 0.03$
$\Gamma_{21,M1}^0$ (eV)	$5.57 \pm 0.11$	$5.3 \pm 0.2$	$5.01 \pm 0.11$
$\gamma_{21,E2}$ ( $10^{-22} \times \text{eV}^{-3}$ )	$-4.2 \pm 1.2$	$-4 \pm 500$	$0.9 \pm 59.2$
$\Gamma_{21,E2}^0$ (meV)	$1.9 \pm 1.2$	$< 10 \text{ meV}$	$< 1 \text{ meV}$
$\gamma_{21,\alpha_2}$ ( $\sqrt{\text{keV}}$ )	$-29.9^{+0.3}_{-1.5}$	$-29.3 \pm 0.5$	$28.6 \pm 0.3$
$\Gamma_{21,\alpha_2}^0$ (MeV)	$1701 \pm 27$	$1601 \pm 45$	$1546 \pm 25$
$E_{22}$ (keV)	$16629 \pm 11$	$16588 \pm 5$	$16590 \pm 5$
$\gamma_{22,M1}$ ( $10^{-11} \times \text{eV}^{-1}$ )	$11.6 \pm 0.7$	$12.7 \pm 0.4$	$12.9 \pm 0.4$
$\Gamma_{22,M1}^0$ (meV)	$27.9 \pm 1.7$	$38 \pm 2$	$38 \pm 2$
$\gamma_{22,\alpha_2}$ ( $\sqrt{\text{keV}}$ )	[3.1]	[3.1]	[3.1]
$\Gamma_{22,\alpha_2}^0$ (keV)	[108]	[108]	[108]
$E_{23}$ (keV)	[16922]	$16912 \pm 25$	$16910 \pm 23$
$\gamma_{23,M1}$ ( $10^{-11} \times \text{eV}^{-1}$ )	$3.2^{+1.7}_{-0.9}$	$4.3 \pm 0.8$	$4.5 \pm 0.7$
$\Gamma_{23,M1}^0$ (meV)	$0.8 \pm 0.8$	$1.4 \pm 0.5$	$1.6 \pm 0.5$
$\gamma_{23,\alpha_2}$ ( $\sqrt{\text{keV}}$ )	[2.2]	[2.2]	[2.2]
$\Gamma_{23,\alpha_2}^0$ (keV)	[74]	[74]	[74]
$E_{24}$ (MeV)	–	$24 \pm 3$	[24]
$\gamma_{24,M1}$ ( $10^{-11} \times \text{eV}^{-1}$ )	–	$-1.1 \pm 0.2$	$-1.8 \pm 0.2$
$\Gamma_{24,M1}^0$ (meV)	–	$57 \pm 20$	$160 \pm 40$
$\gamma_{24,\alpha_2}$ ( $\sqrt{\text{keV}}$ )	–	$38 \pm 7$	$35.9 \pm 1.8$
$\Gamma_{24,\alpha_2}^0$ (MeV)	–	$20 \pm 8$	$18.0 \pm 1.8$
$\chi^2/\text{ndf}$	878/735	838/731	808/730
$P$ (%)	0.02	0.36	2.3

free excitation spectrum from 1 to 17 MeV. The  $\gamma$  decay widths have been determined using both integration and R-matrix analysis.

The results of the R-matrix analysis show that the ground state contributes significantly to the full energy range and dominates the spectrum below 2 MeV. This implies that simply integrating the excitation energy spectrum would overestimate the decay strength to the first excited state. In order to achieve a good fit to data, it is necessary to include a  $2^+$  background pole. This indicates that the spectrum has non-resonant continuum contributions. Additionally, we find tentative evidence for a broad  $0^+$  state at 12 MeV. A similar measurement of the 18.1 MeV  $1^+$  state in  $^8\text{Be}$  could further illuminate this.

The extracted widths for the  $2^+$  doublet is in agreement with previous measurements, while the results for the ground and first excited state differ by 8 and 34% respectively. A comparison with GFMC calculations shows significant differences between 13 and 34%. Determination of the  $1^+$  isospin mixing might bring clarification.

## Acknowledgements

The authors would like to thank Jonas Refsgaard for his invaluable input on R-matrix theory. Furthermore, we would like to thank Folmer Lyckegaard for manufacturing the target. We also acknowledge financial support from the European Research Council

under ERC starting grant LOBENA, No. 307447. OSK acknowledges support from the Villum Foundation.

## References

- [1] S. Pastore, R.B. Wiringa, S.C. Pieper, R. Schiavilla, Quantum Monte Carlo calculations of electromagnetic transitions in  $^8\text{Be}$  with meson-exchange currents derived from chiral effective field theory, *Phys. Rev. C* 90 (2) (2014) 024321, <https://doi.org/10.1103/PhysRevC.90.024321>, <https://link.aps.org/doi/10.1103/PhysRevC.90.024321>.
- [2] S. Baroni, P. Navrátil, S. Quaglioni, Unified ab initio approach to bound and unbound states: no-core shell model with continuum and its application to  $^7\text{He}$ , *Phys. Rev. C, Nucl. Phys.* 87 (3) (2013) 1, <https://doi.org/10.1103/PhysRevC.87.034326>, arXiv:1301.3450.
- [3] W.A. Fowler, C.C. Lauritsen, Gamma-radiation from light nuclei under proton bombardment, *Phys. Rev.* 76 (1949) 314.
- [4] D. Zahnow, C. Angulo, C. Rolfs, S. Schmidt, W.H. Schulte, E. Somorjai, The  $S(E)$  factor of  $^7\text{Li}(p,\gamma)^8\text{Be}$  and consequences for  $S(E)$  extrapolation in  $^7\text{Be}(p,\gamma)^8\text{B}$ , *Z. Phys. Hadrons Nucl.* 351 (2) (1995) 229–236, <https://doi.org/10.1007/BF01289534>, <http://adsabs.harvard.edu/abs/1995ZPhyA.351..229Z>.
- [5] P. Paul, D. Kohler, K.A. Snover, Magnetic dipole transitions and isospin in  $\text{Be}^8$ , *Phys. Rev.* 173 (4) (1968) 919–930, <https://doi.org/10.1103/PhysRev.173.919>, <https://link.aps.org/doi/10.1103/PhysRev.173.919>.
- [6] W.E. Sweeney, J.B. Marion, Gamma-ray transitions involving isobaric-spin mixed states in  $\text{Be}^8$ , *Phys. Rev.* 182 (4) (1969) 1007–1021, <https://doi.org/10.1103/PhysRev.182.1007>, <https://link.aps.org/doi/10.1103/PhysRev.182.1007>.
- [7] E.K. Warburton, R-matrix analysis of the  $\beta^{\pm}$ -delayed alpha spectra from the decay of  $^8\text{Li}$  and  $^8\text{B}$ , *Phys. Rev. C* 33 (1) (1986) 303–313, <https://doi.org/10.1103/PhysRevC.33.303>, <https://link.aps.org/doi/10.1103/PhysRevC.33.303>.

- [8] D. Tilley, J. Kelley, J. Godwin, D. Millener, J. Purcell, C. Sheu, H. Weller, Energy levels of light nuclei, *Nucl. Phys. A* 745 (3–4) (2004) 155–362, <https://doi.org/10.1016/j.nuclphysa.2004.09.059>.
- [9] E. Caurier, P. Navrátil, W.E. Ormand, J.P. Vary, Intruder states in  $^8\text{Be}$ , *Phys. Rev. C* 64 (5) (2001) 051301, <https://doi.org/10.1103/PhysRevC.64.051301>, <https://link.aps.org/doi/10.1103/PhysRevC.64.051301>.
- [10] A.J. Krasznahorkay, M. Csatlós, L. Csige, Z. Gácsi, J. Gulyás, M. Hunyadi, I. Kuti, B.M. Nyakó, L. Stuhl, J. Timár, T.G. Tornyi, Z. Vajta, T.J. Ketel, A. Krasznahorkay, Observation of anomalous internal pair creation in  $^8\text{Be}$ : a possible indication of a light, neutral boson, *Phys. Rev. Lett.* 116 (4) (2016) 042501, <https://doi.org/10.1103/PhysRevLett.116.042501>, <https://link.aps.org/doi/10.1103/PhysRevLett.116.042501>.
- [11] J. Kozaczuk, D.E. Morrissey, S.R. Stroberg, Light axial vector bosons, nuclear transitions, and the  $^8\text{Be}$  anomaly, *Phys. Rev. D* 95 (11) (2017) 115024, <https://doi.org/10.1103/PhysRevD.95.115024>, <http://link.aps.org/doi/10.1103/PhysRevD.95.115024>.
- [12] O. Tengblad, U. Bergmann, L. Fraile, H. Fynbo, S. Walsh, Novel thin window design for a large-area silicon strip detector, *Nucl. Instrum. Methods Phys. Res., Sect. A, Accel. Spectrom. Detect. Assoc. Equip.* 525 (3) (2004) 458–464, <https://doi.org/10.1016/j.nima.2004.01.082>.
- [13] M. Alcorta, O. Kirsebom, M. Borge, H. Fynbo, K. Riisager, O. Tengblad, A complete kinematics approach to study multi-particle final state reactions, *Nucl. Instrum. Methods Phys. Res., Sect. A, Accel. Spectrom. Detect. Assoc. Equip.* 605 (3) (2009) 318–325, <https://doi.org/10.1016/j.nima.2009.03.246>.
- [14] M. Munch, O.S. Kirsebom, J.A. Swartz, K. Riisager, H.O.U. Fynbo,  $^8\text{Be}$  excitation spectrum (Feb. 2018), <https://doi.org/10.5281/zenodo.1174127>.
- [15] W.A. Fowler, C.C. Lauritsen, T. Lauritsen, Gamma-radiation from excited states of light nuclei, *Rev. Mod. Phys.* 20 (1) (1948) 236–277, <https://doi.org/10.1103/RevModPhys.20.236>, <https://link.aps.org/doi/10.1103/RevModPhys.20.236>.
- [16] M. Munch, R-matrix parametrization for  $\gamma$  decays to unbound states, arXiv:1802.09297.
- [17] M. Munch, O. S. Kirsebom, J. Refsgaard, Open R-matrix (Feb. 2018). <https://doi.org/10.5281/zenodo.1174079>.
- [18] G. Bortels, P. Collaers, Analytical function for fitting peaks in alpha-particle spectra from Si detectors, *Int. J. Radiat. Appl. Instrum., Part A, Appl. Radiat. Isot.* 38 (10) (1987) 831–837, [https://doi.org/10.1016/0883-2889\(87\)90180-8](https://doi.org/10.1016/0883-2889(87)90180-8).
- [19] U. Bergmann, K. Riisager, A systematic error in maximum likelihood fitting, *Nucl. Instrum. Methods Phys. Res., Sect. A, Accel. Spectrom. Detect. Assoc. Equip.* 489 (1–3) (2002) 444–447, [https://doi.org/10.1016/S0168-9002\(02\)00864-1](https://doi.org/10.1016/S0168-9002(02)00864-1).
- [20] F.C. Barker, P.B. Treacy, Nuclear levels near thresholds, *Nucl. Phys.* 38 (1) (1962) 33–49, [https://doi.org/10.1016/0029-5582\(62\)91014-3](https://doi.org/10.1016/0029-5582(62)91014-3), [http://www.osti.gov/energycitations/product.biblio.jsp?osti\\_id=4783132](http://www.osti.gov/energycitations/product.biblio.jsp?osti_id=4783132).
- [21] F.D. Becchetti, C.A. Fields, R.S. Raymond, H.C. Bhang, D. Overway, Ghost anomaly in  $^8\text{Be}$  studied with  $^9\text{Be}(p, d)$  at  $E_p = 14.3$  and 26.2 MeV, *Phys. Rev. C* 24 (6) (1981) 2401–2408, <https://doi.org/10.1103/PhysRevC.24.2401>, <https://link.aps.org/doi/10.1103/PhysRevC.24.2401>.
- [22] S. Hyldegaard, Beta-decay studies of  $^8\text{Be}$  and  $^{12}\text{C}$ , Ph.D. thesis, Aarhus University, 2010, [https://wiki.kern.phys.au.dk/Solveig\\_Hyldegaard.pdf](https://wiki.kern.phys.au.dk/Solveig_Hyldegaard.pdf).
- [23] V. Meyer, H. Müller, H. Staub, R. Zurmühle, The  $\gamma$ -radiation of the  $\text{Li}^7(p, \gamma)$  resonance at 441.3 keV, *Nucl. Phys.* 27 (2) (1961) 284–293, [https://doi.org/10.1016/0029-5582\(61\)90350-9](https://doi.org/10.1016/0029-5582(61)90350-9).
- [24] A. Boyle, The spin of the 2.9 MeV state of  $\text{Be}^8$ , *Nucl. Phys.* 1 (8) (1956) 581–584, [https://doi.org/10.1016/S0029-5582\(56\)80078-3](https://doi.org/10.1016/S0029-5582(56)80078-3).
- [25] I.S. Grant, Radiative transitions in  $^8\text{Be}$ , *Proc. Phys. Soc.* 76 (5) (1960) 737–744, <https://doi.org/10.1088/0370-1328/76/5/313>.
- [26] B. Mainsbridge, The angular distributions of the gamma radiation from the  $\text{Li}^7(p, \gamma)\text{Be}^8$  reaction from  $E_p = 200$  keV, *Nucl. Phys.* 21 (1960) 1–14, [https://doi.org/10.1016/0029-5582\(60\)90023-7](https://doi.org/10.1016/0029-5582(60)90023-7).
- [27] F. Barker, Intermediate coupling shell-model calculations for light nuclei, *Nucl. Phys.* 83 (2) (1966) 418–448, [https://doi.org/10.1016/0029-5582\(66\)90582-7](https://doi.org/10.1016/0029-5582(66)90582-7).

# R-Matrix parametrization for $\gamma$ decays to unbound states

Michael Munch

Institute of Physics and Astronomy, Aarhus University, Denmark

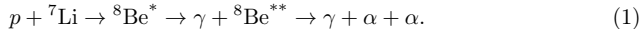
October 11, 2018

## 1 Introduction

R-matrix theory was originally developed to describe nuclear reactions [1]. The framework was further extended to describe  $\beta$  decay to unbound states [2, 3]. However, at the time of writing, no clear description of  $\gamma$  decays to unbound states exist. Such a description will be presented in this note.

## 2 R-matrix parameterization

The motivation for this note is the following reaction



It will be assumed that the initial reaction proceeds through a single isolated resonance in the compound system. Under these conditions, the treatment is quite similar to that of  $\beta$  decays of  ${}^8\text{B}$  and  ${}^8\text{Li}$  [2, 3]. The notation is that of Ref. [1] unless stated otherwise.

Using the formalism in Ref. [1, XIII.2] the reaction is described as a sequential process. Figure 1 illustrates the general case in which an isolated initial level  $\lambda$  is populated via channel<sup>1</sup>  $\alpha$  and decays via channel  $\alpha'$  to an unbound fragment in a state  $\lambda'$  and internal energy  $E'_2$ , which finally decays via the open channel  $r'$ . The differential cross section for this reaction is given as

$$\frac{d\sigma_{\alpha\alpha'}(E'_2 r')}{dE'_2} = \frac{\pi}{k_\alpha^2} \sum_{c c'} \frac{g_J \Gamma_{\lambda c} \delta\Gamma_{\lambda' c'}(E'_2 r')}{(E_\lambda + \Delta_\lambda - E)^2 + (\Gamma_\lambda/2)^2}, \quad (2)$$

where  $c$  (and  $c'$ ) specifies the two subsystems, their spins, the channel spin  $s$  and their relative angular momentum  $\ell$ . Note that the notation in Ref. [1] is ambiguous, so here we use  $\delta\Gamma_{\lambda' c'}(E'_2 r') \equiv \frac{d\Gamma_{\lambda' c'}(E'_2 r')}{dE'_2}$ .

Generally, the integral of  $\delta\Gamma_{\lambda' c'}(E'_2 r')$  should be included in  $\Gamma_\lambda$ , however, the photon channels do not contribute significantly, so the width of the initial level can be approximated with the particle width  $\Gamma_\lambda \approx \sum_{c_p} \Gamma_{\lambda c_p}$ . Additionally, for a narrow entry level, this can be rewritten into the familiar Breit-Wigner form

$$\frac{d\sigma_{\alpha\alpha'}(E'_2 r')}{dE'_2} = \frac{\pi}{k_a^2} \sum_{s\ell s'\ell'} g_J \frac{\Gamma_{\lambda c}^0 \delta\Gamma_{\lambda' c'}^0(E'_2 r')}{(E_\lambda^0 - E)^2 + (\sum_{c_p} \Gamma_{c_p}^0/2)^2}, \quad (3)$$

where parameters with superscript 0 are so-called observed parameters [4].

---

<sup>1</sup>Here  $\alpha$  and  $\alpha'$  is the notation used for a channel not an  $\alpha$  particle.

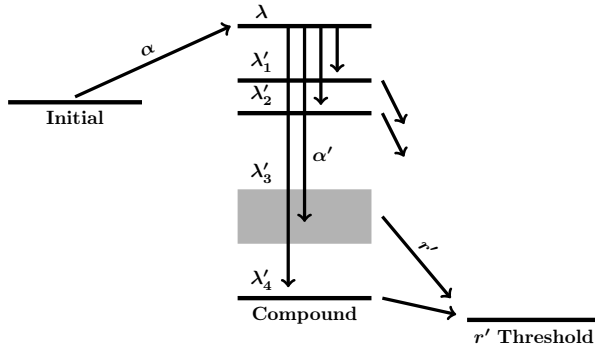


**Figure 1:** Sketch of the general decay scheme. A resonance  $\lambda$  in the compound system is formed via channel  $\alpha$ . This resonance decays to another unbound compound level  $\lambda'$  via a  $\gamma$ -channel  $\alpha'$ . The unbound level subsequently decays via  $r'$ .

Due to their small coupling to the nucleus, photon channels can be included in R-matrix theory using a perturbation approach. Ref. [1, XIII.3] has derived the theory for one photon without damping, which applies to this case. Within this framework particle and photon channels can be treated almost identically, except photon channels should not be included in the level matrix. Additionally, one can work directly with observable parameters if one uses the Brune formalism [4]. With this formalism the level matrix is defined as

$$\begin{aligned}
 [\tilde{\mathbf{A}}^{-1}]_{\lambda\mu} = & (\tilde{E}_\lambda - E)\delta_{\lambda\mu} - \sum_c \tilde{\gamma}_{\lambda c} \tilde{\gamma}_{\mu c} (S_c + iP_c) \\
 & + \sum_c \begin{cases} \tilde{\gamma}_{\lambda c}^2 S_{\lambda c} & \text{for } \lambda = \mu, \\ \tilde{\gamma}_{\lambda c} \tilde{\gamma}_{\mu c} \frac{S_{\lambda c}(E - \tilde{E}_\mu) - S_{\mu c}(E - \tilde{E}_\lambda)}{E_\lambda - \tilde{E}_\mu} & \text{for } \lambda \neq \mu, \end{cases} \quad (4)
 \end{aligned}$$

where  $\tilde{E}$  is the observable resonance energy and  $\tilde{\gamma}_{\lambda c}$  the reduced width coupling of a level  $\lambda$  to a channel  $c$ .  $P_c$  and  $S_c$  are respectively the penetrability and shift function as defined in regular R-matrix theory [1] with  $S_{\lambda c} = S_c(\tilde{E}_\lambda)$ .

The partial width for emission of a  $L$ -wave photon with energy  $E$  from a level  $\lambda$  is related to its reduced width via  $\Gamma_{\lambda L} = 2E^{2L+1} \gamma_{\lambda L}^2$ . The partial width for a particle is given as  $\Gamma_{\lambda c} = 2P_c \gamma_{\lambda c}^2$ . In order to have a symmetric notation we define the  $\gamma$  penetrability as  $P_L \equiv E^{2L+1}$ .

Following Ref. [5] we adopt the following expression to describe the differential partial width of the intermediary state

$$\delta\Gamma_{\lambda c'(E_2^{r'})}^0 = \frac{2P_{c'}2P_{r'}}{2\pi} \left| \sum_{\nu\mu} \tilde{\gamma}_{\lambda c'(\nu)} \tilde{\gamma}_{\mu r'} \tilde{A}_{\nu\mu} \right|^2. \quad (5)$$

This reduces to (XIII 2.10) of Ref. [1] for the case of a single isolated intermediary resonance,

$$\delta\Gamma_{\lambda c'(E_2^{r'})}^0 = \frac{1}{2\pi} \frac{\tilde{\Gamma}_{\lambda c'(\lambda')} \tilde{\Gamma}_{\lambda' r'}}{(\tilde{E}_{\lambda'} + \Delta_{\lambda'} - E_2^r)^2 + (\tilde{\Gamma}_{\lambda'}/2)^2}. \quad (6)$$

The observed partial decay width of  $\lambda$  to a specific resonance  $\lambda'$  is then given as the integral over the resonance peak. For an isolated intermediary level the shift function is

approximately linear over the resonance and the integral can be performed analytically

$$\Gamma_{\lambda c'(\lambda')}^0 = \int_{\lambda'} \delta\Gamma_{\lambda c'(E_2' r')}^0 dE_2' \approx \frac{2P_{c'} \tilde{\gamma}_{\lambda c'(\lambda')}^2}{1 + \sum_c \tilde{\gamma}_{\lambda c}^2 \frac{dS_c}{dE} \Big|_{\bar{E}_{\lambda'}}}. \quad (7)$$

This is identical to the expression for the observed width in Ref. [4].

Inserting eq. (7) into eq. (2) or eq. (3) yields the full expression. Contributions from the same multipolarity is summed coherently while contributions from different multipolarities are added incoherently.

### 3 Conclusion

Combining the R-matrix theory for sequential decays with a level density inspired from  $\beta$  decay studies, it is possible to describe  $\gamma$  decays to unbound states.

### Bibliography

- [1] A. M. Lane and R. G. Thomas. R-Matrix Theory of Nuclear Reactions. *Reviews of Modern Physics*, 30(2):257–353, apr 1958.
- [2] FC Barker. 2+ States of 8Be. *Australian Journal of Physics*, 22(3):293, 1969.
- [3] E. K. Warburton. R-matrix analysis of the  $\beta^\pm$ -delayed alpha spectra from the decay of Li8 and B8. *Physical Review C*, 33(1):303–313, jan 1986.
- [4] C. R. Brune. Alternative parametrization of R-matrix theory. *Physical Review C*, 66(4):044611, oct 2002.
- [5] FC Barker. Consistent Description of Unbound States Observed in Scattering and Reactions. *Australian Journal of Physics*, 41(6):743, 1988.





## The partial widths of the 16.1 MeV $2^+$ state in $^{12}\text{C}$

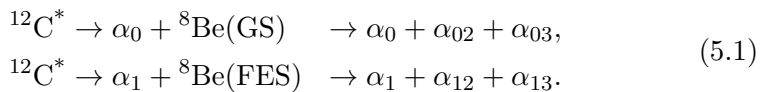
This chapter reports on a measurement of the  $^{11}\text{B}(p, \alpha)$  cross section for the 16.1 MeV resonance in  $^{12}\text{C}$ . The aim of the measurement was to resolve discrepancies regarding the partial widths of this resonance.

The chapter begins with a summary of the current state of affairs for the  $^{11}\text{B}(p, \alpha)$  cross section, which also serves as a motivation for the present experiment. This is followed by a presentation of the current state-of-the-art  $^{12}\text{C}$  break-up model, which is used in the normalization procedure. From then on the chapter will focus on the 16.1 MeV state and the experiment at hand; describing the method and results. The discussion focuses on the results obtained and its consequences for the recommended  $^{11}\text{B}(p, \alpha)$  reaction rate. The results were published in ref. [112] and the paper can be found at page 91.

### 5.1 Motivation

Motivated by a desire to gain insight into nuclear structure, reaction mechanisms, and astrophysics, the break-up of  $^{12}\text{C}$  into three  $\alpha$  particles has been studied since the days of Lord Rutherford [120]. The reaction mechanism for the  $^{12}\text{C} \rightarrow 3\alpha$  break-up was the subject of intense research in the 1960s and 70's [121–125], where it was found to proceed predominantly as a sequential

break-up via the two lowest states in  $^8\text{Be}$



This reaction has primarily been studied by bombarding  $^{11}\text{B}$  with protons and observing the emitted  $\alpha$  particles. For decays proceeding via the narrow  $^8\text{Be}$  ground state (GS), the reaction is approximately two-body kinematics and a sharp peak is observed at high energy. This can be seen in figure 3 in the paper at the end of this chapter. In addition, one observes a continuum of particles at lower energy from the subsequent  $^8\text{Be}$  break-up. This reaction

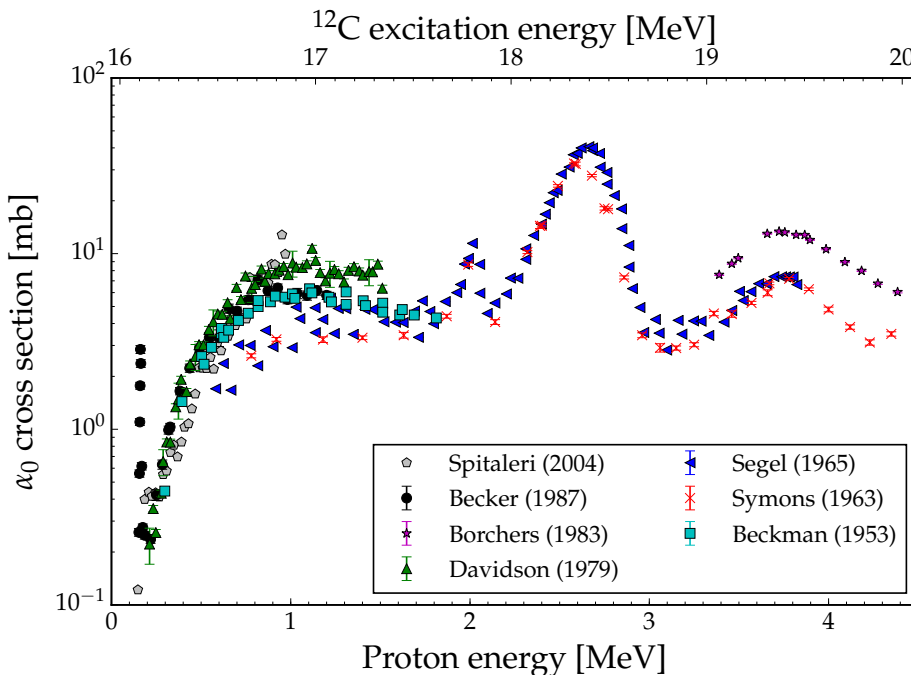


Figure 5.1:  $^{11}\text{B}(p, \alpha_0)$  cross section. Data from refs. [113–119]

cross section should be straight-forward to measure. However, the situation is less than stellar as can be seen from fig. 5.1, which shows all of the available data [113–119]. In addition, only a single measurement has been performed at the 16.1 MeV resonance corresponding to a proton energy of 161 keV. The  $\alpha_1$  channel proceeding through the first excited state (FES) in  ${}^8\text{Be}$  is more difficult to characterize, as there is generally no clear way to identify  $\alpha_1$  from the secondary  $\alpha$  particles and a complete kinematic characterization requires simultaneous detection of two of three final state particles. If only the energy of one  $\alpha$  particle is measured, the observed spectrum shows a broad distribution, as seen in figure 3 in the paper. Figure 5.2 shows the

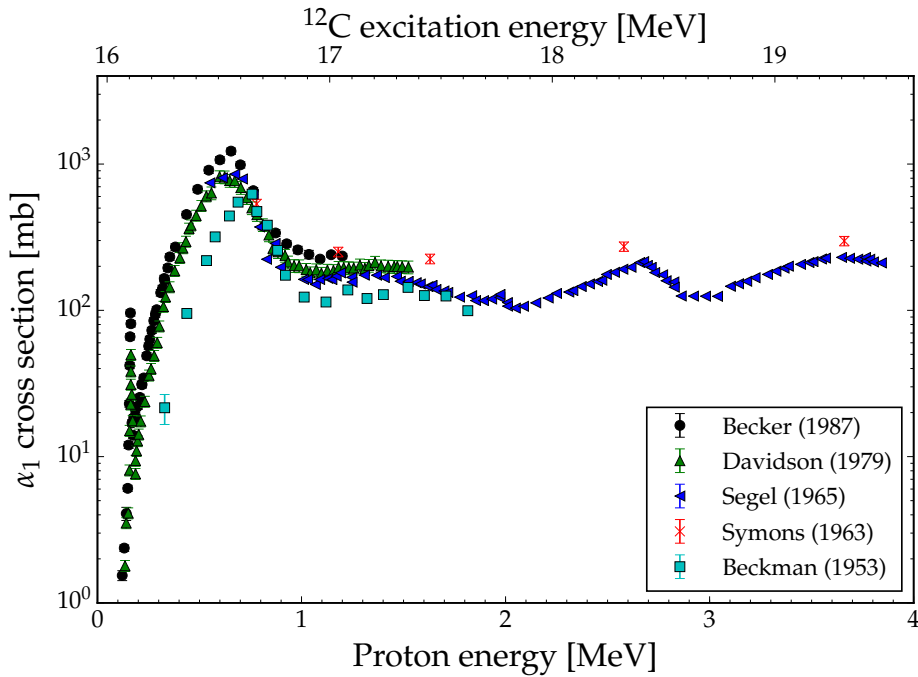


Figure 5.2:  ${}^{11}\text{B}(p, \alpha_1)$  cross section. Data from refs. [113–116, 118]

cross sections measured for the  $\alpha_1$  channel [113–115, 118].

The  $^{11}\text{B}(p, 3\alpha)$  reaction is a strong candidate for an aneutronic fusion reactor, i.e. a fusion reactor almost<sup>1</sup> without neutrons in the final state, unlike the alternative deuterium-tritium (D–T) reaction. Such a reactor would be operated at a temperature corresponding to a few hundred keV and the reaction would thus predominantly proceed through the 16.1 and 16.6 MeV states.

Due to the substantial inconsistencies in the cross sections, it seems obvious to re-investigate this reaction – starting with the resonance at 16.1 MeV.

## 5.2 The triple- $\alpha$ break-up

Before describing the experiment at hand let us dwell a bit on the reaction mechanism since the 16.1 MeV resonance played a crucial role in refining it.

For three-body final states there are 9 momentum components, but due to energy- and momentum conservation only 5 of these are independent. Hence, it is possible to perform a complete kinematic characterization of a decay with a simultaneous measurement of the position and energy of two out of three particles. Due to energy conservation, it is possible to map the energy distribution of the three particles into a two-dimensional distribution with coordinates defined as

$$x = \frac{\epsilon_1 + 2\epsilon_2 - 1}{\sqrt{3}} \quad y = \epsilon_1 - 1/3, \quad (5.2)$$

where  $\epsilon_i = E_i^{\text{cm}}/E_{\text{tot}}$  with  $E_i^{\text{cm}}$  as the kinetic center-of-mass (CM) energy of particle  $i$  and  $E_{\text{tot}}$  the total kinetic energy. The resulting distribution is called a Dalitz plot [126]. Figure 5.3 illustrates the coordinate definition. Due to energy and momentum conservation, points are constrained to be within the circle. The figure also shows the naively expected distribution for decays proceeding via the  $^8\text{Be}$  GS or FES. The GS is seen along the edge of

---

<sup>1</sup>Some neutrons will be released through reactions such as  $^{11}\text{B}(p, n)^{11}\text{C}$  and  $^{10}\text{B}(\alpha, n)^{13}\text{N}$ .

the circle, corresponding to  $\alpha_0$  taking the majority of the energy. The band is narrow due to the sharpness of the  ${}^8\text{Be}$  GS<sup>2</sup>. The band corresponding to decays via the FES is shifted relative to the GS band corresponding to its  $\sim 3\text{ MeV}$  excitation energy and it is broader. Note that the GS decay is forbidden for unnatural parity states due to spin-parity conservation.

The study of these distributions was the subject of many experiments in the 1960s and 70s. These experiments typically employed small ( $\leq 3 \times 3$  mm) rotatable detectors and collected multiplicity 2 coincidences. Figure 5.4 and 5.5 show the Dalitz plots obtained by refs. [127, 128] for the 16.1 and

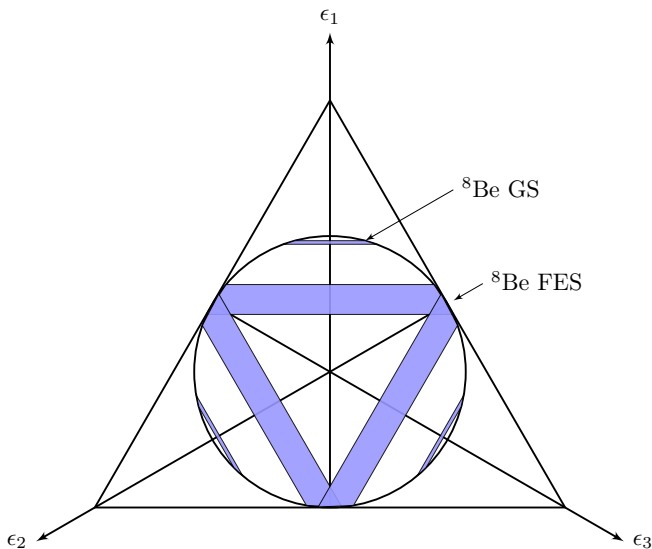


Figure 5.3: Dalitz plot with the coordinates defined in eq. (5.2). The triangle corresponds to energy conservation and the circle to momentum conservation. The blue bands sketch the naively expected distribution from a sequential decay. Note that the plot is six-fold symmetric and can be folded into a single sector.

---

<sup>2</sup>This neglects the “ghost anomaly” as seen in chapter 4.

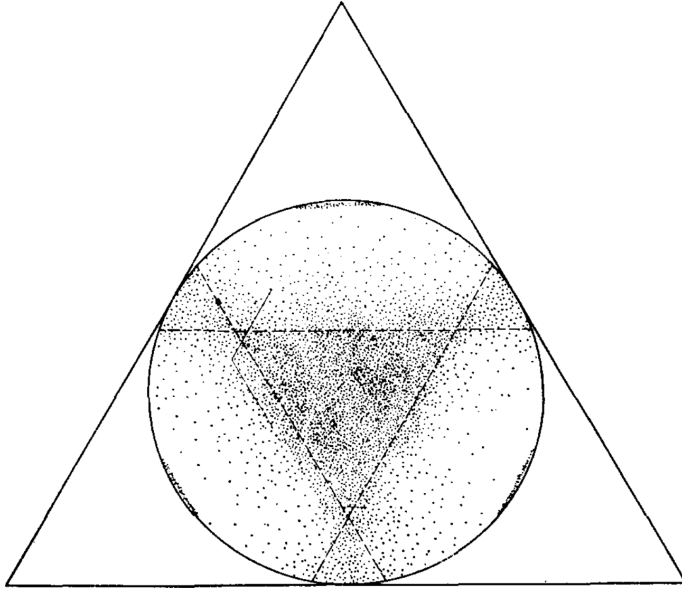


Figure 5.4: Dalitz plot for the  $2^+$  16.1 MeV resonance corresponding to  $E_p = 161$  keV. Note the filled center. Figure from ref. [127].

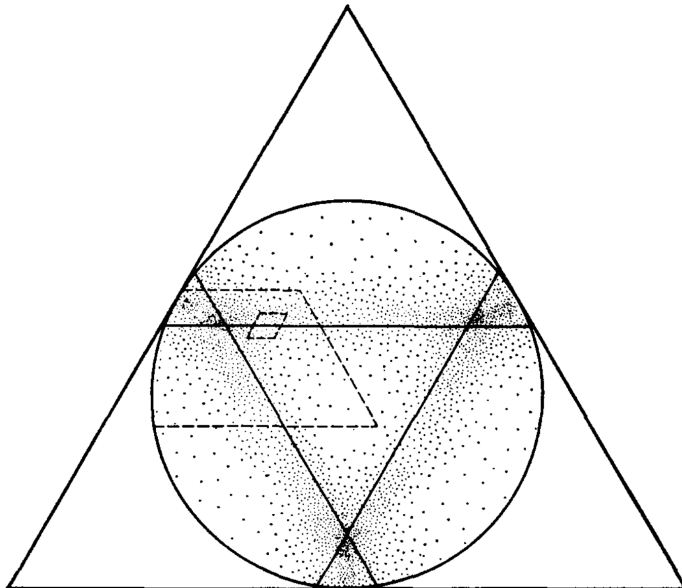


Figure 5.5: Dalitz plot for the  $2^-$  16.6 MeV resonance corresponding to  $E_p = 675$  keV. Note the plot is only filled along the lines corresponding to decays via the FES in  $^8\text{Be}$  as decays via the GS is forbidden due to spin-parity conservation. Figure from ref. [128].

16.6 MeV states. While the latter neatly conforms to the naive expectations, the former Dalitz plot is filled in the middle, which cannot be explained with a naive sequential model. This lead Kamke *et al.* to postulate a “direct decay” model, which does not proceed via resonances in  $^8\text{Be}$ , but couple directly to a  $3\alpha$  final state. As such a model leads to more equal<sup>3</sup> energy sharing between the particles, the model could explain the observation. However, this special treatment of the 16.1 MeV resonance caused some controversies. Shortly after this claim, alternative models were put forward that provided a unified description of the break-up. These were more sophisticated sequential models, which included interference terms due to the Bose symmetry of the final state [125, 129].

In recent years this area of research has received new interest due to the advancement of large-area segmented silicon detectors, which allow studies to be performed in far greater detail. This has lead to a series of investigations, specifically, the 12.7 MeV state [130], the 11.8, 12.7 and 13.4 MeV states [131], the Hoyle state [132] and the 16.1 MeV state [133]. In all cases, a modified version of the model proposed in ref. [134], was found to be in good agreement with the observations. This model will be referred to as the Balamuth reaction mechanism. It was also used, in the present experiment, to calculate the  $\alpha_1$  detection efficiency and will be explained briefly.

Following the notation of ref. [133], the  $^{12}\text{C}$  resonance is assumed to be created with a specific spin and projection  $(j, m)$ . This resonance decays by emitting an  $\alpha$  particle  $\alpha_1$ , with energy  $E_1$ , and angular momentum  $\ell$ , to a  $^8\text{Be}$  state with energy  $E'_0$ , and spin  $j'$ , with an unobserved projection  $m'$ . The  $^8\text{Be}$  resonance subsequently decays to two  $\alpha$  particles<sup>4</sup>,  $\alpha_2$  and  $\alpha_3$ , with relative kinetic energy  $E_{23}$ , in the  $^8\text{Be}$  rest frame. The parametrization of the intermediate resonance is performed using the R-matrix framework. If the initial state is  $j = 2$  with positive parity and decays via the FES of  $^8\text{Be}$   $j' = 2$  then the allowed angular momenta are  $\ell = 0, 2, 4$  and  $\ell' = 2$ . It will

---

<sup>3</sup>The center of the Dalitz plot corresponds to exact equal sharing of the energy.

<sup>4</sup>The notation used here conflicts with the one in eq. (5.1). In the present case, the index is only used for enumeration.

be assumed that the decay predominantly occurs via a single  $\ell$ . This yields the following expression for the decay weight

$$f_{1,23} = \sum_{m'} (\ell m - m' j' m' | j m) Y_{\ell}^{m-m'}(\Theta_1, \Phi_1) Y_{\ell'}^{m'}(\theta_2, \phi_2) \times \frac{[(\Gamma/E_1^{\frac{1}{2}})(\Gamma'/E_{23}^{\frac{1}{2}})]^{\frac{1}{2}} e^{i(\omega-\phi)} e^{i(\omega'-\phi')}}{E'_0 - E_{23} - \gamma'^2[S'(E_{23}) - S(E'_0)] - i\frac{1}{2}\Gamma'}, \quad (5.3)$$

where the following notation from ref. [133] has been used:

- $E_i$  = kinetic energy of  $\alpha_i$  in the  $^{12}\text{C}$  rest frame,
- $E_{ij}$  = relative kinetic energy of  $\alpha_i$  and  $\alpha_j$ ,
- $(\Theta_i, \Phi_i)$  = emission angles of  $\alpha_i$  in the  $^{12}\text{C}$  rest frame,
- $(\theta_i, \phi_i)$  = emission angles of  $\alpha_i$  in the  $^8\text{Be}$  rest frame,
- $j, j'$  = total angular momentum,
- $m, m'$  = angular momentum projection,
- $\ell, \ell'$  = orbital angular momentum,
- $\Gamma, \Gamma'$  = partial decay width,
- $\gamma, \gamma'$  = reduced width,
- $S, S'$  = shift function,
- $P, P'$  = penetrability factor,
- $\omega, \omega'$  = coulomb phase shift,
- $\phi, \phi'$  = hard-sphere phase shift,
- $E'_0$  = level energy of the  $2^+$  resonance in  $^8\text{Be}$ .

Primed variables refer to the  $^8\text{Be}$  system. Taking a closer look at eq. (5.3), one finds that the first part accounts for the spin coupling and angular distribution while the last part is the regular R-matrix single-level expression with the exception of the numerator, where the two-body phase space factor has been removed,  $\Gamma \rightarrow \Gamma/E^{\frac{1}{2}}$ . The full decay weight is given by the product of the three-body phase space and eq. (5.3). The former can be calculated easily [135].



Note that the above expression assumes a definite decay ordering and must be symmetrized accordingly. This is easily achieved with a coherent sum of the cyclic permutation. The expression is also summed<sup>5</sup> over the unobserved  $m$

$$|f|^2 = \sum_m |f_{1,23} + f_{2,31} + f_{3,12}|^2. \quad (5.4)$$

It was pointed out by ref. [130] that the above expression assumes that the second decay occurs sufficiently distant from the initial decay that the primary and secondary  $\alpha$  particles do not interact. However, using a simple classical expression to estimate the separation yields  $\sim 15$  fm at which the interaction is non-negligible. This can be somewhat remedied using a simple ad-hoc correction, where the penetrability is modified such that  $\alpha_1$  first tunnels to the channel radius in the  $\alpha_1$ - $^8\text{Be}$  system and then to infinity in the  $\alpha_1$ - $\alpha_2$  and  $\alpha_1$ - $\alpha_3$  system. This final-state correction was the topic of a recent article which investigated the effects on the break-up of the Hoyle state [43].

### 5.3 The 16.1 MeV state

At a proton energy of  $\sim 162$  keV, both the  $\alpha_0$  and  $\alpha_1$  cross sections show a clearly defined narrow peak – increasing the yield by roughly an order of magnitude. This corresponds to the 16.1 MeV state in  $^{12}\text{C}$ , which is  $\sim 5$  keV wide. The resonance has spin-parity  $2^+$  and was first assigned  $T = 1$  by Oppenheimer *et al.* in order to explain how a resonance unbound by approximately 8 MeV could have such a narrow width.

For a narrow isolated resonance the reaction cross section,  $\sigma_{ab}$ , is directly related to the partial channel widths,  $\Gamma_x$ . On resonance, this relation is given by

$$\sigma_{ab} = 4\pi\lambda^2\omega \frac{\Gamma_a\Gamma_b}{\Gamma^2}, \quad (5.5)$$

---

<sup>5</sup>This is done with an incoherent sum in ref. [134] although this seems unjustified as the spherical harmonics are only orthogonal when integrated over the unit sphere.

where  $\omega$  is the statistical spin factor,  $\lambda$  the Compton wavelength of the initial system and  $\Gamma$  the resonance width. As stated above, the 16.1 MeV state has primarily been studied in  $(p, x)$  reactions on  $^{11}\text{B}$ . Above the proton threshold the open channels are  $\alpha$ ,  $p$  and  $\gamma$ . However, for the 16.1 MeV resonance it is unfeasible to measure  $\Gamma_p$  directly and it must instead be inferred indirectly via eq. (5.5) and measurements of its  $\alpha$  and  $\gamma$  decay properties. Table 2 in the article lists the different extracted  $\Gamma_p$  values and two clear clusters can be observed. This discrepancy also leads to two different  $\Gamma_p$  values in two recent reviews [74, 133].

The introduction of the article at the end of this chapter summarizes and discusses the different measurements that have been used to calculate the values in Table 2. Here, I will focus on the  $\alpha$  cross section. As  $\Gamma_\alpha \approx \Gamma$  it is possible to directly extract  $\Gamma_p$  from a measurement of  $\sigma_{p\alpha} = \sigma_{p\alpha 0} + \sigma_{p\alpha 1}$ . There exist three measurements of  $\sigma_{p\alpha}$  at the 16.1 MeV resonance [116, 118, 137] with the measurement of ref. [118] being inconsistent with the other two. In all three experiments, the cross section was derived from the number of counts observed in one detector. However, the different authors do not agree on the normalization for  $\alpha_1$ . Refs. [116, 137] argue that they detected one out of three particles and thus divide their observed number of counts by 3, while ref. [118] argues that they observed either the primary  $\alpha$  particle or both secondary particles and divide by 2. This discrepancy is present over the full energy scale as can be seen in fig. 5.2. However, based on theoretical calculations of the opening angle of the secondary  $\alpha$  particles [138] and the experimental setup in ref. [118] the latter claim seems very unlikely.

A measurement of  $\sigma_{p\alpha}$  could resolve both the  $\Gamma_p$  discrepancy and the normalization issue. As can be seen from fig. 5.2, resolving the normalization issue could have an impact over the full energy range.

## 5.4 Method

In order to circumvent the normalization issue of ref. [116, 118, 137], the aim of the experiment was to observe all  $\alpha$  particles from the  $^{12}\text{C}$  break-up in coincidence. To this end, charged particles were detected with an array

of four large-area double-sided silicon strip detectors (DSSD) with a solid angle coverage of approximately 40%. An illustration of the array can be seen in figure 2 in the article. The resonance was populated by bombarding a  $39(3) \mu\text{g cm}^{-2}$  99% enriched  $^{11}\text{B}$  target with a beam of  $\text{H}^{3+}$ . The beam current was primarily limited by the rate in the forward detector and was kept below 0.5 nA.

The data was analyzed using two different methods, which I will quickly summarize. For details, please consult the article at the end of this chapter.

The first method undertook an analysis similar to what could be done by refs. [116, 118, 137]. The method consists of transforming all hits to the beam-target CM assuming they are  $\alpha$  particles. The resulting spectrum can be seen in Figure 3 in the article. Gating on the high-energy  $\alpha_0$  peak, it is possible to project the CM angular distribution, which can be seen in Figure 5. This is fitted with Legendre polynomials and the integrated number of counts are extracted from the 0'th order term.

The alternative method focuses on triple coincidences. For each triplet, it assumes that each hit is an  $\alpha$  particle and calculates the CM energy and momentum from the lab energy and position. In addition, it calculates the  $^{12}\text{C}$  excitation energy. Figure 6 in the article shows the calculated total momentum vs. the excitation energy. The 16.1 MeV resonance is clearly defined, with random coincidences stretching up as a band to the left. From the CM energies, it is possible to extract a Dalitz plot, which can be seen in fig. 5.6. This Dalitz plot neatly illustrates the need for the Balamuth reaction mechanism described in section 5.2 as the filled center clearly does not correspond to the naive reaction mechanism. From this plot, it is easy to identify the two  $\alpha$  channels. The detection efficiency for the two channels is determined with a Monte Carlo simulation. For the GS channel,  $\alpha_0$  is emitted according to the observed angular distribution and the secondary particles emitted isotropically. For the FES channel, the three  $\alpha$  particles are emitted according to the Balamuth reaction mechanism. In this analysis, there is no normalization ambiguity since all three  $\alpha$  particles are observed.

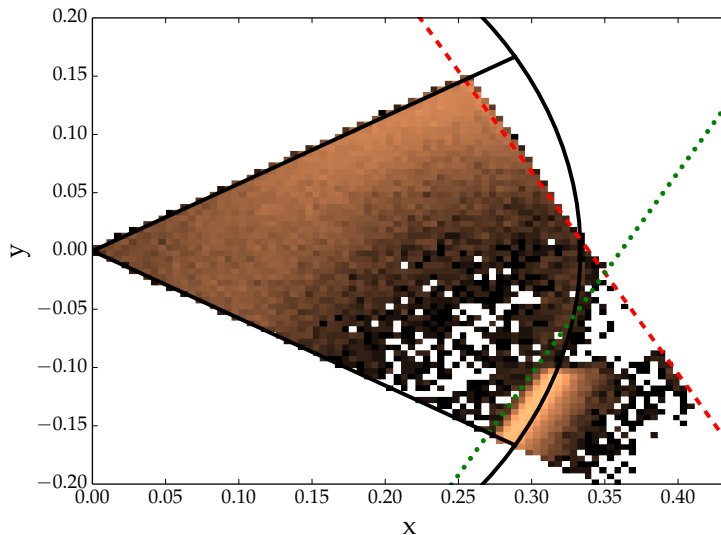


Figure 5.6: Dalitz plot of the detected triplet of  $\alpha$  particles. The circle indicates the constraints imposed by energy-momentum conservation. The dashed red line indicates the low energy cut-off. The dotted green line indicates the distinction between decays via the  $\alpha_0$  (right) and  $\alpha_1$  (left) channels. The coordinates are defined in eq. (5.2) and are unitless.

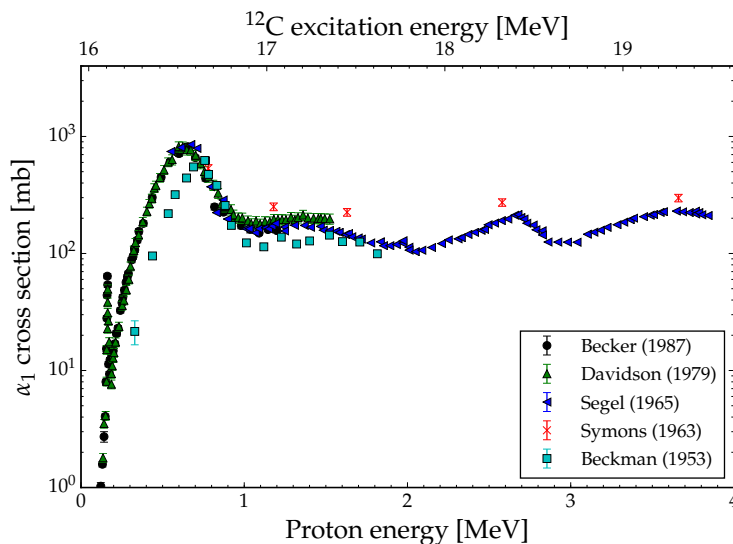


Figure 5.7:  $^{11}\text{B}(p, \alpha_1)$  cross section. Axis truncated to 1 mb. Data from [113–116, 118]. Becker (1987) has been scaled by 2/3. Beckman (1953) appears to have an energy calibration issue.

## 5.5 Results and discussion

The result of the experiment is two cross sections

$$\begin{aligned}\sigma_{p\alpha 0} &= 2.03(14) \text{ mb} \\ \sigma_{p\alpha 1} &= 38(5) \text{ mb},\end{aligned}$$

where the former is the weighted average of the single and triple analysis. The  $\alpha_0$  cross section is in excellent agreement with the result of ref. [118]. The  $\alpha_1$  cross section is in good agreement with ref. [137] and also with ref. [118] – provided the latter is scaled by a factor of  $\frac{2}{3}$ . The present measurement is not consistent with the result reported by ref. [116]. However, with the  $\alpha_1$  cross section of ref. [118] scaled by  $\frac{2}{3}$  the overall agreement is substantially improved as can be seen in fig. 5.7, although small deviations can still be seen around 1.5 MeV. From these cross sections it is possible to extract  $\Gamma_p = 19(3)$  eV. The implications of this are discussed in detail in the article.

The authors of ref. [118] were deeply involved with the NACRE compilation of astrophysical reaction rates [140]. In order to obtain a parameterization, they rescaled the results from refs. [115, 116] by a factor of  $\frac{3}{2}$ , while the unscaled results were used to obtain lower limits on the rate. The authors of NACRE noted a 20 % discrepancy for  $T_9 < 5$  compared to a previous evaluation [141], that most likely used the alternative normalization. In addition, they also remarked that the discrepancy was larger at higher temperatures. An updated evaluation, NACRE II, was published in 2013 [139] by a different group of authors. As such, they were not aware of the normalization issue and opted to use the Becker normalization while remarking: “*The origin of the large (and asymmetric) uncertainty given in NACRE for the lower limits is unclear.*” [139]. The impact of this wrong assessment can be gauged from fig. 5.8, which shows the recommended NACRE II rate in units of the recommended NACRE rate. The NACRE uncertainties are also shown. The lower limit corresponds to the normalization adopted by refs.[115, 116, 137]. From this, it can be estimated that the value recommended by NACRE II is off by as much as a factor of 2 depending on the temperature.

As a finishing remark, ref. [118] writes: “*The extrapolated  $S(E)$  factor at zero energy, offers a somewhat more optimistic prospect for  $^{11}\text{B}(p, 3\alpha)$* ”

as an advanced fusion fuel than previously envisioned.”. In fact multiple later investigations of the feasibility of  $^{11}\text{B}(p, 3\alpha)$  fusion have based their conclusions on these cross sections [142–145]. While it is difficult to gauge the specific effect in the various investigations, it is clear that a reduction of the primary reaction cross section by a factor of  $\frac{2}{3}$  will make it more difficult to achieve break even.

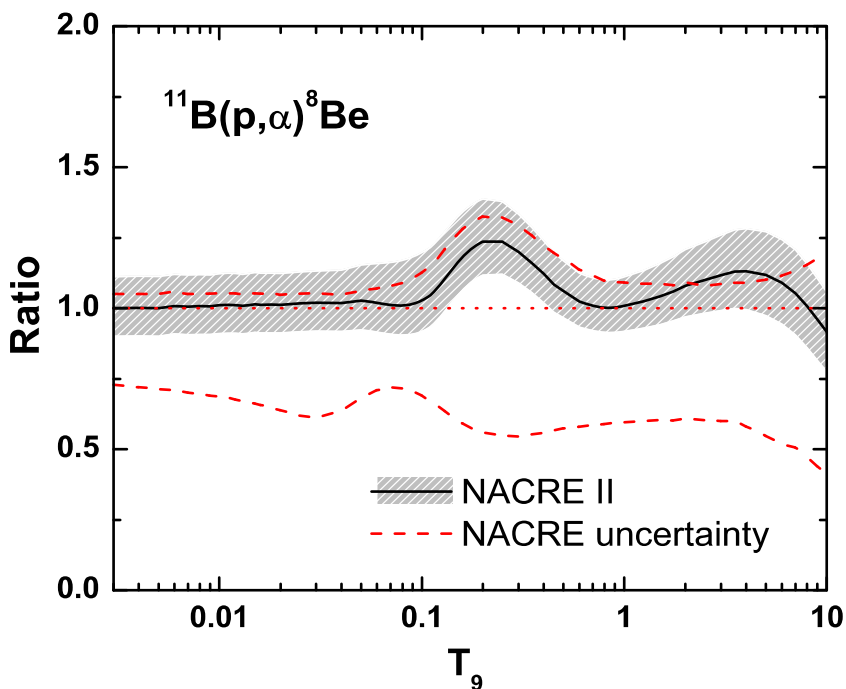


Figure 5.8: NACRE II [139] reaction rate in units of the NACRE [140] adopt value. The lower limit corresponds to the normalization of dividing by 3. As such, the recommended value by NACRE II is off by as much as a factor of 2. Figure from ref. [139].

## 5.6 Conclusion and outlook

In this experiment, the break-up of the 16.1 MeV state into three  $\alpha$  particles has been investigated using the  $p + {}^{11}\text{B}$  reaction and the  $\sigma_{p\alpha 0}$  and  $\sigma_{p\alpha 1}$  reaction cross sections were determined. The  $\alpha_0$  cross section was determined both from single-particle spectra and coincident detection of all three particles and the results were consistent. The  $\alpha_1$  cross section was only studied using coincident detection. The resulting cross section was consistent with ref. [137] and also with ref. [118] – provided the latter is scaled by a factor  $\frac{2}{3}$ . However, the present measurement is not consistent with the measurement by ref. [116]. If the entire dataset of ref. [118] is scaled in this manner it is in excellent agreement with ref. [116] above the 16.1 MeV resonance. From this measurement and the theoretical considerations of ref. [138] it is recommended that the NACRE and NACRE II reaction rates are revised.

From the four consistent measurements of  $\sigma_{p\alpha}$ , an improved value for the partial proton width  $\Gamma_p = 21.0(13)$  eV was derived. From this value, an improved partial  $\gamma_0$  width was derived. This is inconsistent with the direct measurement by ref. [146]. As the discrepancy cannot be explained, it is recommended that the experiment is repeated. It was also found that the  $\alpha$  yield reported by ref. [147] is most likely overestimated.

While rescaling the  $\alpha_1$  cross sections reported by ref. [118] by  $\frac{2}{3}$  resolves the  $\alpha_1$  discrepancies, there are still plenty of issues with the  $\alpha_0$  channel. In order to resolve these issues, data has been collected for the  $(p, \alpha)$  reaction with a proton energy from 0.5 to 3.5 MeV in steps of approximately 100 keV. The analysis of this is currently ongoing. In principle, this data could also be used to determine the  $\alpha_1$  cross section. However, in this analysis, it would be necessary to take the reaction mechanism into account. This is non-trivial if there are coherent contributions from several broad resonances. Essentially, one would fit eq. (5.3), expanded to include multiple initial states and multiple angular momenta, to the observed Dalitz plots. However, the first step in such an analysis would be to assess the impact of the reaction mechanism on the detection efficiency. Resolving these discrepancies would most likely have an impact on aneutronic fusion development [142–145] and

boron-based hadron therapy [148].

## 5.7 Contribution

I have been the principal investigator in all aspects of this work, including data collection, data analysis and writing the article. The implementation of the Balamuth reaction mechanism was made by Jonas Refsgaard. I made small changes to the code in order to optimize its speed.



# The partial widths of the 16.1 MeV $2^+$ resonance in $^{12}\text{C}$

Michael Munch<sup>a</sup> and Hans Otto Uldall Fynbo

Department of Physics and Astronomy, Aarhus University, Ny Munkegade 120, 8000 Aarhus C, Aarhus, Denmark

Received: 30 May 2018 / Revised: 22 July 2018

Published online: 27 August 2018

© The Author(s) 2018. This article is published with open access at Springerlink.com

Communicated by P. Woods

**Abstract.** The 16.1 MeV  $2^+$  resonance in  $^{12}\text{C}$  situated slightly above the proton threshold can decay by proton,  $\alpha$ , and  $\gamma$  emission. The partial width for proton emission cannot be directly measured due to the low proton energy and the small branching ratio. Instead it must be indirectly derived from other observables. However, due to several inconsistent data the derived partial width varies by almost a factor 2 depending on the data used. Here we trace the majority of this inconsistency to different measurements of the  $(p, \alpha)$  cross sections. We have remeasured this cross section using modern large area silicon strip detectors allowing to measure all final state particles, which circumvents a normalization issue affecting some of the previous measurements. Based on this we determine  $\Gamma_p = 21.0(13)$  eV. We discuss the implications for other observables related to the 16.1 MeV  $2^+$  resonance and for isospin symmetry in the  $A = 12$  system. In addition, we conclude that the dataset currently used for the NACRE and NACRE II evaluation of the  $^{11}\text{B}(p, 3\alpha)$  reaction should be scaled by a factor of 2/3. This impacts the reaction rate accordingly.

## 1 Introduction

Situated just above the proton threshold, the 16.1 MeV  $2^+$  state in  $^{12}\text{C}$  has been the subject of numerous studies [1–14] with the most recent compilation published in ref. [15] and a detailed review of the decay properties of the 16.1 MeV state given in ref. [12]. The state has primarily been investigated with the  $p + ^{11}\text{B}$  reaction and it is known to decay via proton,  $\alpha$  particle and  $\gamma$  ray emission as illustrated in fig. 1.

In one of the first applications of the concept of isospin, the narrow width of only roughly 5 keV of this state situated higher than 8 MeV in the  $3\alpha$  continuum was explained by Oppenheimer and Serber to be due to its  $T = 1$  nature [16]. Hence, its dominating  $\alpha$ -decay mode is only possible due to admixtures of  $T = 0$  in the state.

In the narrow resonance limit the measured cross sections,  $\sigma_{px}$ , can be related to the partial widths,  $\Gamma_x$ , of the resonance

$$\sigma_{px} = 4\pi\lambda^2\omega\frac{\Gamma_p\Gamma_x}{\Gamma^2}, \quad (1)$$

where  $\omega = \frac{2J+1}{(2j_0+1)(2j_1+1)}$  with  $J$  the resonance spin and  $j_i$  the spin of the beam and target.  $\lambda = \hbar/E$  is the reduced de Broglie wavelength with the center of mass energy,  $E$ .  $\Gamma_p$  has a key role in this relation, but due to the low proton energy and the fact that  $\Gamma_p/\Gamma \ll 1$ , it is not feasible to measure it directly. Instead,  $\Gamma_p$  must be inferred

from measurements of both  $\Gamma_x$  and  $\sigma_{px}$ . This extraction was performed in both refs. [12,15], however, the resulting proton widths differ by almost a factor of 2.

The decay properties of  $T = 1$  isobaric analog states in the  $A = 12$  system was analysed by Monahan *et al.* [17]. This analysis was based on a comparison of the proton widths in  $^{12}\text{C}$  with the neutron spectroscopic factors in  $^{12}\text{B}$  deduced from the  $^{11}\text{B}(d, p)^{12}\text{B}$  reaction. Good agreement was found for most states with the notable exception of the 16.1 MeV state. The discrepancy was traced to a too large value for the proton width. Recently the  $^{11}\text{B}(d, p)^{12}\text{B}$  reaction was remeasured with a new method which confirmed the spectroscopic factors deduced previously within 25% [18]. The proton width recommended by ref. [15] results in good agreement with this spectroscopic factor, while that of ref. [12] does not. In the following we will summarize the results of previous measurements and attempt to clarify the situation.

$\gamma$  ray emission predominantly occurs to the ground state (GS),  $\gamma_0$ , and the first excited state,  $\gamma_1$ , in  $^{12}\text{C}$ . The cross sections for the  $(p, \gamma)$  reactions were most recently measured by He *et al.* using a thin target for the first time [13]. Here they confirmed the prior cross section measurements [1,4,8,9,14,19,20] yielding a combined result of  $\sigma_{p\gamma_0} = 5.1(5) \mu\text{b}$  and  $\sigma_{p\gamma_1} = 139(12) \mu\text{b}$ . Thus we consider the values for these cross sections to be reliable. Complementary to these measurements, Friebel *et al.* directly measured  $\Gamma_{\gamma_0} = 0.346(41)$  eV using inelastically scattered electrons [10], while Cecil *et al.* have mea-

<sup>a</sup> e-mail: mm@phys.au.dk

**Table 1.** Prior measurements of the  $(p, \alpha)$  channel.

Measurement	$\sigma_{\alpha,0}$ [mb]	$\sigma_{\alpha,1}$ [mb]	$\sigma_{\alpha}$ [mb]	$\sigma_{\alpha,1}/\sigma_{\alpha,0}$	$\Gamma$ [keV]
Huus <i>et al.</i> [1]					$\sim 5$
Beckman <i>et al.</i> [2]	$0.2 \pm 30\%$ <sup>a</sup>	$10 \pm 30\%$ <sup>a</sup>			
Segel <i>et al.</i> [3]				22(3)	
Anderson <i>et al.</i> [4]			41(3) <sup>b</sup>		6.7
Davidson <i>et al.</i> [5]			54(6)		$5.2^{+0.5}_{-0.3}$
Becker <i>et al.</i> [6]	$2.12 \pm 5\%$	$69.6 \pm 5\%$ <sup>c</sup>		33(2)	5.3(2)
Laursen <i>et al.</i> [7]				19.6(19)	

<sup>a</sup> The authors note that the  $\alpha$  particles were “barely detectable” [2]. This result will be disregarded.

<sup>b</sup> Assuming infinite target thickness and using the combined  $\Gamma$  of refs. [4,6] this should be rescaled from 38.5(32) mb.

<sup>c</sup> The authors note that their model did *not* reproduce the  $\alpha_1$  data.

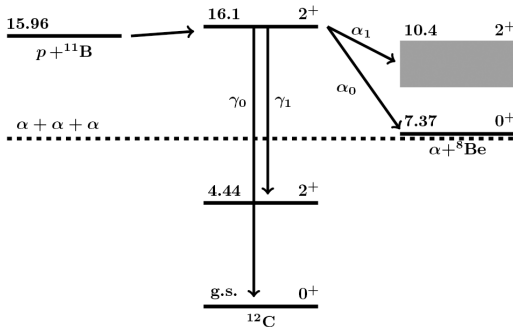


**Fig. 1.** Illustration of the reaction scheme. The 16.11 MeV  $2^+$  state  $^{12}\text{C}$  is populated with the  $p + ^{11}\text{B}$  reaction. The state can either decay via  $\gamma$ ,  $\alpha$  or proton emission. Energies and spin assignments are taken from ref. [15]. Energies are in MeV.

sured the relative yield of  $\gamma$  rays and charged particles;  $\Gamma_{\gamma 0}/\Gamma_{\alpha} = 6.7(3) \times 10^{-5}$  and  $\Gamma_{\gamma 1}/\Gamma_{\alpha} = 2.0(3) \times 10^{-3}$  [8].

The current understanding of the  $\alpha$  particle decay mechanism is a sequential decay proceeding either through the  $^8\text{Be}$  GS,  $\alpha_0$ , or the first excited state,  $\alpha_1$  [7]. The results of prior investigations of the  $(p, \alpha)$  channel are listed in table 1. There are multiple consistent measurements for the resonance width and combining the results from refs. [5,6] yields 5.28(18) keV. As these are extracted from a simple resonance scan we consider them reliable. Two out of three measurements of the  $\alpha_1/\alpha_0$  branching ratio are consistent and, as the measurement by Laursen *et al.* was done with coincident detection of multiple final state particles, we also consider the branching ratio reliable. The measured total cross sections for  $(p, \alpha)$  generally show poor agreement. However, considering the  $(p, \alpha_0)$  reaction yields a distinct high energy peak we expect the  $\sigma_{p,\alpha 0}$  measurement by Becker *et al.* to be accurate [6].

By combining the various measurements for the  $\alpha$ - and  $\gamma$  channels with eq. (1) and approximating  $\Gamma \approx \Gamma_{\alpha}$  it is possible to derive several independent values for  $\Gamma_p$ . These are listed in table 2. Interestingly, the values seem to

**Table 2.** Calculated values for  $\Gamma_p$ . The values are calculated using eq. (1) with the quantities listed in the left column. In all cases  $\Gamma = 5.28(18)$  keV was also used. The approximation  $\Gamma_{\alpha} \approx \Gamma$  was applied.

Method	$\Gamma_p$ [eV]
$\sigma_{p\alpha}$ [4]	20(2)
$\sigma_{p\alpha 0}$ [6] + $\Gamma_{\alpha 1}/\Gamma_{\alpha 0}$ [3,7]	22(3)
$\sigma_{p\alpha}$ [5]	26(3)
$\sigma_{p\alpha}$ [6]	34(6)
$\sigma_{p\gamma 1}$ [13] + $\Gamma_{\gamma 1}/\Gamma_{\alpha}$ [8]	35(3)
$\sigma_{p\gamma 0}$ [13] + $\Gamma_{\gamma 0}/\Gamma_{\alpha}$ [8]	37(6)
$\sigma_{p\gamma 0}$ [13] + $\Gamma_{\gamma 0}$ [10]	38(6)

cluster into two groups, with the measurements for  $(p, \alpha)$  split across the groups.

All of the cross section measurements of the  $(p, \alpha)$  channel were performed with a small energy sensitive detector placed at various angles. The measured energy spectrum was then extrapolated to 0 and integrated. References [4,5] performed a linear extrapolation, while ref. [6] used a sequential decay model. Although Becker *et al.* note their model performed poorly at this resonance, it does *not* explain the discrepancy between the measurements. The key difference is the choice of normalization for the  $\alpha_1$  measurement where Becker *et al.* argue that their detector has either detected the primary alpha particle  $\alpha_1$  or the two secondary  $\alpha$  particles from the subsequent  $^8\text{Be}$  break-up. Thus, they divide their count number by 2. On the contrary, refs. [4,5] argue they observe one out three final state  $\alpha$  particles and divide by a factor of 3. The probability for detecting both secondary  $\alpha$  particles in a single detector was discussed theoretically by Wheeler in 1941 [21]. The probability depends on the opening angle between the secondary  $\alpha$  particles and the aperture of the detector. The opening angle in turn depends on the energy of the  $^8\text{Be}$  system with respect to the  $\alpha$  threshold. This is small for the  $^8\text{Be}$  GS but quite significant for the first excited state. Based on information provided in ref. [6] we have estimated their maximum detector aperture to be of

the order of  $3^\circ$ . In this case the probability for a double hit is minuscule—even for the  $\alpha_0$  channel. Thus, the  $\alpha_1$  results by Becker *et al.* should most likely be scaled by a factor of  $2/3$  making it consistent with the other two measurements. The astrophysical NACRE evaluation [22] explicitly mentions this discussion in their  $^{11}\text{B}(p, 3\alpha)$  evaluation, where they use the dataset of Becker *et al.* for its recommended value while using the dataset of refs. [5, 23] as a lower limit. The updated evaluation NACRE II [24] is less cautious and relies solely on Becker *et al.*

The magnitude of the  $\sigma_{p\alpha}$  cross section has implications beyond nuclear structure. For example the  $^{11}\text{B}(p, 3\alpha)$  reaction is a candidate for a fusion reaction generating energy without neutrons in the final state, see *e.g.* [25]. The rate of this reaction at the energies relevant for a fusion reactor is mainly determined by the 16.1 MeV  $2^+$  and the higher lying 16.6 MeV  $2^-$  resonances. The proton width is related to the  $^{11}\text{B}(d, p)^{12}\text{B}$  reaction by isospin symmetry. In turn, that reaction is used to deduce the  $^{11}\text{B}(n, \gamma)^{12}\text{B}$  reaction cross section, which may play a role in the astrophysical r-process [18].

The object of this paper is to remeasure  $\sigma_{p\alpha}$  in order to clarify the situation. The measurement will circumvent the normalization ambiguity by observing all three particles in coincidence using an array of large area segmented silicon detectors. In this paper we will only address the cross section of the 16.1 MeV state, but the discussion on normalization applies universally to all measurements of this reaction, where the cross section is inferred from a single detector.

## 2 Experiment

A thin foil of  $^{11}\text{B}$ , oriented  $45^\circ$  with respect to the beam axis, was bombarded with a beam of  $\text{H}_3^+$  molecules. A resonance scan was conducted between 460 and 600 keV and afterwards data was collected for 30 hours at 525 keV. The beam was provided by the 5 MV Van de Graaff accelerator at Aarhus University and the beam spot was defined by a pair of  $1 \times 1$  mm vertical and horizontal slits. The energy of the accelerator was prior to the experiment energy calibrated using narrow  $(p, \alpha)$  resonances in  $^{27}\text{Al}$  and the energy resolution was found to be better than a few keV for single charged beams. It should be noted that the energy stability is trifold improved for  $\text{H}_3^+$ .

Upon impact with the target foil the  $\text{H}_3^+$  molecules will break up and additional electron stripping, neutralization and scattering might occur. This affected the integrated beam current, which was measured with a Faraday cup 1 m downstream of the target. The combined effect of this can be determined from the ratio of the observed current both with and without a target foil in the beam. At the beginning of the experiment the effective charge state was determined to be  $1.72(5)e$ . However, this ratio was observed to change during the experiment. We attribute this to carbon build-up on the target. The change in charge state was  $4.33(4) \times 10^{-3} \mu\text{C}^{-1}$ . Correcting for this, a total of  $61(6) \mu\text{C}$  was collected on the resonance.

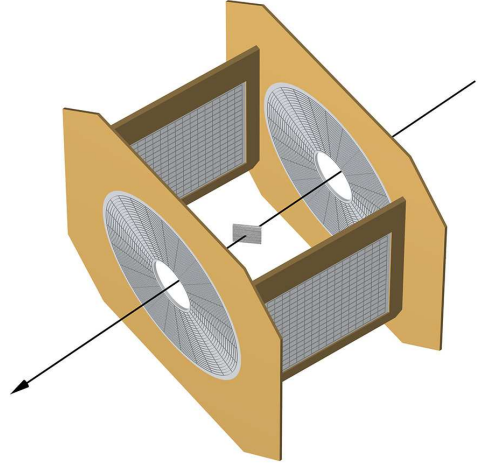


**Fig. 2.** Schematic drawing of the experimental setup. An arrow indicates the incoming proton beam. The enriched boron target was oriented  $45^\circ$  with respect to the beam axis. Two quadratic and two annular double sided silicon strip detector were used to detect outgoing particles. Front and back segmentation is shown simultaneously for clarity.

The target was produced at Aarhus University by evaporation of 99% enriched  $^{11}\text{B}$  onto a  $4 \mu\text{g}/\text{cm}^2$  carbon backing. The thickness was measured by bombarding the target with 2 MeV  $\alpha$  particles and the boron layer either facing towards or away from the beam. Assuming a two layer target the boron thickness can be inferred from the energy shift of particles scattered off the carbon layer using the procedure of ref. [26], but including a correction for the changed stopping power of the scattered particle.

$$t = \frac{\delta E}{K(\theta)S(E_b) + S(K(\theta)E_b)/\cos\theta}, \quad (2)$$

where  $E_b$  the beam energy,  $S$  the stopping power,  $\delta E$  the energy difference and  $K$  is the kinematic factor for the laboratory scattering angle,  $\theta$ , defined as

$$K = \frac{m_b \cos\theta + \sqrt{m_t^2 - m_b^2 \sin^2\theta}}{m_b + m_t}, \quad (3)$$

where  $m_t$ ,  $m_b$  is the mass of the target and beam ion respectively. The cosine factor in eq. (2) corrects for the increased path length for the scattered particle. The result is  $39(3) \mu\text{g}/\text{cm}^2$ . The energy loss for a 525/3 keV proton through this target is 23(2) keV according to the SRIM stopping power tables [27].

Charged particles were observed with an array of double sided silicon strip detectors (DSSD) giving a simultaneous measurement of position and energy. A sketch of the array can be seen on fig. 2. The array consisted of two annular DSSD (S3 from Micron Semiconductors) placed 36 mm up- and downstream of the target; covering the angles between 140 and 165° and 23 and 36° respectively. Each annular ring is approximately 1 mm wide with

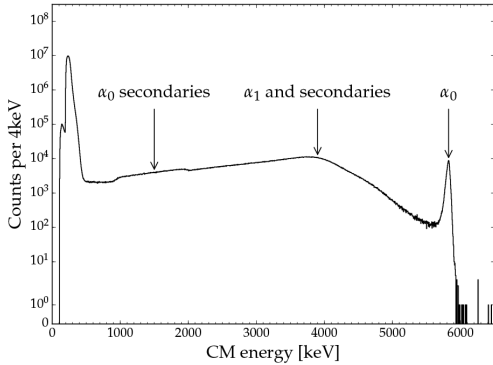


**Fig. 3.** Full CM energy spectrum without any cuts. The high energy peak corresponds to the primary  $\alpha$  particle,  $\alpha_0$ .

an approximate  $2^\circ$  resolution in polar angle. Additionally, two quadratic DSSDs (W1 from Micron Semiconductors) were placed 40 mm from the target center at an angle of  $90^\circ$  with respect to the beam axis. These covered angles between  $60^\circ$  and  $120^\circ$ . All pixels are  $3 \times 3$  mm with an approximate angular resolution of  $4^\circ$ .

### 3 Analysis

The analysis is structured in the following way. First a resonance scan is shown for the  $\alpha_0$  channel. This is followed by an extraction of the  $\alpha_0$  angular distribution and cross section from the multiplicity 1 data. Building upon this follows the analysis of the triple events, *i.e.* events with exactly three alpha particles and afterwards a brief discussion of how the detection efficiencies for the  $\alpha_0$  and  $\alpha_1$  channel have been determined.

#### 3.1 Singles analysis

Assuming all ejectiles to be  $\alpha$  particles the center-of-mass (CM) energy can be determined from the detected position and energy. The full spectrum, without any cuts, is shown in fig. 3. The spectrum shows a clear peak at 5.8 MeV, which is consistent with a sequential decay of the 16.1 MeV state via the GS of  $^8\text{Be}$ . The  $\alpha$  particle giving rise to this peak will be referred to as the primary  $\alpha$  particle. Below the peak is a broad asymmetric distribution, which consists of secondary  $\alpha$  particles and  $\alpha$  particles from the break-up via the first excited state of  $^8\text{Be}$ . At low energy the proton peak is visible. It is double peaked since energy loss corrections are applied as if it was an  $\alpha$  particle.

The primary  $\alpha$  particle is selected by requiring  $E_{\text{CM}} > 5.65$  MeV. Figure 4 shows the  $\alpha_0$  yield as a function of proton energy. The yield is clearly resonant and peaks at  $\sim 175$  keV. The curve shown in the figure is the best

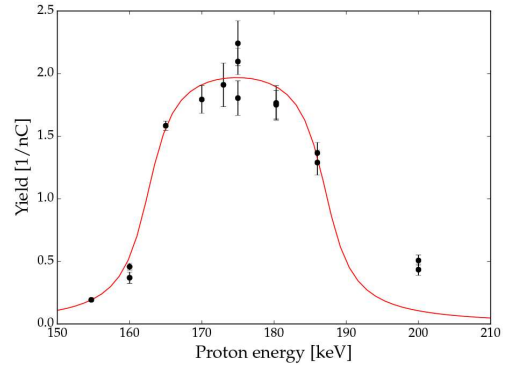


**Fig. 4.** Scan of the 162 keV resonance. The individual data points corresponds to the  $\alpha_0$  yield, while the solid curve is the best fit to eq. (4).

fit to the thick target yield for a Breit-Wigner shaped resonance [28]

$$Y = \left[ \tan^{-1} \frac{E_p - E_r}{\Gamma_{\text{lab}}/2} - \tan^{-1} \frac{E_p - E_r - \Delta E}{\Gamma_{\text{lab}}/2} \right] \times \frac{\Gamma_{\text{lab}} \sigma_{\text{BW}}(E = E_r)}{2\epsilon} \eta, \quad (4)$$

where  $\Gamma_{\text{lab}}$  is the resonance width in the lab system,  $E_p$  is the beam energy,  $E_r$  the resonance energy,  $\Delta E$  the energy loss through the target,  $\eta$  the detection efficiency,  $\sigma_{\text{BW}}$  the resonant Breit-Wigner cross section and  $\epsilon = \frac{1}{N} \frac{dE}{dx}$ , where  $N$  is the number density of target nuclei and  $\frac{dE}{dx}$  the stopping power. Using the factor outside the parenthesis as an arbitrary scaling factor, the best fit was achieved with  $\Delta E = 24.5(9)$  keV,  $E_r = 162.6(5)$  keV and  $\Gamma_{\text{lab}}$  fixed to  $12/11 \cdot 5.28$  keV. The target thickness is consistent with the result obtained from  $\alpha$ -scattering and the resonance energy fits with the recommended literature value [20].

The  $\alpha_0$  angular distribution relative to the beam axis was extracted for the long runs at  $E_p = 175$  keV. The angular distribution, corrected for solid angle, can be seen in fig. 5. The solid line shows the best fit to the lowest five Legendre polynomials.

$$W(\theta) = A \left[ 1 + \sum_{i=1}^4 a_i P_i(\cos \theta) \right]. \quad (5)$$

The coefficients providing the best fit are  $a_1 = -0.358(7)$ ,  $a_2 = 0.249(2)$ ,  $a_3 = -0.106(11)$ ,  $a_4 = -9(20) \times 10^{-3}$  and  $A = 4.253(17) \times 10^4 \text{ sr}^{-1}$ . The lower panel of the figure shows the fit rescaled,  $W(90^\circ) = 1$ , along with the data from refs. [5, 6], which have been rescaled to coincide with the fit at  $90^\circ$ . Good agreement is observed with ref. [5] while the symmetric behavior seen by ref. [6] cannot be reproduced.

The total number of counts is found by integration of eq. (5), *i.e.*  $4\pi A$ . This can be related to the resonant Breit-Wigner cross section using eq. (4)

$$\sigma_{p\alpha,0} = 2.1(2) \text{ mb}. \quad (6)$$

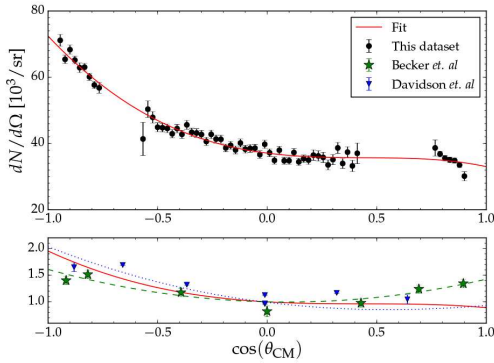


**Fig. 5.** Angular distribution of this dataset corrected for solid angle along with the best fit to eq. (5). The datasets of refs. [5,6] have been rescaled to coincide with the fit at  $90^\circ$ .

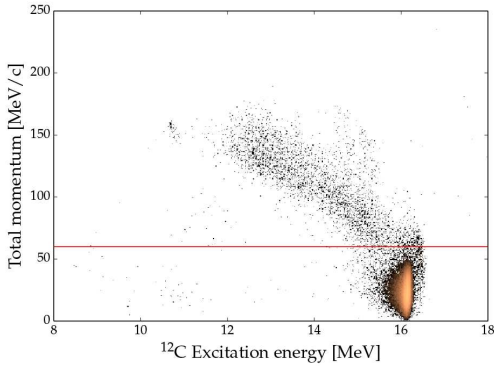


**Fig. 6.** Total momentum of the three particles in the CM vs. the calculated excitation energy of  $^{12}\text{C}$ . The red line corresponds to the cut placed at 60 MeV/c.

The main uncertainty is the variation in the effective charge state.

### 3.2 Extraction of triple events

The end goal of this analysis step is to extract tuples of particles consistent with a decay of the 16.1 MeV state in  $^{12}\text{C}$  into three  $\alpha$  particles. It applies the methods described in ref. [29].

The first and simplest requirement is that at least three particles must be detected in an event. This massively reduces the data, since the majority of events consist of elastically scattered protons. Furthermore, it is required that all three particles are detected within 30 ns of each other. This reduces the background from random coincidences with protons significantly while  $> 99\%$  of good events survive. Additionally, it is required that the sum of CM angles between the CM position vectors must be larger than  $350^\circ$ . All particles surviving these cuts are assumed to be  $\alpha$  particles. From the detected energy and position

it is possible to calculate the four momentum of each particle. From these, one can calculate the total momentum in the CM and the  $^{12}\text{C}$  excitation energy. This is shown in fig. 6, which has a distinct peak at 16.1 MeV. Interestingly, weak peaks are visible at low total momentum and excitation energy lower than 16.1 MeV. These correspond to  $\gamma$  transitions in  $^{12}\text{C}$  as observed in ref. [12]. Projecting the individual energy of the high momentum events it is clear that these correspond to events with one proton and two  $\alpha$  particles. Hence, all events with  $p_{\text{CM}} > 60$  MeV/c are removed.

The classification of whether a tuple corresponds to a decay via the GS or first excited state, can be done based on whether the CM energy of the most energetic particle lies within the high energy peak in fig. 3. This is the same cut used in sect. 3.1. With this classification the count numbers for the two channels are

$$N_0 = 3.318(18) \times 10^4 \quad (7)$$

$$N_1 = 4.33(2) \times 10^4, \quad (8)$$

where the uncertainties are due to counting statistics.

### 3.3 Detection efficiency of the $\alpha_0$ channel

In order to relate the observed number of counts to a yield it is necessary to determine the detection efficiency. For the ground state this is simple. A beam with a  $1 \times 1$  mm profile was generated and propagated to a random depth in the target. Here  $\alpha_0$  was generated and emitted according to the observed angular distribution in fig. 3. The secondary particles were ejected isotropically according to conservation of angular momentum. These particles were propagated out of the target and into the detectors. Energy loss was taken into account using the SRIM energy loss tables [27]. The output of the simulation had a structure which was identical to the data and was thus subjected to the same analysis. From the survival ratio an acceptance was determined

$$\eta_0 = 7.1(3)\%. \quad (9)$$

Correcting for the efficiency gives a cross section of

$$\sigma_{p\alpha,0} = 2.0(2) \text{ mb}, \quad (10)$$

which is consistent with the singles analysis.

### 3.4 Detection efficiency of the $\alpha_1$ channel

The detection efficiency depends heavily on the  $^8\text{Be}$  excitation energy as it determines the opening angle between the secondary  $\alpha$  particles. Laursen *et al.* found that their sequential decay model fully described their data [7]. Thus, events were generated using this model. Propagation and energy loss was done with the same procedure as described in the previous section. From the survival ratio the acceptance was determined to be

$$\eta_1 = 0.49(5)\%. \quad (11)$$

This yields a cross section to the excited channel of

$$\sigma_{p\alpha,1} = 38(5) \text{ mb}. \quad (12)$$

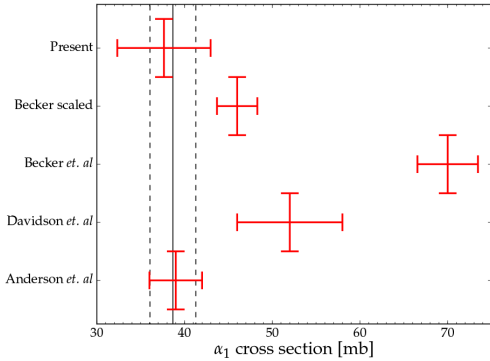


**Fig. 7.** Comparison of the present  $\alpha_1$  cross section with the measurement of refs. [4–6]. Becker scaled is the data from ref. [6] scaled by 2/3. The full line is the mean recommended value while the dashed lines show the one sigma limit. See text for details.

## 4 Discussion

Both values determined for the  $\alpha_0$  cross section are consistent with the measurement by Becker *et al.* The weighted cross section is

$$\sigma_{p\alpha,0} = 2.03(14) \text{ mb.} \quad (13)$$

Comparing the angular distribution in fig. 5 with previous measurements, good agreement is observed for the region around 90 deg. However, while ref. [6] finds the distribution to be nearly symmetric around 90 deg, this conclusion is not supported by the present measurement or ref. [5]. Importantly, the integrated cross section is not very sensitive to the large angle behavior, which explains the good agreement obtained nevertheless.

In order to compare  $\sigma_{p\alpha,1}$  between the different measurements, it is computed as  $\sigma_{p\alpha,1} = \sigma_{p\alpha} - \sigma_{p\alpha,0}$  for refs. [4, 5]. The result is shown in fig. 7 along with the present  $\alpha_1$  cross section and that of ref. [6]. From the figure the excellent agreement between the present measurement and ref. [4] can be observed. Both values deviate more than  $2\alpha$  from the measurement of ref. [5]. We suspect this is due to an overall normalization problem in ref. [5]. The original measurement by ref. [6] differs significantly from all other measurements, but if rescaled by a factor 2/3, corresponding to the different normalization choice, the data point is in agreement within the errors. However, in light of the systematic problems reported by ref. [6] for the 16.1 MeV resonance the value is not included in the recommended value<sup>1</sup>. Instead the recommended  $\alpha_1$  cross section is based on the results from the present experiment and ref. [4]

$$\sigma_{p\alpha,1} = 39(3) \text{ mb.} \quad (14)$$

<sup>1</sup> The short-comings of their model at the 16.1 MeV resonance is due to them neglecting interference terms by summing incoherently over different  $\alpha$  permutations. The importance of interference was demonstrated in the work of refs. [30,31].

Similarly the recommended total  $\alpha$  cross section is

$$\sigma_{p\alpha} = 41(3) \text{ mb.} \quad (15)$$

The ratio of the two  $\alpha$  channels from the present measurement is 19(3), which is consistent with both previous measurements. Combining all three measurements yields

$$\frac{\sigma_{p\alpha,1}}{\sigma_{p\alpha,0}} = 19.9(14). \quad (16)$$

## 5 Derived partial widths

Using the present measurement of the  $(p, \alpha)$  cross section the partial proton width can be determined using eq. (1)

$$\Gamma_p = 19(3) \text{ eV,} \quad (17)$$

while using the combined cross section yields

$$\Gamma_p = 19.7(13) \text{ eV.} \quad (18)$$

Both values are consistent, within the errors, with that of the latest compilation [15], but not with the value favored in the recent review in ref. [12].

Combining this proton width with the results of He *et al.* and  $\Gamma$ , the partial gamma widths can be determined

$$\Gamma_{\gamma 0} = 0.66(9) \text{ eV} \quad (19)$$

$$\Gamma_{\gamma 1} = 18(2) \text{ eV.} \quad (20)$$

These values are consistent with the latest compilation [15], but inconsistent with a direct measurement using inelastically scattered electrons, which measured  $\Gamma_{\gamma 0} = 0.346(41) \text{ eV}$  [10]. While direct measurements should generally be favored, in this case there is multiple independent and consistent measurements of the remaining parameters. In order to resolve this discrepancy we suggest that  $\Gamma_{\gamma 0}$  is remeasured in a direct manner. The argument in the recent review hinged on this value being correct [12].

Combining the improved total  $\alpha$  cross section with the  $\gamma$  cross sections measured by He *et al.* the branching ratio can be determined

$$\frac{\Gamma_{\gamma 0}}{\Gamma_{\alpha}} = 1.18(13) \times 10^{-5} \quad (21)$$

$$\frac{\Gamma_{\gamma 1}}{\Gamma_{\alpha}} = 3.2(3) \times 10^{-3}, \quad (22)$$

which is inconsistent with the measurement by Cecil *et al.* Considering the general spread of the measured  $\alpha$  cross sections, the most likely explanation for this discrepancy is that Cecil *et al.* have overestimated the  $\alpha$  yield.

Using the updated proton width the ratio between the reduced proton and neutron width can be computed. The analysis in ref. [17] was performed with  $\Gamma_p = 69 \text{ eV}$  and an updated value can be computed by scaling accordingly

$$\frac{\gamma_n^2}{2\gamma_p^2} = 0.63. \quad (23)$$

This shows a similar degree of isopin symmetry as the other bound states analysed in the  $A = 12$  system [17].

## 6 Conclusion

Using the  $p + {}^{11}\text{B}$  reaction, the break-up of the 16.1 MeV state in  ${}^{12}\text{C}$  into three  $\alpha$  particles has been studied using an array of large area segmented silicon detectors in close geometry. The decay via the ground state of  ${}^8\text{Be}$  has been studied both with detection of single particles and coincident detection of all three  $\alpha$  particles. The derived cross sections are internally consistent and the combined result is

$$\sigma_{p\alpha,0} = 2.03(14) \text{ mb}, \quad (24)$$

which is consistent with the result of ref. [6].

Currently, there exist multiple incompatible measurements of the decay via the first excited state of  ${}^8\text{Be}$ . This channel was studied using coincident detection of all three  $\alpha$  particles. The coincidence acceptance was determined using the decay model of ref. [7] yielding a model dependent cross section

$$\sigma_{p\alpha,1} = 38(5) \text{ mb}. \quad (25)$$

which is, within the errors, consistent with ref. [4] but not refs. [5, 6].

The inconsistency with ref. [6] is due to their claim of having a substantial chance of detecting two out of three particles with a single detector. This was discussed based on ref. [21]. The chance of this is minuscule and hence the entire  $\alpha_1$  dataset of ref. [6] should be rescaled by a factor 2/3. This has a significant impact on the recommended astrophysical reaction rate, as both NACRE [22] and NACRE II [24] have based their recommended values on the dataset provided by ref. [6]. The recommended reaction rate should thus be scaled accordingly. In addition, this also has implications for the expected yield from an aneutronic fusion reactor.

Combining the present measurement of  $\sigma_{p\alpha}$  with that of ref. [4] a refined partial proton width of  $\Gamma_p = 19.7(13)$  eV was deduced. This in turn, was used to determine the partial gamma widths  $\Gamma_{\gamma 0} = 0.68(8)$  eV and  $\Gamma_{\gamma 1} = 18(2)$  eV, using the combined  $\gamma$  cross sections reported by ref. [13]. The value for  $\Gamma_{\gamma 0}$  differs by roughly a factor of 2 from the direct measurement of ref. [10]. Hence, we recommend that  $\Gamma_{\gamma 0}$  is remeasured. Based on these results, we can no longer recommend the proton width deduced in ref. [12].

Additionally, improved  $\gamma$ - $\alpha$  branching ratios are derived. These are roughly a factor of 2 larger than the measurements published by ref. [8]. We speculate that this discrepancy is most likely due to ref. [8] having overestimated the  $\alpha$  yield.

The recommended value for the proton width can be compared to the spectroscopic factor for the analog state in  ${}^{12}\text{B}$ . By using the analysis presented in [17] the ratio of the corresponding reduced widths is 0.63, which shows a similar degree of isopin symmetry as the other bound states analysed in the  $A = 12$  system. A modern calculation of the proton width would be highly interesting.

We would like to thank Folmer Lyckegaard for manufacturing the target. We also acknowledge financial support from the European Research Council under ERC starting grant LOBENA, No. 307447.

**Open Access** This is an open access article distributed under the terms of the Creative Commons Attribution License (<http://creativecommons.org/licenses/by/4.0>), which permits unrestricted use, distribution, and reproduction in any medium, provided the original work is properly cited.

## References

1. T. Huus, R.B. Day, Phys. Rev. **91**, 599 (1953).
2. O. Beckman, T. Huus, Č. Zupanič, Phys. Rev. **91**, 606 (1953).
3. R.E. Segel, M.J. Bina, Phys. Rev. **124**, 814 (1961).
4. B. Anderson, M. Dwarakanath, J. Schweitzer, A. Nero, Nucl. Phys. A **233**, 286 (1974).
5. J.M. Davidson, H.L. Berg, M.M. Lowry, M.R. Dwarakanath, A.J. Sierk, P. Batay-Csorba, Nucl. Phys. Sect. A **315**, 253 (1979).
6. H.W. Becker, C. Rolfs, H.P. Trautvetter, Z. Phys. A At. Nucl. **327**, 341 (1987).
7. K.L. Laursen, H.O.U. Fynbo, O.S. Kirsebom, K.O. Madsbøl, K. Riisager, K.S. Madsbøll, K. Riisager, Eur. Phys. J. A **52**, 271 (2016) arXiv:1604.01244.
8. F. Cecil, D. Ferg, H. Liu, J. Scorby, J. McNeil, P. Kunz, Nucl. Phys. A **539**, 75 (1992).
9. E.G. Adelberger, R.E. Marrs, K.A. Snover, J.E. Bussolletti, Phys. Rev. C **15**, 484 (1977).
10. A. Friebel, P. Manakos, A. Richter, E. Spamer, W. Stock, O. Titze, Nucl. Phys. A **294**, 129 (1978).
11. S. Stave, M. Ahmed, R. France, S. Henshaw, B. Müller, B. Perdue, R. Prior, M. Spraker, H. Weller, Phys. Lett. B **696**, 26 (2011).
12. K.L. Laursen, H.O.U. Fynbo, O.S. Kirsebom, K.S. Madsbøll, K. Riisager, Eur. Phys. J. A **52**, 370 (2016) arXiv:1610.00509.
13. J.J. He, B.L. Jia, S.W. Xu, S.Z. Chen, S.B. Ma, S.Q. Hou, J. Hu, L.Y. Zhang, X.Q. Yu, Phys. Rev. C - Nucl. Phys. **93**, 1 (2016).
14. D.S. Craig, W.G. Gross, R.G. Jarvis, Phys. Rev. **103**, 1414 (1956).
15. J. Kelley, J. Purcell, C. Sheu, Nucl. Phys. A **968**, 71 (2017).
16. J.R. Oppenheimer, R. Serber, Phys. Rev. **53**, 636 (1938).
17. J.E. Monahan, H.T. Fortune, C.M. Vincent, R.E. Segel, Phys. Rev. C **3**, 2192 (1971).
18. H.Y. Lee, J.P. Greene, C.L. Jiang, R.C. Pardo, K.E. Rehm, J.P. Schiffer, A.H. Wuosmaa, N.J. Goodman, J.C. Lighthall, S.T. Marley *et al.*, Phys. Rev. C **81**, 015802 (2010).
19. F. Ajzenberg, T. Lauritsen, Rev. Mod. Phys. **24**, 321 (1952).
20. F. Ajzenberg-Selove, Nucl. Phys. A **506**, 1 (1990).
21. J.A. Wheeler, Phys. Rev. **59**, 27 (1941).
22. C. Angulo, M. Arnould, M. Rayet, P. Descouvemont, D. Baye, C. Leclercq-Willain, A. Coc, S. Barhoumi, P. Aguer, C. Rolfs *et al.*, Nucl. Phys. A **656**, 3 (1999).
23. R.E. Segel, S.S. Hanna, R.G. Allas, Phys. Rev. **139**, B818 (1965).

24. Y. Xu, K. Takahashi, S. Goriely, M. Arnould, M. Ohta, H. Utsunomiya, Nucl. Phys. A **918**, 61 (2013).
25. D. Moreau, Nucl. Fusion **17**, 13 (1977).
26. M. Chiari, L. Giuntini, P. Mandò, N. Taccetti, Nucl. Instrum. Methods Phys. Res. Sect. B **184**, 309 (2001).
27. J.F. Ziegler, M.D. Ziegler, J.P. Biersack, Nucl. Instrum. Methods Phys. Res. B **268**, 1818 (2010).
28. W.A. Fowler, C.C. Lauritsen, T. Lauritsen, Rev. Mod. Phys. **20**, 236 (1948).
29. M. Alcorta, O. Kirsebom, M. Borge, H. Fynbo, K. Riisager, O. Tengblad, Nucl. Instrum. Methods Phys. Res. Sect. A **605**, 318 (2009).
30. G.C. Phillips, Rev. Mod. Phys. **37**, 409 (1965).
31. K. Schäfer, Nucl. Phys. A **140**, 9 (1970).



**Part II**

**Technique**



## AUSALib

The Aarhus Subatomic group and I are involved in a variety of different experiments. In addition to the experiments reported on here, the group also conducts a fair amount of experiments at the ISOLDE facility at CERN. The experiments range from  $\gamma$ -delayed  $\alpha$ -break-up at low energies to high energy reactions with post-accelerated beams at the HIE ISOLDE facility. While the physics is rather different, the experimental technique is often similar. A collection of double-sided silicon strip detectors (DSSD) and single-sided silicon strip detectors (SSSD) are placed in some geometry around an interaction center. Additional auxiliary detectors might also be used occasionally.

The signals from these detectors are recorded by the data acquisition system (DAQ) using peak sensing Analog to Digital Converter (ADC) and Time to Digital Converter (TDC). As such there is a large overlap in the structure of these different datasets, how they must be processed and the task that must be performed in order to analyze them. For details on the DAQ see chapter 7. The previous modus operandi was that each new analyst started essentially from scratch. This ensures the analyst knows all the gory details of the analysis, but considering the non-trivial task at hand, this is error-prone and slow. Based on this observation it was decided to build a common analysis framework.

The main powers of **AUSALib** come from its abstraction of detectors, specifically their geometry and the concept of an analysis pipeline. This

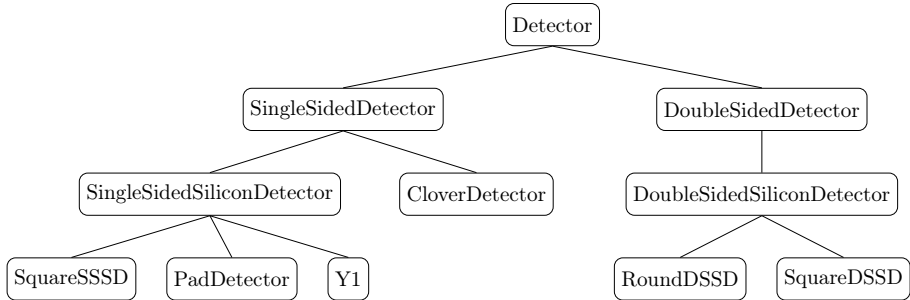


Figure 6.1: **AUSALib** detector hierarchy. The analyst will usually only work directly with the single or double-sided detector abstraction.

chapter will focus on these aspects. In the end, I will show how this facilitates near automatic energy calibration.

## 6.1 Detector abstraction

The detector abstraction provided by **AUSALib** is a description of the geometric properties of the detector and its calibration. It is thus not coupled with the data provided by the detector. Roughly speaking there is a finite but large number of different detector models, but these can be arranged in an infinite number of different constellations. **AUSALib** abstracts these models down to two superclasses: single or double-sided detectors. This is heavily motivated by silicon detectors, which usually are either segmented on one or two surfaces. Figure 6.1 shows the resulting inheritance diagram, where the leaves correspond to specific detector types e.g. SquareDSSD is the W1 detectors used for most of the experiments in the previous chapters. As shown in the figure, this abstraction is also able to encompass germanium (clover) detectors.

As seen in e.g. chapter 5, an important observable when working with multi-particle final states is the individual and combined momentum of the final state particles. In order to calculate this, the position of each detector

segment<sup>1</sup> must be known. The superclasses expose an interface, where the position of a segment can be calculated for a given 1D or 2D index. It is up to the specific detector model to implement this geometry model. Figure 6.2 shows an illustration of the models used for square and round DSSDs. While their geometry is quite different their position and orientation in space can be specified by three vectors: central position, normal and orientation. Both models are generic and can calculate the geometry for a given number of front and back strips and different strip pitch. Hence, SquareDSSD is the **AUSALib** model used for both the W1 and BB7 detectors, which consist of  $16 \times 16$  and  $32 \times 32$  strips respectively.

The flexibility of this approach was illustrated when the wedge-shaped detector YY1 from Micron Semiconductor Ltd. [149] was added a few years after the inception of **AUSALib**. This was simply a matter of adding another class to **AUSALib** and required no changes to the remaining code. This is

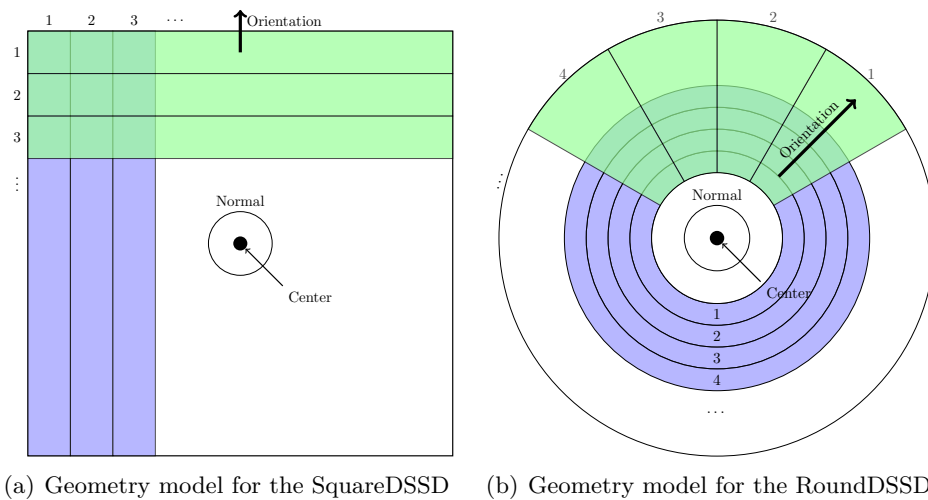


Figure 6.2

---

<sup>1</sup>Pixels for a DSSD, strip for a SSSD.

generally referred to as “change by addition” and avoids introducing bugs into previously validated code paths.

## 6.2 Setup file

In order for the detector abstraction and analysis pipeline to be useful, it must be easy for the analyst to specify their detector setup and what data corresponds to which detector. In **AUSALib** this is done with a setup file; an excerpt of one describing a W1 detector can be seen in listing 6.1. Line 2 specifies the name of the detector within this setup as “DetX”. Line 3 states that detector specific parameters can be found in **AUW1\_60\_00.json**. This file contains parameters, such as number of strips, their pitch, the detector thickness, detector model etc. The name of the file is also part of a naming convention stating that the detector is a W1 detector belonging to Aarhus University and is  $\sim 60\ \mu\text{m}$  thick and is assigned id 00. This name is written on the actual detector. **AUSALib** ships with a library of these files; one for

Listing 6.1: Example from setup file describing a W1 detector located at (33, 0, 0)mm facing in the negative x direction.

```
1  {
2    "name"      : "DetX",
3    "file"     : "AUW1_60_00.json",
4    "calibration" : "DetX.cal",
5    "position"  : {"x": "33 mm", "y": "0 mm", "z": "0 mm"},
6    "normal"    : {"x": "-1 mm", "y": "0 mm", "z": "0 mm"},
7    "orientation" : {"x": "0 mm", "y": "1 mm", "z": "0 mm"},
8    "frontMapping": {"prefix": "DETXF",
9      "multiplicity": "", "segment": "I",
10     "tdc": "_T", "adc": "_E"},
11   "backMapping": {"prefix": "DETXB",
12     "multiplicity": "", "segment": "I",
13     "tdc": "_T", "adc": "_E"},
14 }
```

each detector in our possession. The lines below the geometry information (8-13) specify the data mapping i.e. which entries belong to “DetX”.

At the beginning of a new experiment the analyst will write a setup file, which contains such an entry for each detector. This file completely specifies the full detector constellation and data mapping. While this might seem like a small thing it allows analysis code to be reused across multiple experiments by only replacing the setup file.

### 6.3 Analysis pipeline

The analysis flow within **AUSALib** is structured as a pipeline as illustrated by fig. 6.3. The DAQ delivers raw data, which is then unpacked, sorted, identified and in the end physical parameters are reconstructed. The last step will be referred to as event building as it implies to reconstruction of the physical event. Each level implies an increasing level of sophistication in the analysis. The output from each step, except for the DAQ, is a file with a ROOT **TTree** structure. That also means analysis and cross checks can easily be performed after each part of the pipeline. The pipeline design is very useful during an experiment as it is not necessary to run a very sophisticated analysis just to check that all strips are working and have a good resolution. In the following section the different steps will be described in more detail.

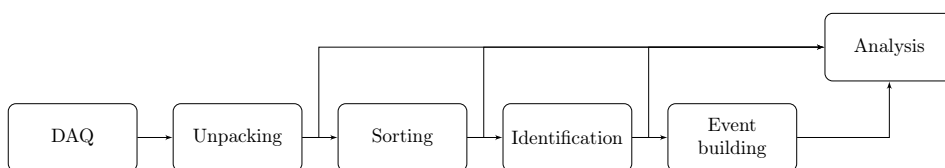


Figure 6.3: **AUSALib** analysis pipeline. The DAQ produces raw data, which is then unpacked, sorted, identified and in the end events are build. Each step, except the DAQ, produces a ROOT **TTree** structure, which can be analyzed.

**Unpacking** is the process of converting the raw file produced by the DAQ into a ROOT `TTree` suitable for analysis. This task is performed using `ucesb`<sup>2</sup> unpacker generator [150]. In order to unpack a set of data, the user must specify the structure of the data input. What modules were used, what were their addresses, in which order do their data occur etc. This is done using a simple text file. In addition, the user must specify a mapping between DAQ modules and detectors i.e. that ADC 7 channel 9 corresponds to detector 5 front strip 1. For details, the reader is referred to the documentation [150]. Typically the unpacker specification is written by the DAQ expert during the experiment and is just provided to the analyst.

The important part is that `ucesb` does, in fact, check every single bit and will complain if it does not match the specification. Thus, if a file unpacks successfully one can be certain that the DAQ provided data according to its specification. However, the data might still suffer from noise issues etc.

The unpacker specifications for the Aarhus 5MeV setup and various ISOLDE experiments can be found online [151].

**Sorting** within nuclear physics is a term used, when scanning through data looking for the signal of interest i.e. sorting is analysis code. Within `AUSALib` the sorting process is more general purpose and is generally applied to data prior to any attempts of analysis. An illustration of the sorting

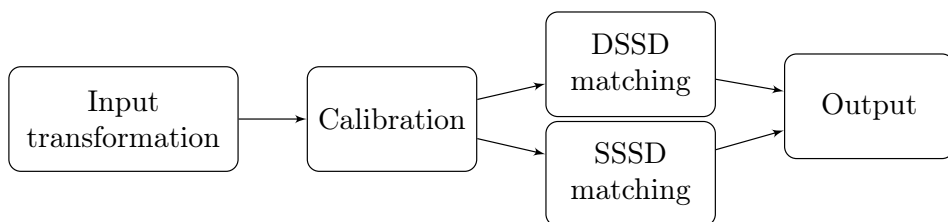


Figure 6.4: Sorting pipeline. First, an optional user-defined input transformation is performed. This is followed by a calibration and matching step.

---

<sup>2</sup>Acronym for: unpack and check every single bit



process is shown in fig. 6.4 and it consists of a calibration and matching step with an optional user-defined input transformation at the beginning. The input transformation is usually used, when the input data is not the output from `ucesb` and does not match with the `AUSALib` format.

The calibration step is straightforward as it applies a linear calibration to the ADC input to calculate the energy in keV.

The purpose of the matching step is to determine which pixel of a DSSD was hit. Remember, a DSSD has orthogonal strips along its two surfaces and a particle passing through will give rise to a signal on both sides. If there is only one signal in each side, then these must match. However, multiple particles might hit the same detector or a strip could pick up noise. In this case, one must determine, which front strip *matches* with which back strip. The simplest algorithm for this is *greedy minimal difference*, which is illustrated in fig. 6.5. It simply computes the energy difference between all front-back pairs and selects the pair with smallest difference. This pair is then excluded from further matches. It continues picking the pair with the

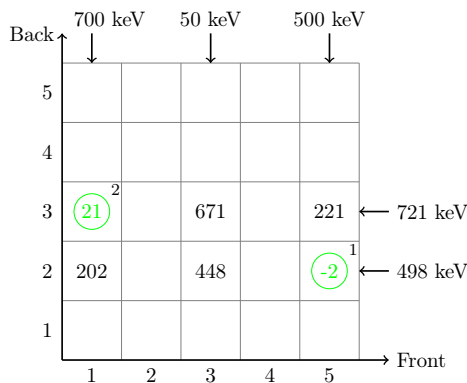


Figure 6.5: Illustration of the *greedy minimal difference* algorithm for three hits in the front and two in the back. The algorithm computes the difference between all front and back hits and picks the pair with the lowest difference. A hit is only used once. In the example, the green pairs have been selected. The small numbers in the upper right corner show the picking order.

lowest difference until there are no more candidates or the difference exceeds a certain threshold. The SSSD matching, for the detectors implemented so far, does not require this level of sophistication. Here, a simple low energy cut is imposed to remove noise.

However, this *greedy minimal difference* generally fails if a particle hits the inter-strip region. In this case, the signal can be split over two neighboring strips [152]. This is called sharing. Additionally, it is also possible that two particles hit the same strip on one side and different strips on the other side. This is called summing. These cases can be recovered by using a non-greedy matcher which considers all possible combinations of regular hits, sharing and summing. It computes the sum of the squared difference between front and back pairs and selects the solution corresponding to the overall smallest difference.

Due to the detector input mapping, which was described in section 6.2, this part of the pipeline can be handled by a general purpose executable, the **Sorter** [153]. The configuration of the matching routine is stored in a text file.

After the sorting stage, the output file has calibrated energies and angles relative to the beam axis. This normally suffices for the relatively simple analysis performed while an experiment takes place.

**Identification** is the task of determining the particle type (id) of a given hit i.e. whether a hit corresponds to a proton, an  $\alpha$  particle or something else. This determination can be done in different ways. The standard technique is to use a silicon telescope with a thin front detector and a relatively thick detector behind it. As the energy loss scales with  $Z^2$  and  $A$  of the incoming ion, the energy deposition in the front detector differs for different isotopes. Thus, a plot of the energy deposited in the front detector vs. the full energy gives rise to so-called “banana plots” as can be seen in fig. 6.6. By placing 2D cuts in this plot the particle can be identified. Alternatively, if the particle has insufficient energy to penetrate the front detector, it might be possible to exclude certain types of particles. In some cases, it might not be possible to perform a unique identification. If so, this step outputs all the

possible candidates. Hence, there is a one-to-many relation between a hit and its possible identifications.

For each proposed identity the energy is corrected for losses in the detector dead layers and the target. The target is modeled as a stack of box-shaped layers and a routine have been implemented to perform corrections for any number of layers and orientations.

Like the previous step, this step has also been encapsulated in a general purpose executable, the **Identifier** [154]. Specification of the particle id cuts etc. happen via command line arguments. After this step, the particle id ( $A, Z$ ) and loss corrected energy have been added to the output file.

**Event building** takes the identified hits from the previous stage and attempts to build events from them. It is given one or more desired final

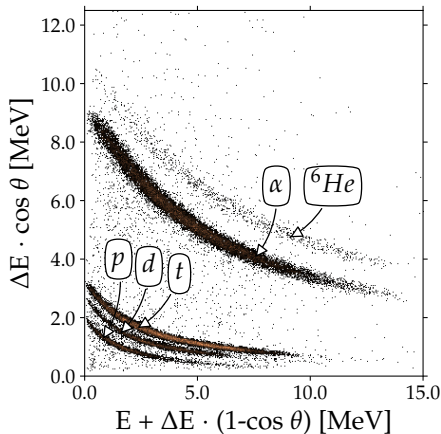


Figure 6.6: “Banana plot” showing the energy in the thin front detector vs. the full energy. The hyperbolic shape of the bands corresponds to the  $1/\beta^2$  dependence of the Bethe-Bloch formula. The cosine factor corrects for differences in effective detector thickness. From this plot, it is possible to identify five different isotopes. Figure courtesy of Jesper Halkjær.

states such as  $2\alpha$  or  $3\alpha + \gamma$  and it will find the different subsets of identified particles that correspond to such a final state without using a hit multiple times. For each identification, it calculates the four-momentum based on the corrected energy, the detector pixel position and target center. The proposed events are subjected to a number of user-specified cuts such as energy conservation, momentum in the center-of-mass (CM) summing to zero, maximal time difference less than  $x$  etc. The event building comes with a variety of implemented cuts and defines a general cut interface such that custom cuts can easily be added.

Due to the need of adding user-defined cuts the event building stage is supplied as a library, the **EventBuilder** [155]. There also exists a standard template, which can be used for new experiments.

**Event analysis** is performed on the output from the event building stage. For each particle in the final state, it has the four-momentum and particle id. Its task is to calculate the observables of interest e.g. excitation energy, single particle CM energy, CM angles etc. The previous modus operandi was to place these parameters into histograms with different histograms corresponding to different cuts in the analysis. However, recently the group have transitioned<sup>3</sup> into outputting the analysis results into a ROOT **TTree** structure. This allows for a faster and more dynamic post-processing of the analysis results without the need to rerun the analysis.

## 6.4 Energy loss

An important part of any experiment with charged particles is corrections for energy losses. These losses can occur in any material between the reaction point and the active part of the detector, though the two main contributors are the target foil and inactive layers on the surface of detectors.

While rough estimates can be computed with the Bethe stopping power formula, in practice tabulated values as these account for effects such as shell effects, straggling etc. In **AUSALib** the tables from GEANT4 [156],

---

<sup>3</sup>Thanks to a suggestion from Håkan Johansson.

ICRU [157], and SRIM [158] are included. All three tables provide the stopping power,  $\frac{dE}{dx}$ , while the latter also provides ranges,  $R(E)$ .

In order to compute the energy loss from the range, it must be interpolated. In **AUSalib** the interpolation can be performed either using a cubic spline or a set of least-squares optimized B-splines [159]. The benefit of the latter method is reduced oscillations in interpolation as can be seen in fig. 6.7. With an interpolation in place the energy loss for a given initial energy,  $E_i$ , and material thickness,  $\delta$ , is computed by first determining the full range of the initial energy,  $R(E_i)$ . One then subtracts the thickness and computes the energy corresponding to the reduced range,  $E(R(E_i) - \delta)$ . The energy loss is then given by the difference. The benefit of this solution is speed as the energy loss can be computed by a lookup in two tables.

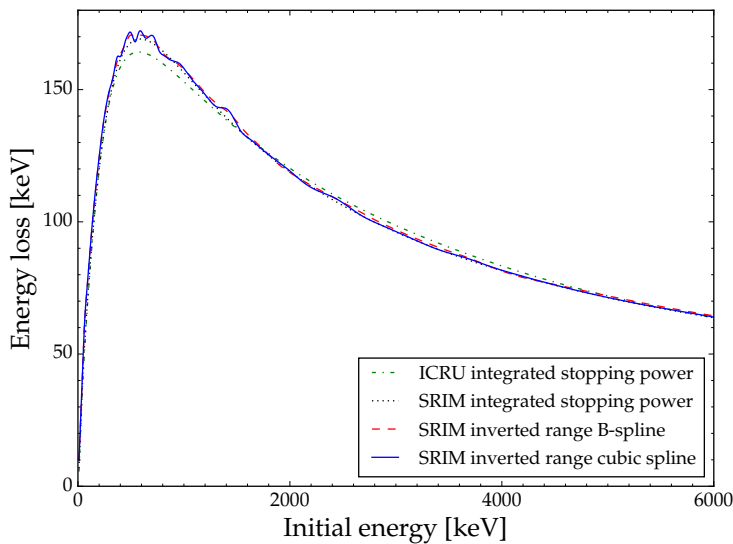


Figure 6.7: Comparison of the full energy of an  $\alpha$  particle through 500 nm silicon. The difference between ICRU and SRIM amount to 7 keV at the peak. Note the oscillations of the cubic spline at the peak.

In addition, since the range table includes effects such as straggling it is generally more accurate.

An alternative method to compute the energy loss is to integrate the stopping power

$$\Delta E = \int_0^\delta \left. \frac{dE}{dx} \right|_{E=E(x)} dx, \quad (6.1)$$

with the additional stopping requirement  $E \geq 0$ . This is an ordinary differential equation with the small twist that the stopping power is tabulated in terms of energy while the integration is in terms of distance. It can be computed using solvers for ordinary differential equation from e.g. GSL [160]. The stopping power table is interpolated using the same methods described in the previous paragraph.

Figure 6.7 shows a comparison between the different methods for the ICRU and SRIM tables. Specifically, the figure shows the total energy loss of an  $\alpha$  particle in 500 nm silicon. Notice the oscillations of the cubic spline SRIM calculation. Most of this is rectified using the fitted B-splines. The difference between ICRU and SRIM is roughly 7 keV at the peak.

## 6.5 Calibration

For the majority of experiments and detectors, it is possible to perform an energy calibration with an  $\alpha$  source<sup>4</sup>. At Aarhus University we use a 1 kBq source with  $^{148}\text{Gd}$ ,  $^{239}\text{Pu}$  and  $^{244}\text{Cm}$ . Each of these isotopes gives rise to a nearly mono-energetic peak. For a typical experiment there are between 100 and 200 individual detector channels and thus it can easily take a few hours of analysis to determine the calibration parameters manually. The discussion below is specific to DSSDs, but can easily be extended to include SSSDs.

When performing a calibration the  $\alpha$  source is usually mounted facing the detector. The  $\alpha$  particles emitted by the source will then give rise to a spectrum of discrete peaks in each strip as seen in fig. 6.9. However,

---

<sup>4</sup>5 MeV  $\alpha$  particles are not stopped in thin 20  $\mu\text{m}$  silicon detectors

the detector has most likely a thin inactive dead layer before the active detecting layer as illustrated in fig. 6.8. In the case of a W1 detector, the p+n junction side may have an electrode grid [161]. The effect of the dead layer is to lower the measured energy such that for a given  $\alpha$  particle energy,  $E$ , the detected energy,  $E'$ , will depend on the thickness of the detector dead layer,  $\Delta$ , as well as the entry angle  $\theta$  in the following way

$$E' = E - \frac{\Delta}{|\cos \theta|} \cdot \frac{dE}{dx}. \quad (6.2)$$

This difference is quite significant for S3 detectors, which have a deadlayer of approximately 500 nm and 4.5  $\mu\text{m}$  on its two surfaces [162]. This corresponds, respectively, to a shift of 96 keV and 833 keV for a 3 MeV  $\alpha$  particle at normal incidence. The shift for a given isotope can be calculated automatically if the detector- and source geometry is known i.e. if a setup file is provided. The source geometry and isotopes are provided by the user as a text based input file with a syntax similar to the setup file.

A calibration tool must perform the following tasks: collect a spectrum for each strip, perform peak finding for each spectrum, determine  $E'$  for each  $\alpha$  line for each strip and perform a linear fit between the peak positions and associated channel numbers.

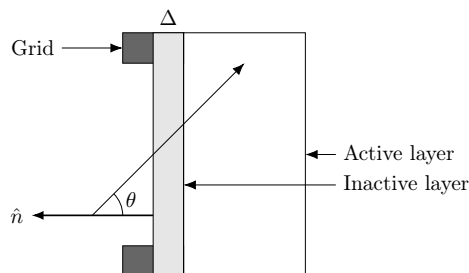


Figure 6.8: Model of detector dead layers. The detector will measure the energy deposited in the active region. Thus, loss in the inactive dead layer or the electrode grid will lower the measured energy. The thickness of the grid is approximately 200 nm [161].

**Spectrum collection** is trivial – provided the analyst has specified the data mapping in the setup file. In this case, **AUSALIB** handles looping over all events in the file and fills a histogram for each strip.

**Peak finding** is generally quite complicated. However, for the restricted case of well separated peaks without background, as seen in fig. 6.9, it can be done robustly. The algorithm works in two steps. The first step determines a rough peak location by finding the tallest peak in the spectrum. It then excludes a region of  $\pm W/2$  around this peak and finds the tallest peak in the remaining spectrum. It does so for each isotope in the source. In the simplest case the substructure of the peak, which can be seen in fig. 6.10, is ignored and the output from the first step is used to fit the main peak with a Gaussian function in the region  $\pm 2\sigma$  around the peak. However, if energies and intensities are provided for the sub-peaks, then a more complete fit can

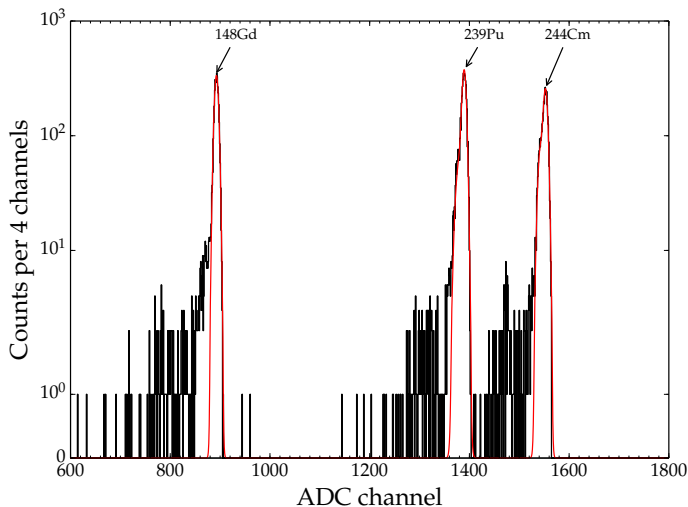


Figure 6.9: Example spectrum for a single strip for a  $^{148}\text{Gd}$ ,  $^{239}\text{Pu}$  and  $^{244}\text{Cm}$  source. Each isotope gives rise to a nearly mono-energetic peak.



be performed. For robustness, the peak intensities and energy differences are fixed to the provided values. However, as the spectrum is uncalibrated, the algorithm requires the number of channels corresponding to this energy difference and thus an initial energy calibration must be assumed. This is taken from a linear fit to the initial rough peak determination. The peaks are then fitted based on this guess and a linear calibration extracted. This is then used as an improved guess. This procedure is repeated until the energy calibration converges. An example of such a fit to the two main peaks from  $^{244}\text{Cm}$  is shown in fig. 6.10. Calibrations performed using this method is usually self-consistent within  $\sim 2$  keV.

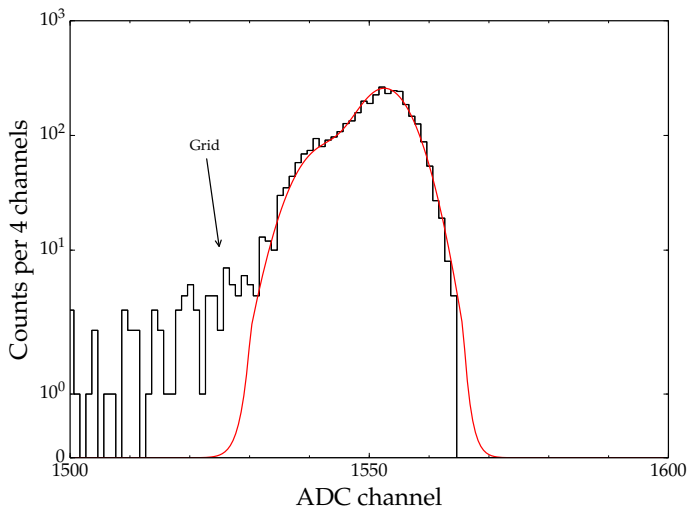


Figure 6.10: Close-up of the  $^{244}\text{Cm}$  peak shows the peak sub-structure. The small structure below the peak is from  $\alpha$  particles passing through the electrode grid on the W1 detector surface. This peak is not included in the fit. The remaining structure is intrinsic to the isotope.

**Shift calculation** is a simple geometric problem. In order to calculate the detected energy in a strip eq. (6.2) should be averaged over the entire strip surface. This average can be approximated with the average of the energy loss in each sub-pixel of the strip weighted by the pixel solid angle. This can be written as

$$E' = E - \frac{1}{\Omega_{\text{strip}}} \sum_{\text{pixels}} \Delta E_{\text{pixel}} \Omega_{\text{pixel}}, \quad (6.3)$$

where  $\Delta E_{\text{pixel}}$  is the last term of eq. (6.2) evaluated at the pixel center. The energy loss is calculated using the methods described in section 6.4.

It should be noted that the accuracy of this shift calculation can be improved by performing a per-pixel calibration. However, as this would require a substantial increase in source exposure and the current level of accuracy is sufficient, we have opted not to do this.

This procedure requires knowledge of the source position, which can be obtained by optimizing the source position under the assumption that the source is an isotropic point source. Alternatively, one can optimize the source position under the assumption that the observed number of counts in a pixel are continuous as function of distance to the source. One then optimizes the source position in order for this to be well described by a fourth order polynomial. **AUSALIB** can perform both of these optimizations. However, the implementation builds on the ideas by Gunvor Koldste and the reader is referred to her thesis for details [163].

**Calibration conclusion** With the detector and source geometry provided externally by the user, it is again possible to build a general purpose executable. In this case, it is **Calibrator** and it automates the calibration procedure almost completely [164]. With this program, it is possible to extract precise calibration parameters for a full array in a matter of minutes. In addition, it performs advanced outlier detection in order to alert the user of potential problems. This is especially important during the setup phase of an experiment, where potential problems can still be resolved.

## 6.6 Conclusion and outlook

As is hopefully clear now, the pipeline design of **AUSALib** allows the analyst to move from raw DAQ data to identified events by running three pre-built executables. Combined with the power of setup files and near automatic calibration, this has greatly reduced the time and skill required to extract the signals of interest. In addition, this has also greatly enhanced the analysis collaboration within the group. After a few hectic years of development, **AUSALib** has now reached a stable phase. I don't foresee a large need for new development before the current DAQ is upgraded to a digital DAQ that also provides signal traces.

In summary, **AUSALib** is now a mature analysis framework that handles most of the grunt work associated with the analysis of DSSD data. Now the analyst "just" has to understand the physics of the output.

## 6.7 Contribution

**AUSALib** is the result of the combined work of several people within the Aarhus Subatomic group mainly Alan Howard, Jesper H. Jensen, Oliver S. Kirsebom and myself. However, I have an essential role in the development and have contributed with roughly 80% of the code.



## Data acquisition

The data acquisition system (DAQ) is an essential part of most experiments in nuclear physics without which there would be no data to analyze. During my Ph.D. I have performed significant upgrades of the Aarhus DAQ and a copy of this system have been used for numerous experiments at the ISOLDE facility at CERN.

A DAQ typically consists of a number of different components. Figure 7.1 gives an overview of these and also which components interact. Roughly speaking, the components to the left of the readout are the front-end components, while the components to the right are the back-end. The readout serves as the bridge between them. This division is also a physical division where the front-end is specialized electronic hardware and are typically housed in crates such as NIM and VME, while the back-end software is typically running on a regular desktop computer, which is connected to the VME controller.

The first part of this chapter will focus on the front-end electronics. As the front-end is mainly built from off-the-shelf electronics, this is essentially a condensed summary of how these modules operate. This is followed by a few sections describing the back-end and some associated services that make DAQ operation easier. The recent upgrades of the readout system were published in ref. [165] and the paper can be found at page 139.

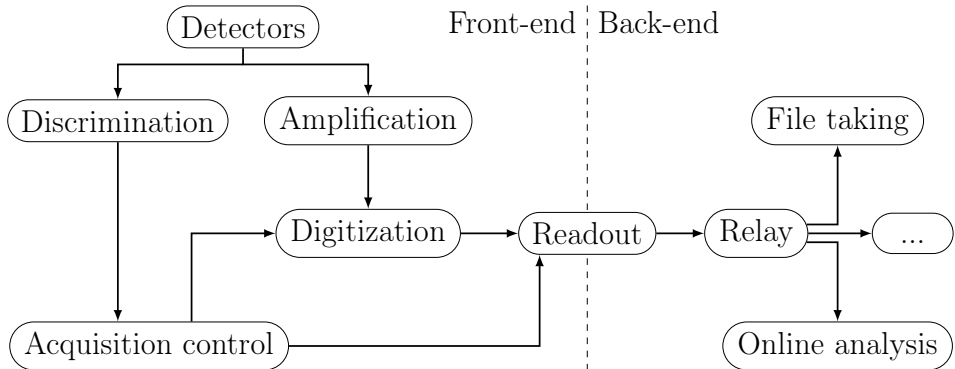


Figure 7.1: Schematic overview of the different DAQ elements. The detector output is connected to discriminators and amplifiers. The amplified signal is given to digitization modules, which will perform a conversion if triggered by the acquisition control. The readout empties the digitization modules and sends the data over the network to the back-end relay where it is recorded and online analysis performed. Figure adapted from Jesper Halkjær.

## 7.1 Front-end

### Triggering

Generally, in nuclear physics experiments, there is a certain probability distribution in time that a reaction will happen. A well-known example of this is a radioactive source where this gives rise to an exponentially decaying activity. In contrast to this is a typical Bose-Einstein condensate experiment, where the experimentalist knows the condensate will drop when released from the trap.

This naturally leads to the concept of triggering<sup>1</sup>. Generally speaking, triggering is used to select which data to acquire based on when something “interesting” happens. In this system, there are two levels of triggers. There

<sup>1</sup>Triggering is found at all levels of data acquisition. An extreme application can be found in ref. [166].

are the low-level triggers generated for each detector. This is done with discriminator units, such as a leading edge or constant fraction discriminator, attached to each signal. While their mode of operation is slightly different they both emit a logic signal when the input signal crosses a preset threshold. These individual triggers are then combined into a single global trigger called the **MASTER\_START (MS)** using some logic coincidence function. When a **MS** occurs data is acquired by all digitization modules. The trigger implementation described here is a synchronous trigger system i.e. all modules acquire data simultaneously.

The implementation of the trigger logic will be described in section 7.2

## Digitization

**Analog chain** is responsible for the signal processing prior to digitization. When a charged particle traverses a silicon detector it will on average create  $\frac{E}{3.62\text{eV}}$  electron-hole pairs due to ionization [167]. A 9 MeV particle will thus give rise to a charge release of the order of 0.3 pC. As such a small signal is rather prone to noise it is amplified close to the detector in a pre-amplifier, which also performs charge to voltage conversion by charging a capacitor. The voltage output has a fast rise time and a long tail and the pulse height is proportional to the current. This signal is fed to a secondary amplifier, which applies an adjustable gain and performs bandwidth limitation (shaping) in order to improve the signal-to-noise ratio. In our case, this amplifier also houses the discriminator units. Thus, the amplifier will output a shaped signal and a logic discriminator output for each input. In addition, it will output a logic **OR** of all the discriminator signals, which is used by the trigger logic.

**Energy** information is encoded in the height of the pulse maximum of the secondary amplifier. This information is digitized using a peak-sensing Analog to Digital Converter (ADC). The basic operating principle is to digitize the potential of a capacitor, which is only charged when the input potential is higher than the capacitor potential. It is up to the experimentalist to define the region of interest i.e. the time window in which the

maximum must be determined. This is done with a **GATE** signal, which is typically between 1 and 5  $\mu\text{s}$  long. After the **GATE** the ADC will perform the digitization. This typically takes between 1 and 8  $\mu\text{s}$  depending on the ADC module. During the conversion the ADC is **BUSY** i.e. it cannot accept a new **GATE**. On relatively modern ADC modules the digitized pulse heights are written to an internal output buffer and the ADC can accept a new **GATE** while the old event is being read out. When the buffer becomes full the ADC becomes **BUSY**. Modules are typically able to store between a few and some thousand events.

**Time** information is encoded in the fast-rising leading edge of the pre-amp output. This leading edge is what causes the discriminator unit to fire. A Time to Digital Converter (TDC) module is used to time-stamp the arrival time of the discriminator pulse. The timing resolution is of the order 100 ps, which is achieved using a combination of clock counting and interpolation (see ref. [168] for details). The TDC modules usually operate in a so-called “trigger matching mode”. When the module receives a trigger (typically **MS** delayed by  $\sim 1 \mu\text{s}$ ) it will write the timestamp of all channels that fired within a predefined window to an output buffer. Like the ADC, it will assert **BUSY** if its output buffer becomes full.

## 7.2 Acquisition control

The acquisition control (AcqC) is the nexus of the front-end as illustrated by fig. 7.2. Its main task is to implement the logic function for the global trigger decision based on the individual sub-triggers i.e. to generate *the MS*. Based on this **MS** it must generate the logic signals for the DAQ modules, which is a gate signal for the ADC and a trigger signal for the TDC. However, as this is a synchronous DAQ all modules must acquire data simultaneously and thus a **MS** must *not* be generated if *any* module is busy. In addition, the readout software requires periods without any triggers. These periods are called dead time (DT). The readout uses these periods to validate synchronicity i.e. that all modules have acquired the same number of events. In the following



DT, is used generally for periods of time when trigger requests are rejected.

Traditionally, all of this functionality has been implemented by combining multiple discrete logic and gate generator NIM modules. Combining, in this case, means connecting with wires. However, scaling this method beyond a few detectors quickly becomes time-consuming and error-prone. The latter is especially problematic at user-facilities where time to set experiments up is usually constrained. Documentation is also rather challenging, often relying on pictures.

The Aarhus DAQ instead uses a single FPGA to perform all of the AcqC. The FPGA is housed on a VULOM4B module [169] and it is running the TRLO II firmware [170]. The firmware implements all of the above functionality and more. Specifically, it implements a trigger state machine, which is perfectly non-paralyzable meaning that trigger requests arriving

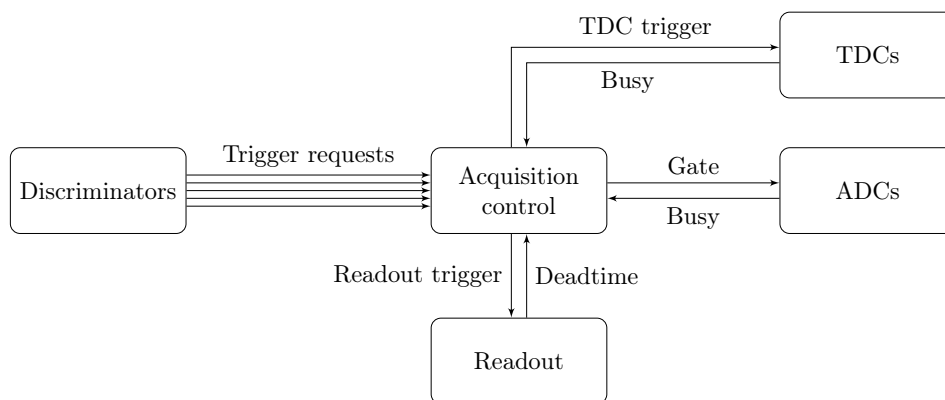


Figure 7.2: Overview of the many tasks of the AcqC. The AcqC receives trigger requests from the individual detectors. These must be combined into a MS with gates and triggers for the digitization modules. The AcqC must respect the busy and DT from the modules and the readout. The AcqC must also periodically trigger the readout software, which checks module synchronicity.

during DT will *not* extend the DT but are simply rejected [171]. For a non-paralyzable acquisition and a stream of Poisson distributed trigger requests, it is possible to analytically calculate the fraction of accepted events, called the live time fraction<sup>2</sup>

$$\mathcal{L} = \frac{1}{1 + f_r \Delta t}, \quad (7.1)$$

where  $f_r$  is the trigger request frequency and  $\Delta t$  the dead time per event [171]. The trigger state machine allows the user to define up to 16 different trigger conditions, which will cause a **MS**. In addition, it is possible to downscale the individual conditions. Downscaling in this context means only generating a **MS** for every  $1/n$  time the trigger condition occurs. This can be used to e.g. preferentially accept rare multi-particle events over elastic scattering events.

When the state machine generates a **MS**, it can, in addition, send a trigger<sup>3</sup> to the readout. Specifically, it sets a 4 bit trigger register which is detected either by the CPU polling or the AcqC may issue an interrupt. The readout is free to react how it pleases to this trigger. Often it will empty the digitization modules, but these triggers can also be used to signal “beam arrives soon” for example. The important part is that the AcqC will assert DT until the readout signals that it can continue. In the simplest case, the AcqC will accept a single event and ask the readout to empty the modules. Thus  $\Delta t$  from eq. (7.1) is the sum of the digitization and readout time with some additional overheads. This severely limits the achievable throughput. This overhead can be amortized, to some degree, by letting the modules acquire multiple events into an internal buffer before performing a readout. The widely used CAEN V785 can store 32 events. This reduces the overheads associated with polling and CPU task switching, but the data

---

<sup>2</sup>Just to clarify: the live time is the periods of time in which the DAQ will accept triggers. The live time fraction,  $\mathcal{L}$ , is the fraction of requests accepted. However, often one is sloppy and refers to both as live time. Similarly, in dead time the DAQ will reject event and the dead time fraction,  $\mathcal{D}$ , is the fraction of events rejected.

<sup>3</sup>Apologies, but in a DAQ many things are called a trigger. To summarize: there is the TDC trigger, discriminator trigger, global trigger (**MS**) and the readout trigger. All of them are different.

transfer is still performed within dead time. In the article at the end of this chapter, it is shown that  $\Delta t$  can be made approximately equal to the digitization time if the DAQ modules are continuously emptied in between readout triggers. This dramatically increases the achievable throughput. The changes required for the AcqC is to only seldom trigger the readout e.g. every 8192 events instead of every 32. The reader is referred to the paper for details.

In this section, I have only scratched the surface of the capabilities of the TRLO II firmware and the interested reader is referred to the documentation for details [172]. However, I will mention another *very* important feature. The configuration of TRLO II is entirely text-based and thus it is possible to automatically perform documentation of the configuration for every single run. This is especially important in the hectic start-up phase of an experiment.

### 7.3 Readout

The readout serves as the bridge between front-end modules and the back-end. So far the discussion has been general, but in this section, it will be restricted to front-end modules housed in a VME crate, which also defines a bus standard [173, 174].

The readout must be able to interact with the AcqC, extract data from the front-end modules and transfer this data over the network. If multiple VME crates are used it must also be able to merge the data stream from these. Luckily, the first and last task are handled by general purpose DAQ frameworks such as MBS [175] and drasi<sup>4</sup> [176]. When using these frameworks one is thus only responsible for the actual readout. In this case, the user-supplied code is called during start-up and when a readout trigger has been received. The readout code is executed by a Single Board Computer (SBC) situated in the VME crate. At Aarhus University we have a Motorola MVME 5500 [177] and a CES RIO4-8072 [178] at our disposal.

---

<sup>4</sup>In fact drasi refers to itself as an “data pump” as its main task is to move and merge data.

The task of the readout is quite straightforward. It must configure the modules during start-up and afterward, it must empty the module buffers into an output buffer on the SBC, verify data integrity and module synchronicity. Module synchronicity is verified by comparing each module event counter with the AcqC event counter. If either data integrity or synchronicity checks are violated the readout must alert the operator. Optionally, it might also attempt to recover the situation automatically by performing a reset.

All of these tasks are performed by the Nustar Readout Library (nurdlib — formerly known as vmlib) [179]. Specification and configuration of the modules are handled with a simple text file. Thus no recompilation is required for different experiment/module configurations. All of this facilitates code reuse and thorough testing.

As described in the previous section, the DT can be drastically reduced by continuously emptying the module buffers. To this end, a callback function was added to drasi, which is called whenever a readout trigger is *not* present. In addition, nurdlib was substantially modified to allow this different mode of operation. This included greedily reading module buffers, buffer merging and parsing of an arbitrary buffer. See the paper at the end of this chapter for additional details.

## 7.4 Multiple crates

The above two sections describe the operation of a single crate DAQ. However, the number of detector channels in recent experiments at ISOLDE has necessitated the use of two VME crates. Luckily the design easily scales horizontally.

An illustration of a two crate system can be seen in fig. 7.3. Note that each crate is essentially identical to the single crate system shown in fig. 7.2. The AcqC of each crate is responsible for generating the trigger and gates for the modules of this crate. The difference is that the global trigger decision is handled entirely in the master AcqC, which then propagates the MS and readout trigger to all slave crates, where they are further distributed by the

slave AcqC. In turn, the master AcqC must respect the busy and DT from all slave crates. This ensures that a **MS** is not generated while any crate is busy. The slave busy is a logical **OR** of all module busies in that crate.

This design requires no changes in the readout function except that data must be tagged with a crate number. This tag is usually included in the event header preceding the module data. The data from all the crates are collected and merged in a single event builder. As the DAQ is synchronous the merging is performed based on event counters. The event builder also acts as the relay seen in fig. 7.1.

## 7.5 Back-end

The two primary tasks of the back-end are to store the collected data and perform some level of online analysis of the incoming data. The analysis must be performed with sufficient sophistication that the experimentalist

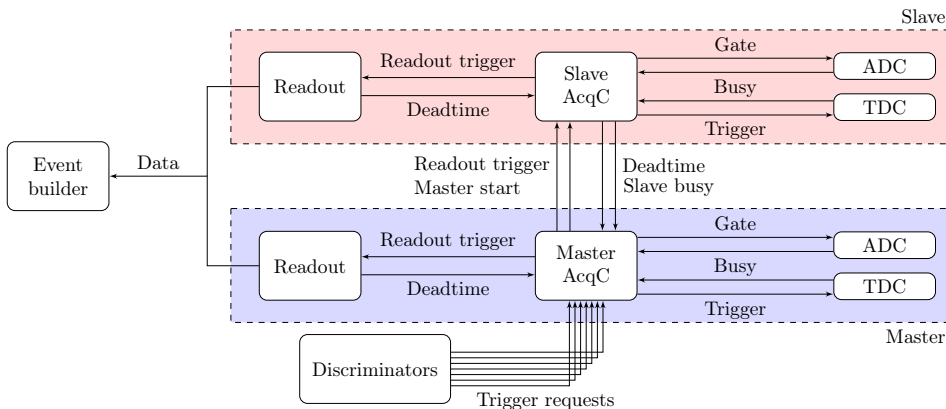


Figure 7.3: Illustration of a two crate DAQ. Each crate is essentially identical to a single crate DAQ as seen in fig. 7.2. All trigger decisions are handled by the master AcqC and propagated to the slave AcqC. Slave busy and DT are propagated to the master. This design can be extended to multiple slaves.

can verify that the incoming data is sound.

Figure 7.1 shows the back-end receiving a stream of data from the readout. This stream is received by a relay, which is normally running on a different computer than the readout node. The relay then distributes the data to multiple clients thus ensuring minimal load of the readout node. The design is “open-ended” as it does not limit the number of clients that can process the data on-the-fly. The relay operates two data streams in different modes. The first stream is operated in “weak-hold” mode, where connected clients must consume all data. If a client falls behind, the relay will block the acquisition. The second stream is operated in “no-hold” mode, which will not block if clients cannot keep up. The first stream is used for essential clients such as file taking, while the second stream is for expendable clients such as online analysis.

### **go4cesb**

**go4cesb** is an online analysis library built by combining **ucesb** [150] and **GSI G04** [180]. **G04** is used as a sophisticated histogram viewer, allowing the user to seamlessly interact with histogram i.e. zoom, fit etc., while a background thread continuously fills them with incoming data. In principle, **G04** is able to receive the data stream from the relay server. However, **G04** does not provide any simple means to perform data unpacking and requires the user to implement a custom unpacker per experiment. So instead a custom event source has been implemented, which uses **ucesb** under the hood. With this design, a **ucesb** unpacker process is spawned from within **G04**. This process connects to the relay server and performs the unpacking of the incoming data. The unpacked data is then sent via a UNIX pipe to the **G04** process. The data has the same format as in the regular **AUSAlib** analysis pipeline and it is trivial to apply the regular **AUSAlib** matching routines on it.

After the matching has been performed it is up to the user to perform an analysis suitable for their experiment. However, as the data format is now identical to when performing a regular **AUSAlib** analysis after the sorting stage, regular analysis code can be reused for this. In addition, there is a

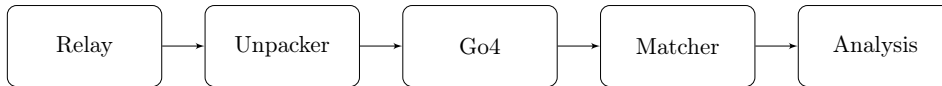


Figure 7.4: Go4cesb event pipeline. A `ucesb` unpacker receives a data stream from the relay and performs the unpacking. The unpacked data is sent to the `Go4` process via a UNIX pipe. Inside the `Go4` process, the unpacked data is matched and then handed to the user for analysis.

large overlap in the relevant analysis for all experiments and to facilitate code reuse a library of different analysis routines is provided along with `go4cesb`. These different analysis routines are applied in parallel and can be enabled/disabled with a simple configuration file.

### File taking

File-taking is performed by a `ucesb` client connected to the relay, which writes all data to file. The client is running on a different computer than the readout node. Data is written in the GSI list mode data (`lmd`) format [181] and slightly compressed using `gzip`. The main point of the `gzip` compression is to add a CRC-32 checksum such that data bitrot is detectable. For convenience and easier recovery in case of failure, a new file is opened for every 100 MB of data.

In a previous edition of the DAQ, the readout node was directly responsible for writing data to a file. However, during an experiment, it was discovered that the network file system (`nfs`) on the readout node was broken. This caused data to be discarded for large periods of time. With the relay/client design the readout node only needs functional TCP sockets.

## 7.6 DaqC

At this point, all the different components from fig. 7.1 have been described. Together they constitute the DAQ; each piece with a specific purpose. However, an experiment typically lasts at least  $5 \times 24$  hours and a DAQ

expert cannot be present at all times. It must thus be possible for a novice to operate the DAQ. To the extent possible the system should also be “self-healing” i.e. try to recover from failures.

To this end, Daq Controller (DaqC) have been built. To the operator, it presents a simple overview of the status of the various DAQ services as can be seen in fig. 7.5. In addition, it is possible to configure the trigger condition and the right pane allows the operator to open a file and see the latest files. For an experiment that is running, this is all that is needed.

The screenshot displays the DaqC graphical user interface, divided into several sections:

- Service Status (1):** A vertical stack of service status cards.
  - RIO2** and **RIO7**: Green status indicators.
  - Readout**: Shows "Events/s: 849" and "kByte/s: 11" with a "2/2" indicator.
  - Relay**: Shows "Processed: 805" and "Errors: 0".
  - Go4**: Shows "Running".
  - Sync**: Shows "Remote host:" and "Idle".
  - Mesytec**: Shows "Last check: Invalid date" and "Unknown".
- Active Trigger (2):** A table showing the current active trigger configuration.
 

Active trigger: POIS_PULSER			
T1	T2	T3	T4
T5	T6	T7	T8
T9	T10	T11	T12
T13	T14	POIS_PULSER	UNI_PULSER
- File List (3):** A table showing a list of files.
 

Nr.	Beam	Target	Energy	Start	Stop
25			None None	2018-06-15 15:00:14	2018-06-15 15:01:14
24			None None	2018-06-14 17:40:48	2018-06-14 17:42:18
23			None None	2018-06-14 17:27:50	2018-06-14 17:29:46
22			None None	2018-06-14 17:23:26	2018-06-14 17:27:21
21			None None	2018-06-14 17:14:48	2018-06-14 17:18:54
20			None None	2018-06-14 16:54:52	2018-06-14 16:58:52
19			None None	2018-06-14 16:46:28	2018-06-14 16:50:44
18			None None	2018-06-14 16:42:56	2018-06-14 16:45:24
17			None None	2018-06-14 16:28:44	2018-06-14 16:30:25
- File Selection (3):** A section with a blue "Start" button, the text "Not taking any file!", and a "File directory: /home/acquser/data/raw (390 GB left)" label with a "100M" dropdown menu.

Figure 7.5: Graphical user interface as presented by DaqC. (1) gives the status of the various service i.e. if the SBC is online, whether the relay is running etc. (2) shows the current active trigger. (3) allows the operator to start a new file.



Internally DaqC consists of a watch-dog, a dependency tree specifying the start-up order and a specification of how to interact with the different services i.e. query status, stop, start etc. Once a second the watch-dog will query all services for their status. If a service reports problems the watch-dog will attempt to restart it – provided its dependencies are running, e.g. the online analysis is not started if the relay is not running. This essentially allows a novice operator to start the entire DAQ by just running DaqC.

When opening a file DaqC will prompt the operator to fill out a run-sheet with meta information such as facility, experiment number, beam ion, beam energy etc. This information is editable up to and including when the file is closed. The idea is that any relevant information can easily be noted in the run-sheet. This information is stored locally and optionally also sent to a central database as described later in section 7.8. In addition to the information provided by the operator, DaqC will also log any additional meta information available. This includes trigger condition, front-end module configuration etc. This information is recorded at the beginning and end of every run such that changes during the run can be identified. To ensure data is not lost due to, e.g. disk failure, fire, power loss, etc., it is frequently uploaded to an out-of-lab facility.

## 7.7 Monitoring

Experiments, especially at user facilities where time is constrained, are typically quite hectic and evolve substantially over the course of a few days. Thus, it is very important to determine whether experimental conditions right now are within the expected region e.g. has the yield dropped significantly or is the DAQ dead time higher than normal? This has often required a meticulous regimen of procedures that the people on shift must perform. In the last two years, we have instead opted for an automated solution as it offers superior results with a granularity of a few seconds compared to 5 minutes at best with procedures. This has freed-up people on shift to perform more sophisticated analysis of the acquired data.

The automated solution is based on the two open-source tools InfluxDB [182] and Grafana [183]. InfluxDB is a time-series database, which essentially means it excels in storing series of time-stamped values. It is possible to query the database using a SQL-like language. InfluxDB is quite versatile since it can accept values from any network connected source capable of performing an http request. During an experiment, we typically store everything from detector leakage current to the number of proton pulses delivered by CERN. Another common data source is a quick-and-dirty yield estimate i.e. some simple online analysis attached to the data relay.

Grafana serves as the graphical user interface to InfluxDB. It allows easy definition of several dashboards showing multiple graphs of relevant time series. An example of such a graph can be seen in fig. 7.6. Generally, these dashboards allow the operator to quickly gauge the “health status” of the experiment and also spot trends on longer timescales.

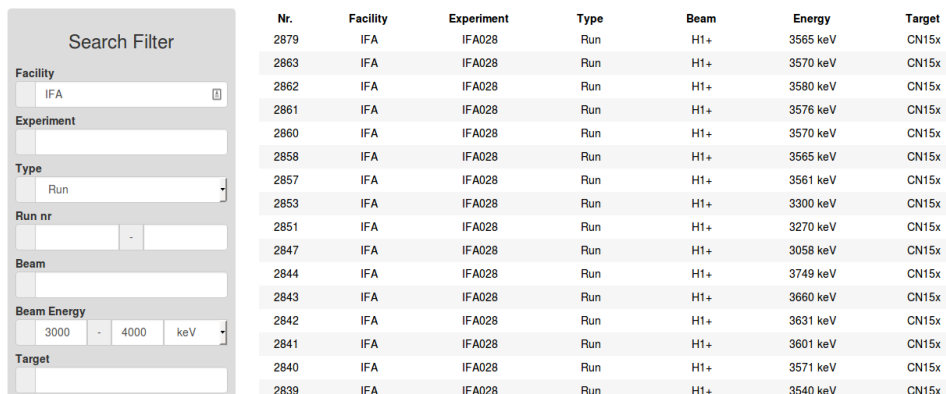


Figure 7.6: Number of  $\alpha$  particles observed in five different detectors per 10 s. The full range of the ordinate is 24 hours. A slow downward trend can be observed from the thick red line at 16:00 and forward. This was due to target deterioration.

At the time of writing multiple experiments at ISOLDE and Jyväskylä have adopted InfluxDB and Grafana to monitor their experiments.

## 7.8 RunDB and RUP

The 5 MV Van de Graaff (VdG) accelerator was recommissioned at the beginning of 2012 and since then a long series of experiments have been conducted with it. While the detector data is stored to disk by the DAQ it is equally important to store metadata. For experiments at the VdG such meta information includes the beam energy, beam particle, magnetic field setting etc. While most of this information could be collected automatically with a modern accelerator the VdG control system is completely analog and this information must be recorded manually by the operator. This is done with DaqC (see section 7.6) which stores the meta information locally but also sends a copy to a server running RunDB (Run DataBase). RunDB stores the meta information in a SQL database and makes it easily



The image shows the RunDB user interface. On the left is a 'Search Filter' panel with the following fields: Facility (text input: IFA), Experiment (text input), Type (dropdown menu: Run), Run nr (text input), Beam (text input), Beam Energy (range input: 3000 - 4000 keV), and Target (text input). On the right is a table with 7 columns: Nr., Facility, Experiment, Type, Beam, Energy, and Target. The table contains 15 rows of data representing search results.

Nr.	Facility	Experiment	Type	Beam	Energy	Target
2879	IFA	IFA028	Run		3565 keV	CN15x
2863	IFA	IFA028	Run	H1+	3570 keV	CN15x
2862	IFA	IFA028	Run	H1+	3580 keV	CN15x
2861	IFA	IFA028	Run	H1+	3576 keV	CN15x
2860	IFA	IFA028	Run	H1+	3570 keV	CN15x
2858	IFA	IFA028	Run	H1+	3565 keV	CN15x
2857	IFA	IFA028	Run	H1+	3561 keV	CN15x
2853	IFA	IFA028	Run	H1+	3300 keV	CN15x
2851	IFA	IFA028	Run	H1+	3270 keV	CN15x
2847	IFA	IFA028	Run	H1+	3058 keV	CN15x
2844	IFA	IFA028	Run	H1+	3749 keV	CN15x
2843	IFA	IFA028	Run	H1+	3660 keV	CN15x
2842	IFA	IFA028	Run	H1+	3631 keV	CN15x
2841	IFA	IFA028	Run	H1+	3601 keV	CN15x
2840	IFA	IFA028	Run	H1+	3571 keV	CN15x
2839	IFA	IFA028	Run	H1+	3540 keV	CN15x

Figure 7.7: RunDB user interface. The left pane allows the user to input search criteria. In this case, runs at IFA with an energy between 3 and 4 MeV. The right pane shows the query result. In this case, various runs with a proton beam and a CNx target.

searchable via a web page. The user interface can be seen in fig. 7.7. For instance, it is possible to search for all experiments at Aarhus, which were performed in 2016 with a  $^{11}\text{B}$  target.

Run UnPacker (RUP) works together with RunDB. It receives all the data files from the various experiments. Unpacks the files (see section 6.3) and notifies RunDB where both the raw and unpacked files can be found. In this manner, it is possible for the analyst to directly download the data files through RunDB.

## 7.9 Alternatives

The current trend in data acquisition for nuclear physics is a move towards free-running<sup>5</sup> digital DAQ. Essentially this corresponds to each detector channel being self-triggering i.e. digitization of a single data channel will occur if the input passes a certain threshold. This can be implemented using fast ( $\geq 50$  MHz) digitizers connected to an FPGA, which also can provide the full signal trace into the data stream. This could potentially also allow for detection and recovery of pile-up, which would allow experiments to run with higher rates. Examples of such systems can be found in refs. [184–187]. Generally, a free running DAQ will produce more data with a vast majority corresponding to uninteresting events. In order to reduce the data amount a software-defined global trigger can be implemented [188]. As the software-defined trigger has additional information available it can possibly perform a more sophisticated trigger decision than what is possible in hardware, while at the same time taking some fraction of data unfiltered in order to determine the effect of the trigger during offline analysis. Generally, as more functionality is moved from hardware to software/firmware it allows for more flexibility.

This is an area under fast development. The group has not transitioned yet but development in this direction is ongoing. So far, a small demonstration project has been built using a few GSI FEBEX modules [187].

---

<sup>5</sup>This is also called trigger-less. Although this is a misnomer.

## 7.10 Toggle mode

Until the acquisition is upgraded to a fully digital system one has to make the most of what is available. Due to its age, there are quite a few CAEN V785 [189] peak sensing ADCs available. However, their conversion time of  $\sim 7\mu\text{s}$  is quite slow compared  $\sim 1.6\mu\text{s}$ <sup>6</sup> for modern equipment such as the Mesytec MADC32 [190].

However, it is possible to mask some of this conversion time by connecting an input to two different ADCs and toggling between which one performs the conversion<sup>7</sup>. Thus ADC 1 would convert event 1 and ADC 2 would convert event 2 etc. This requires the concept of two separate gates and busies as illustrated in fig. 7.8. Operating in this manner the DAQ is only busy if both chains of modules are busy. Incidentally, it also increases the depth of the module buffer by a factor of 2.

The toggle handling has been incorporated into the TRLO II firmware by Håkan Johansson. A benchmark of the system using six CAEN V785

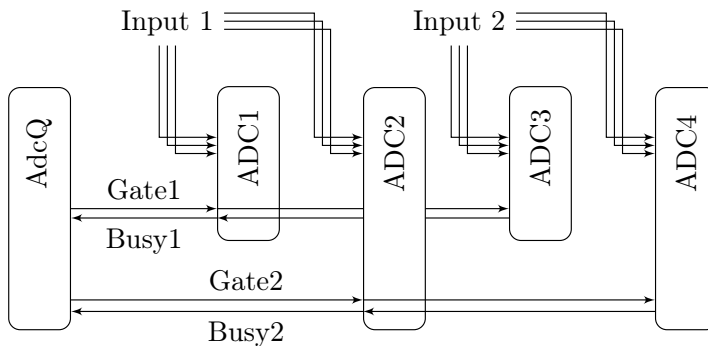


Figure 7.8: Illustration of toggle mode. Each input is connected to two ADCs. The AcqC will toggle between the two ADCs. Global busy is asserted when both sub-busies are asserted.

<sup>6</sup>MADC32 conversion time for 4k normal resolution which is what the V785 provides.

<sup>7</sup>Idea from Mesytec which provide similar a capability just with one module.

providing two data words per module per event is shown in fig. 7.9. The dashed curve in the figure shows the maximum theoretical performance of a non-toggling module. A vast improvement in the live-time fraction is observed for all frequencies. The effective conversion time is extracted from the best fit to eq. (7.1) (solid line) and is  $\sim 1 \mu\text{s}$ , i.e. comparable to modern state-of-the-art peak sensing ADCs.

## 7.11 Conclusion and outlook

In this chapter, I have described the various components that constitute the Aarhus DAQ. With the development described in the following paper,

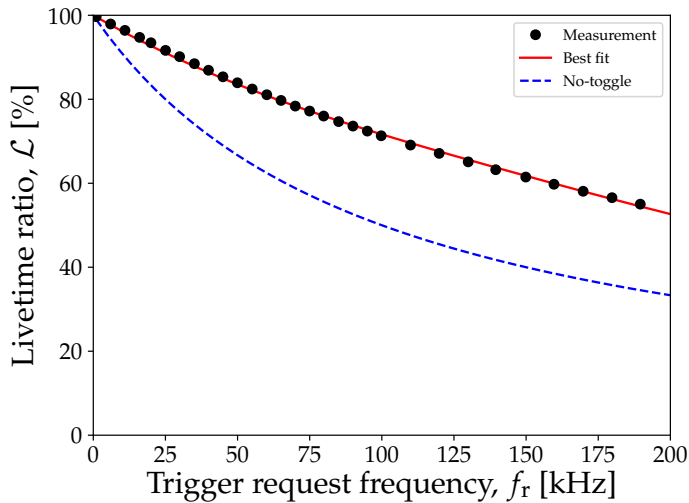


Figure 7.9: Measured live time fraction vs. trigger request frequency. Data points are the measured performance for the toggle system. The dashed line is the theoretical live time fraction for a stock CAEN V785. The solid line is the best fit to eq. (7.1). The conversion time per event is reduced from  $\sim 7 \mu\text{s}$  to  $\sim 1 \mu\text{s}$ .

I would estimate that this system is the current state-of-the-art in terms of speed for a VME-based DAQ with analog signal processing. With the development of especially DaqC and nurdlib the Aarhus DAQ is both versatile and user-friendly and the InfluxDB/grafana combination provides excellent monitoring capabilities.

An upcoming project is to replace the **Go4** based online analysis. The issue is that it is only possible to view predefined histograms. Instead, a system which allows the user to on-the-fly view property A versus property B under condition C for the last X minutes is highly desired. A prototype of such a system is under development by Bastian Löher, but some work is still required.

On a longer timescale, the current DAQ based on analog signal processing will most likely be replaced with a digital DAQ. However, this requires a serious investment, so the analog DAQ still has a place to fill for years to come.

## 7.12 Contribution

The work presented here is the result of close collaboration with multiple people, specifically Håkan Johansson, Hans Törnqvist, Bastian Löher and Jesper H. Jensen.

- DaqC and RunDB have been developed in collaboration with Jesper H. Jensen.
- drasi, TRLO II and ucesb are primarily developed by Håkan Johansson. I have contributed with a number of patches to the projects, but my main contribution has been real-life testing and pushing the envelope of their capabilities.
- nurdlib is primarily a creation of Bastian Löher and Hans Törnqvist. I have contributed with a significant number of patches related to the correct operation of various CAEN and Mesytec modules. The readout routines described in the following paper is based on a forked version of nurdlib.

- RUP is developed by me.

The following paper is based on an idea proposed by Håkan Johansson [191]. I have adapted `nurdlib` to work in this mode of operation and performed the majority of the system characterization. Jesper H. Jensen has extended this work to multiple crates and characterized the impact of network transfer. Additional testing was performed by Hans Törnqvist and Bastian Löher.



# VME Readout At and Below the Conversion Time Limit

M. Munch, J. H. Jensen, B. Löher, H. Törnqvist, and H. T. Johansson

**Abstract**—The achievable acquisition rates of modern triggered nuclear physics experiments are heavily dependent on the readout software, in addition to the limits given by the utilized hardware. This paper presents an asynchronous readout scheme that significantly improves the livetime of an otherwise synchronous triggered VME-based data acquisition system. A detailed performance analysis of this and other readout schemes, in terms of the basic data transfer operations, is described. The performance of the newly developed scheme as well as synchronous schemes on two systems has been measured. The measurements show excellent agreement with the detailed description. For the second system, which previously used a synchronous readout, the deadtime ratio is at a 20 kHz trigger request frequency reduced by 30 % compared to the nearest contender, allowing 10 % more events to be recorded in the same time. The interaction between the network and readout tasks for single-core processors is also investigated. A livetime ratio loss of a few percent can be observed, depending on the size of the data chunks given to the operating system kernel for network transfer. With appropriately chosen chunk size, the effect can be mitigated.

**Index Terms**—VME, data acquisition, nuclear physics, readout, asynchronous, livetime, deadtime, triggers, performance evaluation, buffering.

## I. INTRODUCTION

**M**OST modern nuclear physics experiments have detectors, front-end electronics, computer control, and network. The role of the front-end electronics is to digitize the detector signals such that they can be analyzed. Modular front-end electronics are typically housed in crates such as NIM, FASTBUS, CAMAC or VME, where the latter three also contain a bus on the crate backplane. A typical crate configuration consists of a group of front-end modules together with a controlling single board computer (SBC). The task of the SBC is to acquire data from the front-end modules and transfer it over the network to permanent storage and online

M. Munch and J. H. Jensen are with the Department of Physics and Astronomy, Aarhus University, 8000 Aarhus C, Denmark.

B. Löher and H. Törnqvist are with the Institut für Kernphysik, Technische Universität Darmstadt, 64289 Darmstadt, Germany, and the GSI Helmholtzzentrum für Schwerionenforschung GmbH, 64291 Darmstadt, Germany.

H. T. Johansson is with the Department of Physics, Chalmers University of Technology, SE-412 96 Göteborg, Sweden.

The work of M. Munch was supported by the European Research Council under ERC starting grant LOBENA, No. 307447.

The work of J. H. Jensen was supported by the Danish Council for Independent Research – Natural Sciences under grant DFF – 4181-00218.

B. Löher and H. Törnqvist were supported by the GSI-TU Darmstadt cooperation agreement.

The work of H. T. Johansson was supported by the Swedish Research Council under grant 822-2014-6644 and the Lars Hierta Memorial Foundation.

analysis. The speed, overhead, and serialization effects of this transfer naturally limit the maximum achievable acquisition rate, characterized by the rate of accepted triggers.

This article will focus on VME-based [1] readout systems. The purpose is not to introduce new electronics. Instead, we aim at better utilizing the commercially available modules by generally introducing an extreme asynchronous multi-event readout scheme called *shadow readout*. The main speedup is achieved by almost completely decoupling the readout from the conversion sequence, thereby significantly lowering the readout overhead associated with each accepted trigger. In addition, the coincidence information leading to each trigger is recorded, thus not sacrificing event selection flexibility for speed. It is also shown that the remaining system deadtime can be accurately described based on the timing of basic data transfer operations.

The article is structured in the following way: First, the existing solutions are reviewed, and the necessary concepts in order to model the deadtime and efficiency of the different readout modes are introduced. This is followed by a brief discussion of various modes of VME access. We then describe our implementation and the caveats that arise from having a single-core SBC. Finally, we benchmark the improved readout scheme versus the other strategies on two different systems.

Throughout the article, measured data are shown with point-like markers, and general trends of models are shown as curves.

## II. EXISTING SOLUTIONS

With CAMAC systems, LeCroy introduced fast readout using the FERA bus in the early 80s, which transfers data at 10 Mword/s (16-bit) [2]. With conversion times, at that time, usually around 3  $\mu$ s/channel or 25  $\mu$ s for an 8-channel module, a crate with 50 words of data per event (after zero-suppression) would be read out in 5  $\mu$ s. Thus the readout overhead was much smaller than the conversion time.

FASTBUS modules [3], even though known for their high channel density and thus long total module conversion times, usually had multi-event buffers, allowing readout of previous events while converting new ones, completely hiding the readout.

The current state of affairs for VME based readout systems is that nearly all front-end modules are capable of storing multiple converted events in an internal memory buffer. The Daresbury MIDAS [4] and BARC-TIFR LAMPS [5] utilize these buffers fully to decouple readout from conversion. In this

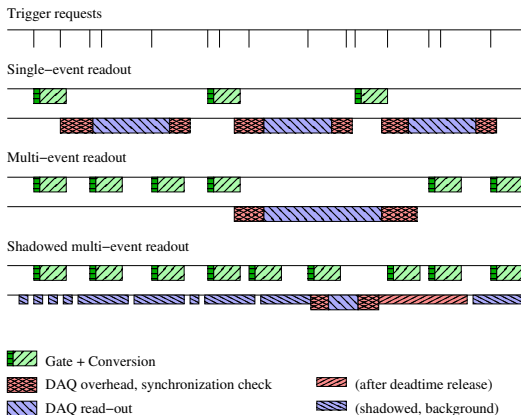


Fig. 1. Single, multi-event, and shadow multi-event readout. Multi-event readout allows event data to accumulate in the module buffers before readout, amortizing the overhead over several events. Shadow readout continuously empties the modules during conversions, thus reducing the work during global deadtime.

scheme, the module buffers are continuously emptied by the crate controller. Only if a module becomes full, will it assert a long busy; halting the acquisition until the SBC empties a part of the module buffer. This mode, however, is only available for the Silena S9418 front-end modules in MIDAS [6], and the LAMPS is hampered by large overhead times in the associated CAEN VME controller [7]. However, the above systems are exceptions, and the multi-event buffers are often not utilized to their full extent, or not at all. Fig. 1 illustrates the three principal modes in which a readout system can be operated when front-end modules have buffers. In the simplest case, the front-end acquires an event and waits for the readout to transfer it. This is called single-event mode. Typically, the data transfer will take significantly longer than the conversion time due to various overheads. These overheads can be partially amortized by filling the front-end buffers before performing a readout. This is called multi-event mode. However, the number of events that can be acquired in one go is limited to the shallowest buffer. To the best of our knowledge, common general-purpose nuclear physics data acquisition systems, such as MIDAS (PSI/TRIUMF) [8], MBS (GSI) [9], and RIBFDAQ (RIKEN) [10], use versions of these schemes, where the SBC must interact with the trigger logic for every readout round.

In order to minimize the transfer times, when running in single event mode, the Modular Controller (MOCO) [11] was recently developed at RIKEN. This innovative design is an adapter board with an FPGA and a USB interface which is installed between a front-end module and the VME crate backplane. With MOCO installed, the data lines of the front-end module are not connected to the backplane. Instead, the FPGA communicates directly with the front-end module. The FPGA can then transfer the data to the controlling computer via USB. The two main benefits of this solution are cost and parallelization of the readout of multiple modules.

In this article, we will show that a continuous readout mode,

operating beyond the depth of the multi-event buffers, can be applied generally, without introducing new electronics.

### III. DEADTIME MODELING

In this section, we develop a framework to describe the deadtime of a system. This model will be used to analyze the systems in Section VII.

Assume that the front-end electronics and readout system is provided with a stream of Poisson-distributed trigger requests, with an average frequency  $f_r$ , of which it can accept some frequency  $f_a$ . The livetime ratio is the fraction of accepted trigger requests:

$$\mathcal{L} = \frac{f_a}{f_r} = \frac{1}{1 + f_r \Delta t}. \quad (1)$$

$\Delta t$  is the amount of time per event that the system is blocked. The last equality assumes the deadtime to be non-extending, and the formula is derived in [12]. The livetime ratio is related to the deadtime ratio via  $\mathcal{D} = 1 - \mathcal{L} = f_a \Delta t$ .

We carefully differentiate between a system in deadtime and the deadtime ratio,  $\mathcal{D}$ . A system in deadtime rejects events while the deadtime ratio is the fraction of rejected events. The same differentiation is made between the livetime and the livetime ratio,  $\mathcal{L}$ .

It is often necessary to consider a distinct contribution to the total system deadtime: busy. Busy signals come from front-end modules, and is also autonomously released by those. It is generally asserted during gate and conversion, and when the data buffer of a module is full. The more regular deadtime is initiated by the trigger logic, and removed by the SBC readout software. As far as trigger acceptance is concerned, both have the same effect: inhibit triggers.

While running, the system must perform the following tasks (with associated processing times):

- 1) apply the gate of each accepted event,  $t_g$ ;
- 2) convert the event,  $t_c$ ;
- 3) poll for data,  $t_p$  (per poll);
- 4) readout overhead (e.g. determine data amount),  $t_o$ ;
- 5) read data,  $t_d$ ;
- 6) check module synchronicity,  $t_s$ ;
- 7) transfer data over the network,  $t_n$ .

The two first are handled by the front-end electronics, the other by the SBC. Some of the tasks happen during either live- or deadtime, depending on the design of the system. Thus the minimal deadtime ratio is given by the fraction of time modules are busy converting data:

$$\mathcal{B} = f_a(t_g + t_c). \quad (2)$$

If the system is designed such that it reads one single event at a time, and will not accept new events while reading data, then the readout time is  $(t_p + t_o + t_d + t_s)$ , since the system must poll for data, determine the amount of data, read the data and check for synchronicity. Since the likelihood that a random trigger request occurs during deadtime is simply the total fraction of time the system will not accept triggers, the deadtime ratio is

$$\mathcal{D} = \mathcal{B} + f_a(t_p + t_o + t_d + t_s). \quad (3)$$

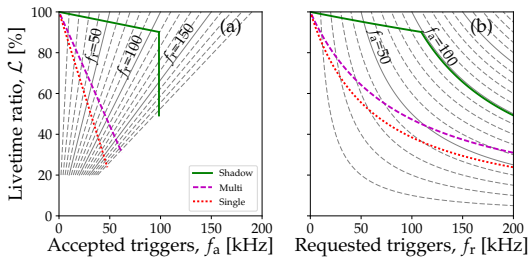


Fig. 2. Schematic performance of shadow, multi-event, and single-event modes, with  $t_d = 10 \mu\text{s}$ ,  $t_c = 1 \mu\text{s}$  and  $t_o = 5 \mu\text{s}$ . Both figures show the same systems, (a) as a function of  $f_a$  and (b) as a function of  $f_r$ . The background lines show constant  $f_r$  and  $f_a$ , respectively.

However, this scheme suffers the overhead of  $t_p + t_o + t_s$  for every event. If the front-end electronic modules have buffers of a certain depth  $n_b$ , then the cost of polling, general readout overhead, and synchronization can be amortized:

$$\mathcal{D} = \mathcal{B} + f_a \left( t_d + \frac{t_o + t_p + t_s}{n_b} \right). \quad (4)$$

This mode of operation is commonly referred to as multi-event mode with the former called single-event mode. In this case,  $t_d$  can often also be reduced as the larger amounts of data per transfer may profit from faster transfer modes.

If, however, the system can simultaneously accept new events and transfer data, then  $\mathcal{D}$  may be further reduced:

$$\mathcal{D} = \mathcal{B} + f_a \frac{\alpha t_d + t_o + t_p + t_s}{n_s}. \quad (5)$$

$n_s$  is the number of events accepted before synchronicity is checked and  $\alpha$  is the average number of events remaining to read out during deadline. The fraction of events read during deadline is thus  $\alpha/n_s$ .  $\alpha \geq 0$  but will typically only be a few events. It should be noted that  $n_b$  for many older modules is typically 32 or less, while newer modules might store a few hundred events. However,  $n_s$  can in principle be made arbitrarily large, and thus the deadline can be reduced to the busy time,  $\mathcal{D} \approx \mathcal{B}$ .

The above has not considered the available data transfer bandwidth, which may also limit the maximum event rate that can be accepted:

$$f_{a,\max} = \frac{1}{(t_d + \frac{t_o + t_p}{n_b} + \frac{t_s}{n_s})}. \quad (6)$$

In practice, the achievable frequency will be slightly lower due to various other overheads such as network transfer. Above this request frequency, the livetime ratio just deteriorates while no more events are accepted and is simply described:

$$\mathcal{L} = \frac{f_{a,\max}}{f_r}. \quad (7)$$

The livetime of the system is thus given by whichever of (1) or (7) is smaller:

$$\mathcal{L} = \min \left( \frac{1}{1 + f_r \Delta t}, \frac{f_{a,\max}}{f_r} \right). \quad (8)$$

TABLE I  
TRANSFER TIME OF TWO DIFFERENT SBCs WITH VARIOUS MODULES.

SBC	Module	SiCy	SiCy DMA	BLT	MBLT
MVME	DMA setup	-		16.7 ( $n = 1$ )	
	MTDC-32	1.21			
	MADC-32	1.26	0.49	0.44	0.33
	VULOM4b (TRLO II)	1.37	0.65		
RIO4	(M)BLT setup	-		6.5 + $n \cdot 4.3$	
	MTDC-32	0.40		0.17	0.09
	MADC-32	0.45		0.22	0.12
	VULOM4b (TRLO II)	0.60			
	V785	0.50		0.19	0.15
	V1190	0.45		0.18	0.10

Table I shows the measured transfer times in  $\mu\text{s}$  per 32-bit word for two different SBCs and various modules. The additional SBC setup overhead of starting DMA (direct memory access) or block transfers depend on how many,  $n$ , are scheduled at the same time. DMA allows multiple adjacent SiCy requests to be scheduled together on the MVME. The MTDC-32 [13] and MADC-32 [14] are from Mesytec, the V785 [15] and V1190 [16] from CAEN, and the VULOM4b [17] from GSI and is running the TRLO II firmware [18].

For shadow readout,  $\Delta t$  is expected to be approximately equal to the gate and conversion time  $t_g + t_c$ . The livetime characteristics of the different readout schemes are illustrated in Fig. 2, where also the hard limit nature of  $f_{a,\max}$  is clearly seen.

In practice, the transition between the two domains is smooth, and thus a smoothed minimum function should be used, e.g.

$$\min_k(x, y) = -\frac{1}{k} \ln(e^{-kx} + e^{-ky}). \quad (9)$$

With  $k$  as a smoothing factor.

#### IV. VME TRANSFER TIME

The time it takes for the basic operation of transferring a 32 bit-data word essentially determines  $t_p$ ,  $t_o$ ,  $t_d$ , and  $t_s$ . Generally, VME access can be divided into two categories, namely single cycle (SiCy) or block transfer, where the latter can transfer either 32 (BLT) or 64 (MBLT) bits at a time [1]. There is also 2eVME and 2eSST [19] (both are block transfer modes), but these are not widely supported in front-end modules.

SiCy transfers single data words with minimal overhead. Thus with module  $i$  producing  $d_i$  words, the data transfer time with SiCy reads is

$$t_d = \sum_i d_i t_{i,\text{SiCy}}. \quad (10)$$

Since the designs of the individual modules also affect the word transfer times,  $t_{\text{SiCy}}$  has a module dependence,  $t_{i,\text{SiCy}}$ . While block transfers are asymptotically faster per word ( $t_{i,\text{block}} < t_{i,\text{SiCy}}$ ), they may require significant setup times in the SBC:

$$t_d = \sum_i (t_{\text{setup}} + d_i t_{i,\text{block}}). \quad (11)$$

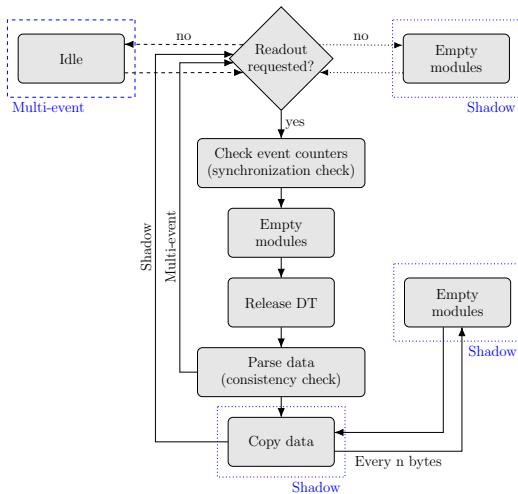


Fig. 3. Flow diagram for multi-event and shadow readout. In multi-event mode, idle time is spent doing nothing or work for other processes. In shadow mode, partial module readout is continuously performed. In both cases, the main readout will look for a readout request, which has asserted deadline and will then transfer the (remaining) data and ensure that all modules are in sync. Then deadline is released. Since data copy in shadow mode may be a lengthy process, the modules are regularly emptied during copying.

It is, however, possible to amortize this setup time by performing a so-called chained block transfer, whereby data is read from multiple modules during the same transfer<sup>1</sup>:

$$t_d = t_{\text{setup}} + \sum_i d_i t_{i,\text{block}}. \quad (12)$$

With  $c_i$  being the number of reads required to determine the amount of data and ensure synchronicity for each module,  $t_o + t_s$  can be expressed analogous to (10):

$$t_o + t_s = \sum_i c_i t_{i,\text{SiCy}}. \quad (13)$$

So far the discussion has been general. However, to evaluate actual systems, it is necessary to measure the transfer times. Table I shows the measured read transfer time for a selection of commercial modules when read using either a Motorola<sup>2</sup> MVME5500 [20] (MVME) or a CES<sup>3</sup> RIO4-8072 [21] (RIO4) SBC. Both are operated with a Linux kernel [22], [23], versions 2.4.21 and 2.6.33, respectively. These transfer times will be used in Section VII when modeling readout systems with these components.

Comparing the MVME and RIO4 SiCy transfer times in Table I, the RIO4 is generally three times faster per word. Note that the timing differences between modules for the same SBC are roughly equal for the two SBCs. This reflects the fact that

<sup>1</sup>Note that chained block transfers are not an additional VME transfer mode, but something some modules can be configured to arrange together, e.g. by using the IACK backplane chain for communicating a token between the modules.

<sup>2</sup>Motorola's Embedded Communications Computing business was acquired by Emerson in 2007.

<sup>3</sup>CES was acquired by Mercury Systems, Inc. in 2016.

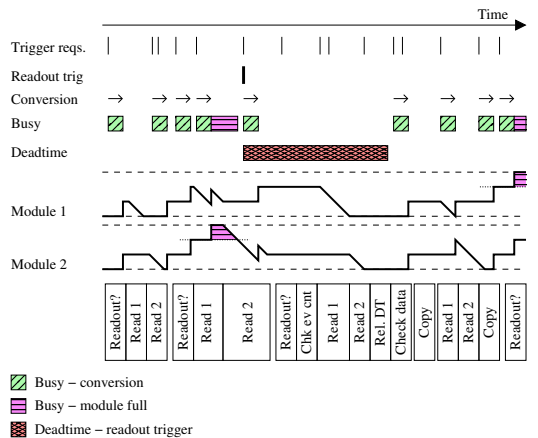


Fig. 4. Example of SBC activity during shadow readout. The SBC repeatedly empties module buffers. Thus, when entering deadline, the modules will be almost empty. While deadline is asserted, event counters will be checked and the little remaining data transferred. After deadline has been released, data will be consistency-checked and copied to the actual output buffer. The module graphs show their buffer fill levels. Busy is asserted both due to gate-conversion, and when any module buffer is full (above dotted lines). In this example, the module buffers can hold three events.

it is the module VME access handling that determines these differences.

The measurements also clearly show that (M)BLT is significantly faster per word than SiCy, but has a considerable setup overhead.

## V. IMPLEMENTATION

In Fig. 3 the work performed by the readout loop is sketched as a flow diagram. Generally, the SBC will either poll a register or be notified via an interrupt that a readout should be performed. The trigger logic has then asserted deadline. When the readout request is found, the SBC will check all module event counters and move the remaining data from all front-end modules to a CPU buffer. Then it can release the deadline, allowing the front-end modules to acquire more data while the SBC performs any further consistency checks of the acquired data. Afterward, it will resume waiting for the next readout request.

The difference between multi-event and shadow readout is the activities taking place while waiting for a readout request. In the multi-event case, the SBC is mostly idle, except for network transfer tasks.

The shadow readout on the other hand tries to continually transfer data from the front-end modules. This is illustrated for a two-module system in Fig. 4, which also shows the pausing when a module buffer becomes full and the deadline management.

In the simplest case, the data from each module is transferred to a separate buffer. This avoids potentially fragmenting events, and the collected data can easily be consistency checked. In this fashion, it is no longer needed to limit  $n_s$  to the module buffer depth  $n_b$ . Instead, the limitation for  $n_s$  is the

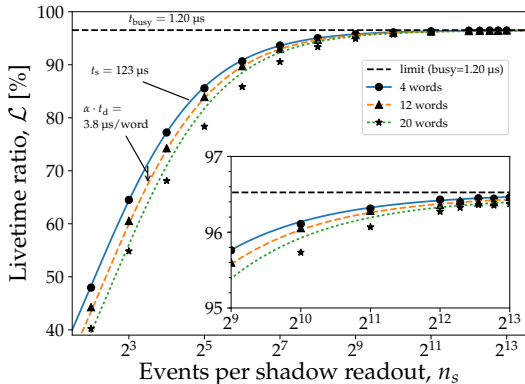


Fig. 5. The  $\mathcal{L}$  dependence on the number of events per shadow readout for an MVME and MADC-32 system with  $t_g + t_c = 1.2 \mu\text{s}$  and  $f_r = 30 \text{ kHz}$ .  $\mathcal{L}$  converges to the conversion limit (dashed horizontal line) when  $n_s$  is increased. With lower  $n_s$ , the overhead and synchronization time is amortized over fewer events. With larger event sizes (varying  $d_i$ ), the amount of remaining data to read during deadline after each  $n_s$  block of events increases.

available RAM and the desire to perform regular synchronicity checks. The dependence on  $n_s$  is illustrated in Fig. 5, which shows  $\mathcal{L}$  for a system which has a conversion time  $t_c = 1.2 \mu\text{s}$  (dashed horizontal line) and produced  $d_i = 4, 12$ , or 20 words per event with  $f_r = 30 \text{ kHz}$ . The figure shows two essential features of the shadow readout:  $\mathcal{L}$  converges towards the limit set by conversion times when  $n_s$  is increased. Additionally,  $\mathcal{L}$  only shows a weak dependence on event size with less than 0.5% variation in  $\mathcal{L}$  when  $n_s = 8 \text{ k}$ .

The virtual module buffers must eventually be copied to an output buffer. This is done after the consistency check as shown in the flow diagram. However, since a substantial amount of data may have been collected, this can easily take several milliseconds, which may be longer than module buffers can continue to store new events, causing them to assert busy signals. In order to avoid this, each module is assigned two memory buffers operated in a “ping-pong” fashion such that new data is transferred into the currently active buffer. When the modules have been emptied during deadtime, the other buffer becomes active and will be filled with new data. The data from the inactive buffer is copied in chunks interleaved with frequent calls to the shadow readout routine. This is illustrated with the read of the modules in-between the copy blocks in Fig. 4.

We have implemented this readout scheme with a modified version of the readout library `nurdlib` (formerly known as `vmelib`) [24]. When the readout polling is performed by the surrounding DAQ framework code, it is necessary to also modify that. The change essentially amounts to one single line of code—a callback routine to allow data transfers in the background while no readout request is detected.

Hardware requirements are the same for multi-event and shadow readout, i.e. there must be an acquisition control module that rejects events whenever deadline or busy is

TABLE II  
CPU TIME OF NETWORK CALLS

SBC	Buffer	Network CPU time
MVME5500	32Mi	$1.4 \mu\text{s} + w \cdot 8.8 \text{ ns}$
	64ki	$1.1 \mu\text{s} + w \cdot 3.3 \text{ ns}$
RIO4	32Mi	$4.5 \mu\text{s} + w \cdot 9.5 \text{ ns}$
	64ki	$2.3 \mu\text{s} + w \cdot 3.8 \text{ ns}$
E3-1286v6 (Intel x86, 4.5 GHz)	32Mi	$0.41 \mu\text{s} + w \cdot 0.091 \text{ ns}$
	64ki	$0.37 \mu\text{s} + w \cdot 0.065 \text{ ns}$

Table II shows the CPU time per network `write` call of  $w$  bytes for two different SBCs, and a modern server CPU for reference. The values are averages for either a large or a small buffer, the latter typically fitting in low-level CPU cache. The former are representative for DAQ network transfers from large event accumulation buffers.

asserted. This module, which issues the readout requests, must be able to keep track of how many events have been acquired and only request a deadtime-asserting readout after a sufficient number ( $n_s$ ). In our setup, all these tasks are performed by the TRLO II firmware [18] running on the GSI VULOM4b module [17].

To allow the most flexible use of the data from a multi-event readout system, it is necessary also to be able to record for each trigger the detector coincidences that caused the trigger to be selected. This trigger coincidence pattern is recorded for each event by the TRLO II firmware. In order to trust the system, it is also necessary to verify that each trigger has been seen by each module once (none lost, none spurious). This is done by comparing the event counters in the modules regularly, i.e. during each deadtime period. This is enough since a correctly working system would never have mismatches, making any deviation significant. `Nurdlib` already performs these checks strictly.

Note that shadow readout causes almost continuous activity on the VME backplane during analog conversion. We have found that this is no problem, provided that the electronic modules and pre-amplifiers etc. are properly grounded.

## VI. SINGLE CORE CAVEAT

Both the MVME and RIO4 have single-core processors, which poses some challenges related to the kernel scheduler of the operating system. The main issue is the conflict between readout and network transfer. The SBC must transfer the data to either an event builder or non-volatile storage, meaning time not spent emptying modules, see Table II. It will, therefore, lower the maximum rate that can be handled. However, before that, it can also impact the livetime of the system, if the network preparation happens in such large uninterrupted chunks that the module buffers become full. This is shown in Fig. 6, where  $\mathcal{L}$  drops by a few percent in the naive case where the network transfer is issued with too large buffers sent to the `write` system call. The kernel takes too long to complete the request, which causes the drop in  $\mathcal{L}$ . This can be mitigated by breaking the transfer preparation into multiple chunks, each with a call to `write` directly followed by yielding the timeslot of the network thread (by `sched_yield`). This allows the readout thread to cycle through the modules for each `write`.

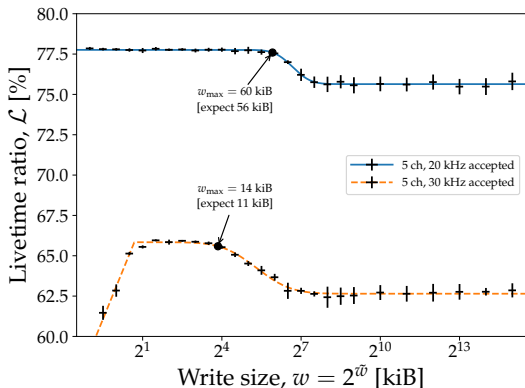


Fig. 6.  $\mathcal{L}$  as a function of network preparation chunk size  $w$ , for two different average trigger rates. The system consists of a RIO4 with a VULOM4b and six CAEN V785s, delivering 33 words per event (5 channels per ADC). When the chunk size exceeds  $w_{\max}$ , the livetime ratio drops due to module buffers occasionally becoming full while the CPU is occupied with network processing. Also, too small chunk sizes cause losses, due to CPU time lost on performing unnecessarily many calls.

The drop in  $\mathcal{L}$  can be described by considering the maximum time each network preparation chunk should take:

$$t_{n,\max} = \beta \frac{n_b}{f_{a,\max}} - \left( t_d + \frac{t_o}{n_b} \right). \quad (14)$$

The first term is the average time the module buffer can handle, and the second term the CPU time spent on the readout. The factor  $\beta$  accounts for the fact that a Poisson-distributed trigger will sometimes issue a burst of many triggers in an unusually short time interval than the long-term average, and thus fill the buffer more quickly.

The maximum time can, by using the values of Table II, also be expressed as a maximum chunk size, which can be used to control the network processing:

$$w_{\max} = 2^{\bar{w}_{\max}} = \frac{t_{n,\max}}{t_{\text{write}/B}}. \quad (15)$$

The drop in the livetime ratio as  $w$  exceeds  $w_{\max}$  (as shown in Fig. 6) can be fitted by

$$\mathcal{L}_1 = \mathcal{L}_{\max} - \mathcal{L}_{\text{drop}} \left( \frac{1}{2} + \frac{1}{2} \operatorname{erf} \frac{\bar{w} - \bar{w}_0}{\bar{w}_\sigma} \right). \quad (16)$$

We use the “error function” (erf) to describe the slight but measurable drop in  $\mathcal{L}$  around write size  $2^{\bar{w}_0}$ .

Using too small chunk sizes, however, will introduce a steep loss, due to the overhead of very many write calls. This is seen for the 30 kHz case in Fig. 6.

The above description has been checked for many combinations of trigger frequencies and event sizes, as presented in Fig. 7. For each case,  $w_{\max}$  has been determined from fits of (16) as in Fig. 6 with the value  $2^{\bar{w}_{\max}} = 2^{\bar{w}_0 - \bar{w}_\sigma}$ . The curves thus describe estimates of the maximum write size that can be used without affecting performance. At buffer sizes above 64 kiB, the fit assumes that the network overhead is

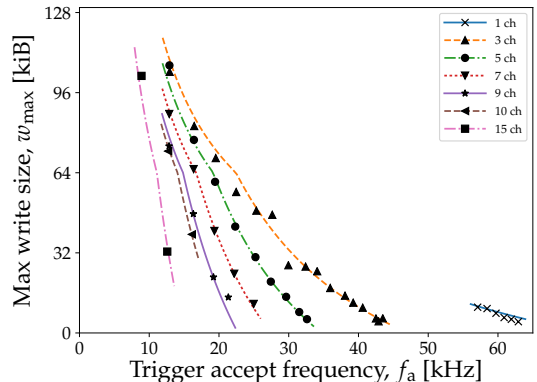


Fig. 7. The maximum chunk write size  $w_{\max}$  for the system in Fig. 6, determined for many combinations of event sizes and trigger rates. The event sizes are varied by activating a different number of channels in the ADCs.

twice as large, matching the measured data. We have however not been able to attribute this effect to a specific cause. The best fit value of  $\beta = 0.79$  corresponds to bursts happening 10% to 1% of times for  $f_a$  in the range 10 kHz to 50 kHz. The percentages were obtained from simulations of Poisson-distributed triggers taking a non-extending 10  $\mu$ s busy-time into account for stretches of  $n_b = 32$  accepted triggers.

Even if the negative impact on the livetime is only a few percent, mitigation is important since the effect is enhanced for multi-node systems as the trigger requests which become blocked on each node are independent. This cumulative effect is illustrated in Fig. 10(b).

This effect would not be an issue on a multi-core SBC, as one core would be dedicated to the readout, while another would handle non-critical tasks such as network transfers.

## VII. SYSTEM CHARACTERIZATION

In this section, we will benchmark the shadow readout system versus a regular multi-event readout system using two different sets of modules. Each set is part of actual experiments. The first system was used for the ISOLDE (CERN) [25] and the second one is the current system used at the Aarhus 5 MV accelerator.

In all cases, the trigger requests are either provided by a CAEN DT5800D detector emulator (pulser) [26], which can provide a Poisson distributed trigger sequence with a given rate, or by equivalent functionality directly in the trigger logic firmware. The trigger requests are sent to the VULOM4b running the TRLO II firmware, which handles the busy and deadtime logic. It also provides scaler values for the total number of trigger requests and the number of accepted requests.

Throughout the article, measured data are shown with point-like markers, and general trends of models are shown as curves. For illustration, some models are also evaluated for configurations that have not been tested.

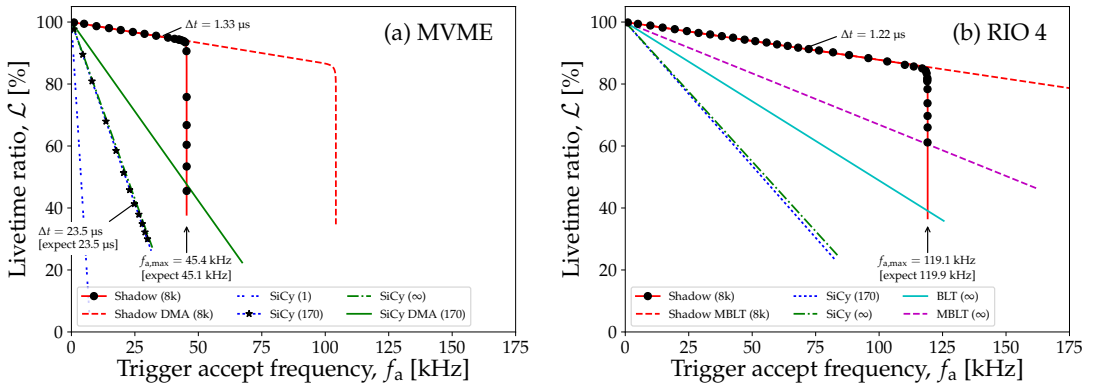


Fig. 8. Livetime ratio  $\mathcal{L}$  as a function of accepted trigger frequency for the MVME and RIO4 SBCs reading from the VULOM4b, MADC-32, and MTDC-32 using various readout modes, with in total 17 words per event. The round data points show the measured  $\mathcal{L}$  for shadow readout, while the stars are for multi-event mode, both with SiCy readout. The numbers in parentheses are the number of events accepted before the SBC readout function is invoked.  $\infty$  corresponds to the limit of zero overhead. Note that the lower performance of the MVME SBC, see Table I, only affects the maximum number of events taken,  $f_{a,\max}$ , not the per-event deadline at lower rates.

#### A. IS633 system

This is a simple configuration designed to run with very low deadline. It consists only of an SBC, VULOM4b, Mesytec MADC-32 and Mesytec MTDC-32. In order to achieve high livetime, the MADC is configured in bank toggle mode [14]. In this mode, the MADC toggles between which of its two ADCs that digitize the signals and can thus accept a new event while still processing the previous one. The gate was set to  $1\ \mu\text{s}$  and the module in 4k mode which has a conversion time of  $1.6\ \mu\text{s}$ . The module will thus only assert busy if three events arrive within a  $2.6\ \mu\text{s}$  window. However, in practice, pile-up is best avoided, and thus TRLO II emitted a  $1\ \mu\text{s}$  busy after every accepted event.

The modules were configured such that the VULOM4b produced 3 words of data per event, the MADC-32 12, and the MTDC-32 2. The busy was a logical OR between the three modules. The modules could store 170, 481, and 2891 events, respectively. An additional 66 words (mainly scaler values) were produced and read once per readout request.

1) *Multi-event mode*: Fig. 8 shows the livetime ratio as a function of the trigger request frequency when using either the MVME or RIO4. For the MVME,  $\mathcal{L}$  has been measured for multi-event mode using SiCy readout and a buffer depth of 170. The curve through the data points is (1) with  $\Delta t = 23.3\ \mu\text{s}$ . This corresponds to an effective  $t_c = 1.3\ \mu\text{s}$ , the expected  $t_d = 21.5\ \mu\text{s}$ , and a combined overhead per event of  $0.53\ \mu\text{s}$ . The green dash-dotted curve shows the expected behavior with zero overhead ( $\infty$  multi-events) and it would only provide a slight improvement since the data transfer dominates the deadline (curve overlaps with SiCy(170) in the figure). The RIO4 system would perform significantly better with a SiCy readout time per event of only  $8\ \mu\text{s}$ . Fig. 8(b) also shows the curves corresponding to 32- and 64-bit block transfer in the limit of zero overhead per event. Using block transfer, the per-event readout time would be reduced to 4.1

or  $2.3\ \mu\text{s}$ , respectively.

2) *Shadow mode*: Fig. 8 also shows the measured  $\mathcal{L}$  for shadow readout doing SiCy reads with a shadow buffer depth of 8192 events. Up to  $f_{a,\max}$ , the data points follow (1) with  $\Delta t$  roughly equal to the gate time. According to the models discussed earlier ((6) together with values from Section IV), the maximum accept frequency the MVME can sustain is  $46.4\ \text{kHz}$  while the RIO can handle  $125\ \text{kHz}$ . Note that up to the respective  $f_{a,\max}$ , the MVME and RIO4 deliver essentially the same livetime performance.

If the maximum bandwidth of SiCy transfers becomes the limiting factor, one could combine block transfer with shadow readout. The red dashed curves labeled *Shadow DMA* or *MBLT* in Fig. 8 show such configurations. In this case, the limiting factor is the block transfer overhead, with an expected  $f_{a,\max} = 388\ \text{kHz}$  for the RIO4 with this particular setup and number of channels.

#### B. Aarhus system

The other system consists of a RIO4, VULOM4b, and six CAEN V785 ADCs. This system is used at the Aarhus University 5 MV accelerator. To mimic actual production conditions, each ADC module was configured to produce 5 words per event while the VULOM4b produced 3. In total 33 words were produced per event with an additional 66 words produced once per readout.

The CAEN V785 has a 32-entry multi-event buffer and a total conversion time of  $7.06\ \mu\text{s}$ , which includes settling times etc. Additionally, a  $3\ \mu\text{s}$  gate is used. Hence, the expected deadline per trigger is  $10.06\ \mu\text{s}$ . It should also be noted that chained block transfer is not advantageous for the V785, as it only can deliver one event per transfer for these modules. Since we have more events than modules, we will instead model the simultaneous scheduling of 6 block transfers. This has an overhead of  $32\ \mu\text{s}$ , i.e.  $1\ \mu\text{s}$  per event.

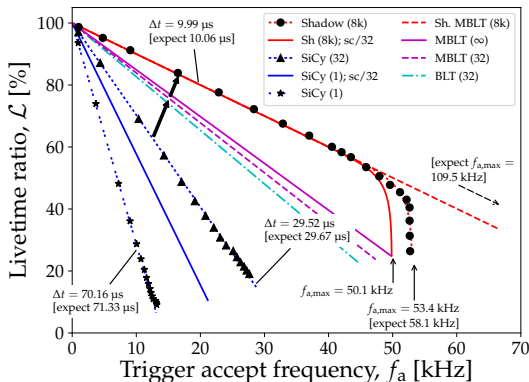


Fig. 9. Livetime ratio  $\mathcal{L}$  as a function of accepted trigger frequency for a RIO4 with a VULOM4b and six CAEN V785s for various readout modes. Each event consists of 33 words. The round data points show the measured  $\mathcal{L}$  for shadow readout. The numbers in parentheses are the number of events accepted before the SBC readout function is invoked.  $\infty$  corresponds to the limit of zero overhead. *sc/32* denotes that scaler data is recorded every 32 events, providing a fair comparison with multi-event readout. The values displayed are from fits, while the expected values are predictions based on the values in Table I. The thick arrows indicate the improvement obtained over the previously used multi-event mode at working conditions of 20 kHz requested trigger rate. The deadline ratio is halved and the accepted and thus recorded trigger rate increased by 30%.

In practice, readout with (M)BLT of the CAEN V785 is troublesome with some modern SBCs, since the data length cannot be queried beforehand and instead is marked with a VME `BERR*` signal. While allowed by the standard, this interacts badly with some SBC block transfer drivers since they do not report the number of actually transferred words, and thus obliterates much of the benefits. In the model, we have assumed that the SBC driver provides the needed information.

Another issue with (M)BLT of the CAEN V785 is that the busy release after conversion is delayed until the ongoing VME transfer has completed [27]. This will inflate the effective conversion time. This effect has also been ignored in the model.

Fig. 9 shows the results obtained for the shadow readout and the measured and estimated behavior of various multi-event modes. The SiCy data transfer time per event is 17  $\mu$ s, while BLT and MBLT take 6.3 and 5  $\mu$ s, respectively. This includes the block transfer overhead of  $\sim 15\%$  compared to the transfer time. However, even in the limit of zero overhead, block transfer does not converge to the limit of conversion and gate time. On the other hand, the data obtained show that SiCy shadow readout can maintain the limit and keep up with the data rate until  $\sim 53$  kHz, and to  $\sim 50$  kHz when scaler readout for every 32nd event is included.

### C. Network impact

The above measurements were done without network transport, in order to simplify the system descriptions. The data rates, at a few MB/s, do not use any significant CPU resources

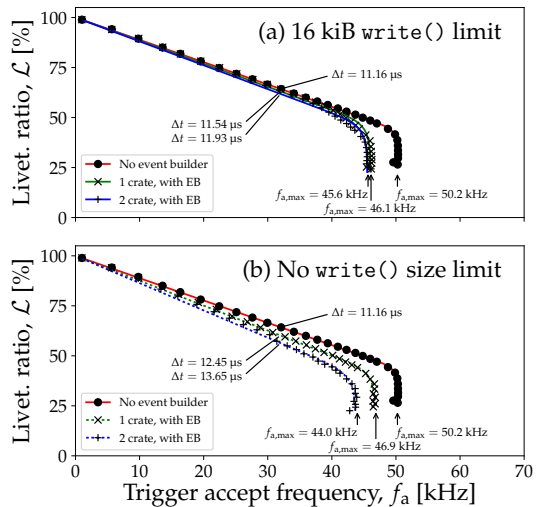


Fig. 10. Livetime ratio  $\mathcal{L}$  as a function of accepted trigger frequency for the same system as in Fig. 9, with network transport of data to a common event builder (cross markers), and a multi-crate system with two duplicate crates (plus markers). The measurement without network transport (circles) is also shown. In (a), the network `write` calls are limited to 16 kiB. Note that before  $f_{a,\max}$  is reached,  $\mathcal{L}$  is in all cases essentially given by  $\mathcal{B}$ , i.e. it is virtually unaffected by the network transport. In (b), the network `write` calls have no limit and thus cause additional downtime due to module buffers becoming full while the CPU is busy with network processing. The additional downtime occurs for independent events, accumulating the effect for multi-crate systems.

for network processing. This is seen in Fig. 10(a) for a single-crate system with and without network transport, where the network overhead due to sending 6.3 MB/s in 16 kiB chunks should use 6.1% CPU time according to Table II. The lowering of  $f_{a,\max}$  from 50.2 kHz to 46.1 kHz corresponds to 8.2%.

### D. Multi-crate system

The shadow readout mode can also be applied to multi-crate systems. The Aarhus system described above (RIO4, VULOM4b, and six CAEN ADCs) was duplicated in a second crate, and is operated together with the first in a master-slave configuration. The data from both systems are sent to an event builder PC for merging. The master start signal is used to generate gates for the modules in both crates for each trigger. The master crate generates the readout triggers, and by means of a TRIVA [28] mimic connection [18] they are distributed to be handled simultaneously by the slave system. The readout deadline is the logical OR combination of the deadline in the two systems. The busy signals are handled similarly, i.e. busy reported by any module in the total system inhibits further triggers.

The upper plot in Fig. 10 shows that the trigger and shadow readout operation is virtually unaffected by the second crate provided that the execution time of each network `write` call is limited. The lower plot shows how stalls due to too long network processing that happen at independent events cause losses that scale with the number of involved readout nodes.



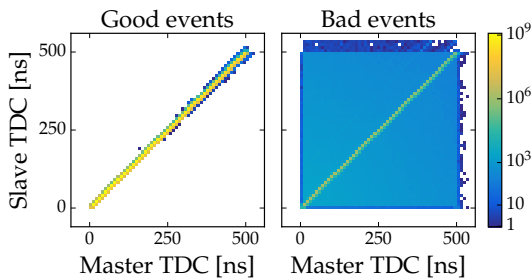


Fig. 11. The clean diagonal line demonstrates the ability to detect and discard spurious triggers in a multi-crate system. Shown is the simultaneous measurement of  $3.1 \cdot 10^{10}$  events with the same signal in both the master and slave system. Here, the slave system has in addition to the correct common triggers also intentionally received a low rate of spurious, i.e. wrong, master starts. This gives rise to  $4.2 \cdot 10^7$  bad events. Potentially bad events are, within each shadow readout block of events, detected by event count mismatches between the data from the systems.

### E. Multi-crate event correlations

In any multi-event readout scheme, event mixing is a potential cause of severe data corruption, which can look deceptively correct. By having taken multi-event to the extreme, shadow readout is particularly exposed to this. Multi-crate systems naturally also have more vulnerable components.

To show that the regular synchronisation and event counter checks are effective against unintentional event-mixing due to spurious triggers also in shadow readout multi-crate systems, a two-crate system, each with one TDC (CAEN V775), was set up. The TDCs are as usual given the same start signal, and one channel in each TDC is fed the same stop signal, which should give a 1:1 correlation graph for corresponding events, see Fig. 11(a). The stop signal is generated from the start with a random delay of 0 ns to 500 ns.

To inject errors, spurious triggers are injected with about 1 Hz in the slave system and its TDC. This introduces additional events from the slave TDC, which cause following events to be erroneously combined between the two systems, until the next synchronization check.

Potentially bad events are separated from the presumed good ones during analysis by the detection of event counter mismatches between the master and slave systems. This is seen in Fig. 11(a), where no mixed correlations are observed among the presumed good events. The bad events still have a pronounced diagonal, since only events in a readout block after the spurious trigger are affected, while the detection granularity is entire readout blocks.

## VIII. CONCLUSION AND OUTLOOK

Three principle ways to operate VME-based readout systems for multi-event capable digital acquisition modules have been described. These schemes are single-event, multi-event, and shadow readout. The necessary considerations to describe the performance of these schemes in terms of total system deadtime, based on the timing of individual operations, have been detailed. From these considerations, it is expected that the deadtime ratio for a scheme in which data readout is

performed asynchronously to the conversion should converge to the limit of the busy time of the front-end electronics. An implementation of such a scheme was then presented in some detail, and it was shown that the deadtime ratio converges—as long as the VME bus has sufficient bandwidth for the total data rate, using either single-cycle access or block transfer. Finally, a benchmark of two different systems with shadow readout was shown. In both cases, the shadow readout scheme achieved higher livetime than the alternative readout schemes, even when the latter used faster block transfer modes.

At the time of writing, a shadow readout system has been running for several months at the Aarhus University 5 MV accelerator without problems, and the methods have been successfully used for the IS633 and IS616 experiments at CERN ISOLDE.

### ACKNOWLEDGMENT

The authors would like to extend their thanks to Dr. N. Kurz for the work to provide a stable Linux environment with block transfer modes for the RIO4 SBC. The authors would like to extend their thanks to the Daresbury NPG for providing the MVME Linux environment.

### REFERENCES

- [1] *American National Standard for VME64*, ANSI/VITA Standard 1.0-1994 (S2011), 1994.
- [2] *CAMAC Model 4300B, 16 Channel, Fast Encoding and Readout ADC (FERA)*, LeCroy, Chestnut Ridge, NY, 1986.
- [3] R. Larsen, "Introduction to the FASTBUS standard data bus," *Interfaces in Computing*, vol. 1, no. 1, pp. 19–31, 1982.
- [4] V. Pucknell and D. Laff, "MIDAS the Multi Instance Data Acquisition System." [Online]. Available: <http://npg.dl.ac.uk/MIDAS/>
- [5] A. Kumar, A. Chatterjee, K. Mahata, and K. Ramachandran, "Development of Data Acquisition Software for VME Based System," in *Proc. of PCaPAC2012*, Kolkata, India, pp. 35–36.
- [6] *Silena 9418 Acquisition Control module*, accessed: 2018-04-18. [Online]. Available: <http://npg.dl.ac.uk/MIDAS/VME/sac.html>
- [7] K. Ramachandran, private communication, May 2018.
- [8] S. Ritt and P. Amaudruz, "The MIDAS data acquisition system," in *Proc. IEEE 10th Real Time Conf.*, 1997, pp. 309–312. [Online]. Available: [http://daq.triumf.ca/~daqweb/ftp/publications/rt97\\_paper.ps](http://daq.triumf.ca/~daqweb/ftp/publications/rt97_paper.ps)
- [9] H. G. Essel and N. Kurz, "The general purpose data acquisition system MBS," *IEEE Trans. Nucl. Sci.*, vol. 47, no. 2, pp. 337–339, 2000.
- [10] H. Baba *et al.*, "New data acquisition system for the RIKEN Radioactive Isotope Beam Factory," *Nucl. Instrum. Methods Phys. Res. A*, vol. 616, no. 1, pp. 65–68, 2010.
- [11] —, "Parallel Readout VME DAQ system," *RIKEN Accelerator Progress Report*, vol. 50, p. 224, 2017.
- [12] G. F. Knoll, *Radiation Detection And Measurement*, 4th ed. Wiley, 2010.
- [13] *Mesytec TDC data sheet V2.6*, mesytec GmbH & Co. KG, Putzbrunn, Germany, accessed: 2018-08-28. [Online]. Available: <https://www.mesytec.com/products/datasheets/MTDC-32.pdf>
- [14] *Mesytec ADC data sheet V2.1*, mesytec GmbH & Co. KG, Putzbrunn, Germany, accessed: 2018-08-28. [Online]. Available: <https://www.mesytec.com/products/datasheets/MADC-32.pdf>
- [15] *Mod. V785, 16/32 Channel Peak Sensing ADC*, CAEN, Feb 2012.
- [16] *Mod. V1190, Multihit TDC*, CAEN, Nov 2016.
- [17] J. Hoffman, *VULOM4b data sheet*, 2013, accessed: 2017-05-10. [Online]. Available: [http://www.gsi.de/fileadmin/EE/Module/VULOM/vulom4b\\_3.pdf](http://www.gsi.de/fileadmin/EE/Module/VULOM/vulom4b_3.pdf)
- [18] H. T. Johansson, M. Heil, B. Löher, H. Simon, and H. Törnqvist, "TRLO II - friendly FPGA trigger control," in *GSI Scientific Report 2013*. Darmstadt, Germany: GSI, 2014, p. 354. [Online]. Available: <http://repository.gsi.de/record/68045>
- [19] *2eSST*, ANSI/VITA Standard 1.5-2003 (S2014), 2003.

- [20] *MVME5500 Single-Board Computer Programmer's Reference Guide*, Motorola Inc., Tempe, AZ, Oct 2003. [Online]. Available: <http://npg.dl.ac.uk/documents/edoc249/reference.pdf>
- [21] *RIO4-8072 User Manual, version 1.0*, CES, Geneva, Switzerland, Nov 2009.
- [22] "Installation of MIDAS application packages for MVME5500 Linux," Feb 2005, accessed: 2018-09-23. [Online]. Available: <http://npg.dl.ac.uk/MIDAS/download/mcglinux.html>
- [23] N. Kurz and J. Adamczewski-Musch, *GSI Data Acquisition System MBS Release Notes V6.2*, GSI, Darmstadt, Germany, Apr 2013.
- [24] B. Löher, A. Charpy, H. T. Johansson, H. Simon, and H. Törnqvist, "The DAQ readout library vmeLib," in *GSI Scientific Report 2014*. Darmstadt, Germany: GSI, 2015, p. 192. [Online]. Available: <http://repository.gsi.de/record/183940>
- [25] R. Catherall *et al.*, "The ISOLDE facility," *Journal of Physics G: Nuclear and Particle Physics*, vol. 44, no. 9, p. 094002, sep 2017.
- [26] *User Manual UM3074, Digital Detector Emulator*, CAEN, Jan 2016.
- [27] CAEN, private communication, April 2018.
- [28] J. Hoffmann, N. Kurz, and M. Richter, *TRIVA, VME Trigger Module*, GSI, Darmstadt, Germany, 2007.

## Summary and outlook

In this thesis I have summarized and elaborated on four different experiments. With the  $^{23}\text{Na}(\alpha, p)$  experiment we found that the spectacular claims of Almaraz-Calderon *et al.* were not correct. With the  $^{12}\text{B}$   $\beta$  decay experiment we found the updated value proposed by Hyldegaard was indeed correct. In the  $^7\text{Li}(p, \gamma)$  experiment we managed to measure the full excitation spectrum above 1 MeV. The subsequent R-matrix analysis led to a tentative  $0^+$  state in  $^8\text{Be}$ , which interestingly coincides with No Core Shell Model calculations. With the  $^{11}\text{B}(p, 3\alpha)$  experiment we clarified the situation with multiple inconsistent results for the 16.1 MeV resonance. Specifically we found that the entire  $\alpha_1$  dataset from Becker *et al.* should be rescaled by a factor of  $2/3$  and the value for  $\Gamma_{\gamma,0}$  measured by Friebe *et al.* is most likely off by roughly a factor of two. On the technical side I have shown the power of an analysis pipeline, allowing a large part of the analysis code to be written once. For the data acquisition I have explained various components and their interactions. With the latest upgrade to shadow readout I believe the system is as good as it gets.

Except for the  $^{23}\text{Na}(\alpha, p)$  experiment, which have now been measured by three independent groups, the remaining experiments point forwards to new experiments. With the Aarhus University Van de Graaf able to accelerate ions of  $^1\text{H}$ ,  $^3\text{He}$  and  $^4\text{He}$  over a potential between approximately 0.1 and 4 MV there is quite a few options considering beam time is not a limiting factor. For  $^{11}\text{B}(p, 3\alpha)$  data have already been acquired between 0.5

and 3.5 MeV, but an analysis of the  $\alpha_1$  channel is going to be challenging. For  ${}^7\text{Li}(p, \gamma)$  data is being acquired at higher energies, but we are waiting for an enriched  ${}^7\text{Li}$  target. Data have been acquired for the  ${}^{15}\text{N} + p$  reaction and an analysis of the  $(p, \alpha)$  channel performed. However, a search for a  $4\alpha$  sequentially decaying via states in  ${}^8\text{Be}$  have yet to be carried out. Options such as  ${}^{10}\text{Be}(p, p')$  have also been discussed. With the recent upgrades of the data acquisition system and **AUSALib** having reached maturity for a long time we are in a good place to continue.

In addition to the experiments conducted at Aarhus University, I also had the chance to participate in an experiment at the  $\gamma$ -beam facility HI $\gamma$ S at Duke University. The experiment sought to measure the cross section for the  ${}^7\text{Li}(\gamma, \alpha)$  reaction motivated by recent *ab initio* calculations [192, 193]. The data analysis has been finalized but the normalization is still pending. In this context it is interesting to note that the ELI-NP  $\gamma$ -beam facility is coming online in the next few years promising an order of magnitude increase in intensity compare to HI $\gamma$ S. With such a facility it would be obvious to expand the investigations of the  ${}^{12}\text{C}(\gamma, \alpha)$  reaction in order to shed more light on the  $2^+$  Hoyle state excitation.

## List of Figures

2.1	Illustration of the $^{23}\text{Na}(\alpha, p)^{26}\text{Mg}$ reaction. A quasi-continuum of states in $^{27}\text{Al}$ is populated using the $^{23}\text{Na} + \alpha$ reaction. The excited state decays to $^{26}\text{Mg}$ via proton emission. . . . .	7
2.2	Proton spectra measured by Almaraz-Calderon <i>et al.</i> with the titanium background subtracted. Note that $p_1$ can only be distinguished for the highest two energies. For the lowest energy only an upper bound for $p_0$ was determined. Figure from ref. [17].	9
2.3	Comparison between all recent measurement of the $^{23}\text{Na}(\alpha, p)$ cross section [2, 17, 20–22]. Note that the result by AC have been rescaled. The result from Tomlinson <i>et al.</i> deviates slightly around 2.75 MeV. Figure from ref. [22]. . . . .	11
3.1	. . . . .	21
(a)	“Ikeda diagram” illustrating the different cluster configurations in four nucleon nuclei and their proposed energy. Figure from ref. [27]. . . . .	21
(b)	Comparison between theoretical and experimental level schemes. Note that the Hoyle state (7.65 MeV, $0^+$ ) is not reproduced. Figure from ref. [26]. . . . .	21

3.2	Observed cluster structures in AMD calculations of $^{12}\text{C}$ . The figures shows the density in a plane for the lowest three $0^+$ states. Note the $\alpha + {}^8\text{Be}$ structure of the Hoyle state while the ground state (GS) looks like a compressed triangle. Figure from ref. [40].	24
3.3	Observed $^{12}\text{C}$ excitation spectrum in the $\beta$ decay of $^{12}\text{N}$ . This spectrum is for $^{12}\text{C}$ break-up through the ${}^8\text{Be}$ GS. Note the broad featureless nature of most of the spectrum. Figure from ref. [52].	27
3.4	The level profile of the Hoyle state for decays via $\alpha + {}^8\text{Be}(\text{GS})$ . The peak height is normalized to 1 and the axis truncated. The high energy tail is called the “ghost anomaly” and the peak to tail ratio is roughly 10:1. The different curves correspond to different widths of the Hoyle state.	27
3.5	Illustration of the radiative decay of the Hoyle state. It can either $\gamma$ decay via the first excited state (FES), which subsequently decays to the GS. Alternatively, it may decay directly to the GS by emitting an $e^-e^+$ pair or a conversion electron. Both the GS and FES are fed in the $\beta$ decay of the $^{12}\text{B}$ GS.	28
3.6	Calculated reaction rate with the Hoyle state, $3^-$ and $2^+$ . The $3^-$ state has a small impact for energies above 0.25 MeV, while the $2^+$ has a significant impact irrespective of its location. Figure from ref. [48].	30
4.1	The lower part of the ${}^8\text{Be}$ level scheme. All levels are unbound. The three lowest resonances are highly clustered. The $2^+$ doublet at 16.6 and 16.9 MeV is isospin mixed.	42
4.2	A radial square well potential of depth $V_0$ and width $R_0$ . The particle has a positive energy $E$ and is unbound.	45
4.3	Single particle resonances in $n + {}^7\text{Be}$ with $R_0 = 1.4 \text{ fm} \cdot (1^{1/3} + 7^{1/3}) \approx 4 \text{ fm}$ and $V_0 = 50 \text{ MeV}$ evaluated with eq. (4.7). Note in this simple picture the amplitude of the interior wave function can only be equal to the exterior amplitude.	47

4.4	The observed branching ratio for the $\beta$ decay of $^8\text{B}$ along with best fit to an R-matrix model (dashed red) with $2^+$ 3 MeV state (dotted blue), $2^+$ doublet (dot dashed purple) and a $2^+$ 37 MeV background pole (dot dashed green). Figure from ref. [86]. . .	49
4.5	The observed number of $2\alpha$ coincidences from the $\beta$ decay of $^8\text{B}$ by refs. [86, 95]. The most recent experiment improved the counting statistics by approximately a factor of 100. Figure courtesy of Andreas Gad [95]. . . . .	49
4.6	Recorded $\gamma$ spectrum using a Ge(Li) detector. The photopeak at 17.6 MeV from the GS transition is visible, but the region below is dominated by escape peaks and Compton edges. The room background dominates the low energy region. Figure from ref. [79]. . . . .	51
4.7	Recorded $\gamma$ ray spectrum using the $12 \times 12$ -in NaI crystal BICRON. The transitions to the GS and FES are visible, but room background and response tails dominate the low energy spectrum. Figure from ref. [79]. . . . .	51
4.8	$\alpha$ -gated $\gamma$ ray spectrum observed in a $3 \times 3$ -in NaI crystal. The solid line gives the energy calibration. Figure from ref. [96]. . .	52
4.9	Position spectrum measured with a magnetic spectrometer and a position sensitive detector. The solid line is “approximate line shapes”. Figure from ref. [97]. . . . .	52
4.10	Illustration of the reaction. The 17.6 MeV resonance is populated using the $p + ^7\text{Li}$ reaction. The resonance might subsequently $\gamma$ decay to lower lying resonances or the continuum, which then $\alpha$ decays. $p + ^7\text{Li}$ may also couple directly to the $2\alpha$ channel. Figure from ref. [72] . . . . .	55
4.11	. . . . .	56
4.12	Difference in center-of-mass (CM) energy for all possible $\alpha\alpha$ pairs. The various circles shows different background reactions, while the dashed contour highlight the events corresponding to $\gamma$ -delayed $\alpha$ break-up. Figure from ref. [72]. . . . .	56
(a)	Detection efficiency as a function of $^8\text{Be}$ excitation energy. The efficiency is essentially flat and $\sim 6\%$ . . . . .	56

(b)	Observed peak from the direct $\alpha$ particles. With no response effects, a sharp 10 keV wide peak at 17.64 keV would be observed. . . . .	56
4.13	Observed excitation spectrum and best fit to the three different R-matrix models. Figure from ref. [72]. . . . .	60
5.1	$^{11}\text{B}(p, \alpha_0)$ cross section. Data from refs. [113–119] . . . . .	76
5.2	$^{11}\text{B}(p, \alpha_1)$ cross section. Data from refs. [113–116, 118] . . . . .	77
5.3	Dalitz plot with the coordinates defined in eq. (5.2). The triangle corresponds to energy conservation and the circle to momentum conservation. The blue bands sketch the naively expected distribution from a sequential decay. Note that the plot is six-fold symmetric and can be folded into a single sector. . . . .	79
5.4	Dalitz plot for the $2^+$ 16.1 MeV resonance corresponding to $E_p = 161$ keV. Note the filled center. Figure from ref. [127]. . . . .	80
5.5	Dalitz plot for the $2^-$ 16.6 MeV resonance corresponding to $E_p = 675$ keV. Note the plot is only filled along the lines corresponding to decays via the FES in $^8\text{Be}$ as decays via the GS is forbidden due to spin-parity conservation. Figure from ref. [128]. . . . .	80
5.6	Dalitz plot of the detected triplet of $\alpha$ particles. The circle indicates the constraints imposed by energy-momentum conservation. The dashed red line indicates the low energy cut-off. The dotted green line indicates the distinction between decays via the $\alpha_0$ (right) and $\alpha_1$ (left) channels. The coordinates are defined in eq. (5.2) and are unitless. . . . .	86
5.7	$^{11}\text{B}(p, \alpha_1)$ cross section. Axis truncated to 1 mb. Data from [113–116, 118]. Becker (1987) has been scaled by 2/3. Beckman (1953) appears to have an energy calibration issue. . . . .	86
5.8	NACRE II [139] reaction rate in units of the NACRE [140] adopt value. The lower limit corresponds to the normalization of dividing by 3. As such, the recommended value by NACRE II is off by as much as a factor of 2. Figure from ref. [139]. . . . .	88



6.1	AUSALib detector hierarchy. The analyst will usually only work directly with the single or double-sided detector abstraction. . .	102
6.2	. . . . .	103
(a)	Geometry model for the SquareDSSD . . . . .	103
(b)	Geometry model for the RoundDSSD . . . . .	103
6.3	AUSALib analysis pipeline. The data acquisition system (DAQ) produces raw data, which is then unpacked, sorted, identified and in the end events are build. Each step, except the DAQ, produces a ROOT TTree structure, which can be analyzed. . .	105
6.4	Sorting pipeline. First, an optional user-defined input transformation is performed. This is followed by a calibration and matching step. . . . .	106
6.5	Illustration of the <i>greedy minimal difference</i> algorithm for three hits in the front and two in the back. The algorithm computes the difference between all front and back hits and picks the pair with the lowest difference. A hit is only used once. In the example, the green pairs have been selected. The small numbers in the upper right corner show the picking order. . . . .	107
6.6	“Banana plot” showing the energy in the thin front detector vs. the full energy. The hyperbolic shape of the bands corresponds to the $1/\beta^2$ dependence of the Bethe-Bloch formula. The cosine factor corrects for differences in effective detector thickness. From this plot, it is possible to identify five different isotopes. Figure courtesy of Jesper Halkjær. . . . .	109
6.7	Comparison of the full energy of an $\alpha$ particle through 500 nm silicon. The difference between ICRU and SRIM amount to 7 keV at the peak. Note the oscillations of the cubic spline at the peak.	111
6.8	Model of detector dead layers. The detector will measure the energy deposited in the active region. Thus, loss in the inactive dead layer or the electrode grid will lower the measured energy. The thickness of the grid is approximately 200 nm [161]. . . . .	113
6.9	Example spectrum for a single strip for a $^{148}\text{Gd}$ , $^{239}\text{Pu}$ and $^{244}\text{Cm}$ source. Each isotope gives rise to a nearly mono-energetic peak. . . . .	114

- 6.10 Close-up of the  $^{244}\text{Cm}$  peak shows the peak sub-structure. The small structure below the peak is from  $\alpha$  particles passing through the electrode grid on the W1 detector surface. This peak is not included in the fit. The remaining structure is intrinsic to the isotope. . . . . 115
- 7.1 Schematic overview of the different DAQ elements. The detector output is connected to discriminators and amplifiers. The amplified signal is given to digitization modules, which will perform a conversion if triggered by the acquisition control. The readout empties the digitization modules and sends the data over the network to the back-end relay where it is recorded and online analysis performed. Figure adapted from Jesper Halkjær. . . . 120
- 7.2 Overview of the many tasks of the acquisition control (AcqC). The AcqC receives trigger requests from the individual detectors. These must be combined into a **MASTER\_START** (MS) with gates and triggers for the digitization modules. The AcqC must respect the busy and dead time (DT) from the modules and the readout. The AcqC must also periodically trigger the readout software, which checks module synchronicity. . . . . 123
- 7.3 Illustration of a two crate DAQ. Each crate is essentially identical to a single crate DAQ as seen in fig. 7.2. All trigger decisions are handled by the master AcqC and propagated to the slave AcqC. Slave busy and DT are propagated to the master. This design can be extended to multiple slaves. . . . . 127
- 7.4 Go4cesb event pipeline. A **ucesb** unpacker receives a data stream from the relay and performs the unpacking. The unpacked data is sent to the **Go4** process via a UNIX pipe. Inside the **Go4** process, the unpacked data is matched and then handed to the user for analysis. . . . . 129
- 7.5 Graphical user interface as presented by DaqC. (1) gives the status of the various service i.e. if the Single Board Computer (SBC) is online, whether the relay is running etc. (2) shows the current active trigger. (3) allows the operator to start a new file. 130

7.6 Number of  $\alpha$  particles observed in five different detectors per 10 s. The full range of the ordinate is 24 hours. A slow downward trend can be observed from the thick red line at 16:00 and forward. This was due to target deterioration. . . . . 132

7.7 RunDB user interface. The left pane allows the user to input search criteria. In this case, runs at IFA with an energy between 3 and 4 MeV. The right pane shows the query result. In this case, various runs with a proton beam and a CNx target. . . . 133

7.8 Illustration of toggle mode. Each input is connected to two ADCs. The AcqC will toggle between the two ADCs. Global busy is asserted when both sub-busies are asserted. . . . . 135

7.9 Measured live time fraction vs. trigger request frequency. Data points are the measured performance for the toggle system. The dashed line is the theoretical live time fraction for a stock CAEN V785. The solid line is the best fit to eq. (7.1). The conversion time per event is reduced from  $\sim 7 \mu\text{s}$  to  $\sim 1 \mu\text{s}$ . . . . . 136



## Abbreviations

<b>AcqC</b>	acquisition control
<b>ADC</b>	Analog to Digital Converter
<b>AGB</b>	asymptotic giant branch
<b>CM</b>	center-of-mass
<b>DAQ</b>	data acquisition system
<b>DaqC</b>	Daq Controller
<b>DSSD</b>	double-sided silicon strip detector
<b>DT</b>	dead time
<b>FES</b>	first excited state
<b>FWHM</b>	full width at half max
<b>GFMC</b>	Green's function Monte Carlo
<b>GS</b>	ground state
<b>lmd</b>	list mode data
<b>MS</b>	MASTER_START

**NCSM** No Core Shell Model

**nfs** network file system

**PEP** Pauli Exclusion Principle

**SBC** Single Board Computer

**SSSD** single-sided silicon strip detector

**TDC** Time to Digital Converter

**VdG** Van de Graaff

## Bibliography

- [1] F. C. Barker. *Australian Journal of Physics* 41 (1988), p. 743. DOI: [10.1071/PH880743](https://doi.org/10.1071/PH880743).
- [2] A. M. Howard *et al.* *Physical Review Letters* 115 (2015), p. 052701. DOI: [10.1103/PhysRevLett.115.052701](https://doi.org/10.1103/PhysRevLett.115.052701). arXiv: [1506.05983](https://arxiv.org/abs/1506.05983).
- [3] A. Coc, J.-P. Uzan, and E. Vangioni. *Journal of Cosmology and Astroparticle Physics* 2014 (2014), pp. 050–050. DOI: [10.1088/1475-7516/2014/10/050](https://doi.org/10.1088/1475-7516/2014/10/050). arXiv: [1403.6694](https://arxiv.org/abs/1403.6694).
- [4] E. M. Burbidge *et al.* *Reviews of Modern Physics* 29 (1957), pp. 547–650. DOI: [10.1103/RevModPhys.29.547](https://doi.org/10.1103/RevModPhys.29.547).
- [5] F.-K. Thielemann *et al.* *Annual Review of Nuclear and Particle Science* 67 (2017), pp. 253–274. DOI: [10.1146/annurev-nucl-101916-123246](https://doi.org/10.1146/annurev-nucl-101916-123246). arXiv: [1710.02142](https://arxiv.org/abs/1710.02142).
- [6] S. P. W. Merrill. *The Astrophysical Journal* 116 (1952), p. 21. DOI: [10.1086/145589](https://doi.org/10.1086/145589).
- [7] W. A. Mahoney *et al.* *The Astrophysical Journal* 262 (1982), p. 742. DOI: [10.1086/160469](https://doi.org/10.1086/160469).
- [8] R. Diehl. *Reports on Progress in Physics* 76 (2013), p. 026301. DOI: [10.1088/0034-4885/76/2/026301](https://doi.org/10.1088/0034-4885/76/2/026301).
- [9] N. Prantzos and R. Diehl. *Physics Reports* 267 (1996), pp. 1–69. DOI: [10.1016/0370-1573\(95\)00055-0](https://doi.org/10.1016/0370-1573(95)00055-0).

- [10] R. Diehl *et al.* *Nature* 439 (2006), pp. 45–7. DOI: [10.1038/nature04364](https://doi.org/10.1038/nature04364).
- [11] S. Plueschke *et al.* (2001). arXiv: [astro-ph/0104047](https://arxiv.org/abs/astro-ph/0104047).
- [12] L. Bouchet, E. Jourdain, and J.-P. Roques. *The Astrophysical Journal* 801 (2015), p. 142. DOI: [10.1088/0004-637X/801/2/142](https://doi.org/10.1088/0004-637X/801/2/142).
- [13] J. Knödseder. *The Astrophysical Journal* 510 (1999), pp. 915–929. DOI: [10.1086/306601](https://doi.org/10.1086/306601).
- [14] C. Iliadis *et al.* *The Astrophysical Journal Supplement Series* 193 (2011), p. 16. DOI: [10.1088/0067-0049/193/1/16](https://doi.org/10.1088/0067-0049/193/1/16).
- [15] J. Kuperus. *Physica* 30 (1964), pp. 2253–2260. DOI: [10.1016/0031-8914\(64\)90052-7](https://doi.org/10.1016/0031-8914(64)90052-7).
- [16] D. P. Whitmire and C. N. Davids. *Physical Review C* 9 (1974), pp. 996–1001. DOI: [10.1103/PhysRevC.9.996](https://doi.org/10.1103/PhysRevC.9.996).
- [17] S. Almaraz-Calderon *et al.* *Physical Review Letters* 112 (2014), p. 152701. DOI: [10.1103/PhysRevLett.112.152701](https://doi.org/10.1103/PhysRevLett.112.152701).
- [18] T. Rauscher and F.-K. Thielemann. *Atomic Data and Nuclear Data Tables* 79 (2001), pp. 47–64. DOI: [10.1006/adnd.2001.0863](https://doi.org/10.1006/adnd.2001.0863).
- [19] P. Mohr. *The European Physical Journal A* 51 (2015), p. 56. DOI: [10.1140/epja/i2015-15056-5](https://doi.org/10.1140/epja/i2015-15056-5).
- [20] S. Almaraz-Calderon *et al.* *Physical Review Letters* 115 (2015), p. 179901. DOI: [10.1103/PhysRevLett.115.179901](https://doi.org/10.1103/PhysRevLett.115.179901).
- [21] J. R. Tomlinson *et al.* *Physical Review Letters* 115 (2015), p. 052702. DOI: [10.1103/PhysRevLett.115.052702](https://doi.org/10.1103/PhysRevLett.115.052702).
- [22] M. L. Avila *et al.* *Physical Review C* 94 (2016), p. 065804. DOI: [10.1103/PhysRevC.94.065804](https://doi.org/10.1103/PhysRevC.94.065804).
- [23] N. J. Hubbard. “Studies of the nuclear structure of  $^{12}\text{C}$  and the astrophysical production of  $^{23}\text{Na}$ .” PhD thesis. 2018.
- [24] F. Hoyle. *The Astrophysical Journal Supplement Series* 1 (1954), p. 121. DOI: [10.1086/190005](https://doi.org/10.1086/190005).



- [25] M. Munch *et al.* *Physical Review C* 93 (2016), p. 065803. DOI: [10.1103/PhysRevC.93.065803](https://doi.org/10.1103/PhysRevC.93.065803). arXiv: [1601.02853](https://arxiv.org/abs/1601.02853).
- [26] S. Karataglidis *et al.* *Physical Review C* 52 (1995), pp. 861–877. DOI: [10.1103/PhysRevC.52.861](https://doi.org/10.1103/PhysRevC.52.861).
- [27] K. Ikeda, N. Takigawa, and H. Horiuchi. *Progress of Theoretical Physics Supplement* E68 (1968), pp. 464–475. DOI: [10.1143/PTPS.E68.464](https://doi.org/10.1143/PTPS.E68.464).
- [28] P. Strehl and T. Schucan. *Physics Letters B* 27 (1968), pp. 641–643. DOI: [10.1016/0370-2693\(68\)90303-1](https://doi.org/10.1016/0370-2693(68)90303-1).
- [29] I. Sick and J. McCarthy. *Nuclear Physics A* 150 (1970), pp. 631–654. DOI: [10.1016/0375-9474\(70\)90423-9](https://doi.org/10.1016/0375-9474(70)90423-9).
- [30] A. Nakada, Y. Torizuka, and Y. Horikawa. *Physical Review Letters* 27 (1971), pp. 1102–1102. DOI: [10.1103/PhysRevLett.27.1102.2](https://doi.org/10.1103/PhysRevLett.27.1102.2).
- [31] A. Nakada, Y. Torizuka, and Y. Horikawa. *Physical Review Letters* 27 (1971), pp. 745–748. DOI: [10.1103/PhysRevLett.27.745](https://doi.org/10.1103/PhysRevLett.27.745).
- [32] J. Okołowicz, W. Nazarewicz, and M. Płoszajczak. *Fortschritte der Physik* 61 (2013), pp. 66–79. DOI: [10.1002/prop.201200127](https://doi.org/10.1002/prop.201200127). arXiv: [1207.6225](https://arxiv.org/abs/1207.6225).
- [33] D. Brink and C. Bloch. *Proceedings of the International School of Physics “Enrico Fermi” Course XXXVI*. 1966.
- [34] A. Tohsaki *et al.* *Nuclear Physics A* 738 (2004), pp. 259–263. DOI: [10.1016/J.NUCLPHYSA.2004.04.042](https://doi.org/10.1016/J.NUCLPHYSA.2004.04.042).
- [35] Y. Funaki *et al.* *Physical Review C* 80 (2009), p. 064326. DOI: [10.1103/PhysRevC.80.064326](https://doi.org/10.1103/PhysRevC.80.064326).
- [36] N. T. Zinner and A. S. Jensen. *Physical Review C* 78 (2008), p. 041306. DOI: [10.1103/PhysRevC.78.041306](https://doi.org/10.1103/PhysRevC.78.041306). arXiv: [0712.1191](https://arxiv.org/abs/0712.1191).
- [37] Y. Funaki *et al.* *The European Physical Journal A* 28 (2006), pp. 259–263. DOI: [10.1140/epja/i2006-10061-5](https://doi.org/10.1140/epja/i2006-10061-5).
- [38] Y. Kanada-En’yo and H. Horiuchi. *Progress of Theoretical Physics Supplement* 142 (2001), pp. 205–263. DOI: [10.1143/PTPS.142.205](https://doi.org/10.1143/PTPS.142.205).

- [39] R. Roth, T. Neff, and H. Feldmeier. *Progress in Particle and Nuclear Physics* 65 (2010), pp. 50–93. DOI: [10.1016/j.pnnp.2010.02.003](https://doi.org/10.1016/j.pnnp.2010.02.003). arXiv: [1003.3624](https://arxiv.org/abs/1003.3624).
- [40] Y. Kanada-En'yo. *Progress of Theoretical Physics* 117 (2007), pp. 655–680. DOI: [10.1143/PTP.117.655](https://doi.org/10.1143/PTP.117.655).
- [41] D. Dell'Aquila *et al.* *Physical Review Letters* 119 (2017), p. 132501. DOI: [10.1103/PhysRevLett.119.132501](https://doi.org/10.1103/PhysRevLett.119.132501).
- [42] R. Smith *et al.* *Physical Review Letters* 119 (2017), p. 132502. DOI: [10.1103/PhysRevLett.119.132502](https://doi.org/10.1103/PhysRevLett.119.132502).
- [43] J. Refsgaard *et al.* *Physics Letters B* 779 (2018), pp. 414–419. DOI: [10.1016/j.physletb.2018.02.031](https://doi.org/10.1016/j.physletb.2018.02.031). arXiv: [1712.05251](https://arxiv.org/abs/1712.05251).
- [44] Y. Funaki *et al.* *Physical Review C* 67 (2003), p. 051306. DOI: [10.1103/PhysRevC.67.051306](https://doi.org/10.1103/PhysRevC.67.051306).
- [45] Y. Funaki *et al.* *The European Physical Journal A* 24 (2005), pp. 321–342. DOI: [10.1140/epja/i2004-10238-x](https://doi.org/10.1140/epja/i2004-10238-x).
- [46] F. C. Barker and P. B. Treacy. *Nuclear Physics* 38 (1962), pp. 33–49. DOI: [10.1016/0029-5582\(62\)91014-3](https://doi.org/10.1016/0029-5582(62)91014-3).
- [47] M. Itoh *et al.* *Physical Review C* 84 (2011), p. 054308. DOI: [10.1103/PhysRevC.84.054308](https://doi.org/10.1103/PhysRevC.84.054308).
- [48] M. Freer *et al.* *Physical Review C* 80 (2009), p. 041303. DOI: [10.1103/PhysRevC.80.041303](https://doi.org/10.1103/PhysRevC.80.041303).
- [49] M. Freer *et al.* *Physical Review C* 86 (2012), p. 034320. DOI: [10.1103/PhysRevC.86.034320](https://doi.org/10.1103/PhysRevC.86.034320).
- [50] W. R. Zimmerman *et al.* *Physical Review Letters* 110 (2013), p. 152502. DOI: [10.1103/PhysRevLett.110.152502](https://doi.org/10.1103/PhysRevLett.110.152502).
- [51] W. R. Zimmerman. “Direct observation of the second 2+ state in  $^{12}\text{C}$ .” PhD thesis. University of Connecticut, 2013.
- [52] S. Hyldegaard *et al.* *Physical Review C* 81 (2010), p. 024303. DOI: [10.1103/PhysRevC.81.024303](https://doi.org/10.1103/PhysRevC.81.024303).

- [53] C. W. Cook *et al.* *Physical Review* 107 (1957), pp. 508–515. DOI: [10.1103/PhysRev.107.508](https://doi.org/10.1103/PhysRev.107.508).
- [54] D. E. Alburger. *Physical Review C* 16 (1977), pp. 2394–2400. DOI: [10.1103/PhysRevC.16.2394](https://doi.org/10.1103/PhysRevC.16.2394).
- [55] H. O. U. Fynbo *et al.* *Nature* 433 (2005), pp. 136–9. DOI: [10.1038/nature03219](https://doi.org/10.1038/nature03219).
- [56] C. Diget *et al.* *Nuclear Physics A* 760 (2005), pp. 3–18. DOI: [10.1016/j.nuclphysa.2005.05.159](https://doi.org/10.1016/j.nuclphysa.2005.05.159).
- [57] S. Hyldegaard *et al.* *Physics Letters B* 678 (2009), pp. 459–464. DOI: [10.1016/j.physletb.2009.06.064](https://doi.org/10.1016/j.physletb.2009.06.064).
- [58] F. Ajzenberg-Selove. *Nuclear Physics A* 506 (1990), pp. 1–158. DOI: [10.1016/0375-9474\(90\)90271-M](https://doi.org/10.1016/0375-9474(90)90271-M).
- [59] E. J. Öpik. *Stellar Models with Variable Composition. II. Sequences of Models with Energy Generation Proportional to the Fifteenth Power of Temperature*. DOI: [10.2307/20488524](https://doi.org/10.2307/20488524).
- [60] E. E. Salpeter. *The Astrophysical Journal* 115 (1952), p. 326. DOI: [10.1086/145546](https://doi.org/10.1086/145546).
- [61] J. Kelley, J. Purcell, and C. Sheu. *Nuclear Physics A* 968 (2017), pp. 71–253. DOI: [10.1016/J.NUCLPHYSA.2017.07.015](https://doi.org/10.1016/J.NUCLPHYSA.2017.07.015).
- [62] M. Chernykh *et al.* *Physical Review Letters* 105 (2010), p. 022501. DOI: [10.1103/PhysRevLett.105.022501](https://doi.org/10.1103/PhysRevLett.105.022501). arXiv: [1004.3877](https://arxiv.org/abs/1004.3877).
- [63] E. L. Brady and M. Deutsch. *Physical Review* 72 (1947), pp. 870–871. DOI: [10.1103/PhysRev.72.870](https://doi.org/10.1103/PhysRev.72.870).
- [64] J. Refsgaard. “Resonances, R-matrix - Rotations in  $^{12}\text{C}$ ?” PhD thesis. 2016.
- [65] B. M. Alshahrani. “Measurement of the radiative branching ratio for the Hoyle state using cascade gamma decays.” PhD thesis. Australian National University, 2016.

- [66] T. Kibedi. *Proceedings of XII International Symposium on Nuclei in the Cosmos — PoS(NIC XII)*. Trieste, Italy: Sissa Medialab, 2013, p. 203. DOI: [10.22323/1.146.0203](https://doi.org/10.22323/1.146.0203).
- [67] Y. Funaki *et al.* *Journal of Physics: Conference Series* 436 (2013), p. 012004. DOI: [10.1088/1742-6596/436/1/012004](https://doi.org/10.1088/1742-6596/436/1/012004).
- [68] Y. Funaki *et al.* *Physical Review Letters* 101 (2008), p. 082502. DOI: [10.1103/PhysRevLett.101.082502](https://doi.org/10.1103/PhysRevLett.101.082502).
- [69] K. C. W. Li *et al.* *Physical Review C* 95 (2017), p. 031302. DOI: [10.1103/PhysRevC.95.031302](https://doi.org/10.1103/PhysRevC.95.031302).
- [70] J. A. Swartz *et al.* *Proceedings of the 4th International Conference on the State of the Art in Nuclear Cluster Physics (SOTANCP4)*. 2018. arXiv: [1810.07053](https://arxiv.org/abs/1810.07053).
- [71] M. Alcorta *et al.* *EPJ Web of Conferences*. Vol. 66. EDP Sciences, 2014, p. 07001. DOI: [10.1051/epjconf/20146607001](https://doi.org/10.1051/epjconf/20146607001).
- [72] M. Munch *et al.* *Physics Letters B* 782 (2018), pp. 779–784. DOI: [10.1016/j.physletb.2018.06.013](https://doi.org/10.1016/j.physletb.2018.06.013). arXiv: [1802.10404](https://arxiv.org/abs/1802.10404).
- [73] J. D. Cockcroft and E. T. S. Walton. *Proceedings of the Royal Society A* 137 (1932), pp. 229–242. DOI: [10.1098/rspa.1932.0133](https://doi.org/10.1098/rspa.1932.0133).
- [74] D. Tilley *et al.* *Nuclear Physics A* 745 (2004), pp. 155–362. DOI: [10.1016/j.nuclphysa.2004.09.059](https://doi.org/10.1016/j.nuclphysa.2004.09.059).
- [75] S. Pastore *et al.* *Physical Review C* 90 (2014), p. 024321. DOI: [10.1103/PhysRevC.90.024321](https://doi.org/10.1103/PhysRevC.90.024321).
- [76] P. Descouvemont and D. Baye. *Reports on Progress in Physics* 73 (2010), p. 036301. DOI: [10.1088/0034-4885/73/3/036301](https://doi.org/10.1088/0034-4885/73/3/036301). arXiv: [1001.0678](https://arxiv.org/abs/1001.0678).
- [77] F. C. Barker, H. Hay, and P. Treacy. *Australian Journal of Physics* 21 (1968), p. 239. DOI: [10.1071/PH680239](https://doi.org/10.1071/PH680239).
- [78] F. C. Barker. *Australian Journal of Physics* 22 (1969), p. 293. DOI: [10.1071/PH690293](https://doi.org/10.1071/PH690293).

- [79] D. Zahnow *et al.* *Zeitschrift für Physik A Hadrons and Nuclei* 351 (1995), pp. 229–236. DOI: [10.1007/BF01289534](https://doi.org/10.1007/BF01289534).
- [80] J. Cerny, B. G. Harvey, and R. H. Pehl. *Nuclear Physics* 29 (1962), pp. 120–136. DOI: [10.1016/0029-5582\(62\)90171-2](https://doi.org/10.1016/0029-5582(62)90171-2).
- [81] E. K. Warburton. *Physical Review C* 33 (1986), pp. 303–313. DOI: [10.1103/PhysRevC.33.303](https://doi.org/10.1103/PhysRevC.33.303).
- [82] M. S. Fayache *et al.* *Physical Review C* 57 (1998), pp. 2351–2358. DOI: [10.1103/PhysRevC.57.2351](https://doi.org/10.1103/PhysRevC.57.2351).
- [83] J. Humblet, A. Csótó, and K. Langanke. *Nuclear Physics A* 638 (1998), pp. 714–726. DOI: [10.1016/S0375-9474\(98\)00419-9](https://doi.org/10.1016/S0375-9474(98)00419-9).
- [84] M. Bhattacharya and E. G. Adelberger. *Physical Review C* 65 (2002), p. 055502. DOI: [10.1103/PhysRevC.65.055502](https://doi.org/10.1103/PhysRevC.65.055502).
- [85] M. Bhattacharya, E. G. Adelberger, and H. E. Swanson. *Physical Review C* 73 (2006), p. 055802. DOI: [10.1103/PhysRevC.73.055802](https://doi.org/10.1103/PhysRevC.73.055802).
- [86] S. Hyldegaard. “Beta-decay studies of  $^8\text{Be}$  and  $^{12}\text{C}$ .” PhD thesis. Aarhus University, 2010.
- [87] M. S. Fayache *et al.* *Physical Review C* 59 (1999), pp. 2958–2959. DOI: [10.1103/PhysRevC.59.2958](https://doi.org/10.1103/PhysRevC.59.2958).
- [88] F. C. Barker. *Physical Review C* 59 (1999), pp. 2956–2957. DOI: [10.1103/PhysRevC.59.2956](https://doi.org/10.1103/PhysRevC.59.2956).
- [89] E. Caurier *et al.* *Physical Review C* 64 (2001), p. 051301. DOI: [10.1103/PhysRevC.64.051301](https://doi.org/10.1103/PhysRevC.64.051301).
- [90] P. Maris, J. P. Vary, and P. Navrátil. *Physical Review C* 87 (2013), p. 014327. DOI: [10.1103/PhysRevC.87.014327](https://doi.org/10.1103/PhysRevC.87.014327).
- [91] R. B. Wiringa *et al.* *Physical Review C* 88 (2013), p. 044333. DOI: [10.1103/PhysRevC.88.044333](https://doi.org/10.1103/PhysRevC.88.044333).
- [92] C. Iliadis. *Nuclear Physics of Stars*. Wiley-VCH, 2007. ISBN: 3527406026.
- [93] T. Berggren. *Nuclear Physics A* 109 (1968), pp. 265–287. DOI: [10.1016/0375-9474\(68\)90593-9](https://doi.org/10.1016/0375-9474(68)90593-9).

- [94] K. Fosseze *et al.* *Physical Review C* 96 (2017), p. 024308. DOI: [10.1103/PhysRevC.96.024308](https://doi.org/10.1103/PhysRevC.96.024308).
- [95] A. M. G. Gad. “An experimental study of the 8B  $\beta$  decay.” MA thesis. Aarhus University, 2018, p. 86.
- [96] P. Paul, D. Kohler, and K. A. Snover. *Physical Review* 173 (1968), pp. 919–930. DOI: [10.1103/PhysRev.173.919](https://doi.org/10.1103/PhysRev.173.919).
- [97] W. E. Sweeney and J. B. Marion. *Physical Review* 182 (1969), pp. 1007–1021. DOI: [10.1103/PhysRev.182.1007](https://doi.org/10.1103/PhysRev.182.1007).
- [98] T. W. Bonner and J. E. Evans. *Physical Review* 73 (1948), pp. 666–674. DOI: [10.1103/PhysRev.73.666](https://doi.org/10.1103/PhysRev.73.666).
- [99] W. A. Fowler, C. C. Lauritsen, and T. Lauritsen. *Reviews of Modern Physics* 20 (1948), pp. 236–277. DOI: [10.1103/RevModPhys.20.236](https://doi.org/10.1103/RevModPhys.20.236).
- [100] P. C. Price. *Proceedings of the Physical Society. Section A* 67 (1954), pp. 849–851. DOI: [10.1088/0370-1298/67/9/415](https://doi.org/10.1088/0370-1298/67/9/415).
- [101] B. Mainsbridge. *Nuclear Physics* 21 (1960), pp. 1–14. DOI: [10.1016/0029-5582\(60\)90023-7](https://doi.org/10.1016/0029-5582(60)90023-7).
- [102] B. Mainsbridge. *Australian Journal of Physics* 13 (1960), p. 204. DOI: [10.1071/PH600204](https://doi.org/10.1071/PH600204).
- [103] S. Cavallaro, R. Potenza, and A. Rubbino. *Nuclear Physics* 36 (1962), pp. 597–614. DOI: [10.1016/0029-5582\(62\)90486-8](https://doi.org/10.1016/0029-5582(62)90486-8).
- [104] J. Ulbricht *et al.* *Nuclear Physics A* 287 (1977), pp. 220–236. DOI: [10.1016/0375-9474\(77\)90493-6](https://doi.org/10.1016/0375-9474(77)90493-6).
- [105] O. S. Kirsebom *et al.* *Physics Letters B* 680 (2009), pp. 44–49. DOI: [10.1016/j.physletb.2009.08.034](https://doi.org/10.1016/j.physletb.2009.08.034).
- [106] K. L. Laursen *et al.* *The European Physical Journal A* 52 (2016), p. 370. DOI: [10.1140/epja/i2016-16370-0](https://doi.org/10.1140/epja/i2016-16370-0). arXiv: [1610.00509](https://arxiv.org/abs/1610.00509).
- [107] G. Bortels and P. Collaers. *International Journal of Radiation Applications and Instrumentation. Part A. Applied Radiation and Isotopes* 38 (1987), pp. 831–837. DOI: [10.1016/0883-2889\(87\)90180-8](https://doi.org/10.1016/0883-2889(87)90180-8).

- [108] A. M. Lane and R. G. Thomas. *Reviews of Modern Physics* 30 (1958), pp. 257–353. DOI: [10.1103/RevModPhys.30.257](https://doi.org/10.1103/RevModPhys.30.257).
- [109] R. E. Azuma *et al.* *Physical Review C* 81 (2010), p. 045805. DOI: [10.1103/PhysRevC.81.045805](https://doi.org/10.1103/PhysRevC.81.045805).
- [110] M. Munch (2018). arXiv: [1802.09297](https://arxiv.org/abs/1802.09297).
- [111] M. Munch, O. S. Kirsebom, and J. Refsgaard. *Open R-matrix*. Feb. 2018. DOI: [10.5281/zenodo.1174079](https://doi.org/10.5281/zenodo.1174079).
- [112] M. Munch and H. O. Uldall Fynbo. *The European Physical Journal A* 54 (2018), p. 138. DOI: [10.1140/epja/i2018-12577-3](https://doi.org/10.1140/epja/i2018-12577-3). arXiv: [1805.10924](https://arxiv.org/abs/1805.10924).
- [113] O. Beckman, T. Huus, and Č. Zupančič. *Physical Review* 91 (1953), pp. 606–609. DOI: [10.1103/PhysRev.91.606](https://doi.org/10.1103/PhysRev.91.606).
- [114] G. Symons and P. Treacy. *Nuclear Physics* 46 (1963), pp. 93–107. DOI: [10.1016/0029-5582\(63\)90567-4](https://doi.org/10.1016/0029-5582(63)90567-4).
- [115] R. E. Segel, S. S. Hanna, and R. G. Allas. *Physical Review* 139 (1965), B818–B830. DOI: [10.1103/PhysRev.139.B818](https://doi.org/10.1103/PhysRev.139.B818).
- [116] J. M. Davidson *et al.* *Nuclear Physics, Section A* 315 (1979), pp. 253–268. DOI: [10.1016/0375-9474\(79\)90647-X](https://doi.org/10.1016/0375-9474(79)90647-X).
- [117] F. Borchers *et al.* *Nuclear Physics A* 405 (1983), pp. 141–158. DOI: [10.1016/0375-9474\(83\)90328-7](https://doi.org/10.1016/0375-9474(83)90328-7).
- [118] H. W. Becker, C. Rolfs, and H. P. Trautvetter. *Zeitschrift für Physik A Atomic Nuclei* 327 (1987), pp. 341–355. DOI: [10.1007/BF01284459](https://doi.org/10.1007/BF01284459).
- [119] C. Spitaleri *et al.* *Physical Review C* 69 (2004), p. 055806. DOI: [10.1103/PhysRevC.69.055806](https://doi.org/10.1103/PhysRevC.69.055806).
- [120] M. L. E. Oliphant and L. Rutherford. *Proceedings of the Royal Society A: Mathematical, Physical and Engineering Sciences* 141 (1933), pp. 259–281. DOI: [10.1098/rspa.1933.0117](https://doi.org/10.1098/rspa.1933.0117).
- [121] D. Dehnhard, D. Kamke, and P. Kramer. *Physics Letters* 3 (1962), pp. 52–55. DOI: [10.1016/0031-9163\(62\)90199-3](https://doi.org/10.1016/0031-9163(62)90199-3).

- [122] J. Bronson *et al.* *Nuclear Physics* 68 (1965), pp. 241–269. DOI: [10.1016/0029-5582\(65\)90643-7](https://doi.org/10.1016/0029-5582(65)90643-7).
- [123] Y. Chen *et al.* *Nuclear Physics A* 106 (1967), pp. 1–13. DOI: [10.1016/0375-9474\(67\)90823-8](https://doi.org/10.1016/0375-9474(67)90823-8).
- [124] J. Quebert and L. Marquez. *Nuclear Physics A* 126 (1969), pp. 646–670. DOI: [10.1016/0375-9474\(69\)90854-9](https://doi.org/10.1016/0375-9474(69)90854-9).
- [125] K. Schäfer. *Nuclear Physics A* 140 (1970), pp. 9–22. DOI: [10.1016/0375-9474\(70\)90880-8](https://doi.org/10.1016/0375-9474(70)90880-8).
- [126] R. Dalitz. *Philosophical Magazine* 44 (1953), pp. 1068–1080. DOI: [10.1080/14786441008520365](https://doi.org/10.1080/14786441008520365).
- [127] D. Dehnhard, D. Kamke, and P. Kramer. *Annalen der Physik* 469 (1964), pp. 201–220. DOI: [10.1002/andp.19644690311](https://doi.org/10.1002/andp.19644690311).
- [128] D. Kamke and J. Krug. *Zeitschrift für Physik* 201 (1967), pp. 301–322. DOI: [10.1007/BF01326819](https://doi.org/10.1007/BF01326819).
- [129] G. C. Phillips. *Reviews of Modern Physics* 37 (1965), pp. 409–417. DOI: [10.1103/RevModPhys.37.409](https://doi.org/10.1103/RevModPhys.37.409).
- [130] H. O. U. Fynbo *et al.* *Physical Review Letters* 91 (2003), p. 082502. DOI: [10.1103/PhysRevLett.91.082502](https://doi.org/10.1103/PhysRevLett.91.082502).
- [131] O. S. Kirsebom *et al.* *Physical Review C* 81 (2010), p. 064313. DOI: [10.1103/PhysRevC.81.064313](https://doi.org/10.1103/PhysRevC.81.064313).
- [132] O. S. Kirsebom *et al.* *Physical Review Letters* 108 (2012), p. 202501. DOI: [10.1103/PhysRevLett.108.202501](https://doi.org/10.1103/PhysRevLett.108.202501).
- [133] K. L. Laursen *et al.* *The European Physical Journal A* 52 (2016), p. 271. DOI: [10.1140/epja/i2016-16271-2](https://doi.org/10.1140/epja/i2016-16271-2). arXiv: [1604.01244](https://arxiv.org/abs/1604.01244).
- [134] D. P. Balamuth, R. W. Zurmühle, and S. L. Tabor. *Physical Review C* 10 (1974), pp. 975–986. DOI: [10.1103/PhysRevC.10.975](https://doi.org/10.1103/PhysRevC.10.975).
- [135] F. E. James. CERN, 1968. DOI: [10.5170/CERN-1968-015](https://doi.org/10.5170/CERN-1968-015).
- [136] J. R. Oppenheimer and R. Serber. *Physical Review* 53 (1938), pp. 636–638. DOI: [10.1103/PhysRev.53.636](https://doi.org/10.1103/PhysRev.53.636).



- [137] B. Anderson *et al.* *Nuclear Physics A* 233 (1974), pp. 286–296. DOI: [10.1016/0375-9474\(74\)90456-4](https://doi.org/10.1016/0375-9474(74)90456-4).
- [138] J. A. Wheeler. *Physical Review* 59 (1941), pp. 27–36. DOI: [10.1103/PhysRev.59.27](https://doi.org/10.1103/PhysRev.59.27).
- [139] Y. Xu *et al.* *Nuclear Physics A* 918 (2013), pp. 61–169. DOI: [10.1016/j.nuclphysa.2013.09.007](https://doi.org/10.1016/j.nuclphysa.2013.09.007).
- [140] C. Angulo *et al.* *Nuclear Physics A* 656 (1999), pp. 3–183. DOI: [10.1016/S0375-9474\(99\)00030-5](https://doi.org/10.1016/S0375-9474(99)00030-5).
- [141] G. R. Caughlan and W. A. Fowler. *Atomic Data and Nuclear Data Tables* 40 (1988), pp. 283–334. DOI: [10.1016/0092-640X\(88\)90009-5](https://doi.org/10.1016/0092-640X(88)90009-5).
- [142] A. Picciotto *et al.* *Physical Review X* 4 (2014), p. 031030. DOI: [10.1103/PhysRevX.4.031030](https://doi.org/10.1103/PhysRevX.4.031030).
- [143] C. Baccou *et al.* *Laser and Particle Beams* 33 (2015), pp. 117–122. DOI: [10.1017/S0263034615000178](https://doi.org/10.1017/S0263034615000178).
- [144] Y. K. Kurilenkov, V. P. Tarakanov, and S. Y. Gus'kov. *Journal of Physics: Conference Series* 774 (2016), p. 012133. DOI: [10.1088/1742-6596/774/1/012133](https://doi.org/10.1088/1742-6596/774/1/012133).
- [145] D. Giulietti *et al.* *Nuclear Instruments and Methods in Physics Research Section B: Beam Interactions with Materials and Atoms* 402 (2017), pp. 373–375. DOI: [10.1016/j.nimb.2017.03.076](https://doi.org/10.1016/j.nimb.2017.03.076).
- [146] A. Friebel *et al.* *Nucl. Phys. A* 294 (1978), pp. 129–140. DOI: [10.1016/0375-9474\(78\)90399-8](https://doi.org/10.1016/0375-9474(78)90399-8).
- [147] F. Cecil *et al.* *Nucl. Phys. A* 539 (1992), pp. 75–96. DOI: [10.1016/0375-9474\(92\)90236-D](https://doi.org/10.1016/0375-9474(92)90236-D).
- [148] L. Giuffrida *et al.* *AIP Advances* 6 (2016). DOI: [10.1063/1.4965254](https://doi.org/10.1063/1.4965254). arXiv: [1608.06778](https://arxiv.org/abs/1608.06778).
- [149] *YY1 data sheet*. Accessed: 2018-05-10. Micron Semiconductor Ltd. URL: <http://www.micronsemiconductor.co.uk/product/yy1/>.
- [150] H. T. Johansson. *The ucesb unpacker generator*. 2010.

- [151] M. Michael and J. H. Jensen. *Unpacker specification*. URL: <https://git.kern.phys.au.dk/ausa/unpacker>.
- [152] D. Torresi *et al.* *Nuclear Instruments and Methods in Physics Research Section A: Accelerators, Spectrometers, Detectors and Associated Equipment* 713 (2013), pp. 11–18. DOI: [10.1016/J.NIMA.2013.02.027](https://doi.org/10.1016/j.nima.2013.02.027).
- [153] M. Michael *et al.* *Sorter*. URL: <https://git.kern.phys.au.dk/ausa/Sorter>.
- [154] M. Michael, J. H. Jensen, and O. S. Kirsebom. *Identifier*. URL: <https://git.kern.phys.au.dk/ausa/Identifier>.
- [155] M. Michael, J. H. Jensen, and O. S. Kirsebom. *Eventbuilder*. URL: <https://git.kern.phys.au.dk/ausa/EventBuilder>.
- [156] S. Agostinelli *et al.* *Nuclear Instruments and Methods in Physics Research Section A: Accelerators, Spectrometers, Detectors and Associated Equipment* 506 (2003), pp. 250–303. DOI: [10.1016/S0168-9002\(03\)01368-8](https://doi.org/10.1016/S0168-9002(03)01368-8).
- [157] M. J. Berger *et al.* *Journal of the International Commission on Radiation Units and Measurements* os25 (1993). DOI: [10.1093/jicru/os25.2.Report49](https://doi.org/10.1093/jicru/os25.2.Report49).
- [158] J. F. Ziegler, M. D. Ziegler, and J. P. Biersack. *Nuclear Instruments and Methods in Physics Research B* 268 (2010), pp. 1818–1823. DOI: [10.1016/j.nimb.2010.02.091](https://doi.org/10.1016/j.nimb.2010.02.091).
- [159] D. Eberly. *Least-Squares Fitting of Data with B-Spline Curves*. Feb. 2014. URL: <https://www.geometrictools.com/Documentation/BSplineCurveLeastSquaresFit.pdf> (visited on 07/24/2018).
- [160] M. Galassi. *GNU Scientific Library Reference Manual*. Bristol: Network Theory Ltd., 2006. ISBN: 0954161734.
- [161] O. Tengblad *et al.* *Nuclear Instruments and Methods in Physics Research Section A: Accelerators, Spectrometers, Detectors and Associated Equipment* 525 (2004), pp. 458–464. DOI: [10.1016/j.nima.2004.01.082](https://doi.org/10.1016/j.nima.2004.01.082).

- [162] N. Clarke, Micron Semiconductors Ltd. Private communication. March 2017.
- [163] G. T. Koldste. “Deciphering drip-line decays — the case of 31 Ar.” PhD thesis. Aarhus University, 2015.
- [164] M. Michael and J. H. Jensen. *Calibrator*. URL: <https://git.kern.phys.au.dk/ausa/Calibrator>.
- [165] M. Munch *et al.* *Submitted* (2018). arXiv: 1810.03574.
- [166] CMS Collaboration. *Journal of Instrumentation* 12 (2017), pp. 01020–01020. DOI: 10.1088/1748-0221/12/01/P01020. arXiv: 1609.02366.
- [167] W. R. Leo. *Techniques for Nuclear and Particle Physics Experiments: A How-to Approach*. Springer, 1994. ISBN: 3540572805.
- [168] *HPTDC - High Performance Time to Digital Converter*. Version 2.2. CERN. Feb. 2009.
- [169] J. Hoffman. *VULOM4B data sheet*. Feb. 2013. URL: [https://www.gsi.de/fileadmin/EE/Module/VULOM/vulom4B\\_3.pdf](https://www.gsi.de/fileadmin/EE/Module/VULOM/vulom4B_3.pdf) (visited on 10/20/2018).
- [170] H. T. Johansson *et al.* *GSI Sci. Rep.* (2013), p. 354. DOI: 10.15120/GR-2014-1-FG-S-FRS-15.
- [171] G. F. Knoll. *Radiation Detection And Measurement, 4Th Edition*. Wiley India, 2011. ISBN: 0470131489.
- [172] H. T. Johansson. *TRLO II - flexible FPGA trigger control*. 2018. URL: <http://fy.chalmers.se/~f96hajo/trloii/> (visited on 06/28/2018).
- [173] *American National Standard for VME64*. Standard. ANSI/VITA, 1994.
- [174] *2eSST*. Standard. ANSI/VITA, 2003.
- [175] H. G. Essel and N. Kurz. *Nucl. Sci. IEEE Trans.* 47 (2000), pp. 337–339. DOI: 10.1109/23.846176.

- [176] H. T. Johansson. *drasi — data acquisition*. 2018. URL: <http://fy.chalmers.se/~f96hajo/drasi/doc/> (visited on 06/27/2018).
- [177] *MVME5500 Single-Board Computer Programmer's Reference Guide*. Motorola Inc. Tempe, AZ, Oct. 2003.
- [178] *RIO4-8072 User Manual, version 1.0*. CES. Geneva, Switzerland, Nov. 2009.
- [179] B. Löher *et al.* *GSI Sci. Rep.* (2014), p. 192. DOI: [10.15120/GR-2015-1-MU-NUSTAR-NR-08](https://doi.org/10.15120/GR-2015-1-MU-NUSTAR-NR-08).
- [180] J. Adamczewski *et al.* *IEEE Transactions on Nuclear Science* 51 (2004), pp. 565–570. DOI: [10.1109/TNS.2004.828632](https://doi.org/10.1109/TNS.2004.828632).
- [181] N. Kurz and J. Adamczewski-Musch. *GSI Data Acquisition System MBS Release Notes V6.2*. GSI. Darmstadt, Germany, Apr. 2013.
- [182] InfluxData. *InfluxDB*. Version 1.4.2. June 27, 2018.
- [183] Grafana Labs. *Grafana*. Version 5.1.0. June 27, 2018.
- [184] I. Lazarus *et al.* *IEEE Transactions on Nuclear Science* 48 (2001), pp. 567–569. DOI: [10.1109/23.940120](https://doi.org/10.1109/23.940120).
- [185] H. Peng *et al.* *2007 IEEE Nuclear Science Symposium Conference Record*. IEEE, pp. 3328–3331. DOI: [10.1109/NSSMIC.2007.4436846](https://doi.org/10.1109/NSSMIC.2007.4436846).
- [186] E. Pollacco *et al.* *Nuclear Instruments and Methods in Physics Research Section A: Accelerators, Spectrometers, Detectors and Associated Equipment* 887 (2018), pp. 81–93. DOI: [10.1016/J.NIMA.2018.01.020](https://doi.org/10.1016/J.NIMA.2018.01.020).
- [187] I. Rusanov *et al.* (2014). DOI: [10.15120/GR-2014-1-FG-CS-04](https://doi.org/10.15120/GR-2014-1-FG-CS-04).
- [188] A. Charpy *et al.* *Technical Report for the Design of the NUSTAR Data Acquisition System*. GSI/FAIR, 2018.
- [189] *V785 data sheet*. Rev. 13. CAEN S.p.A. Dec. 2012.
- [190] *MADC-32 data sheet*. v. 2.1\_03. mesytec.
- [191] H. T. Johansson. “The DAQ always runs.” Licentiate Thesis. Chalmers University of Technology, 2006.

- [192] T. Neff. *Physical review letters* 106 (2011), p. 042502. DOI: [10.1103/PhysRevLett.106.042502](https://doi.org/10.1103/PhysRevLett.106.042502).
- [193] P. Navrátil, R. Roth, and S. Quaglioni. *Physics Letters, Section B: Nuclear, Elementary Particle and High-Energy Physics* 704 (2011), pp. 379–383. DOI: [10.1016/j.physletb.2011.09.079](https://doi.org/10.1016/j.physletb.2011.09.079). arXiv: [1105.5977](https://arxiv.org/abs/1105.5977).

